Steel Fibre-Reinforced Concrete:

Multi-scale Characterisation towards Numerical Modelling

by

Stephan Zeranka

Dissertation presented for the degree of

Doctor of Philosophy in the Faculty of Engineering

at Stellenbosch University

Supervisor: Prof. Gideon P.A.G van Zijl

December 2017

Declaration

By submitting this dissertation electronically, I declare that the entirety of the work contained therein is my own, original work, that I am the sole author thereof (save to the extent explicitly otherwise stated), that reproduction and publication thereof by Stellenbosch University will not infringe any third party rights and that I have not previously in its entirety or in part submitted it for obtaining any qualification.

December 2017

UNIVERSITEIT·STELLENBOSCH·UNIVERSITY
jou kennisvennoot • your knowledge partner

Plagiaatverklaring / Plagiarism *Declaration*

1 Plagiaat is die oorneem en gebruik van die idees, materiaal en ander intellektuele eiendom van ander persone asof dit jou eie werk is.
Plagiarism is the use of ideas, material and other intellectual property of another's work and to present is as my own.

2 Ek erken dat die pleeg van plagiaat 'n strafbare oortreding is aangesien dit 'n vorm van diefstal is.
I agree that plagiarism is a punishable offence because it constitutes theft.

3 Ek verstaan ook dat direkte vertalings plagiaat is.
I also understand that direct translations are plagiarism.

4 Dienooreenkomstig is alle aanhalings en bydraes vanuit enige bron (ingesluit die internet) volledig verwys (erken). Ek erken dat die woordelikse aanhaal van teks sonder aanhalingstekens (selfs al word die bron volledig erken) plagiaat is.
Accordingly all quotations and contributions from any source whatsoever (including the internet) have been cited fully. I understand that the reproduction of text without quotation marks (even when the source is cited) is plagiarism.

5 Ek verklaar dat die werk in hierdie skryfstuk vervat, behalwe waar anders aangedui, my eie oorspronklike werk is en dat ek dit nie vantevore in die geheel of gedeeltelik ingehandig het vir bepunting in hierdie module/werkstuk of 'n ander module/werkstuk nie.
I declare that the work contained in this assignment, except where otherwise stated, is my original work and that I have not previously (in its entirety or in part) submitted it for grading in this module/assignment or another module/assignment.

15043568 **Studentenommer / *Student number***	 **Handtekening / *Signature***
S. Zeranka **Voorletters en van / *Initials and surname***	12 September 2017 **Datum / *Date***

Abstract

In recent years, Steel Fibre-Reinforced Concrete (SFRC) applications have increased in quantity and variety, due to its potential to partially or totally replace conventional reinforcement (*rebar* or welded mesh). Methods for material characterisation, constitutive modelling and design must therefore be improved in order to facilitate the demand for greater structural application of SFRC.

A large database of experimental data and empirical models from the analysis of scaled or full-scale shear-critical SFRC structural beams has accumulated. It is therefore concluded from a survey that material-level characterisation and constitutive modelling may be more beneficial in facilitating the demand for greater structural application. Consequently, the primary mechanisms governing the fundamental behaviour of SFRC need to be characterised in order to produce a direct definition of the material's constitutive model.

Far less work has been done on the direct shear response of fibre reinforced concretes. Even fewer investigations attempt to link the Micro-scale (i.e. the transverse pull-out of steel fibres) to the Meso-scale (i.e. at the scale of a single crack) for Mode II fracture. At the time of publication of *Soetens & Matthys (2012)*, only one other study, *Lee & Foster (2006)* was known that applies this method for investigating the Mode II fracture of SFRC.

Analogous to existing numerical tools for reinforced concrete (RC) membrane elements, research towards a constitutive material model and numerical procedure for the analysis of SFRC membrane elements is considered to be essential. A direct and rational approach to model the generic material response also has the potential to allow for tailoring and optimisation in material and structural design.

Three scales of observation or analysis are defined in this dissertation, namely the Micro-scale (single fibre level), Meso-scale (single crack level) and Macro-scale (structural level). Here attention is given only to the Micro and Meso-scale.

In order to contribute to multi-scale characterisation towards constitutive and numerical modelling, the outcomes of this dissertation in sequence are: Adapt a composite design procedure and develop a SFRC; Classify the composite in terms of standard performance indicators and testing procedures; Design, fabricate and execute experimental tests to characterise the Mode I and Mode II fracture at the Micro and Meso-scale of observation; Develop a material model and verify it numerically: This requires the implementation of an analytical formulation of the material model into a numerical procedure. The material model is calibrated with the experimental data and verified via a Finite Element (FE) representation of the experimental Meso-scale test. Finally, an empirical model is also developed which reconciles the fibre component with the Mode II Meso-scale response.

Two useful technologies are utilised to assist in material characterisation, Computed Tomography (CT-scan) and Digital Image Correlation (DIC). The CT-scanning facility provides valuable insight into the fibre distribution and the ability to analyse and quantify the fibre orientation distribution is a powerful tool. The non-contact measurement method (Aramis DIC) proved invaluable in determining the specimen shear displacement and rotation.

This dissertation provides insight into experimental design for the fundamental fracture modes of SFRC. A contribution is made to the limited literature available on the link between the single fibre transverse pull-out response and the composite Mode II fracture behaviour. The numerical and empirical models developed simulate the composite response well, given their relative simplicity and limited experimental data. The constitutive model and numerical procedure should aid in material design and provide a foundation for defining material laws.

Opsomming

Staalvesel-bewapende beton (SVBB) het die potensiaal om tradisionele bewapening in beton gedeeltelik, of selfs totaal te vervang. Gevolglik het SVBB toepassings die afgelope jare toegeneem, nie net in hoeveelheid nie, maar ook in verskeidenheid. Om die aanvraag vir meer strukturele toepassings van SVBB te fasiliteer, moet metodes vir materiaalkarakterisering, konstitutiewe modellering en ontwerp verbeter word.

Die aanvanklike fokus van hierdie verhandeling was die studie van volskaal en/of afgeskaalde bewapende SVBB balke onderworpe aan skuifdominante faling. 'n Literatuurstudie is uitgevoer met die gevolgtrekking dat 'n groot databasis van eksperimentele data en empiriese modelle versamel het oor die afgelope 40 tot 50 jaar. Enige nuwe bydrae tot hierdie navorsingsveld vereis die analise van meerdere vlakke van die strukturele probleem, deur middel van materiaalvlak karakterisering en konstitutiewe modellering. Gevolglik moet die hoof meganismes wat die fundamentele gedrag van SVBB oorheers gekarakteriseer word ten einde 'n direkte definisie van die materiaal se konstitutiewe model te produseer.

Minder aandag is gegee aan die direk skuif/Mode II fraktuur gedrag van vesel-bewapende beton (VBB). Nog minder ondersoeke poog om die Mikro-skaal (d.w.s. die dwars uittrek van enkele staalvesels uit 'n sement matriks) te koppel met die Meso-skaal (d.w.s. die gedrag by 'n enkele kraak in SVBB) vir Mode II fraktuur. So ver die outeur kon vasstel, is daar net twee vorige studies wat dit al ondersoek het, naamlik *Soetens & Matthys (2012)* en *Lee & Foster (2006)*.

Die modellering van SVBB as 'n membraanelement, analoog aan bestaande numeriese metodes vir tradisionele bewapende beton, is gevolg. 'n Direkte en rasionele benadering om die generiese materiaalgedrag te modelleer laat toe vir optimering van materiaal- en struktuur-ontwerp.

Drie vlakke van ondersoek is gedefinieer in hierdie tesis, naamlik die Mikro-vlak (gedrag van 'n enkel vesel), Meso-vlak (gedrag van 'n enkel kraak in SVBB) en Makro-vlak (struktuur vlak). In hierdie verhandeling is aandag gevestig op die Mikro- en Meso-vlak.

Ten einde by te dra tot multivlak karakterisering, en konstitutiewe en numeriese modellering, is die uitkomstes van hierdie tesis soos volg: Ontwikkel 'n mengontwerp prosedure en 'n SVBB; Klassifiseer die meng in terme van standaard gehalte-aanwysers en toetsprosedures; Ontwerp, vervaardig en voer eksperimentele toetse uit om die Mode I en Mode II fraktuur te karakteriseer vir beide die Mikro- en Meso-vlak; Skep 'n materiaalmodel en verifieer dit numeries: Dit vereis die implementering van 'n analitiese formulering van die materiaalmodel in 'n numeriese prosedure. Die materiaalmodel is gekalibreer met die eksperimentele data en geverifieer deur middel van 'n eindige element verteenwoordiging van die eksperimentele Meso-vlak toets. Uiteindelik is 'n empiriese model ook geskep wat die veselkomponent vir Mode II fraktuur (gekarakteriseer deur die Mikro-vlak toetse) versoen met die Mode II Meso-vlak gedrag.

Twee nuttige tegnologieë is gebruik vir materiaal karakterisering, naamlik rekenaar tomografie (X-straal CT-skandering) en digitale beeldkorrelasie (DIC). Die CT-skandering fasiliteit maak dit moontlik om die vesel-verspreiding in 'n proefstuk te kwantifiseer in terme van vesel-oriëntasie, aantal vesels in 'n snit en gemiddelde vesel-verankeringslengte. Die Aramis (DIC) apparaat het dit moontlik

gemaak om proefstuk-verplasings en deformasie te meet sonder montering van instrumentasie direk op die proefstuk. Dit het die meet van skuif-deformasie en rotasie aansienlik vergemaklik.

Ten slotte gee die verhandeling insig in eksperimentele ontwerp vir die fundamentele fraktuur modes van SVBB. ’n Bydrae is gemaak tot die beperkte literatuur beskikbaar vir die koppeling tussen enkel-vesel dwars uittrek gedrag (Mikro-vlak) en die Meso-vlak Mode II fraktuur. Die numeriese en empiriese modelle ontwikkel simuleer die materiaal gedrag goed, ten spyte van hul relatiewe eenvoud en beperkte eksperimentele data. Die konstitutiewe model en numeriese prosedure bied ’n basis vir die definisie van materiaalwette en materiaal-ontwerp.

Acknowledgements

"We never think entirely alone: we think in company, in a vast collaboration; we work with the workers of the past and of the present. In the whole intellectual world… each one finds in those about him (or her) the initiation, help, verification, information, encouragement, that he (or she) needs" – *Sertillanges (1978)*. I therefore express my gratitude to those who have contributed to my academic, professional and personal growth.

To my research supervisor, Prof. Gideon van Zijl: Thank you for your guidance, encouragement, support and constructive criticism.

To Prof. Billy Boshoff: Thank you for your understanding and guidance, and granting me the time and freedom I needed to complete this dissertation during my appointment as the laboratory manager.

To the laboratory staff, including: Johan van der Merwe, Dion Viljoen, Charlton Ramat and Peter Cupido: Thank you for your time, effort and technical assistance.

I also gratefully acknowledge the financial support given by the University of Stellenbosch, Tubular Track, NRF/DAAD and the Wilhelm Frank Bursary, as well as the organisational support from Bekaert, Mapei and PPC Cement in the form of material donations.

Finally, I would like to thank my family and friends for their kind and loving support.

S. Zeranka 2017

Table of contents

Title page i

Declaration ii

Plagiarism declaration iii

Abstract iv

Opsomming vi

Acknowledgements viii

Table of contents ix

Chapter 1: Introduction 1

1.1 Research background and scope 1
1.2 Research objectives and constraints 3
1.2.1 Towards numerical modelling 3
1.2.2 Multi-scale characterisation 3
1.2.3 Research outcomes 3
1.3 Research methodology 4
1.4 Thesis structure 5

Chapter 2: Conceptual and methodological framework 6

2.1 The Macro-scale: Steel fibre reinforcement of shear-critical RC beams 6
2.1.1 Research significance 7
2.1.2 Material parameters and structural enhancement 7
2.1.3 Shear transfer mechanisms 8
2.1.4 The synergetic effect of fibre and stirrup reinforcement 12
2.1.5 Experimental design 12
2.1.6 Modelling 13
2.1.7 Shear design provisions for R-SFRC 14
Conclusions 15
2.2 Steel fibre-reinforced self-consolidating concrete 15
2.2.1 Self-Consolidating Concrete (SCC) 15
2.2.2 Steel Fibre-Reinforced Self-Consolidating Concrete (SFR-SCC) 17
2.3 Mechanical investigations of Mode I fracture at the Meso-scale 18
2.3.1 Specimen shape and dimensions 18
2.3.2 Specimen boundary conditions 19
2.4 Mechanical investigations of Mode II fracture at the Meso-scale 20
2.5 Experimental investigation of axial and transverse fibre pull-out 21
2.5.1 Experimental tests 22
2.5.2 Results and discussion 22
2.6 Digital Image Correlation and Computed Tomography 24

2.6.1 Digital Image Correlation 24
2.6.2 Computed Tomography 25
Summary 26

Chapter 3: Composite design and classification 27

3.1 Composite design method 27
3.1.1 Paste phase 27
3.1.2 Mortar phase 27
3.1.3 Concrete and fibre-reinforcement phase 28
3.2 Constituent properties 29
3.2.1 Fine and coarse aggregate 29
3.2.2 Powder material 31
3.2.3 Admixtures 33
3.2.4 Fibre 33
3.3 Production method 33
3.3.1 Mixing procedure 33
3.3.2 Casting procedure 35
3.3.3 Specimen curing and preparation for testing 35
3.4 Material classification 36
3.4.1 Compressive strength development 36
3.4.2 Elastic compression modulus 36
3.4.3 Post fracture energy and toughness 37
Summary and conclusions 46

Chapter 4: Meso and Micro-mechanical investigation of Mode I fracture 47

4.1 Experimental investigation at the Meso-scale 48
4.1.1 Specimen design 48
4.1.2 Experimental program and production method 53
4.1.3 Test setup and procedure 54
4.1.4 Test results and discussion 55
4.2 Experimental investigation at the Micro-scale 61
4.2.1 Experimental program and production method 61
4.2.2 Test setup and procedure 63
4.2.3 Test results and discussion 63
Summary and conclusions 66

Chapter 5: Meso and Micro-mechanical investigation of Mode II fracture 68

5.1 Experimental investigation at the Meso-scale 69
5.1.1 Specimen design 69
5.1.2 Experimental program and production method 74
5.1.3 Test setup and procedure 75
5.1.4 Test results and discussion 77
5.1.5 Analysis of fibre distribution via Computed Tomography (CT-scan) 85
5.2 Experimental investigation at the Micro-scale 87

5.2.1 Experimental program, specimen design and production method 87
5.2.2 Test setup and procedure 89
5.2.3 Test results and discussion 89
Summary and conclusions 94

Chapter 6: Constitutive model and numerical verification 96

6.1 Modelling concept 96
6.2 Analytical formulation of material model 97
6.2.1 Mode I parameters 98
6.2.2 Mode II parameters 100
6.2.3 Normal stress parallel to crack 101
6.3 Numerical procedure 101
6.3.1 Overview of the procedure: Input and Output 101
6.3.2 Determining and storing the material state: uncracked or cracked 102
6.3.3 Elastic domain (Linear elastic isotropy) 103
6.3.4 Cracked domain: Derivation of stress-strain relation 103
6.3.5 Cracked domain: Procedure 107
6.4 Model verification for a single finite element 108
6.4.1 Material input parameters 108
6.4.2 Element type and dimensions 108
6.4.3 Boundary conditions 108
6.4.4 Analysis output 109
6.5 Model calibration with Meso-scale data 112
6.5.1 Calibration of Mode I model 112
6.5.2 Calibration of Mode II model 113
6.6 Model verification via Meso-scale Iosipescu shear test 114
6.6.1 Model details 114
6.6.2 Analysis output 115
6.7 Empirical link between Micro and Meso-scale data 118
6.7.1 Model description 119
6.7.2 Model input 120
6.7.3 Model validation 120
6.7.4 User-defined fibre orientation analysis and discussion 121
Summary and conclusions 123

Chapter 7: Conclusions and recommendations 124

7.1 Conceptual and methodological framework 125
7.2 Composite design and classification 125
7.2.1 Compressive strength development 125
7.2.2 Elastic compression modulus 125
7.2.3 Wedge-splitting test 125
7.2.4 Flexural response 126
7.3 Meso and Micro-mechanical investigation of Mode I fracture 126

7.3.1 Experimental investigation at the Meso-scale 126
7.3.2 Experimental investigation at the Micro-scale 127
7.4 Meso and Micro-mechanical investigation of Mode II fracture 128
7.4.1 Experimental investigation at the Meso-scale 128
7.4.2 Experimental investigation at the Micro-scale 130
7.5 Constitutive model and numerical verification 130
7.5.1 Model verification via Meso-scale Iosipescu shear test 131
7.5.2 Empirical link between Micro and Meso-scale 131
Summary 132

References **133**

Addenda **139**

A List of abbreviations 139

B List of notations and symbols 140

C Trial self-consolidating mortar designs 143

D Meso and Micro-mechanical investigation of Mode II fracture 145

E FORTRAN code for UMAT 183

F Mode II calibration & verification data 191

G Empirical link between Micro and Meso-scale data 197

Chapter 1

Introduction

1.1 Research background and scope

Fibrous materials have been used since antiquity to reinforce and strengthen brittle building materials. The earliest examples included mixing straw in clay and hair in mortar and plaster (*ACI 544.1R-96, 1996*). Today, a wide range of engineered composites incorporate a variety of fibre-like materials to enhance their properties.

Unreinforced concrete is brittle and has a low tensile strength and strain capacity. Traditionally, steel reinforcing bar or *rebar* is used to overcome these shortcomings and has been applied effectively since the 19th century. However, this type of reinforcement does not change the properties of the concrete composite itself, which is still prone to cracking and liable to reduce the durability and serviceability of the structure.

Research into the addition of short steel reinforcing elements to the concrete mixture, such as nails, wire segments, and metal chips, to improve the properties of concrete, date from 1910 (*ACI 544.1R-96, 1996*). The first major study to evaluate the potential of steel fibre as an alternative reinforcement for concrete was undertaken in the early 1960s (*ACI 544.1R-96, 1996*). Today steel fibre reinforcement has the potential to partially or totally replace conventional reinforcement (rebar or welded mesh). The size of steel fibre-reinforced concrete (SFRC) elements can also be reduced because of the improved durability. In the past, the majority of applications for SFRC were limited to industrial floors and segments for tunnel linings. However, due to the interest in the use of SFRC in structural members, the growth of the prefabrication industry and the demand for more complex structural aesthetics, such as the SFRC Shotcrete shell structure in Valencia, Spain (see *Fig. 1.1a*), SFRC applications have increased in quantity and variety (*de Oliveira, 2010; Bernardi et al., 2012*).

The primary enhancement to concrete, due to fibre reinforcement, is increased toughness, in the form of residual (post-cracking) strength and ductility. This is achieved via the crack 'bridging' ability of individual fibres (see *Fig. 1.1b*), where the width and propagation of a crack is arrested. Fibre-reinforced cement-based composites may generally be classified into two distinct groups, based on whether the uniaxial tensile response of the material is *strain-hardening* (increased resistance after initial cracking) or *strain-softening* (decreased resistance after initial cracking) (*Naaman et al., 2007*). *Fig. 1.2* broadly defines the classification of FRC composites based on tensile response. A *strain-hardening* cement-based composite (or *SHCC*) generates multiple cracks and has greater toughness

and energy absorption capacity, whereas *a strain-softening* composite, the subject of this investigation, undergoes immediate crack localisation and only generates a single crack (*Naaman et al., 2007*). When placed in a structural context, *strain-softening* composites may exhibit improved performance or even hardening-type behaviour due to the redistribution of stresses within the cross-section.

The initial motivation of this dissertation was the envisaged partial and/or complete replacement of conventional shear reinforcement (vertical links or stirrups) with steel fibre-reinforcement in structural RC prismatic beam members subject to shear-dominant loading. The outcomes would be aligned with a case study for a local manufacturer of precast railway lines, Tubular Track.

An extensive literature review, elaborated in *Chapter 2*, spanning the last four to five decades reports on some of the key developments and issues surrounding the topic of SFRC beams subject to shear-dominant loading. In summary, a large database of experimental data and empirical models on scaled or full-scale structural beams has been accumulated. It is therefore concluded from the survey that material-level characterisation and constitutive modelling may be more beneficial in facilitating the demand for greater structural application. Consequently, the primary mechanisms governing the fundamental behaviour of SFRC need to be characterised in order to produce a direct definition of the material's constitutive model.

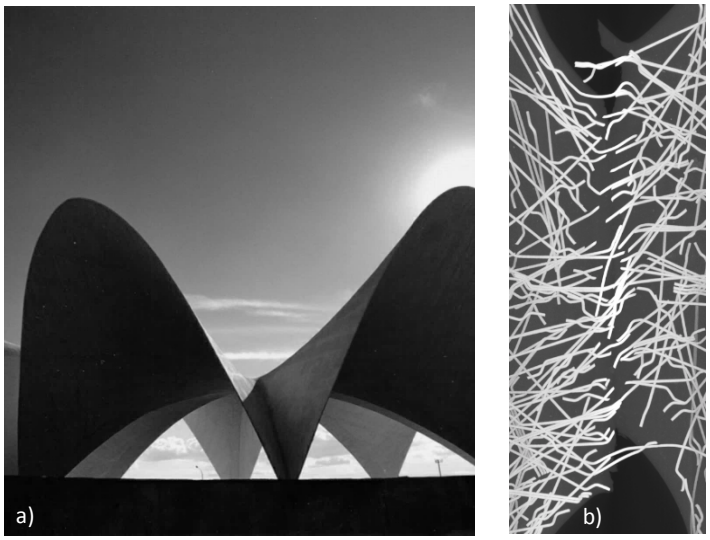

Fig. 1.1 – a) SFRC Shotcrete shell structure in Valencia, Spain (*Bekaert Dramix®; de Oliveira, 2010*); b) Fibres bridging a shear crack - CT-scan (*Zeranka & van Zijl, 2015*)

Several steps have to be taken before a new construction material and/or method can be accepted for a specific application. In reverse order these steps are: (1) Commercial application – reliable and economical structural applications must be identified or created. Production must be aligned with industrialisation in terms of labour, rate of construction and quality control; (2) Standards, certification and design tools – codified design criteria must be established; (3) Design recommendations have to be sourced from national and international standards or guidelines; (4) Development of constitutive material models as the culmination of (5) fundamental research gathered from the research community. This research attempts to contribute to steps no. (4) and (5), in the form of material characterisation and constitutive modelling, while attempting to remain cognisant of the literature and existing debates on all these important steps.

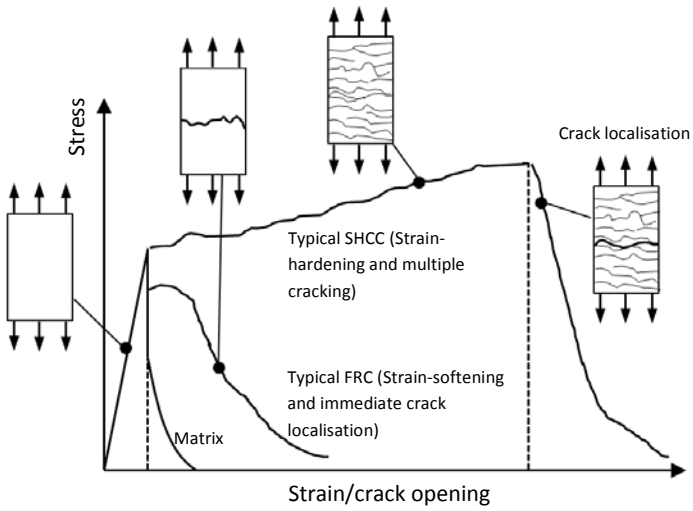

Fig. 1.2 – Classification of FRC composites based on tensile response (*Naaman et al., 2007; Jůn, 2011*)

1.2 Research objectives and constraints

1.2.1 Towards numerical modelling

The majority of research in the field of SFRC is focused on the tensile/Mode I fracture (*Fig. 1.3b*) or flexural properties of the composite and less attention is given to shear or Mode II (*Fig. 1.3c*) fracture (*Soetens & Matthys, 2012*). Limited consideration has also been given to the generic two-dimensional condition where deformational paths (or fracture plane kinematics) are of a mixed mode nature i.e. Mode I (crack opening) and Mode II (crack sliding) interaction. For example, mixed mode behaviour is typical of diagonal shear cracking within the shear span of a RC beam. RC membrane elements subject to general in-plane stresses are the basic components of many RC structures (*Soltani et al., 2003*). Analogous to existing numerical tools for RC membrane elements, research towards a constitutive material model and numerical procedure for the analysis of SFRC membrane elements (*Fig. 1.3a*) is essential. A direct and rational approach to model the generic material response also has the potential to allow for tailoring and optimisation in material and structural design.

1.2.2 Multi-scale characterisation

The scales of observation are defined as the Micro-scale, Meso-scale and Macro-scale (*Jůn, 2011*). The Micro-scale considers the sub-material mechanisms of cracked concrete which may include: tension softening, compression softening and shear (interface roughness and aggregate interlock) and dilatancy stresses. The mechanisms of the reinforcement (fibre) at this scale include the reinforcement-matrix bond, reinforcement deformation and local damage of the matrix induced by the reinforcement. The Meso-scale investigates the composite behaviour within the vicinity of a single, well-defined, localised crack. The Macro-scale of observation refers to the scale of a structural member, where the redistribution of stresses and multiple cracking is permissible.

1.2.3 Research outcomes

In order to contribute to multi-scale characterisation towards constitutive modelling, the outcomes of this dissertation in sequence are: Adapt a composite design procedure and develop a SFRC; Classify the composite in terms of standard performance indicators and testing procedures; Design, fabricate and execute experimental tests to characterise the Mode I and Mode II fracture at the

Micro and Meso-scale of observation; Develop a material model and verify it numerically: This requires the implementation of an analytical formulation of the material model into a numerical procedure. The material model is calibrated with the experimental data and verified via a Finite Element (FE) representation of the experimental Meso-scale test.

The following research constraints are applicable: (1) Mixed mode behaviour is not addressed in this study. Mode I and Mode II fracture is therefore decoupled and no interaction is considered for the most part. The influence of dilatancy and confinement across the shear interface is therefore also ignored; (2) The Micro-scale mechanism is restricted to the fibre component only and is only characterised experimentally. The fibre mechanism is not modelled analytically or numerically at the scale of an individual fibre. An empirical model is however developed which reconciles the fibre component with the Mode II Meso-scale response; (3) The Macro-scale falls outside the scope of this study.

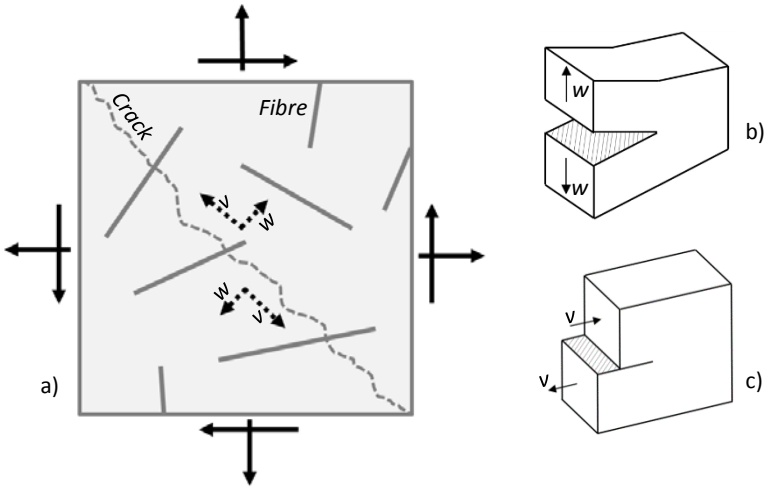

Fig. 1.3 – a) Cracked SFRC membrane element (*w* – crack opening, *v* – crack sliding) (*Bernardi et al., 2012; Soltani et al., 2003*); Fundamental fracture modes: b) Mode I (opening) and c) Mode II (sliding) (*Sun & Jin, 2012*)

1.3 Research methodology

This research is divided into four phases, in the following sequence: The first phase requires the design of a SFRC. The reported synergetic properties of self-consolidating concrete (SCC) and SFRC in terms of rheology and mechanical properties (*Grünewald, 2004*), makes a steel fibre-reinforced self-consolidating concrete or SFR-SCC the most viable choice. The SFR-SCC must comply with chosen rheological/workability and mechanical performance criteria. A parameter study is performed in order to obtain the base composition of the self-consolidating mortar (no fibre, no coarse aggregate) used in this study, using two basic performance criteria, namely mortar rheology in terms of flowability and a target compressive strength. Each composite developed from this base mixture is subjected to standard testing in order to characterise workability, compressive strength development, elastic modulus and post-fracture toughness, thereby classifying the material.

The second and third phases experimentally investigate the Mode I and Mode II fracture respectively at the Micro and Meso-scale. Crack localisation is enforced via specimen geometry and load configuration. Experimental methods to characterise the uniaxial tension and shear behaviour are adopted from the literature and redesigned in accordance with the available testing equipment and

the outcomes of this research. Experimental methods to characterise the shear behaviour include the shear push-off (*Mattock & Hawkins, 1972; Nooru-Mohamed, 1992*) and Ohno (*Arakawa & Ohno, 1957*) beam /Iosipescu (*Iosipescu, 1967*) shear test methods. Numerical/FE refinement in the elastic domain is used in order to optimise specimen (Meso-scale) geometry for the desired stress distributions.

In the fourth and final phase, the constitutive material model is formulated and implemented in a commercial FE program (*Abaqus 6.10*) in the form of a "user-material" subroutine. Finally, the material model is calibrated and verified with the experimental data obtained from the third phase.

1.4 Thesis structure

This dissertation has seven chapters, excluding the preface and addenda and is structured as follows: The *lead-in* part of this dissertation consists of two chapters. The first chapter (*Chapter 1*) is a short specification of the central research questions and defines the background, scope, objectives, constraints, methodology and structure of the thesis. The second chapter (*Chapter 2*) opens with the discussion of the main findings of an extensive literature review (*Zeranka & van Zijl, 2013*) on the steel fibre-reinforcement of structural prismatic beam members subject to shear-dominant loading. The sections that follow are a focused literature review, framed closely around the central research questions discussed in *Chapter 1*. First, the material under investigation (SFRC) is introduced, emphasising its composition and design. Experimental investigations of the Mode I and Mode II fracture, conducted at the Micro and Meso scale are reviewed. Finally, some information is given on the research technologies used in this study, namely Digital Image Correlation and Computed Tomography (CT-scan).

The *core* part of this dissertation contains the key research findings and results and is subdivided into four chapters (*Chapters 3 – 6*). *Chapter 3* presents the process whereby the constituent properties, mixture composition, and production method for SFR-SCC is determined. The composite is also classified in terms of workability, compressive strength, elastic modulus and post-fracture toughness.

Chapters 4 and *5* conduct an experimental investigation of the Mode I and II fracture respectively at the Micro and Meso-scale. For both fracture modes, the specimen design, research parameters, production method, test configuration and results are presented.

Chapter 6 proceeds to outline the development of the material model and numerical procedure to analyse an SFRC membrane element subject to general in-plane stresses. The model and numerical procedure is first verified for a single finite element. Finally, the model is calibrated and verified with the experimental data from *Chapters 4* and *5*. An empirical model which reconciles the fibre component (Micro-scale) with the composite (Meso-scale) response for Mode II fracture is also produced.

The final chapter (*Chapter 7*) summarises the most important findings, opens out into a discussion of wider themes or theoretical implications arising from the research and discusses possible avenues for the next phase of work. This dissertation is also supplemented by a reference list and an appendix, providing the list of notations and symbols used and additional data.

Chapter 2

Conceptual and methodological framework

2.1 The Macro-scale: Steel fibre reinforcement of shear-critical RC beams

An extensive literature review (*Zeranka & van Zijl, 2013*) on the topic of the steel fibre-reinforcement of shear-critical structural beams was conducted by the author at the onset of this research. The main findings of the literature review are reported in this section and include: the significance of this topic, important material parameters and enhancements to structural performance, the resistive mechanisms of shear-critical RC beams and how these are affected by steel-fibre reinforcement, the properties and benefits of a combined reinforcement solution, primary research methods (including experimentation and modelling) employed to date and their capabilities, and current shear design provisions for steel fibre RC beams.

2.1.1 Research significance

Shear failure originates as a tensile failure of the concrete, in the shear span of a RC beam, when the principal tensile stresses exceed the tensile strength of concrete. Diagonal cracks develop and propagate in the beam web and due to the brittle nature of plain concrete in tension, collapse occurs suddenly, shortly after the formation of the first crack. Shear failure is therefore characterised by small deflections and a lack of ductility, and is an undesirable mode of failure.

The steel fibre-reinforcement of shear-critical structural RC beam members has undergone extensive research over the past 40+ years. Many authors have motivated the partial or complete replacement of conventional shear reinforcement with steel fibres. The shear performance of fibrous RC beams has been shown to be similar to beams reinforced with conventional stirrup reinforcement (*Mansur et al., 1986*) and in some instances exhibit improved behaviour (*Narayanan & Darwish, 1987*).

The shear behaviour of RC is however a complex phenomenon, which may lead to a variety of possible shear failure modes, dependent on several interacting shear transfer mechanisms that are difficult to quantify. The shear transfer mechanisms themselves are also influenced by many factors related to the material properties and the structural configuration of the member. Therefore, methods for material characterisation, modelling and design must be improved in order to achieve greater structural application of SFRC.

2.1.2 Material parameters and structural enhancement

Material parameters

The following material properties related to fibre-reinforcement, influence the composite behaviour in general as well as the shear behaviour of reinforced SFRC (R-SFRC) beams: fibre-content, aspect ratio, length, shape (profile and end-anchorage), strength, stiffness and fibre matrix bond.

Fibre content

At lower fibre volumes, the increase in shear strength is proportional to the quantity of fibre; however, the rate of increase is reduced at higher fibre volumes (*Adebar et al., 1997*). In the practical range of typical steel fibres used (0.25 – 2.0% by volume), an optimum fibre dosage appears to lie between 1.0% and 1.5%. Some shear design provisions, such as found in *ACI 318 (2008)* specify a minimum volume percentage of steel fibre of 0.75% of concrete volume, in addition to residual flexural strength requirements of the SFRC.

Fibre stiffness and strength

High-strength fibres may provide an increase in residual capacity compared to normal-strength fibres. This is attributed to the greater plastic strength of fibre hooks (*Dinh et al., 2010*). The beneficial effect of high-strength fibres is however dependent on the properties of the composite, especially the fibre-matrix bond and matrix strength.

Fibre length and aspect ratio

Longer fibres exhibit a more ductile response compared to shorter fibres (*Adebar et al., 1997*). The stress transfer capability of shorter fibres reduces faster than longer fibres, resulting in a faster rate of force transfer to the other shear-resisting mechanisms (*Li et al., 1992*). The fibre factor (F) in *Eq. 2.1* is a combined fibre parameter consisting of the fibre aspect ratio (L_f/d_f), the fibre volume (V_f) and a bond efficiency factor (D_f) which is dependent on the fibre type. The fibre factor has a greater

influence on the shear strength than any individual fibre parameter and is used in most semi-empirical models (*Slater et al., 2012*).

$$F = \left(\frac{L_f}{d_f}\right) \cdot V_f \cdot D_f \tag{2.1}$$

Fibre type/material:
The fibre type or material that performs the best in shear is debatable and requires more comparative studies in the author's opinion. In a study by *Li et al. (1992)*, polyethylene and steel fibres were found to be the most effective in increasing shear strength. *Furlan Jr. & de Hanai (1997)* stated that synthetic fibres are not as effective as steel fibres in increasing the shear strength of concrete beams, due to its low modulus of elasticity. Other differences between the fibre properties, such overall stiffness, geometry, end-anchorage, surface properties etc., need to be isolated and quantified in a meaningful way.

Structural enhancement
Steel fibre-reinforcement increases the initial shear cracking strength (*Roberts & Ho, 1982*) and ultimate shear capacity (*Parra-Montesinos, 2006*) of R-SFRC beams, especially where lower quantities of conventional shear reinforcement are present. A substantial increase in post-cracking/residual strength (*Sharma, 1986*), structural stiffness (*Furlan Jr. & de Hanai, 1997*), ductility, energy absorption and toughness (*Adebar et al., 1997*) is also observed. In general, fibre-reinforcement significantly reduces and in some instances eliminates the occurrence of concrete spalling (*Lim & Oh, 1999*), which improves structural durability (*Li et al., 1992*).

Fibre-reinforcement delays the formation and restrains the opening and propagation of cracks (*Watanabe et al., 2010*), altering the cracking pattern, which can significantly change the overall structural behaviour. Distributed cracking patterns, with more closely spaced cracks, can delay the localisation of a major shear-critical crack (*Minelli & Plizzari, 2008*). This is attributed to a more uniform distribution of stresses in FRC beams, compared to conventional RC beams (*Narayanan & Darwish, 1987*), which improves the transmission of shear load (*Juárez et al., 2007*). Effective crack control also reduces deflections and increases deformation capacity (*Kwak et al., 2002*). The cracking pattern of FRC beams has been observed to be similar to corresponding RC beams with conventional stirrup reinforcement (*Narayanan & Darwish, 1987*). It is has also been postulated that in members without stirrup reinforcement, the effect of beam depth on shear strength is reduced with fibre reinforcement (*Dinh et al., 2011*).

Fibres reduce the strain in conventional rebar, especially in the post-cracking range. The stress in bar reinforcement is therefore reduced and delayed (*Cho & Kim, 2003*), which is an indication that the fibre-concrete is contributing to the shear strength (*Furlan Jr. & de Hanai, 1997*). Ultimately the inclusion of steel fibres can change the mode of failure from a brittle shear failure to a ductile flexural failure, even in the absence of stirrups, allowing the R-SFRC member to reach its full flexural capacity (*Swamy & Bahia, 1985*).

2.1.3 Shear transfer mechanisms

The efficiency of fibre-reinforcement depends on the governing load-carrying mechanisms, which may vary (*Noghabai, 2000*). Fibre-reinforcement is known to enhance many of the shear transfer mechanisms, including:

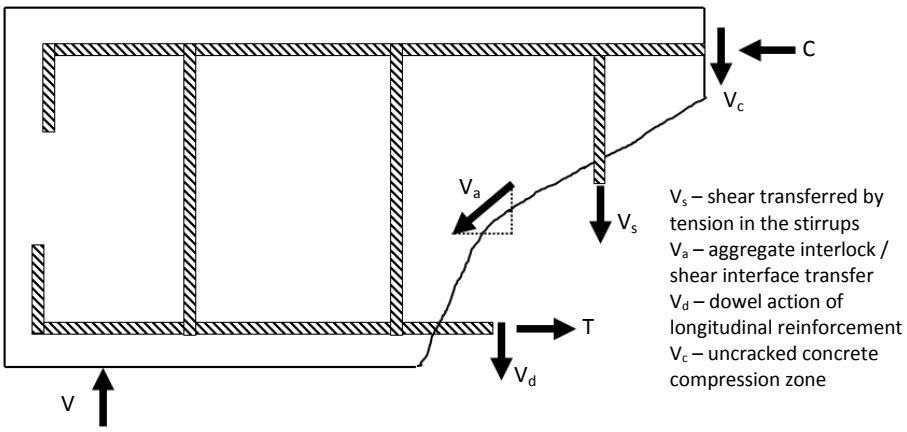

Fig. 2.1 – Internal forces in cracked RC beam (*Wight & MacGregor, 2009; Kong & Evans, 1987*)

Longitudinal reinforcement ratio

The shear resistance increases as the longitudinal (tension) reinforcement ratio increases. The longitudinal reinforcement serves to increase the cracking strength, delaying the formation and propagation of flexural and inclined cracks and increasing the total dowel capacity V_d (*Fig. 2.1* & *Li et al., 1992*). The longitudinal reinforcement ratio also influences the size of the compression zone and the overall structural ductility (*Dinh et al., 2010*). Steel fibre-reinforcement improves the effectiveness of dowel resistance due to its ability to enhance the tensile strength (i.e. greater resistance to the propagation and widening of dowel cracks in the dowel zone along reinforcement) of concrete in the splitting plane along the longitudinal reinforcement (*Li et al., 1992*).

Concrete compressive strength

An increased concrete compressive strength does increase the shear capacity of both RC and R-SFRC beams (*Mansur et al., 1986*). The degree to which steel fibre-reinforcement influences concrete compressive strength varies from a significant increase in compressive strength (*Lim & Oh, 1999*), to a marginal or insignificant increase (*Tan et al., 1993*), especially in low volume fractions (*Dinh et al., 2011*). Even a reduction in compressive strength may be observed, which is attributed to the reduced consolidation of concrete due to the presence of fibres (*Adebar et al., 1997*). The most significant enhancement of steel fibre-reinforcement to the compressive properties of concrete is the substantially higher compressive strain at peak stress compared to ordinary concrete. This is attributed to the confinement provided by the fibres (*Tan et al., 1993*). An increase in residual compressive strength is observed due to the reduced damage in tension (*Minelli & Vecchio, 2004*). This may be beneficial in deeper beams where arch action is prominent and compression forces are transmitted to the supports through compression struts.

Shear span-to-depth ratio

The behaviour of RC beams is greatly influenced by the shear span-to-depth ratio (a_v/d). The failure modes observed as a function of a_v/d are defined as follows (see *Fig. 2.2*):

$a_v/d > 6$: Failure predominantly in flexure

$6 > a_v/d > 2.5$: Flexural crack *a-b* propagates towards the loading point (*a-b-c*) and is typically defined as a *flexure-shear or diagonal crack*. Relatively higher values of a_v/d will result in the diagonal crack spreading to (*e*) and is often called a *diagonal-tension failure*. If a_v/d is relatively low, the diagonal crack tends to stop at some point (*j*), at which point a number of cracks will develop along the longitudinal tension reinforcement. As the load, *V*, is further increased, the diagonal crack widens and propagates along the level of the tension reinforcement (*g-h*). Loss of bond between the reinforcement and concrete usually results, with splitting occurring at the level of the reinforcement. This failure mode is usually called *shear-tension or shear-bond failure*. In both cases, the ultimate load is not much greater than the diagonal cracking load.

$2.5 > a_v/d > 1$: A diagonal crack typically forms independently of a flexural crack. The diagonal crack propagates into the concrete compression zone at the point of loading. Eventually crushing failure will occur in this zone (*shear-compression failure*). The ultimate load may be more than twice the diagonal cracking load.

$a_v/d < 1$: Deep beam behaviour. A diagonal crack forms along a line approximately from the loading to the support point. A crack usually originates as a result of the splitting action due to the compression force transmitted directly from the loading point to the support. When the crack penetrates the concrete compression zone at either the support or loading point, crushing failure of concrete occurs. The ultimate load is typically several times the diagonal cracking load.

Within the bounds of shear failure, the cracking and ultimate shear strength decrease with increasing span-to-depth ratio. This is attributed to arching and dowel action becoming less effective as the span-to-depth ratio increases (*Kwak et al., 2002*). There does appear to be some controversy with regard to when fibre-reinforcement is more effective i.e. for slender or deep beams. According to some authors the rate of increase in shear strength is higher at low values of the span-to-depth ratio and consequently arch action is believed to benefit more from fibre-reinforcement (*Mansur et al., 1986; Narayanan & Darwish, 1987; Ashour et al., 1992*). This is attributed to the greater cohesion of fibre concrete and the improved tensile capacity of the concrete normal to the compression strut direction. Contrary to these findings other authors state that the efficiency of fibres as shear reinforcement increases as the span-to-depth ratio increases. The reasoning is that improvements due to fibre-reinforcement are related directly to the pull-out performance of fibre concrete and the beam action failure mechanism has a greater capacity to utilise the improved material performance due to fibre-reinforcement (*Li et al., 1992; Cucchiara et al., 2004*).

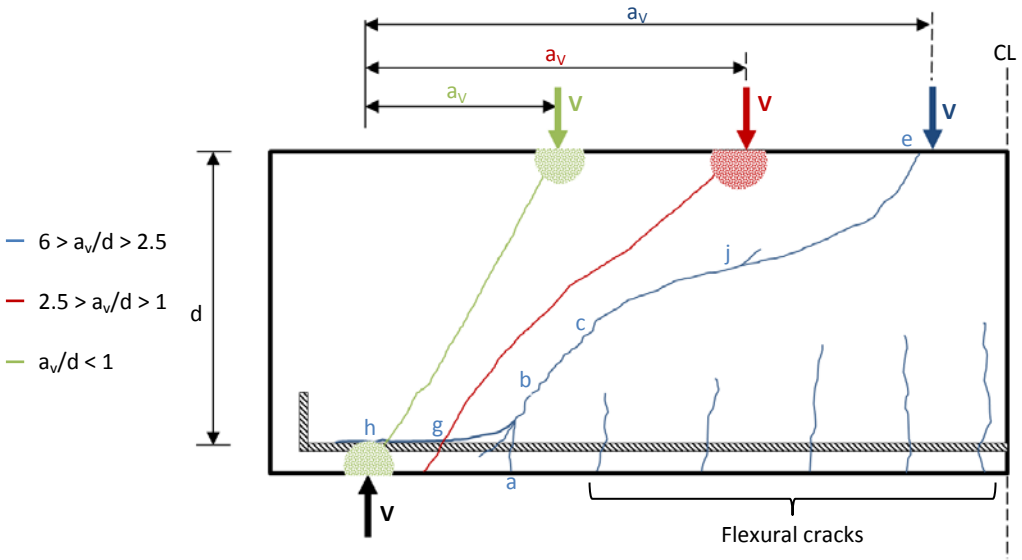

Fig. 2.2 – Influence of shear span-to-depth ratio on shear failure mode (reworked from *Kong & Evans (1987)*)

Aggregate interlock

The aggregate interlock contribution diminishes with increasing crack width and is therefore not reliable. Aggregate interlock is believed to become more effective due to the crack width limitation provided by the fibres, however to the authors' knowledge this has not been investigated in detail. The fibres therefore have a function which is similar to conventional shear reinforcement, but unlike conventional reinforcement are uniformly distributed throughout the member volume (*Sharma, 1986; Wight & Mac-Gregor, 2009*). The contribution of aggregate interlock in shear transfer is mainly influential during shear sliding of diagonal cracks in beams with a span-to-depth ratio greater than 2.5 (i.e. slender beams). The aggregate interlock contribution disappears for deeper beams which fail in arch action, where crack face shearing is negligible (*Li et al., 1992*).

Size effect

In beams without conventional transverse reinforcement, size-effects significantly influence the shear behaviour and fibre-reinforcement is less effective in large-scale beams (*Adebar et al., 1997*). There is a general trend of decreasing shear strength with increasing beam size or depth and this is consistent with results of plain concrete beams as well as theoretical work (*Li et al., 1992*). Few tests have been conducted on large FRC beams and in some cases steel fibres have been shown to be ineffective in preventing catastrophic shear failures in full-scale beams (*Williamson & Knab, 1975 cited by Adebar et al., 1997*). The contribution of fibres is therefore size dependent, whereas the contribution provided by stirrups is expected to be size independent. In larger beams, conventional shear reinforcement is more effective than steel fibres in terms of bearing capacity and ductility. The scale effects can be mostly eliminated using minimum transverse reinforcement (*Minelli & Plizzari, 2008*). Alternatively a reduction in crack spacing due to fibre reinforcement could at least in some instances potentially reduce or eliminate shear-size effects in beams without conventional transverse reinforcement (*Dinh et al., 2010*). A combined stirrup-fibre reinforcement solution is therefore proposed in full-scale RC beams and is discussed next.

2.1.4 The synergetic effect of fibre and stirrup reinforcement

There are design instances where fibre-reinforced beams cannot achieve the same performance as beams containing conventional shear reinforcement. In these cases steel fibres alone are not effective in preventing catastrophic shear failures (*Williamson & Knab, 1975 and Lafraugh & Moustafa, 1975 cited by Swamy & Bahia, 1985*).

There is a limited amount of experimental data on the shear behaviour of beams where a combination of fibres and conventional transverse reinforcement is used (*Cucchiara et al., 2004*). Tests have shown that such a combination can form an effective system of shear reinforcement in a structural member (*Craig, 1984 cited by Sharma, 1986*). Fibres and stirrups in small quantities can be effective to enhance the shear strength, as well as the crack and deformation control, providing ductile post-peak behaviour. Such a reinforcement combination can change the mode of failure and preserve the ductility and integrity of the structural member (*Swamy & Bahia, 1985; Meda et al., 2005*). The amount of stirrups required can be reduced with the introduction of fibre-reinforcement (*Lim & Oh, 1999*). A combined use of fibres and stirrups is believed to be more suitable, because the stirrups allow greater deformation capacity beyond the elastic limit (*Cucchiara et al., 2004*). The conventional shear reinforcement also reduces the scatter in the data and assists in crack width control and consequently assists the bridging of fibres along the diagonal crack, increasing the shear-resistance carried by the steel fibres. Stirrups effectively prevent the rapid opening and propagation of the diagonal crack, which increases the efficiency of the fibres.

In conclusion, there exists a synergetic interaction between the shear resistance mechanisms of stirrups and fibres (*Watanabe et al., 2010*). Other authors have also observed a positive composite effect and efficiency for a combination of stirrups and steel fibres, on the mechanical behaviour (including ultimate load, ductility, post-peak behaviour, toughness and failure pattern). The shear strength has been shown to be approximately proportional to the steel fibre content; however this is dependent on the conventional shear reinforcement ratio (*Ding et al., 2011*). Fibre-reinforcement is less effective at higher conventional shear reinforcement ratios i.e. the rate of improvement with increasing fibre content decreases with increased conventional shear reinforcement (*Ding et al. 2012*). This is attributed to a greater proportion of the load being carried by the stirrups and less by the fibres in the ultimate stages when cracks widen and fibre pull-out occurs (*Swamy & Bahia, 1985*).

2.1.5 Experimental design

Experimental investigations to date have been predominantly shear tests of simply supported RC structural beam members subjected to flexural loading. The parameters related to the specimen geometry, loading configuration and conventional reinforcement are: the shear span-to-effective depth ratio, longitudinal reinforcement ratio, transverse reinforcement ratio and beam depth (size effect). Structural tests are usually accompanied with fracture mechanics tests such as flexural or splitting tests, where the residual post-cracking strength is of primary importance. This is used as input to reconcile material models with the structural response. The material parameters typically include: the concrete compressive strength, fibre content and the fibre properties (length, aspect ratio, strength, mechanical anchorage and profile).

The data typically recorded for these types of tests are the load vs. beam deflection response (at mid-span), crack width, development and patterns, the load at first visible diagonal/shear cracking and ultimate load, failure modes, reinforcement and concrete strains, rotation at supports and specimen curvature.

Far less work has been done on the direct shear response of fibre reinforced concretes (*Soetens & Matthys, 2012; Lee & Foster, 2006*). These types of tests are performed to evaluate the direct/pure shear response in terms of the relative shear interfacial slip and shear capacity i.e. crack sliding or Mode II fracture. Two test methods are typically employed, the shear push-off (or Z-type specimens) (*Lee & Foster, 2006; Tan & Mansur, 1990*) and the shear push-through specimens (*JSCE, 1990*) modified by *Mirsayah & Banthia (2002), Soetens & Matthys (2012), Boulekbache et al. (2012)* and *Malatesta & Contreras (2009)*. Even fewer investigations, attempt to link the pull-out behaviour of single fibres to SFRC under mode II fracture i.e. the transverse pull-out of steel fibres (*Lee & Foster, 2006; Soetens & Matthys, 2012*).

2.1.6 Modelling

A rational and generic model for shear design with fibre-reinforcement requires an understanding of the governing load-carrying mechanisms. Experimentation alone is insufficient to expose the underlying mechanisms. Analytical formulations which implement the theory are required in order to explain the structural behaviour in mechanical terms and to correctly interpret the experimental results. Three modelling strategies, namely empirical and semi-empirical, analytical and numerical are considered. These modelling strategies vary in their complexity and their modelling capability.

Empirical and semi-empirical models

The majority of predictive equations for the shear strength of FRC beams, including those found in most design codes, are empirical or semi-empirical (*Cho & Kim, 2003*), fitted by test data, and therefore are not comprehensive (*Kim et al., 2012*). These types of models can only predict the ultimate shear capacity and in some instances also the cracking shear strength. Typically some form of an existing shear design model for conventional RC (such as those currently implemented in most design codes) is utilised as a framework which is modified to account for the contribution of fibres. Models are typically sourced from the *ACI Building Code (ACI318-08)* or *Eurocode 2 (2003)* and in some instances the theory of concrete plasticity or limit analysis is also used. These models are sometimes used in conjunction with linear or nonlinear regression analysis. Empirical formulas usually evaluate a limited set of parameters that typically include the shear span-depth ratio, beam depth, compressive strength, reinforcement ratio and concrete flexural or tensile strength.

Semi-empirical models place greater emphasis on the fibre contribution. These models differ in their level of consideration. Some models evaluate the fibre contribution at a single fibre level and include such parameters as the fibre distribution, mean fibre pull-out length, average fibre-matrix interfacial bond stress, fibre aspect ratio, fibre volume and bond efficiency factor (*Narayanan & Darwish, 1987; Al-Ta'an & Al-Feel, 1990*). Whereas other models consider the fibre contribution at a composite level, which typically includes a residual post-cracking strength parameter obtained from standard fracture mechanics tests, such as flexural and splitting tensile strength tests (*Mansur et al., 1986; Minelli & Plizzari, 2008; Dinh et al., 2011*).

Analytical models

Analytical models are capable of simulating the stress-strain history and in some instances, the load-deflection response of a member. The model parameters typically include the stress-strain relations for FRC in tension and compression or alternatively the fibres are modelled explicitly as mentioned previously (*Kim et al., 2012*). The earliest work was first performed by *Tan & Mansur (1990)* and then later again by *Tan et al. (1993)*. The theoretical background of these models is based on the softened truss model (*Hsu et al., 1987*) and the modified compression field theory (MCFT) (*Vecchio & Collins, 1986*), which is essentially a smeared, rotating crack model for cracked RC elements. These models have three basic requirements: equilibrium, compatibility and material constitutive equations. The MCFT has been used extensively as the theoretical framework for such models. Nonlinear truss or lattice models which incorporate geometric and mechanical modelling, have also been investigated (*Noghabai, 2000*).

Numerical/Finite element models

Few numerical studies are published concerning FRC structures (*Minelli & Vecchio, 2004*). In order to allow for an appropriate redistribution of stresses in the model, a FE method must be used. These models are capable of simulating the strength, stiffness, ductility, crack pattern development, and failure modes, essentially the complete member response. These types of models allow for a more detailed investigation into the development of shear resistant mechanisms and an accurate evaluation of the fibre contribution to shear resistance is possible (*Minelli &Vecchio, 2006*). The fibre contribution to concrete tension softening and the material nonlinearities is incorporated into the models. In addition, these models may include crack limits, arch action mechanisms and concrete residual strength in the presence of fibres. Once again, models differ in their consideration of fibre-reinforced concrete, which may be on a composite level or single fibre level (*Lee et al., 2012*).The MCFT is once again used as the theoretical framework for the finite element analysis (FEA) and is adapted for FRC in terms of the post-cracking behaviour and local conditions at cracks (*Minelli &Vecchio, 2004*). An extension of the MCFT is the disturbed stress field model (DSFM) which is capable of simulating the crack shear-slip deformation (*Minelli & Vecchio, 2006*).

Recent approaches, including the MCFT or plasticity theory are rational and have physical significance (*Cho & Kim, 2003*). However, a model which is based on FRC performance in terms of the residual post-cracking strength (which is considered to be a significant index for structural design and is obtained through simple fracture mechanics tests), can easily be applied and transferred to practice (*Minelli & Plizzari, 2008*).

2.1.7 Shear design provisions for R-SFRC

There are very few standards or recommendations that allow for the quantification of shear strength and shear ductility enhancement provided by fibre reinforcement (*ACI 544 Committee 2008b, cited by Malatesta & Contreras, 2009*). A design procedure that considers the randomly distributed discrete fibre behaviour across cracks in a rational manner is still rare (*Ding et al., 2012*). The design codes which provide shear design provisions for R-SFRC beams include the *ACI Code (ACI 318-08)*, *fib Model Code 2010* and the *RILEM TC 162-TDF* recommendations. These design provisions are similar in that they all incorporate and specify minimum post-cracking residual strength criteria which are evaluated through flexural test methods.

Conclusions

Based on the findings contained in this review, some omissions and areas of limited research have been identified. Limited research has been performed on examining the fibre pull-out/dowel and aggregate interlock (shear interface roughness) interaction at different loading stages or crack widths. Limited research has been performed on the composite effect of a fibre and conventional stirrup reinforcement combination. Extending the knowledge of the shear transfer mechanisms through carefully designed characteristic testing and the development of a refined analytical model is proposed and postulated to clarify the dominant shear mechanisms and structural resistance of R-SFRC beams.

2.2 Steel fibre-reinforced self-consolidating concrete

SFRC has already been generally introduced in *Chapter 1* and *Section 2.1*, including background, characteristic behaviour and primary mechanisms involved. This section briefly introduces the key characteristics, requirements and design concepts for SCC and SFR-SCC.

2.2.1 Self-Consolidating Concrete (SCC)

SCC does not require vibration for placing and compaction. Even in the presence of congested reinforcement, SCC flows under its own weight and is able to fill formwork and achieve full compaction. SCC achieves a high degree of homogeneity and minimal voids due to its fluidity and segregation resistance. In order to achieve this performance, the SCC must comply with defined requirements for filling ability, passing ability and segregation resistance. A variety of test methods have been developed and applied to determine the key characteristics of SCC. This is discussed under the *Characteristics and requirements for SCC*. Other characteristics not considered here include pump-ability, plastic settlement and washout resistance.

SCC was originally developed in Japan to offset a growing shortage of skilled labour. The earlier development of superplasticisers, for concrete, made SCC technology possible. Today SCC is used for both site and precast applications and has become popular due to several factors including: faster rate of construction, reduction of labour, improved surface quality, ease of placement, improved durability, more design possibilities, reduced concrete sections, lower levels of noise and vibration (due to the elimination of vibrating equipment) and a safer working environment (*EFNARC, 2002*). SCC is typically produced with a low water-cement ratio, resulting in high early strength, which facilitates earlier demoulding and the faster use of elements and structures (*SCCEP, 2005*). A great deal of research has gone into the rheological and mechanical characteristics of SCC with growing applications. This subsection only summarises the most important characteristics and performance requirements for SCC, as well as relevant design principles and test methods.

Characteristics and requirements for SCC

A concrete mix can only be classified as a SCC if the requirements for filling ability, passing ability and segregation resistance are met. Filling ability relates to the ability of fresh SCC to flow into and fill all voids within the formwork, under its own weight. Passing ability refers to the capacity of the SCC to flow through confined spaces and narrow openings, such as areas of congested reinforcement without causing blockage, segregation or loss of homogeneity. Segregation resistance is the

resistance of the constituents of SCC to migration or separation. Mix constituents with a relatively high density or a low surface-to-volume ratio are more likely to segregate from the paste or mortar in which it is suspended.

SCC performance depends on the type of application, and especially on confinement conditions (including element geometry and reinforcement detail), placing equipment, placing methods and finishing method (*SCCEP, 2005*). Several test methods (*Table 2.1*) have been developed to characterise the properties of SCC. Typical performance ranges for SCC are also shown in *Table 2.1*. These test methods are described in *EFNARC (2002)* and *SCCEP (2005)* in detail.

Table 2.1 – Workability test methods and acceptance criteria for SCC (*EFNARC, 2002*)

Property	Test methods	Unit	Typical range
Filling ability	Slump-flow	mm	650 – 800
	T_{500} slump-flow	sec	2 – 5
	V-funnel	sec	6 – 12
	Orimet	sec	0 – 5
Passing ability	L-box	(h_2/h_1)	0.8 – 1.0
	J-Ring	mm	0 – 10
	U-box	(h_2-h_1) mm	0 – 30
	Fill-box	%	90 – 100
Segregation resistance	GTM screen stability test	%	0 – 15
	V-funnel at T_{5min}	sec	0 – (+3)

Design principles to optimise SCC composition

There is no standard method for SCC mix design and many academic institutions and companies have developed their own methods (*SCCEP, 2005*). The composition of SCC is different from conventional vibrated concrete in several respects. SCC normally contains less coarse aggregate, more paste, has a lower water/powder ratio, and has increased quantities of superplasticiser and sometimes the addition of a viscosity modifying admixture (VMA). Optimisation of the aggregate particle size distribution together with the paste fraction in terms of the water/powder ratio and powder composition (including cement, extender and filler materials) is of primary importance.

A procedure for SCC mix design is adapted in *Chapter 3* from a method developed by *Okamura & Ouchi (1999)*. This is a fundamental approach that optimises the SCC at the level of the paste, mortar and concrete. Typical volume percentages of the SCC components are shown in Fig. 2.3. The mix design sequence as outlined by *EFNARC (2002)* is

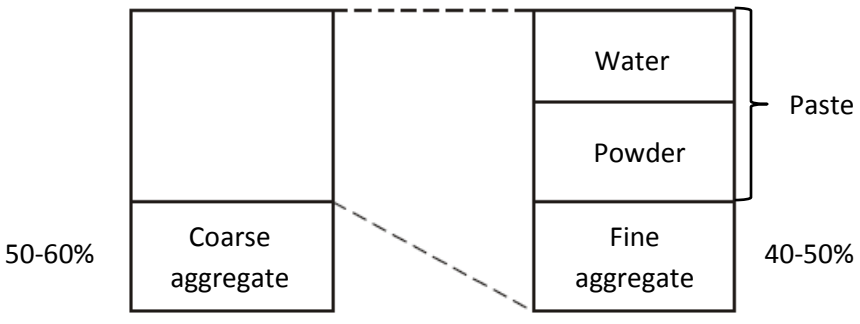

Fig. 2.3 – Components of SCC (*Grünewald, 2004; Okamura & Ouchi, 1999*)

A. Designation of a desired air content (usually set at 2%)
B. Determination of coarse aggregate volume (50-60% of total SCC volume)
C. Determination of fine aggregate volume (40-50% of mortar volume)
D. Design of paste composition
    - Determine water demand of selected powder composition with flow tests at different water contents
E. Determination of optimum water/powder ratio and superplasticiser dosage in mortar
    - Superplasticiser is added to mortar to decrease water demand and analyse its effect in combination with the selected powder composition.
    - Tests with flow cone (240-260 mm) and V-Funnel (7-11 sec) for mortar are performed at varying water/powder ratios and dosages of superplasticiser
    - Adjust the water/powder ratio to achieve the above criteria
    - If these criteria cannot be met, then the combination of materials must be changed. First commence to change the superplasticiser. A second alternative is a different powder composition or new additive. The use of a different cement is a last resort.
F. Select the coarse aggregate content, maximum size and grading appropriate for the application in mind
G. Assess the concrete properties with standard tests

2.2.2 Steel Fibre-Reinforced Self-Consolidating Concrete (SFR-SCC)

The combined benefits of SCC in the fresh state together with the improved mechanical properties of FRC in the hardened state allows for new fields of application. An ideal application would be where a structural element is cast and finished without any reinforcing bar placement or external compaction required.

The performance of FRC is influenced by the fibre type, content, dispersion, orientation and fibre/matrix bond. These factors are influenced by the mix constituents and the mixing and consolidating procedures. The greater workability of SCC can facilitate the uniform dispersion and effective utilisation of fibres (*Grünewald, 2004*).

The addition of fibres (metallic or polymer) may reduce the flowability and passing ability of SCC. This is attributed to the characteristics of the fibre as well as the interaction of the fibre with the granular skeleton of SCC. The fibre characteristics that influence concrete workability are (1) fibre shape and aspect ratio. Fibres are elongated compared to aggregates and have a higher comparative surface area. (2) Fibres typically have a stiffness and density that are different from the other mix constituents, changing the structure of the granular skeleton. (3) Fibres also have different surface properties that may for example be hydrophilic or hydrophobic. (4) Fibre geometry and end anchorage causes increased friction between fibres and aggregates. SFR-SCC design is therefore a compromise between the workability of a SCC and the mechanical properties of a FRC.

Transforming conventional concrete to SFR-SCC

The requirements for conventional SFRC applications are: adequate workability to allow placement, consolidation and finishing with minimum effort; minimise segregation (for which there is a higher potential for FRC) and bleeding; achieve a uniform fibre distribution and avoid the balling of fibres, which is a function of aggregate particle size distribution, fibre aspect ratio, fibre volume, fibre shape and the mixing procedure.

Conventional SFRC mix designs are typically characterised by high powder content, higher fine aggregate content and in some cases an optimised aggregate particle size distribution including a smaller maximum aggregate particle size. Conventional admixtures and pozzolans for air entrainment, water reduction, workability and shrinkage control are used. The conventional concrete composition is therefore modified to accommodate the added fibres, resulting in a mixture composition that more closely resembles a SCC.

The same principles to transform a conventional concrete to a SCC is therefore used to produce a FRC and SFR-SCC, namely:

- Optimise the aggregate particle size distribution
- Limit the quantity of coarse aggregate to meet the demands of passing ability
- Counteract segregation by ensuring adequate paste content and viscosity
- Utilise VMA's if necessary to enhance the stability and robustness of the mixture

2.3 Mechanical investigations of Mode I fracture at the Meso-scale

Uniaxial tension tests are generally accepted as the most direct and appropriate procedure to determine the stress-deformation behaviour under tension. Many experimental tests (direct or indirect) have been developed and test results published, but no comprehensive agreed upon tensile test standard has been established to date (*Naaman et al., 2007*). *RILEM TC 162-TDF (2001)* provides recommendations for testing SFRC softening behaviour.

Conceptually this type of test is simple, but is quite sensitive to details of the test set-up used e.g. boundary conditions at loading ends, specimen geometry (size effect, effect of notches) etc. The test must also allow for the measurement of certain key properties, required to characterise the composite behaviour, including the elastic modulus, first cracking stress, peak tensile stress and corresponding strains.

2.3.1 Specimen shape and dimensions

Specimen shape
Fig. 2.4 shows several test types used (*Naaman et al., 2007*). In *Fig. 2.4a*, thin sheets or plates are loaded via a clamping mechanism onto aluminium plates bonded to the specimen surface. This reduces damage due to clamping. *Fig. 2.4b* shows a dog-bone shaped specimen where the specimen cross-section decreases from the loading end to the body of the specimen. The reduction ensures that failure occurs within the body of the specimen, allowing strain to be measured within the gauge length. A radial or smooth transition from the end of the specimen to the narrow, middle portion appears to be the most appropriate geometric shape to avoid local stress concentrations (*Mechtcherine, 2007*). In *Fig. 2.4c & d* respectively, an un-notched and notched prismatic or cylindrical specimen is bonded to stiff loading platens. The advantage of cylindrical specimens is that they are easily produced and match the shape of cores taken from structures in-situ. One disadvantage of cylinder specimens, which are cast vertically, is an unfavourable fibre orientation with respect to the loading direction. *Fig. 2.4e* is an example of a notched dog-bone shaped specimen with hinged ends. In some cases, it may be necessary to reinforce externally or internally

in the transition region from the point of loading application to the gauge zone. This is done to ensure that failure reliably occurs within the gauge zone or notch.

Fig. 2.4a, b & c are suitable for strain-hardening composites where multiple cracking is present. *Fig. 2.4 d & e* are suitable for the determination of the stress vs crack-opening response and strain-softening composites where localised failure is expected. A notch is required for quasi-brittle materials, in order to ensure stable crack development. This also necessitates a smaller gauge length. Unfortunately, stress concentrations and a multi-axial stress state at the notch is the drawback for enforcing the failure zone via the notch.

Specimen dimensions

Depending on the composite rheology and the size of the largest mix constituents, mainly coarse aggregate particles and fibre, size effects can be significant. Composite performance is linked to fibre distribution and orientation, which is a function of the specimen dimensions and casting procedure. It is therefore important to consider the effect of local material imperfections (in terms of the ratio of defect size to specimen size) as well as how wall effects may influence fibre orientation. A wide variety of specimen dimensions are used in the literature.

The following recommendations for specimen dimensions are given by *Naaman et al. (2007)*:

- Prismatic or cylindrical specimens with a side or diameter of at least 50 mm, 3 x fibre length (L_f), or 6 x maximum aggregate particle size, whichever is larger.
- Gauge length for measuring strain: 2-3 times minimum dimension (side or diameter) of tensile prism
- In the case of thin sheets, the smaller side equates to the thickness of the sheet and the larger dimension must satisfy the above criteria
- Dog-bone shaped and confined ends give the best results

2.3.2 Specimen boundary conditions

The boundary conditions as shown in *Fig. 2.4* can vary from pin-pin (free rotation at both ends), to fixed-pin (rotation permitted at one end), or to fixed-fixed (no rotation permitted at either end). For a fixed-fixed connection, specimen alignment becomes very important to avoid bending moments, due to specimen eccentricity. In the case of pin-pin connections, deformations tend to increase at a faster rate on the side of the specimen where initial cracking occurred. This results in a non-uniform strain distribution and loading becomes increasingly eccentric (*Mechtcherine, 2007*). Non-rotational boundary conditions, if applied correctly, are believed to be the most appropriate, because a uniform strain distribution can be attained over the cross-section (*Mechtcherine, 2007*).

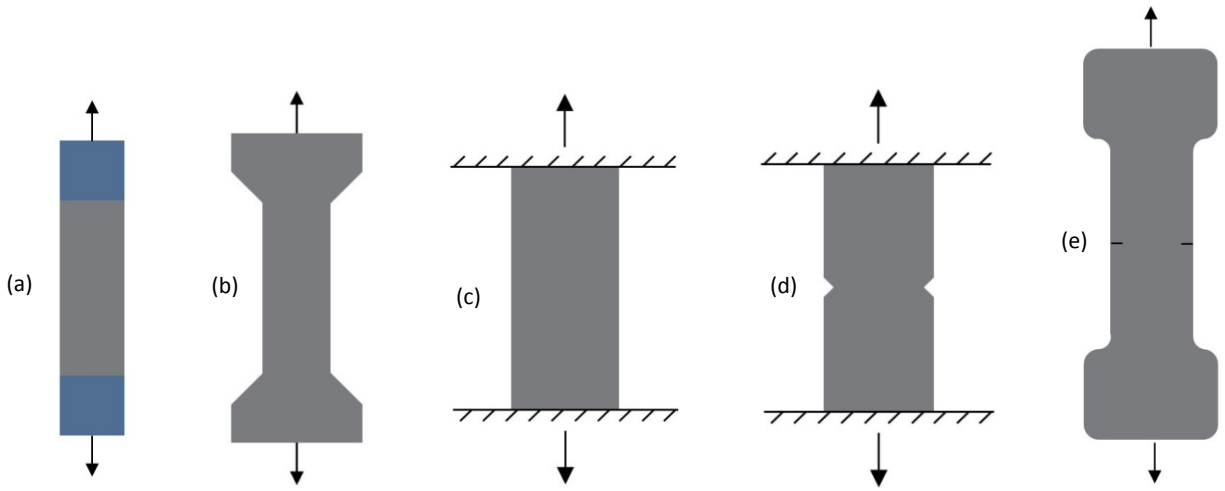

Fig. 2.4 – Tensile test examples for FRC (a) thin sheets; (b) Dog-bone shaped, hinged ends; (c) Bonded ends fixed against rotation; (d) Bonded ends notched and fixed against rotation; (e) Hinged ends notched (*Naaman et al., 2007*)

2.4 Mechanical investigations of Mode II fracture at the Meso-scale

There are a number of important aspects that need to be taken into consideration in the design of a shear parameter test method. Firstly, little or no bending moment must develop over the shear plane. Pure shear values are distorted in the presence of compression and tensile stress and in some cases the mode of fracture can differ. A clear determination of the shear force distribution along the shear plane may be difficult even with small scale specimens. Secondly, it is important to capture the post-fracture behaviour which is an indicator of interfacial fracture energy. The test must therefore be controlled throughout its duration, especially at the point of initial fracture and until total fracture.

A number of test methods, some of which are shown in *Fig. 2.5*, have been proposed and used for a variety of materials. An ideal scenario of pure shear in an interface is illustrated in *Fig. 2.5a*, but cannot be executed experimentally. The shear "push-through" test method (*Fig. 2.5b*) considers the average response of two interfaces. This method is used by the Japanese Society of Civil Engineering (JSCE) in its standard method (*JSCE-G 553, 1999*). This research considers pre-cracking of the shear interface and the push-through method (with its two interfaces) is therefore not a practical candidate.

The Ohno shear beam (*Fig. 2.5c* (*Arakawa & Ohno, 1957*)) theoretically achieves a pure shear condition at the centre of the specimen. A modified version of the Ohno shear beam was developed by *Iosipescu (1967)* and is shown in *Fig. 2.5d*. The narrow rectangular notches in the Ohno specimen are replaced with angular notches at the interface. The reduced interfacial area lowers the bending moment and results in uniform shear over the shear plane.

The "push-off" specimen (*Fig. 2.5e*), was initially proposed by *Mattock & Hawkins (1972)*. Compressive stresses at the top and bottom of the shear plane increase the shear capacity in these zones. This type of test can also be sensitive to the eccentricity of the applied compressive load,

which is translated in flexure instead of shear. The push-off specimen typically requires reinforcement outside the shear plane (*Fig. 2.5e*) to prevent flexural failure of the specimen. The manufacture of these specimens can therefore become a cumbersome procedure and the reinforcement can affect the fibre distribution in the case of SFRC.

Given the objectives of this research the Iosipescu shear test method is considered to be the most appropriate test method.

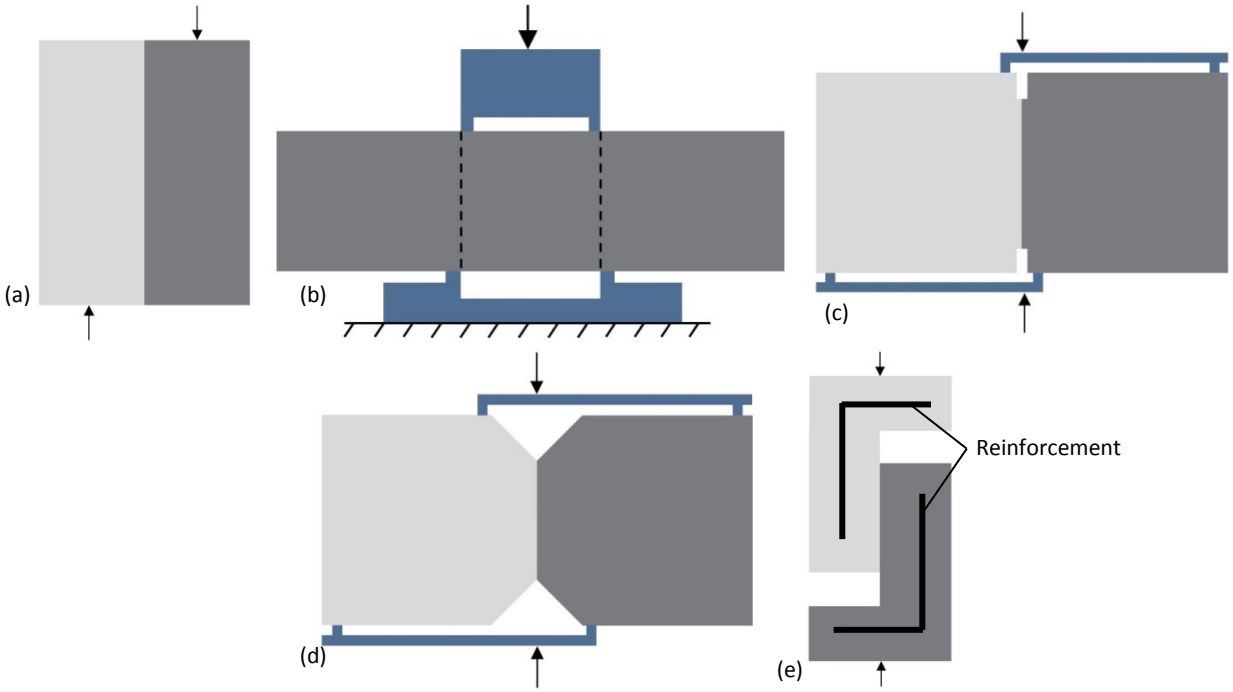

Fig. 2.5 – Shear test methods (a) Ideal, (b) Push-through, (c) Ohno-beam, (d) Iosipescu, (e) Push-off (with reinforcement)

2.5 Experimental investigation of axial and transverse fibre pull-out

Due to the limited experimental characterisation of axial fibre pull-out performed in this study and the abundance of research already conducted on the axial pull-out of straight and hooked-end steel fibres from a cement-based matrix, this topic will not be covered here. The reader is instead directed to work done by: {*Naaman et al. (1989, 1991)*; *Chanvillard, 1999*; *Van Gysel, 1999*; *Alwan et al., 1999* and *Sujivorakul et al., 2000*} - sourced from *Lee & Foster (2006)*; {*Naaman and Shah, 1976*; *Shannag et al., 1997* and *Guerrero and Naaman, 2000*} – sourced from *de Oliveira (2010)*; {*Naaman, 1999*; *Stang & Li, 2001*; *Van Gysel, 2000*; *Weiler et al., 1999* and *Groth, 1996*} – sourced from *Grünewald (2004)*.

The majority of research in this field is mainly focused on the uniaxial tension or flexural behaviour of the composite. Experimental characterisation of the individual fibre pull-out response together with modelling and analysis of the pull-out mechanisms is an advanced modelling and design tool. The following parameters are important: fibre orientation, embedded length, fibre geometry and end anchorage, fibre-matrix bond, fibre and matrix properties including stiffness and strength. Many investigations reconcile the pull-out response of an individual fibre to the composite tensile or

flexural response of SFRC. At the time of publication of *Soetens & Matthys (2012)*, only one study (*Lee & Foster, 2006*) was known that applies the same method for investigating the Mode II fracture of SFRC. The methodology and results of *Soetens & Matthys (2012)* and *Lee & Foster (2006)* are briefly summarised here as background and context for the single fibre transverse pull-out tests conducted in this research.

2.5.1 Experimental tests

Soetens & Matthys (2012)

Soetens & Matthys (2012) performed push-through tests with two vertical sliding planes, each crossed by a single fibre. The method is based on push-through tests on standardized prisms (150 x 150 x 500 mm³), which was first developed by the JSCE (*JSCE-SF6, 1990*) and modified by *Mirsayah & Banthia (2002)*. The test setup is given in *Fig. 2.6*. *Soetens & Matthys (2012)* investigated five fibre orientation angles θ (+60°, +30°, 0°, -30° and -60°), defined in *Fig. 2.6*.

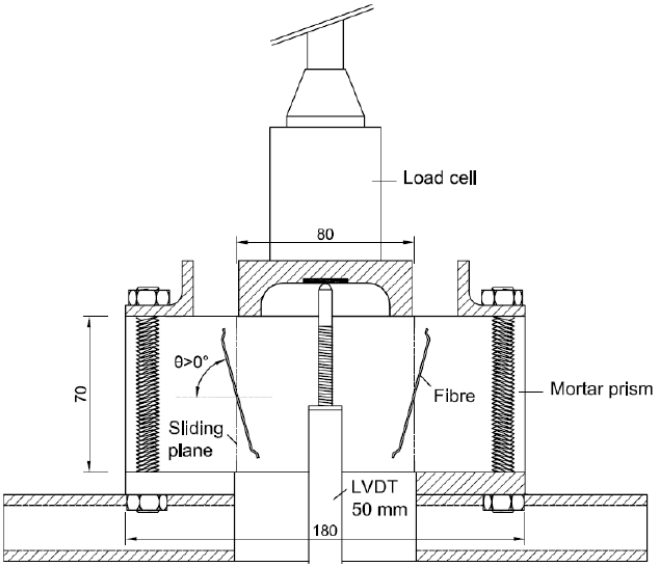

Fig. 2.6 - Single fibre push-through test setup (*Soetens & Matthys, 2012*)

Lee & Foster (2006)

Lee & Foster (2006) investigated the transverse fibre pull-out response via a "push-off" type specimen. The variables considered include: fibre anchorage (hooked-end and straight), fibre orientation and embedded length. A total of six to eight fibres were positioned across the shear plane at a specific embedded length and orientation (see *Fig. 2.7*). The fibre orientations (defined similar to *Soetens & Matthys (2012)* in *Fig. 2.8*) investigated include θ = 0°, ±15° ±30°, ±45°, ±60° and ±75°.

2.5.2 Results and discussion

Soetens & Matthys (2012) and *Lee & Foster (2006)* observed similar characteristic behaviour, despite using different testing methods. Three failure modes were observed, namely (i) fibre pull-out, (ii) fibre rupture and (iii) combined fibre rupture and pull-out. Fibre pull-out is when the fibre is completely pulled out of the surrounding matrix and is characterised by ductile behaviour. Fibre rupture is when the breaking strength of the fibre is reached before the fibre is pulled out.

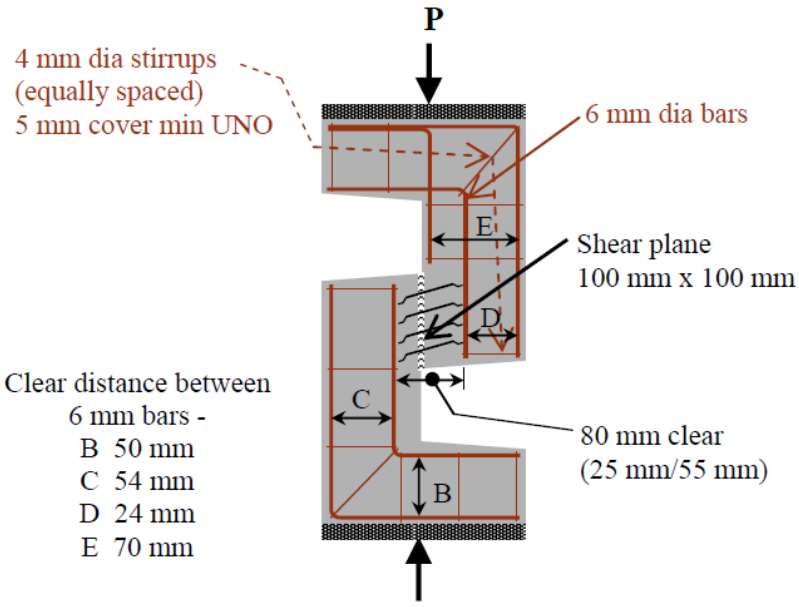

Fig. 2.7 - Push-off specimen dimensions, steel reinforcement and fibre locations for fibre embedded length = $L_f/4$ (*Lee & Foster, 2006*)

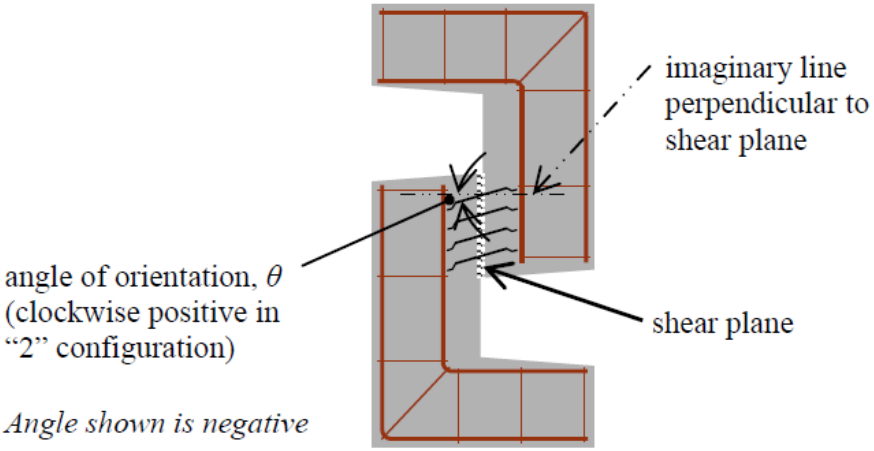

Fig. 2.8 - Determination of angle of orientation (*Lee & Foster, 2006*)

Fibre pull-out

Fibre pull-out (*Fig. 2.10b*) occurs for positive fibre orientations. Tensile loading and debonding of the fibre occurs early with the mechanical bond engaged for small displacements. This can be observed in *Fig. 2.9*, where θ=0°,+30° and +60° reach peak pull-out load at smaller transverse displacements compared to the negative fibre orientations. Notice that transverse displacement at peak pull-out load is increasing for lower orientation angles.

Fibre rupture

Fibres with a negative orientation are more prone to rupture (*Fig. 2.10a*). This is attributed to the greater bending the fibre undergoes resulting in a snubbing effect (*Fig. 2.10c*, *Lee & Foster (2006)*). Significant shear slip occurs before the fibre is fully engaged and as a result of the snubbing effect, the shear interface constrains and abrades against the fibre. This causes higher frictional forces to act on the fibre and leads to the rupture of the fibre before further debonding and slip can occur.

Fibre pull-out and/or rupture: Transition zone

A transition zone exists for orientation angles in the region of -15° ≤ θ ≤ 15° (*Lee & Foster, 2006*), where a combination of fibre pull-out and rupture can occur.

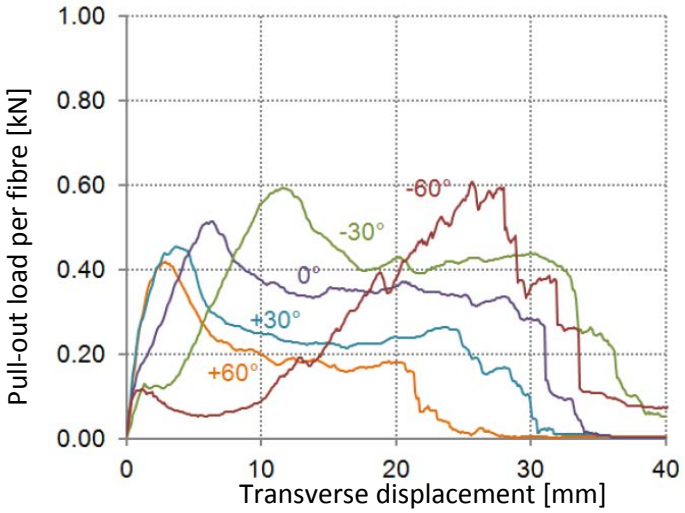

Fig. 2.9 – Average pull-out curves (*Soetens & Matthys, 2012*)

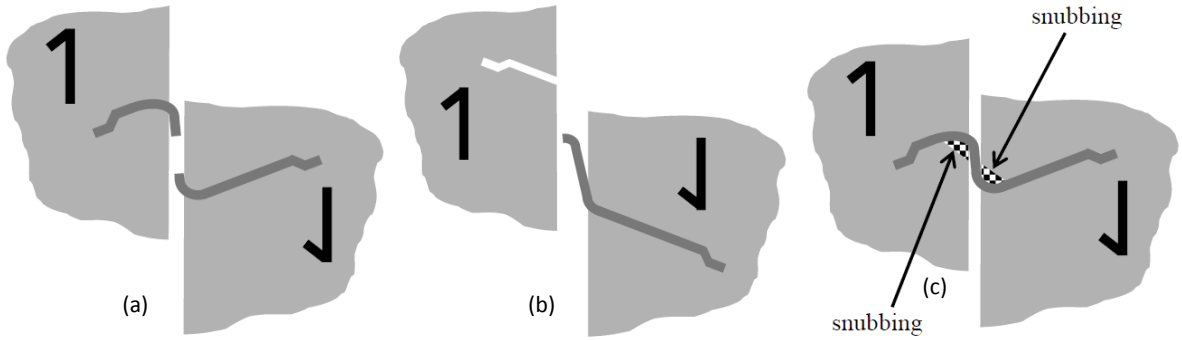

Fig. 2.10 - Fibre failure modes and behaviour: (a) rupture; (b) pull-out; (c) snubbing (*Lee & Foster, 2006*)

2.6 Digital Image Correlation and Computed Tomography

2.6.1 Digital Image Correlation

An optical measurement technique, the ARAMIS system and software (GOM – Optical Measuring Techniques) is used for the experimental investigation in *Chapter 5*. ARAMIS is a non-contact optical 3D deformation measuring system, which analyses, calculates and documents deformations through surface structure recognition. Two calibrated cameras, in a stereo configuration, record digital images at a specified frame rate. The frame rate used, ranges between 1 to 2 images per second. Each image is stored as a 'stage' in a project. The initial image of the specimen in the un-deformed state is defined as the reference stage and deformations are determined relative to this stage. The area of interest is defined on the specimen surface and is divided into a grid consisting of rectangular facets (*Fig. 2.11*), which consists of a specified number of pixels. The facet size ranges from 15 to 32 pixels.

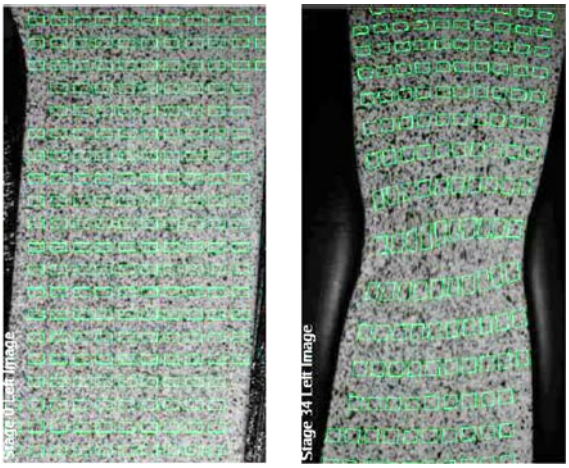

Fig. 2.11 – Specimen states (a) Undeformed state (b) Deformed state with considerable material necking (*Aramis v6.1 User Manual – Software, 2008*)

The image pixels are allocated coordinates and the system determines the 2D coordinates of the facets from the corner points of the facets and the resulting centres. Section lines can be defined via the software, allowing the user to select specified stage points on the surface of the specimen.

Characteristics observed for each facet are used to determine the deformation of the facet in each stage relative to the reference stage. In the case of a homogeneous surface, such as that of concrete, the measuring surface needs to be prepared. The application of a stochastic or sprinkle pattern, such as the one illustrated in *Fig. 2.11*, on the surface of the specimen provides identifiable characteristics.

2.6.2 Computed Tomography

MicroCT scans of steel fibre reinforced specimens are performed at the Stellenbosch CT Facility (*du Plessis et al., 2016*), using a General Electric V|TomeX L240 system. X-ray microCT generates high quality 3D volumetric data of an object. The volume data set typically comprises of up to 2000 x 2000 x 2000 volumetric pixels (voxels), each having a grey value in the range 0 - 65 535, depending on the material density and atomic composition. The associated voxels of denser particles (e.g. steel fibre) inside the material will be brighter (higher grey values) and surrounding material (concrete) will be less bright. This data is typically analyzed in 3D data viewing and analysis software Volume Graphics VGStudioMax 3.0 (*Fig. 2.12*). The software allows for the quantification of the fibre orientation distribution within a volume, as well as the fibre count and embedded length at specified planes.

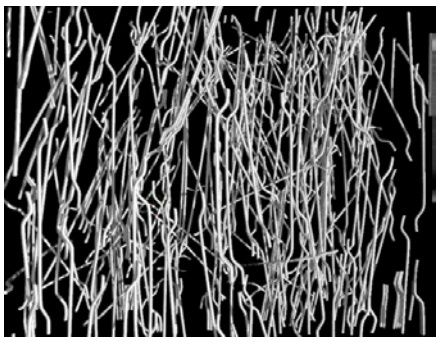

Fig. 2.12 – CT-scan image of steel fibres in a SFRC specimen

Summary

The first section of this chapter discusses the main findings of a literature survey on the steel fibre-reinforcement of structural RC beam members subject to shear-dominant loading. This provides the research background and establishes the broader research context. The remainder of this chapter is a focused literature review, framed closely around the central research questions raised in the previous chapter. First, the material under investigation (SCC and SFRC) is introduced, with emphasis on the key characteristics, requirements and design principles for mixture optimisation. Experimental investigations of the Mode I and Mode II fracture, conducted at the Micro and Meso-scale are reviewed. Finally a brief overview is given for some of the technologies used in this research, namely Digital Image Correlation and Computed Tomography (CT-scan).

Chapter 3

Composite design and classification

This chapter presents the process whereby the mixture composition, constituent properties, and production method for the SFR-SCC is determined. The composite is classified in terms of workability, compressive strength development, elastic modulus and post-fracture toughness.

3.1 Composite design method

The procedure used to design the composite in this research, is based on an approach for developing SCC mixes. The method was developed by *Okamura & Ouchi (1999)* and optimises the composition of SCC on three different levels, namely paste, mortar and concrete. One additional phase, fibre-reinforcement, is considered here as well. The composite phases and constituent volume fractions used in this study are shown in *Fig. 3.1*. Optimisation of the different composite phases is done using relatively narrow ranges of the constituent proportions typically recommended by literature. The criteria used to measure the performance of each composite are based on the rheological (flowability) and mechanical properties (compressive strength) of the composite.

3.1.1 Paste phase

The parameters investigated at the level of the paste include the volumetric water-powder ratio (w/p) and the powder composition, which includes binder (cement and additions/extenders) and inert/filler materials. The parameters varied at the level of the paste are shown in *Table 3.1*.

3.1.2 Mortar phase

In the mortar phase, the fine aggregate volume percentage of mortar is varied between 45% and 50%. Two types of locally available fine aggregate are considered: Malmesbury sand and Philippi sand, which are described in more detail in *Section 3.2*. Two fine aggregate compositions (mass percentage) are also investigated: (1) Malmesbury sand only and (2) a blended sand (70% Malmesbury and 30% Philippi sand by mass).

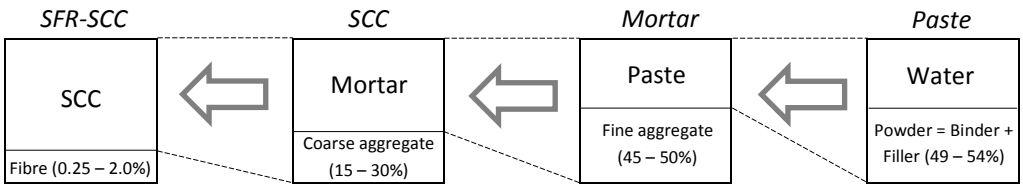

Fig. 3.1 – Composite phases including constituent volume percentage ranges for each phase (Sequence of composite development indicated by arrows)

For each of the base mortar mixtures developed, the slump flow diameter is measured via the flow cone test (*EFNARC, 2002*) for mortars, and if it falls inside the acceptable range of 240 – 260 mm, cubes are cast to be tested at 7, 14 and 28-day strength. A V-funnel test (*EFNARC, 2002*) is recommended in order to determine the flow time of the mortar and properly characterise the workability. A V-funnel test apparatus was however not available at the time and the test was not performed. The T_{500} test (*EFNARC, 2002*; *SCCEP Group, 2005*) is however performed on the final mortar mix design and is found to fall inside the acceptable range.

A total of 30 mortar designs are tested (see *Addendum C*). In addition to the flow cone test, a visual inspection checked the mortar consistency and searched for signs of segregation. The best mortar design is selected based on the mechanical (target 28-day compressive strength of 40-50 MPa) and rheological criteria specified earlier.

The final parameter values selected are given in *Table 3.1*. The initial mix design for the self-consolidating mortar is provided in *Table 3.2*. Unfortunately, soon after the conclusion of this test series, the CEM I cement used was no longer locally available and consequently, is replaced by CEM II 52.5N cement. The powder composition is also adjusted: The total fly ash percentage replacement is reduced to 25% (by mass of powder) and a mineral (dolomitic) filler is introduced at 25% of the total powder mass. The cement (CEM II) therefore constitutes 50% of the powder material mass. All other mix proportions remained the same. The final mortar design is shown in *Table 3.3*.

Table 3.1 – Parameter range and final values for paste and mortar phase

Parameter	Parameter range	Final value
w/p (volume)	0.85, 0.90, 0.95, 1.0 and 1.05	0.90
Cement type	CEM I 52.5, CEM II 42.5	CEM I 52.5
Additions	Fly ash	Fly ash
Addition mass % of powder	40, 45, 50, 55 and 60%	60%
Fine aggregate volume % of mortar	45% and 50%	50%
Fine aggregate composition	Malmesbury only and Blend	Blend 70 : 30

3.1.3 Concrete and fibre-reinforcement phase

Once the mortar composition is determined, the incorporation of a coarse aggregate and fibre fraction is a straight-forward procedure. It is well known that fibre reinforcement reduces the workability of concrete. Consequently the coarse aggregate quantity and grading have to be adjusted to accommodate the fibre. Limits are therefore placed on the coarse aggregate quantity (15-30% of SCC volume or approximately 400-800 kg/m^3) and maximum aggregate particle size (< 13.2 mm).

Table 3.2 – Initial mortar design

Constituent:	**kg/m^3**
OPC CEM I 52.5N	263
Fly ash	395
Mineral filler	0
Water	237
Malmesbury sand	927
Philippi sand	397
Superplasticiser[1]	2.15
Viscosity Modifying Agent (VMA)[2]	0.3
$f_{c,cube\ 28-day}$ [MPa]	38.9

[1]MAPEI Dynamon SP1, [2]MAPEI Viscostar 3K

Table 3.3 – Final mortar design

Constituent:	**kg/m^3**
OPC CEM II 52.5N	357
Fly ash	178
Mineral filler	178
Water	237
Malmesbury sand	927
Philippi sand	397
Superplasticiser[3]	4.43
VMA	0
$f_{c,cube\ 28-day}$ [MPa]	54.1

[3]MAPEI Dynamon SX

A practical range for steel fibre dosage varies between 0.25% and 2.0% of concrete volume. Typically an optimum dosage (in terms of workability and mechanical performance) lies between 0.50% and 1.5%. At this stage the workability of different combinations of coarse aggregate grading, content and fibre dosage needs to be tested to determine the limits of the composite. The acceptance criteria for workability (*EFNARC, 2002*; *SCCEP Group, 2005*) include the slump flow diameter (Abrahams cone) = 600 – 800 mm and T_{500} = 2 – 5 seconds. Ultimately a coarse aggregate content range of 450 – 750 kg/m^3, coarse aggregate size of 6.7 – 13.2 mm and a maximum fibre dosage of 1.0% of concrete volume are selected to represent the majority of the experimental tests conducted.

3.2 Constituent properties

3.2.1 Fine and coarse aggregate

Fine aggregate

Two sands locally available to the Western Cape region, Malmesbury and Philippi sand are used in this research. The average particle size and particle size distribution are determined via the method prescribed in *SANS 201: 2008* and shown in *Figs. 3.2-4* for both sands. *Fig. 3.2* and *3.3(a)* illustrate the percentage mass of fine aggregate passing through each sieve, whereas *Fig. 3.3 (b)* and *3.4* illustrate the percentage mass retained on each sieve. The particle size is taken as the average of the retaining sieve size and the sieve size above e.g. the average particle size retained on the 75 µm sieve is assumed as the average of the 75 µm and 150 µm sieve, which is approximately 113 µm. The properties of each sand are summarised in *Table 3.4*. As mentioned in the previous section, a blended sand ratio of 70:30 by mass of Malmesbury and Philippi sand respectively is used.

Coarse aggregate

A single type of locally available coarse aggregate is considered, namely Greywacke stone. Three standard coarse aggregate size categories are investigated, namely 6.7 mm, 9.5 mm and 13.2 mm. *Fig. 3.5(a)* illustrates the percentage mass of coarse aggregate passing each sieve. *Fig. 3.5(b)* illustrates the percentage mass retained on each sieve, where the particle size is taken as the average of the retaining sieve size and the sieve size above. The properties of the coarse aggregate are summarised in *Table 3.5*.

Table 3.4 – Fine aggregate properties

	Malmesbury sand	**Philippi sand**	**Blended sand**
Avg. particle diameter [µm]	796	447	692
Dust content [%]	6.0	0.4	4.3
Fineness modulus (FM)	2.3	1.7	2.2
Relative density (RD)	2.64	2.67	2.65
Appearance/shape			

Table 3.5 – Coarse aggregate properties

Greywacke	**6.7 mm**	**9.5 mm**	**13.2 mm**
Avg. particle size [mm]	6.0	8.1	10.5
Relative density (RD)	2.73	2.73	2.73
Appearance/shape			

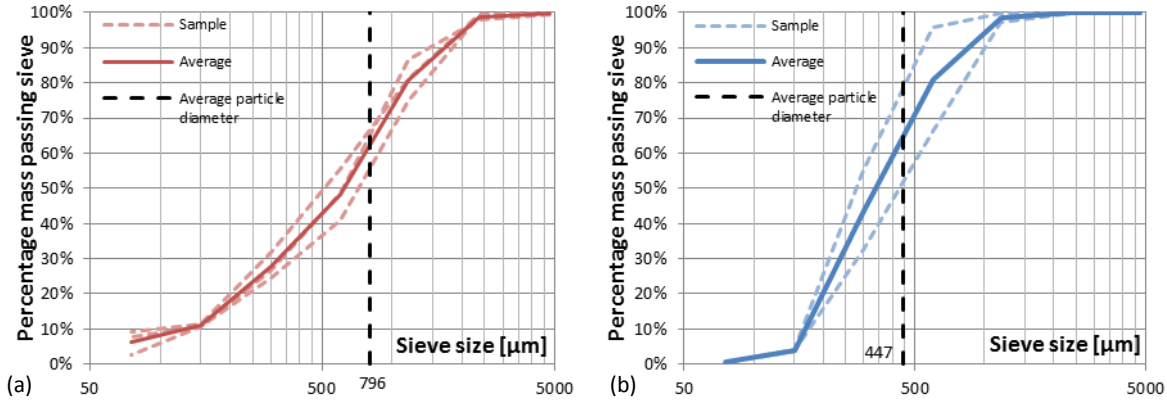

Fig. 3.2 – Particle size distribution of (a) Malmesbury and (b) Philippi sand

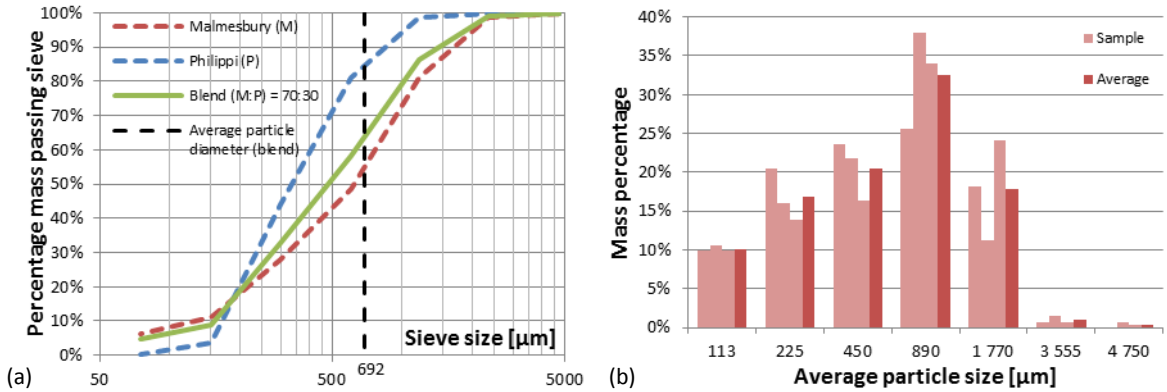

Fig. 3.3 – (a) Particle size distribution of blended sand (b) Particle size distribution (based on average sieve size) of Malmesbury sand

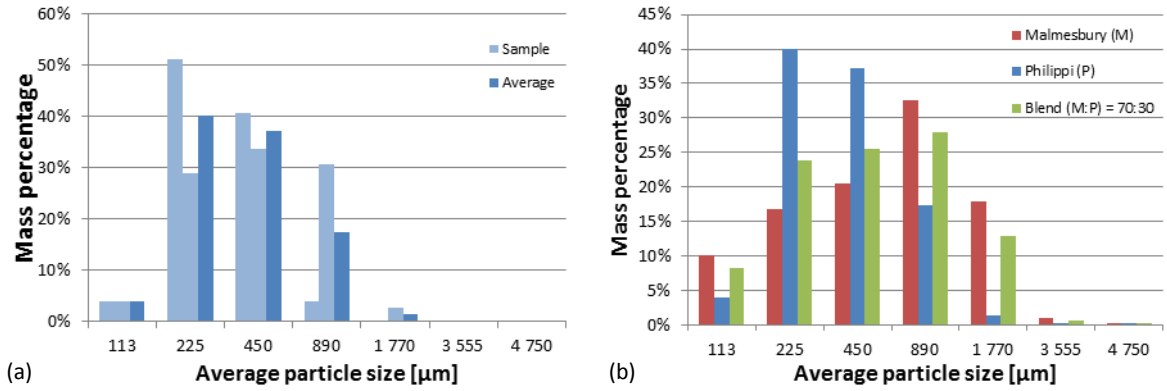

Fig. 3.4 – (a) Particle size distribution (based on average sieve size) of Philippi sand (b) Particle size distribution (based on average sieve size) of Malmesbury, Philippi and blended sand

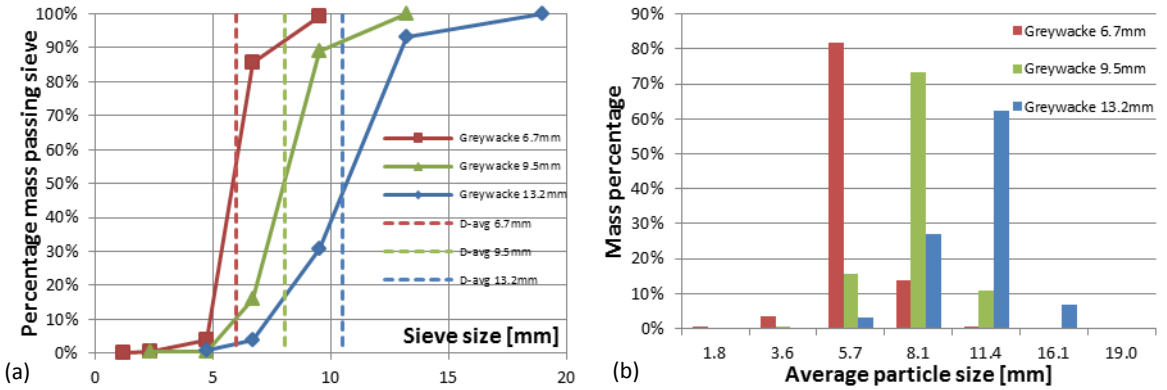

Fig. 3.5 – (a) Particle size distribution and average particle size of Greywacke stone 6.7, 9.5 and 13.2mm (b) Particle size distribution (based on average sieve size) of Greywacke stone 6.7, 9.5 and 13.2mm

3.2.2 Powder material

Cement: OPC CEM II/A-L 52.5N (PPC Cement)

OPC conforms to the 52.5 N strength class of *SANS 50197-1:2013* for common cements and is identified as a Portland Composite Cement CEM II/A-L 52.5 N, where "CEM II/A-L" denotes the addition of between 6 and 20% limestone extender. The characteristics and composition of the cement are summarised in *Table 3.6* and *3.7* respectively. The particle size distribution is shown in *Fig. 3.6 (a)*.

Table 3.6 – Characteristics of OPC CEM II/A-L 52.5N

Relative density	3.14
Calculated surface area cm^2/g	4000
LOI (Loss-on-Ignition) %	2.5 – 4.2

Source: PPC Cement

Table 3.7 – Chemical composition of clinker/cement

Composition	**%**
SiO_2 (Silica)	22.5
Al_2O_3 (Alumina)	3.9
Fe_2O_3 (Iron Oxide)	3.4
MgO (Magnesia)	0.9
CaO (Lime)	66.9
C_3S	59
C_2S	21
C_3A	5
C_4AF	11

Source: PPC Cement

Addition: Fly ash

A siliceous fly ash (DuraPozz®, AshResources) is used. The typical characteristics and chemical composition of the material are provided in *Table 3.8* and *3.9* respectively. The particle size distribution is shown in *Fig. 3.6 (b)*. Durapozz® complies with the chemical and physical requirements of *SANS 50450-1:2014*, Category S.

Table 3.8 – Characteristics of fly ash

Relative density	2.12 – 2.20
Calculated surface area cm^2/g	9500[1]
Moisture content %	<0.2[1]
Colour	pale grey/white
LOI (Loss-on-Ignition) %	0.5 – 2.0
Carbon content %	0.6[1]

[1]DurapozzPro (may differ from Durapozz used) (Source: AshResources)

Table 3.9 – Chemical composition of fly ash

Composition	**%**
CaO (Lime)	4-10
SiO_2 (Silica)	47-55
Al_2O_3 (Alumina)	25-35
Fe_2O_3 (Iron Oxide)	3-4
MgO (Magnesia)	1-2.5

Source: AshResources

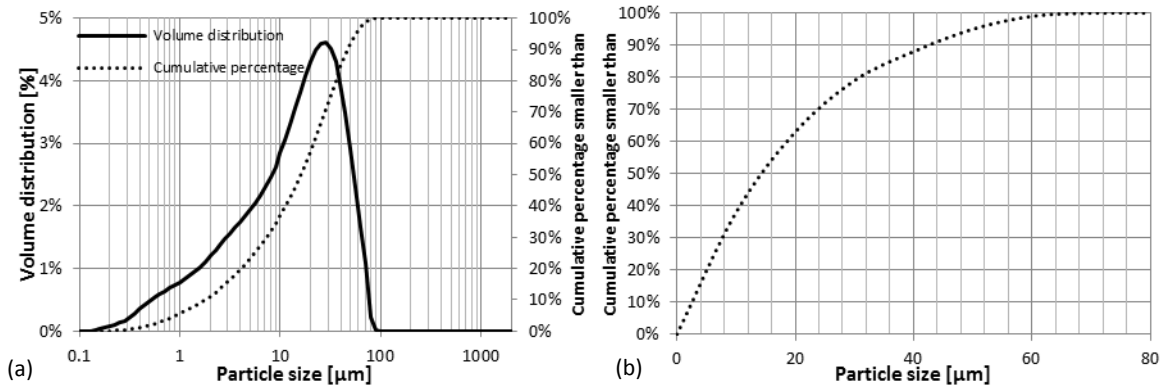

Fig. 3.6 – Particle size distribution of (a) OPC CEM II/A-L 52.5N (Source: *PPC Cement*) and (b) Durapozz® fly ash (cumulative) (Source: *AshResources*)

Mineral filler: Filla 15

SCC typically contains larger volumes of fines/powder material than ordinary concrete. These fines typically constitute reactive materials i.e. cement and some smaller percentage of semi-inert materials e.g. fly ash and inert materials e.g. limestone filler. In order to limit the strength of SCC, still achieve the required workability and reduce cost, an inert mineral filler, which does not contribute to the strength of concrete, while still providing for the required workability is essential. Filla 15 (*Cape Lime*) is a dolomitic filler, which is typically used in the manufacturing of tile cement, plastic, rubber, vinyl floor tiles, paints etc. The composition is approximately 42% $MgCO_3$ and 52% $CaCO_3$, with the remainder impurities which mainly constitute silica. The carbonate is inert and does not participate in the chemical reactions in concrete. The particle size distribution of this material is shown in *Fig. 3.7*, and the relative density of the material is 2.6.

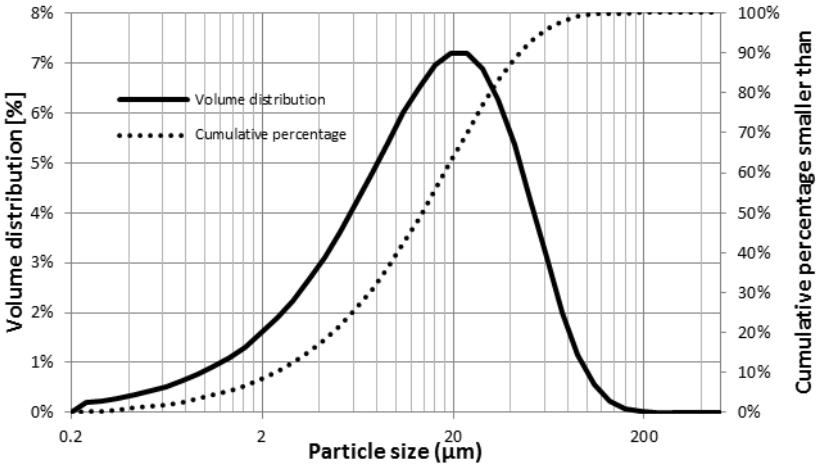

Fig. 3.7 - Particle size distribution of mineral filler (Filla 15) (*Source: Cape Lime*)

3.2.3 Admixtures

Two superplasticisers, Dynamon SP1 and Dynamon SX (MAPEI) are used. Dynamon SP1 is used in conjunction with a VMA, Viscostar 3K (MAPEI). Ultimately Dynamon SX without any VMA was determined to produce the best workability and is used in the remainder of experimental work.

Dynamon SP1/SX

Dynamon SP1 and Dynamon SX are superplasticisers based on a modified acrylic polymer for concrete with low water/powder ratio, high level of workability and in the case of Dynamon SX, long term slump retention, which makes them suitable for the manufacturing of SCC.

Viscostar 3K

Viscostar 3K is an active polymer-based admixture in an aqueous solution. It controls the cohesion of the cementitious paste, avoiding segregation and bleeding of concrete. In this way, it helps maintain the fluidity and passing ability of the concrete.

3.2.4 Fibre

Three fibre types were chosen for the preliminary material classification: Bekaert Dramix ® *RC-65/35-BN*, *RL-45/35-BN* and *RL-45/50-BN*, of which only one fibre type is selected for the remainder of this research. A *ZP 305* fibre is used in a stand-alone shear push-off test series (Not reported in this dissertation). All fibres are made of cold drawn low carbon steel wire. The fibre notations, geometry (*Fig. 3.8*) and material properties are provided in *Table 3.10*.

3.3 Production method

3.3.1 Mixing procedure

The mixing steps and related times are shown in *Table 3.11*. A pan mixer is used for all mixes. First, the dry materials are added to the mixer in the following sequence: sand, powder (cement, additions and filler) and coarse aggregate. The dry components are mixed for 30-45s, at which point water is gradually added to the mix. Depending on the size of the mix (3-80 litres in this study), water addition may take 30-60s. A further 60s are allowed for properly integrating the water into the mix.

Table 3.10 – Fibre properties (Source: Bekaert)

	ZP 305	**RC-65/35-BN**	**RL-45/35-BN**	**RL-45/50-BN**
Nominal length, L [mm]	30	35	35	50
Nominal wire diameter, d [mm]	0.55	0.55	0.75	1.05
Angle through which wire is bent, α, α'	20° (Min.)	20° (Min.)	20° (Min.)	20° (Min.)
Length of bend ends, l, l' [mm]	1.5 – 4.0	1.5 – 4.0	1.5 – 4.0	1.5 – 4.0
Crimp depth, h, h' [mm]	0.75 (Min.)	0.75 (Min.)	0.75 (Min.)	0.75 (Min.)
Radius of bends [mm]	n/a	n/a	n/a	n/a
Aspect ratio (λ = L/d)	54	64	47	48
Tensile yield strength [MPa]	1345	1345	1225	1115
E-modulus [GPa]	210	210	210	210
Shape of fibre	Hooked-end	Hooked-end	Hooked-end	Hooked-end
Form of delivery	Glued strips	Glued strips	Loose	Loose
Appearance:	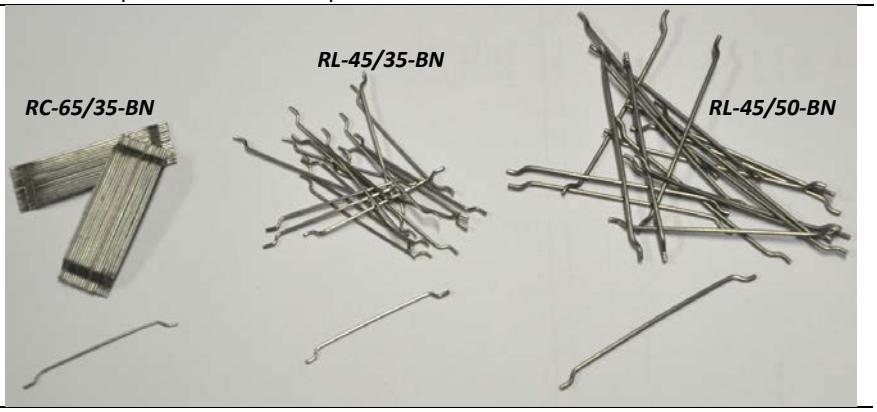			

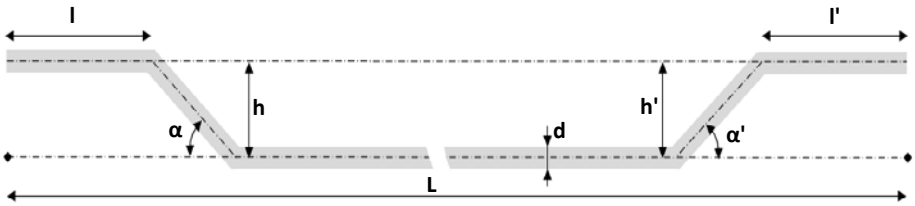

Fig. 3.8 – Fibre geometry (Source: Bekaert)

Before the addition of the admixture(s), the mixer is stopped and the container and mixing blades are checked for segregated materials, which are then reintegrated into the mix. Mixing is then resumed and the superplasticiser is gradually added to the mix over a period of 30-60s, depending on the mix size. A further 1-2 minutes are allowed for integrating the superplasticiser into the mix. If a VMA is also added, the same procedure is repeated as for the superplasticiser. Once the mix has obtained the required consistency of SCC, the steel fibres are gradually introduced by hand. Depending on the quantity of fibre (0.5% - 1.0% of concrete volume for this study) and mix size, fibre addition may take 1-2 minutes. A final 2 minutes of additional mixing is provided to ensure fibres are properly dispersed. The separation time for the glued fibres (e.g. *RC-65/35-BN*) is specified at an indicative value of 120 seconds by the manufacturer. The total mixing time is 7 to 10 minutes.

Each mix undergoes a number of rheological checks, to ensure that it complies with specified criteria. The checks include the measurement of the slump flow diameter and a visual inspection for segregation, bleeding and fibre balling. As mentioned before, the slump flow diameter must fall in the range of 240 – 260 mm for self-consolidating mortar (Mini-cone (*EFNARC, 2002*)) and 600 – 800 mm for SFR-SCC (Abrahams cone (*EFNARC, 2002*)).

Table 3.11 – Mixing procedure

No.	Step	Mixing time [s]
1	Dry constituents including: sand, cement, additions, filler and coarse aggregate dry mixed	30-45
2	Gradual addition of water	30-60
3	Integration of water into mix	60
4	Break: Reintegration of segregated materials	15-30
5	Gradual addition of superplasticiser	30-60
6	Integration of superplasticiser into mix	60-120
7	Gradual addition of steel fibre	60-120
8	Integration of steel fibre into mix	120
	Total mixing time	7 – 10 minutes

3.3.2 Casting procedure

Casting of specimens takes place immediately after mixing. In most cases, the concrete is cast horizontally into specimen moulds which have been prepared with a coating of mould release oil. For some mould geometries, mould release oil is not sufficient to facilitate easy removal of the specimen once it has set in the mould. In these cases, a layer of grease is applied to the mould surfaces. Care is taken to cast specimens in a random fashion, without causing preferential fibre alignment via the casting method. It is important to note that despite the casting method used, a 2-D preferential fibre alignment may still occur, because of the specimen geometry i.e. wall-effects. No vibration is used to consolidate the concrete, with only light tamping/prodding to fill in any remaining gaps and level the specimen.

3.3.3 Specimen curing and preparation for testing

Shortly after casting, specimens are moved to a climate controlled room (temperature 24±2°C and relative humidity 65±2%) for approximately 24-36 hours. The specimens are then removed from their moulds and placed inside a water curing tank (temperature 24±2°C) for an average of 28-35 days or until testing. In some cases, it is necessary to grind the casting face level or create a saw-cut notch in the specimen. Grinding and notching is typically performed 7 days prior to testing and specimens are returned to the curing tank afterwards.

3.4 Material classification

Unless otherwise stated, the *RC-65/35-BN* fibre type is used for all test series.

3.4.1 Compressive strength development

The compressive strength development of the self-consolidating mortar (SCM) and self-consolidating concrete (SCC, V_a = 450 kg/m^3, a = 9.5mm) developed in this study is presented in *Fig. 3.9 (a)*. Specimens are prepared as discussed in the previous section and are tested at approximately 7, 14, 28, 56 and 112 days after casting.

Two specimen sizes are tested, 50 mm cubes (exclusively for mortar with no fibre) and 100 mm cubes (mortar, concrete and SFRC). 50 mm cubes are tested in a Zwick Z250 materials testing machine and 100 mm cubes in a Contest 2MN press. The test rate applied in each case is 90 kN/min for 100 mm cubes and 60 kN/min for 50 mm cubes.

Compression specimens are cast as a control for the experimental programs to follow in *Chapters 4* and *5*. All compressive strength results for this research are summarised in *Fig. 3.9 (b)* for convenience. The average 28-day compressive strength ranges between 50 MPa and 60 MPa, with an average of 56 MPa across all test series. Steel fibre addition marginally increases compressive strength compared to unreinforced mortar or concrete. The 28-day compressive strength achieved for the "classification" tests including the elastic modulus, wedge-splitting and flexural response are also given in *Fig. 3.9 (b)*.

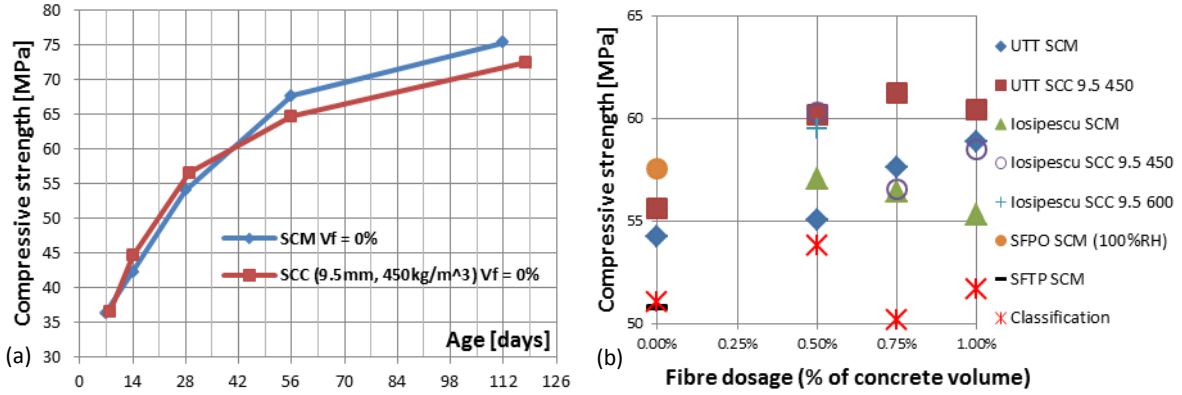

Fig. 3.9 – (a) Compressive strength development: SCM and SCC (100mm cube), (b) 28-day compressive strength (All experimental programs: UTT – Uniaxial Tensile Test (Meso-scale), SFPO – Single Fibre (Axial) Pull-out, SFTP – Single Fibre Transverse Pull-out)

3.4.2 Elastic compression modulus

The method for determining the secant modulus of elasticity in compression as prescribed in the British standard *BS EN 12390-13:2013* produces the elastic moduli of the SFR-SCC as summarised in *Table 3.12*. Three cylindrical specimens (diameter = 100 mm, length = 200 mm) are cast for each fibre dosage (0%, 0.5%, 0.75% and 1.0%). A coarse aggregate volume and particle size of 450 kg/m^3 and 9.5 mm respectively is chosen as representative of the composites developed and the elastic modulus is only determined for these coarse aggregate parameters. Fibre reinforcement has minimal or no effect on the elastic modulus and an average elastic modulus of 41.2 GPa is obtained across all fibre dosages. It is important to note that in most of the tests performed, one or more of

the three strain measurements used to determine the stiffness, deviated from the average strain value by more than the maximum percentage permitted. This is believed to over-estimate the stiffness of the composite by 3 – 4 GPa (compared to *Tab. 5.1-7 fib Model Code 2010*). Future studies using this particular setup should take the necessary steps to improve the experimental setup in terms of instrumentation and specimen alignment.

Table 3.12 – Elastic modulus (V_a = 450 kg/m^3, a = 9.5mm) [GPa]

Specimen no.	0%	0.5%	0.75%	1.0%	V_f
1	42.3	42.4	42.7	39.0	
2	39.9	38.4	47.4	39.7	
3	39.1	43.1	41.6	39.1	
Average	**40.4**	**41.3**	**43.9**	**39.3**	**41.2**

3.4.3 Post fracture energy and toughness

Wedge-splitting test

The wedge splitting test was initially proposed by *Brühwiler & Wittman (1990)* as an alternative method to determine the fracture energy of brittle materials such as concrete. Essentially, the objective of the test is to determine the amount of energy required to split a specimen into two halves. The fracture plane is subjected to a bending moment which results in the vertical propagation of a crack.

The dimensions of the specimen adopted in this study are provided in *Fig. 3.10*. A 100 mm cube specimen is cast with a notch (30 x 20 mm) inserted at the top of the specimen. Seven days prior to testing, a saw-cut notch, 30 mm deep, is made along the length of the cast-in notch. This forces the crack to initiate at the tip of the saw-cut notch. The test configuration and instrumentation are illustrated in *Figs. 3.11-13*. The specimen is centred on a loading platform (*Fig. 3.11*) with a support separation of 50 mm. Two roller fittings are positioned to bear on both inside-edges of the cast-in notch. The wedges then bear onto the rollers which transmit a lateral load, forcing the crack opening displacement (COD). As demonstrated in *Fig. 3.12*, F_v is the vertical load applied by the machine actuator and the splitting force F_h is the horizontal component of the force acting on the rollers. A linear variable displacement transducer (LVDT) is positioned on either side of the specimen as indicated in *Fig. 3.13* to measure the COD. The test rate is controlled by the COD via one of the LVDTs connected to a closed-loop servo-hydraulic testing machine (Instron 50 kN with 8800 controller) at 0.035 mm/min.

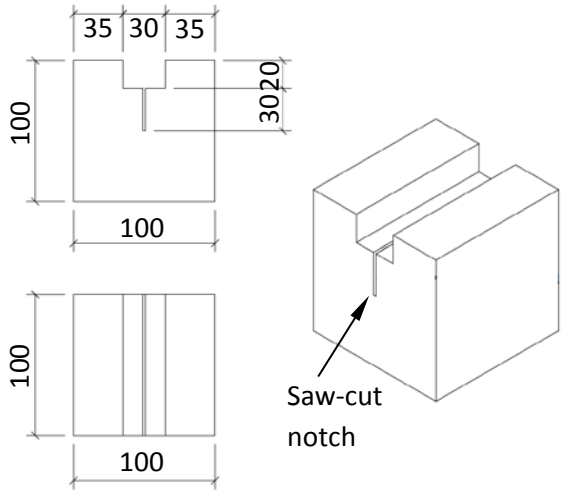

Fig. 3.10 – Wedge splitting test specimen dimensions (*de Villiers, 2015*)

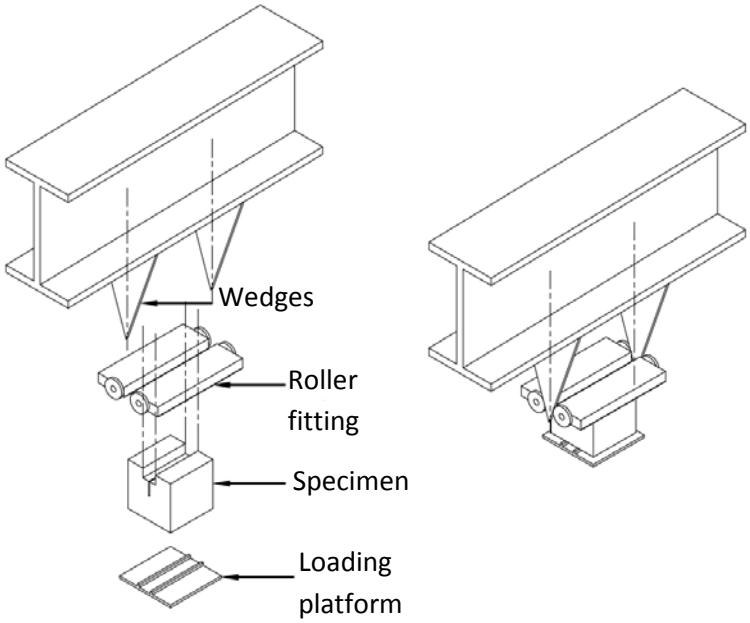

Fig. 3.11 – Schematic representation of wedge splitting test configuration (*de Villiers, 2015*)

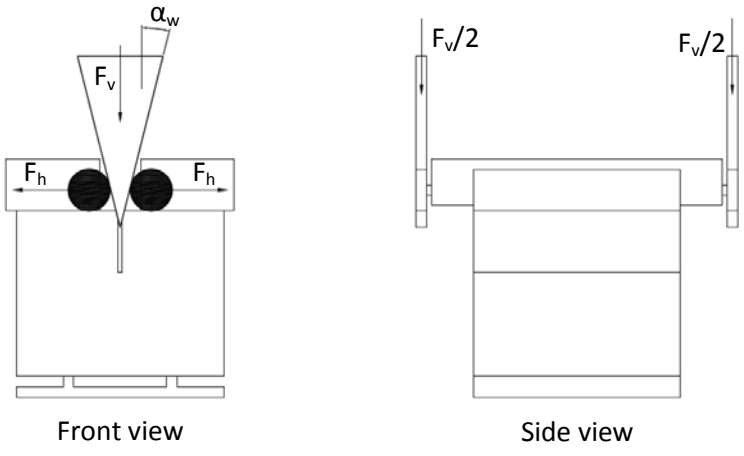

Fig. 3.12 – Schematic representation of specimen load application (*de Villiers, 2015*)

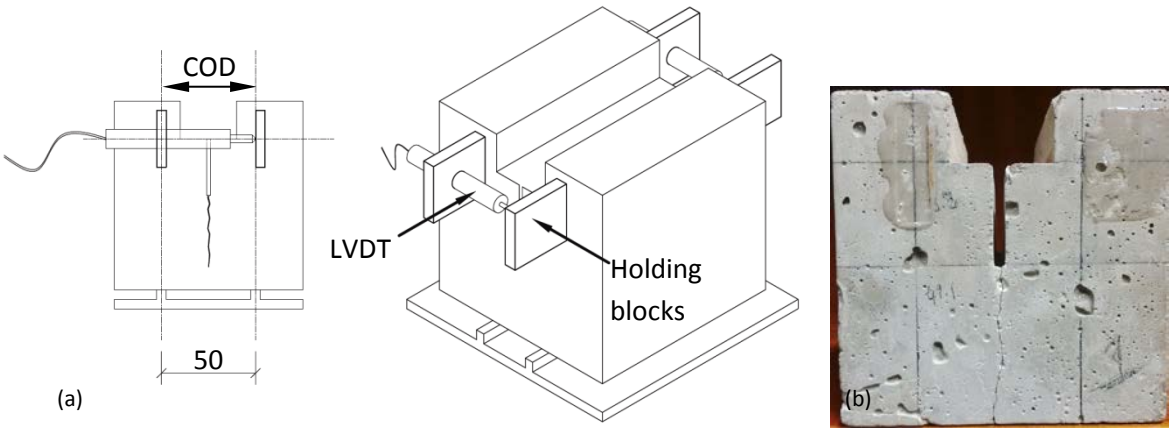

Fig. 3.13 – (a) Test instrumentation (*de Villiers, 2015*) and (b) example of a fractured specimen (V_f = 0%)

The horizontal splitting force, F_h, is determined with *Eq. 3.1*, where α_w is the wedge angle (*Fig. 3.12*). A wedge angle of 14° is used in this instance. The horizontal splitting force (F_h) vs. COD is provided in *Figs. 3.14-15* for the fibre dosages 0 %, 0.5 %, 0.75 % and 1.0 % respectively. The average responses are provided in *Fig. 3.16 (a)*. A total of six specimens were tested for each fibre dosage. In all instances a limit of 1 mm was set on the controlling LVDT (COD) reading, at which point the test would stop. In some cases this limit could not be achieved, because the test control would become unstable. This only occurred for the fibre volume dosage of 0 % and 0. 5% (see *Fig. 3.14 (a, b)*). It is therefore important to correctly interpret the maximum COD achieved as the limit of stable fracture that could be achieved for the setup and control parameters used. For example, for a 0 % fibre dosage, a stable fracture COD of greater than 0.2 mm could not be achieved.

$$F_h = {}^{F_v}/_{(2 \cdot \tan \alpha_w)} \tag{3.1}$$

The fracture energy can be determined by the area underneath the $F_h - COD$ response. The specific fracture energy, G_f [N/m], is defined as the fracture energy normalised with respect to the fracture area of the particular specimen used. In this case the fracture area of the plane through which the specimen cracks is 50 x 100 mm^2. The specific fracture energy is plotted against the COD for each fibre dosage in *Fig.3.16 (b)*.

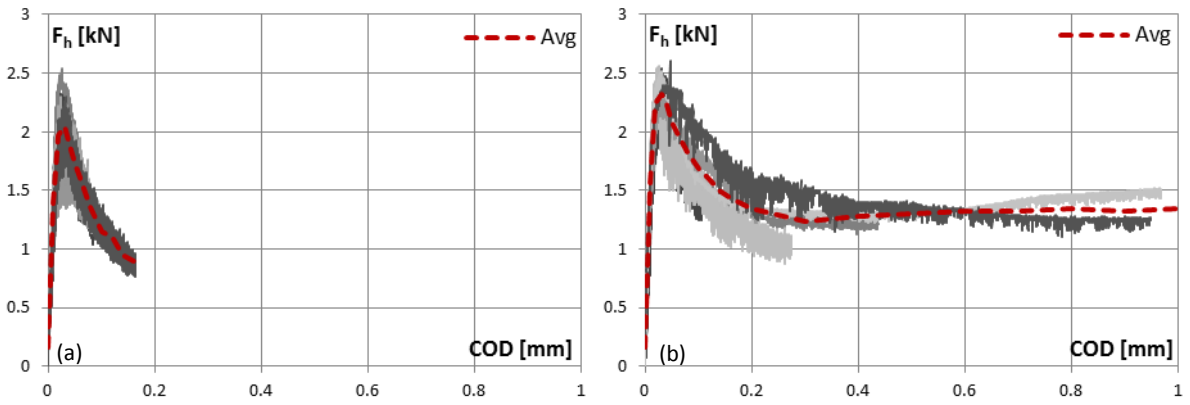

Fig. 3.14 – Horizontal splitting force F_h as a function of crack opening displacement (COD) for V_f = (a) 0% and (b) 0.5%

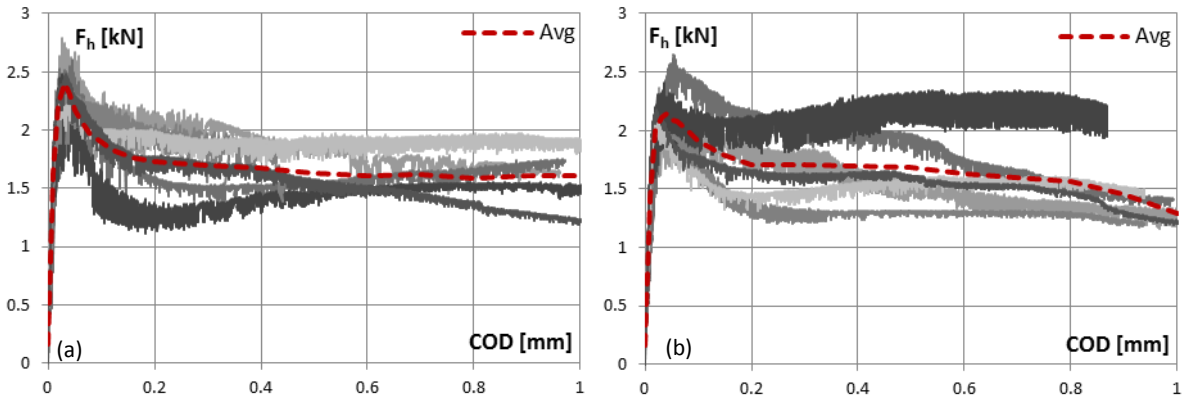

Fig. 3.15 – Horizontal splitting force F_h as a function of crack opening displacement (COD) for V_f = (a) 0.75% and (b) 1.00%

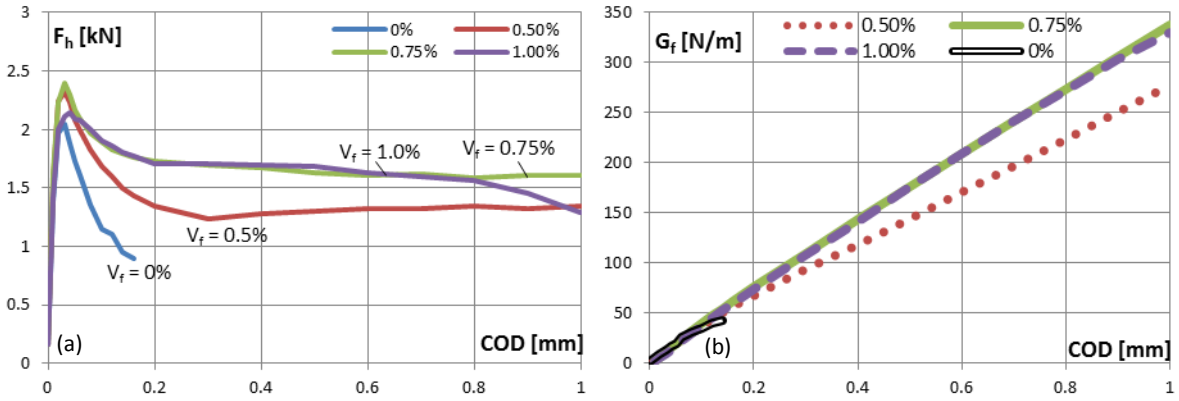

Fig. 3.16 – (a) Average responses, (b) Specific fracture energy - COD

The noise or scatter observed in *Figs. 3.14-15* is believed to be as a result of non-optimal test boundary conditions and control parameter values for the actuator/LVDT control. As anticipated, the ductility, residual capacity and fracture energy increases for a larger fibre dosage. Based on the wedge splitting test, an optimum fibre dosage for this mix design is 0.75%. Increasing the fibre volume fraction beyond 0.75% to 1.0% has no significant benefit for mechanical response.

Flexural response: ASTM C1609 & EN 14651

The classification of FRC is required for performance evaluation and design. In order for this research to be considered design-oriented, the material developed must be evaluated with respect to standard performance and reliability requirements. Two standard test methods and performance criteria for SFRC are therefore used. The first method is *ASTM C1609 (2007)*, which is referenced by the *Building Code Requirements for Structural Concrete (ACI 318-08)*. The second test method, *EN 14651(2005)*, is referenced by *RILEM TC 162-TDF* and the *fib Model Code 2010*. Flexural toughness is the main performance indicator for these design provisions.

ASTM C1609

The flexural performance of FRC is evaluated, using parameters derived from the load-deflection curve of a simply supported (third-point loaded) beam. The method determines the first-peak and peak loads and corresponding stresses using the formula for modulus of rupture, *Eq. 3.2*. Residual flexural resistance is also evaluated at specified deflections. The first-peak, peak, and residual loads are then used to calculate flexural performance parameters.

Specimen toughness, based on the area under the load-deflection curve up to a prescribed deflection can also optionally be determined. Specimen toughness is an indication of the energy absorption capability of the test specimen.

$$f = {}^{PL}/_{bd^2} \tag{3.2}$$

where:

f = flexural strength
P = load
L = span length
b = average width of the specimen at location of fracture
d = average depth of the specimen at location of fracture

Test configuration & instrumentation: The specimen dimensions used in this study are 100 by 100 by 500 mm, tested on a 300 mm span, with roller supports which are free to rotate on their axes (see *Fig. 3.17*). Two electronic displacement transducers (or LVDTs) are mounted at mid-span (one on each side) on a rectangular jig, which surrounds the specimen and is clamped to it at mid-depth directly over the supports. The transducers measure deflection through contact with a bracket attached to the top surface of the specimen. The average of the measurements represents the net deflection. The tests are performed on a Zwick Z250 testing machine.

Test method and procedure: The deflection of the centre of the beam is measured and used to control the rate of increase of deflection. Only one of the LVDTs is used to control the test rate, not the average of the two transducers. The rate of increase of deflection is chosen as 0.10 mm/min until a deflection of 0.5 mm ($L/600$) and then increased to 0.20 mm/min until the specified end-point deflection is reached i.e. 2 mm ($L/150$). Data (load and deflection) is recorded at a sampling frequency of 5Hz.

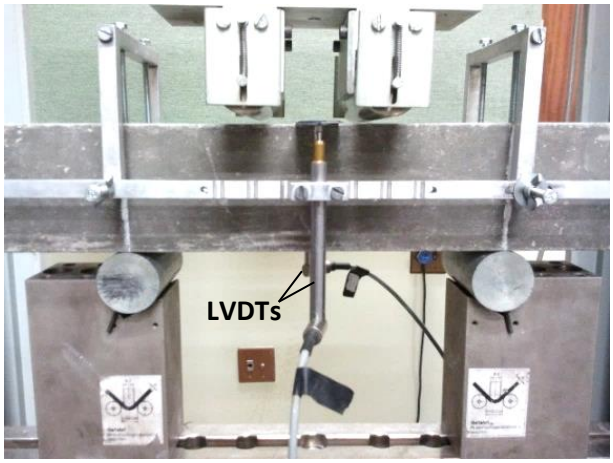

Fig. 3.17 – Test configuration and instrumentation (*ASTM C1609*)

Test results and discussion: The results for the trial SCM (*Table 3.2*) initially developed are provided in *Table 3.13* and *Figs. 3.20-21 (a)*. *Table 3.13* shows the average values of four specimens per fibre type and dosage. There are therefore 48 beams in this test series. A typical flexural response as idealised in *Fig. 3.18* and *Fig. 3.19*, defines the flexural performance parameters. In summary, the *RC-65/35-BN* fibre performs the best overall, as may be expected for a fibre with higher aspect ratio. In general, a fibre dosage greater than 1.0% becomes less effective. This is especially evident for the *RL-45/35-BN* fibre type. Apart from the *RL-45/35-BN* with V_f = 0.5%, all mixes considered in *Table 3.13* meet the minimum performance requirements ($f^D_{300}/f_1 \geq 90\%$ and $f^D_{150}/f_1 \geq 75\%$) for structural shear design as outlined in *ACI 318-08 (5.6.6.2)*. The unloading/reloading cycles visible in *Figs. 3.20-21* are due to the limited reaction speed of the testing machine. The *RC-65/35-BN* fibre is chosen for the experimental programs to follow and given the material performance and workability requirements for SCC, a maximum fibre dosage of 1.0% is proposed.

Table 3.14 provides the flexural performance parameters for the final SFR-SCC design (*Table 3.3*, Fibre type = *RC-65/35-BN*, V_a = 450 kg/m^3, a = 9.5mm). The total load vs. deflection response is shown in *Fig. 3.21 (b)*. Only the 1.0% fibre dosage complies with the recommended performance requirements. This is directly attributed to the greater first peak strength (f_1) achieved for this higher compressive strength class of concrete compared to the preliminary mix design (*Tables 3.2 & 3.13*). It is important to recognise that the compressive strength of the composite still increases significantly beyond the 28-day strength, with 70+ MPa achieved at 112-day age (*Fig. 3.9 (a)*). Future studies that follow on this work should be cognisant of the effect the compressive strength has on the embrittlement of the fibre-reinforced composite. Unfortunately no further time could be allotted to optimise the composite further.

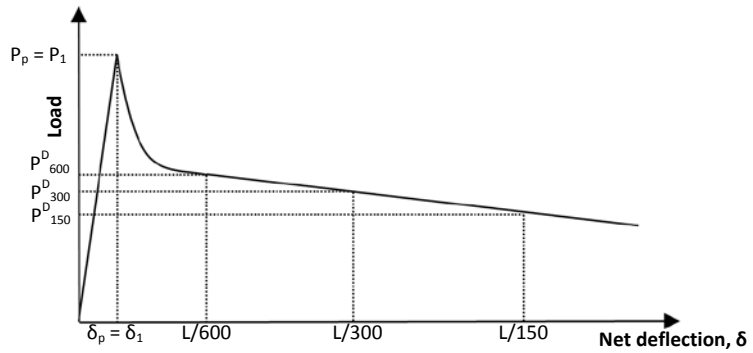

Fig. 3.18 – Parameters for first-peak load equal to peak load (not to scale) (*ASTM C1609*)

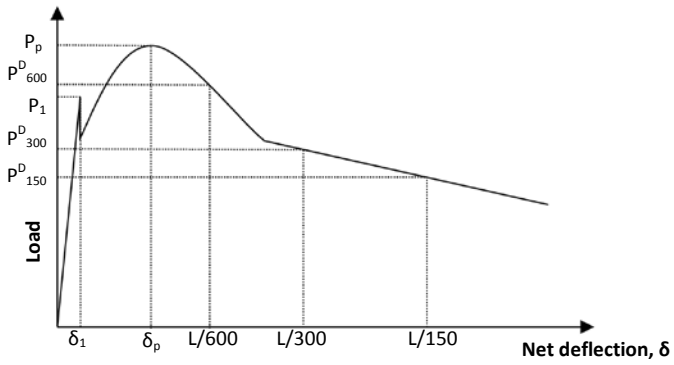

Fig. 3.19 – Parameters when peak load is greater than first-peak load (not to scale) (*ASTM C1609*)

Table 3.13 – Flexural performance parameters for preliminary self-consolidating mortar (Table 3.2)

V_f (%)	$f_{c,cube}$	δ_1	f_1	δ_p	f_p	f_{600}^D	f_{300}^D	f_{150}^D	f_{300}^D/f_1	f_{150}^D/f_1
	MPa	mm	MPa	mm	MPa	MPa	MPa	MPa	%	%
RC-65/35-BN										
0.5%	40.6	0.035	5.40	0.46	6.07	5.71	5.57	4.50	104	84
1.0%	39.1	0.033	5.24	0.57	8.48	8.25	7.47	5.23	142	100
1.5%	38.8	0.034	5.05	0.37	9.37	8.99	7.91	6.14	157	122
2.0%	39.8	0.036	5.28	0.40	10.42	9.92	8.96	7.14	170	135
RL-45/35-BN										
0.5%	39.6	0.032	5.13	0.23	5.37	4.86	4.68	3.47	91	68
1.0%	36.0	0.030	4.95	0.40	7.69	7.27	5.94	4.26	120	86
1.5%	36.4	0.033	5.08	0.41	8.02	7.52	6.10	4.26	120	84
2.0%	32.2	0.035	4.76	0.32	8.08	7.61	6.35	4.79	133	101
RL-45/50-BN										
0.5%	38.6	0.029	4.95	1.21	5.62	4.69	5.37	3.99	109	80
1.0%	36.8	0.034	4.86	0.62	6.53	6.09	5.35	4.30	110	89
1.5%	32.7	0.031	4.66	0.44	7.44	6.79	6.12	4.48	132	97
2.0%	33.2	0.035	4.50	0.39	7.96	7.69	6.74	5.39	150	120

Note: Average values for a sample size of four specimens per fibre type and dosage

Table 3.14 – Flexural performance parameters for final SFR-SCC (Table 3.3, V_a = 450kg/m^3, a = 9.5mm) mix design

V_f (%)	$f_{c,cube}$	δ_1	f_1	δ_p	f_p	f_{600}^D	f_{300}^D	f_{150}^D	f_{300}^D/f_1	f_{150}^D/f_1
RC-65/35-BN	MPa	mm	MPa	mm	MPa	MPa	MPa	MPa	%	%
0.00%	51.0	-	5.49	-	5.49	-	-	-	-	-
0.50%	53.8	0.036	6.32	0.481	7.01	6.54	5.84	2.91	93	46
0.75%	50.2	0.033	6.45	0.489	7.20	6.94	6.37	3.54	99	55
1.00%	51.7	0.036	6.79	0.807	9.15	8.77	8.62	5.43	127	80

Note: Average values for a sample size of three specimens per fibre type and dosage

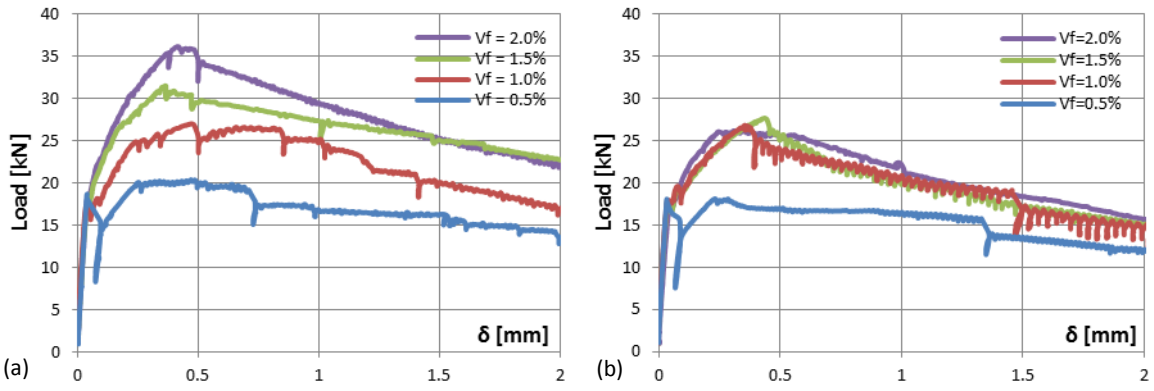

Fig. 3.20 – Typical load-deflection responses (a) *RC-65/35-BN (SCM, CEM I)*, (b) *RL-45/35-BN (SCM, CEM I)*

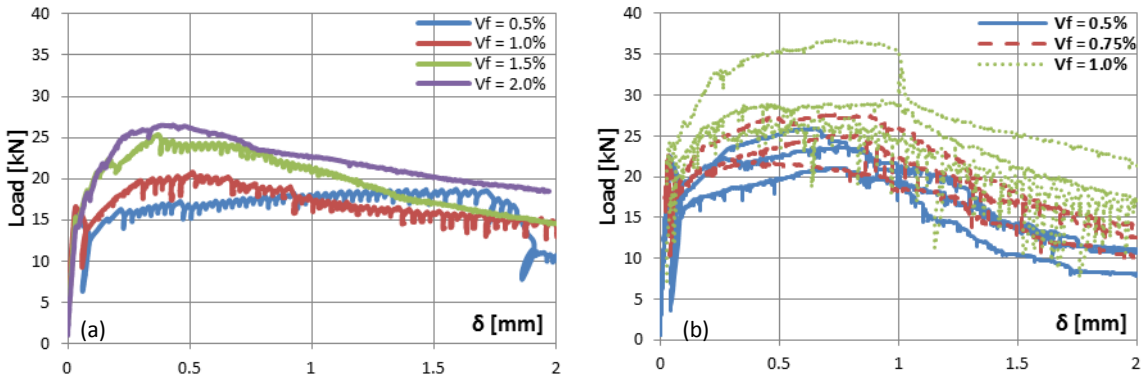

Fig. 3.21 – (a) Typical load-deflection response RL-45/50-BN (SCM, CEM I), (b) Load-deflection for final SFR-SCC (*RC-65/35-BN*, V_a = 450 kg/m^3, a = 9.5 mm)

EN 14651

The method outlined in *BS EN 14651:2005+A1:2007* is used to perform this test series. The residual flexural tensile strength values are determined from the load-crack mouth opening displacement (CMOD) or load-deflection response (see *Fig. 3.22*). The load-CMOD relationship is evaluated to determine the residual flexural tensile strength parameters, f_{Rj} (*Eq. 3.3*). The post-cracking strength of FRC can be classified according to *fib Model Code 2010 5.6.3* using two parameters, namely f_{R1k} (representing the strength interval) and a letter a, b, c, d or e (representing the ratio f_{R3k}/f_{R1k}). According to *fib Model Code 2010 5.6.3*, fibre reinforcement can substitute (also partially) conventional reinforcement at ultimate limit state, if the relations *Eq. 3.4-5* are satisfied. The parameters and ratios for this test series are summarised in *Table 3.15*. Note that *fib Model Code 2010* refers to the characteristic values for the residual flexural tensile strength. Here, the average values of a small sample size (3 specimens) are used to classify the material.

$$f_{R,j} = {}^{3F_j l}\Big/_{2bh_{sp}^2} \tag{3.3}$$

where:

$f_{R,j}$ is the residual flexural tensile strength corresponding to $CMOD = CMOD_j$
F_j is the load corresponding to $CMOD = CMOD_j$
l is the span length;
b is the specimen width;
h_{sp} is the distance between the notch tip and the top of the specimen (125 mm)

$$f_{R1k}/f_{Lk} > 0.4 \tag{3.4}$$

$$f_{R3k}/f_{R1k} > 0.5 \tag{3.5}$$

where f_L is the limit of proportionality (LOP) as defined in *EN 14651*:

$$f_L = {}^{3F_L l}\Big/_{2bh_{sp}^2} \tag{3.6}$$

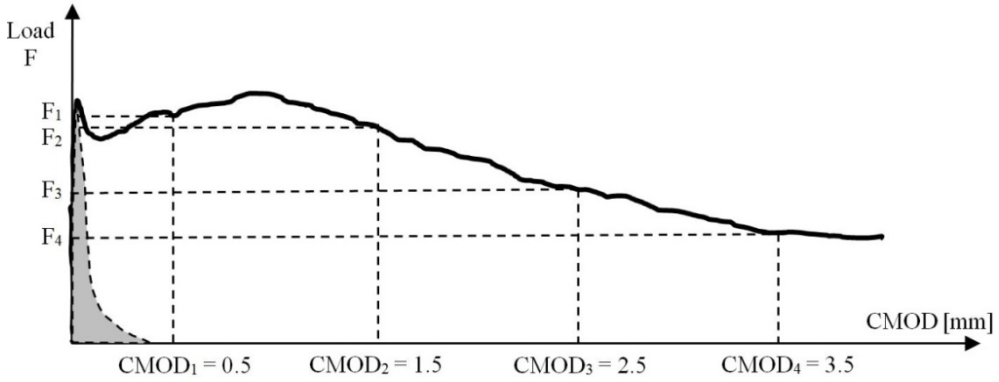

Fig. 3.22 – Typical Load F – CMOD response for FRC (*fib Model Code 2010*)

Test configuration & instrumentation: A simply supported beam is notched and loaded centrally as shown in *Fig. 3.23*. The test specimens are of a nominal size (width and depth) of 150 mm and a length of 550 mm. The span (bottom support separation) is 500 mm. A saw-cut notch (width = 3.1-3.5 mm and depth = 125 mm ± 1 mm) is made 7 days prior to testing. A clip gauge is positioned over the notch (with a gauge distance of 10 mm) via knife edges glued centrally to the bottom surface of the beam.

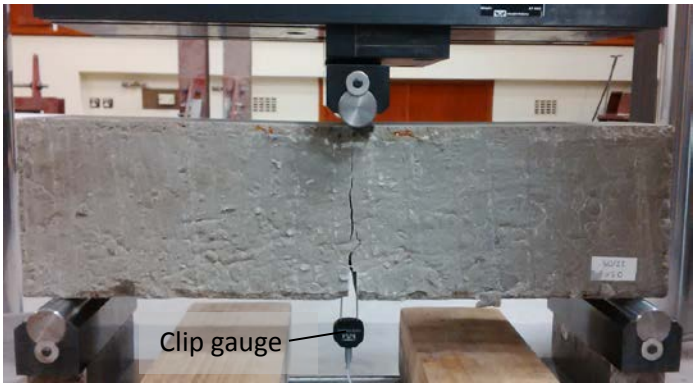

Fig. 3.23 – Test configuration and instrumentation (EN 14651)

Test method and procedure: The testing machine controls the rate of increase of CMOD via the clip gauge. The CMOD increases at a constant rate of 0.05 mm/min until a CMOD of 0.1 mm is reached, at which point, the CMOD increases at a constant rate of 0.2 mm/min. All data is recorded at a sampling frequency of 5Hz. The tests are performed on an Instron 2000KPX-J3A materials testing machine (MTM).

Test results and discussion: The Load – CMOD response for each specimen tested is provided in *Fig. 3.24*. As observed for the wedge-splitting test and to some extent also the ASTM C1609 data, material performance does not improve significantly for a fibre dosage larger than 0.75%. In some cases a higher fibre dosage of 1.0% performs worse than 0.75%. This may be attributed to poorer consolidation for larger fibre dosages. Increasing the fibre dosage does however reduce the amount of scatter/variability in the data, as can be observed in *Fig. 3.24*. Based on the average values (not the characteristic values), the 0.5%, 0.75% and 1.0% composite is classified as “5b”, “6b” and “6b” respectively. *Eqs. 3.4-5* are also satisfied on the basis of the average values given in *Table 3.15*, making this material appropriate for structural use according to *fib Model Code 2010*. It must be

noted that the "jagged" response sometimes encountered (*Fig. 3.24*) is not material behaviour, but is attributed to the bottom roller supports sometimes not rotating freely. This behaviour disappears with proper lubrication of the roller supports.

Table 3.15 – Classification of SFR-SCC (Table 3.3, V_a = 450kg/m^3, a = 9.5mm) according to MC2010 and EN 14651

Parameter	0%	0.50%	0.75%	1.0%
LOP	4.76	5.30	5.35	4.67
$f_{R,1}$	-	5.58	6.96	6.19
Strength interval	-	5	6	6
$f_{R,2}$	-	5.82	7.61	6.81
$f_{R,3}$	-	3.97	5.76	5.38
$f_{R,4}$	-	2.73	4.39	4.25
$f_{R,3}/f_{R,1}$	-	0.71	0.83	0.87
$f_{R,1}/f_L$	-	1.05	1.30	1.32
Classification	-	"5b"	"6b"	"6b"

Note: Average values of three specimens for each fibre dosage

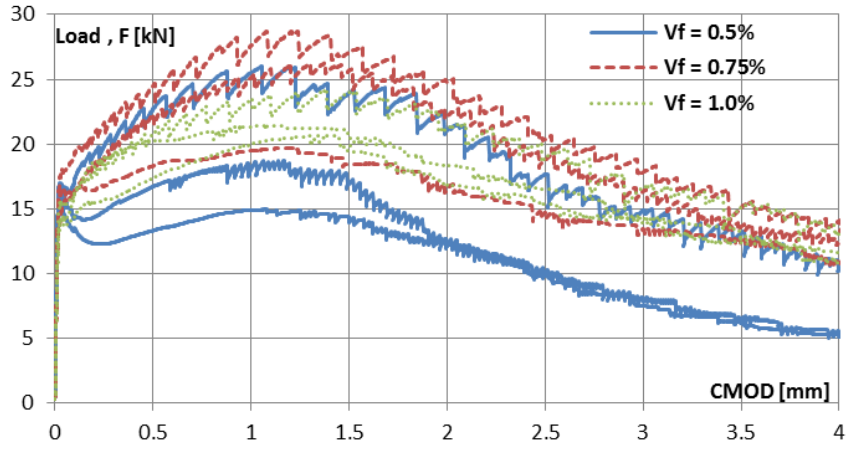

Fig. 3.24 – Load – CMOD response for SFR-SCC (Table 3.3, V_a = 450kg/m^3, a = 9.5mm, V_f = 0.5%, 0.75% and 1.0%)

Summary and conclusions

The composite design method optimises the composite performance at the level of the paste, mortar, concrete and fibre-reinforcement. Practical ranges of the constituent proportions are given. Basic rheological (flowability) and mechanical (compressive strength) performance criteria are used to determine the best mix design. The properties of each of the mix constituents, including the aggregate (fine and coarse); cement, additions and filler materials; admixtures and fibres are presented. The production method is outlined in terms of the mixing, casting, curing, grinding and notching procedures used. The composite developed is classified in terms of compressive strength, elastic modulus and post-fracture energy and toughness.

Based on the outcomes of the parameter study and material classification, the following mix proportions will be used for the experimental programs to follow: volumetric water-powder ratio = 0.9, cement type = CEM II 52.5N, addition (fly ash) mass percentage of powder = 25%, filler mass percentage of powder = 25%, fine aggregate volume percentage of mortar = 50%, fine aggregate composition = 70 : 30 by mass of Malmesbury and Philippi sand respectively, standard coarse aggregate (Greywacke) size = 9.5 mm, coarse aggregate content = 450 – 600 kg/m^3, fibre type = *RC-65/35-BN* and maximum fibre dosage = 1.0%.

Chapter 4

Meso and Micro-mechanical investigation of Mode I fracture

This chapter investigates the Mode I or Uniaxial tensile fracture experimentally. The first section considers the composite behaviour at the Meso-scale i.e. within the vicinity of a single, well-defined, localised crack. Crack localisation is enforced via specimen geometry and load configuration. Experimental methods to characterise the uniaxial tensile behaviour in the form of a uniaxial tensile test (UTT) are adopted from the literature and redesigned in accordance with the available testing equipment and the outcomes of this research. Numerical (finite element) refinement in the elastic domain is used in order to optimise the specimen geometry for the desired stress distributions. The specimen design, experimental program, production method, test setup, procedure and results are discussed. The test results include the tensile stress-crack width response, fracture energy and an analysis of the fibre distribution via X-ray Computed Tomography (CT-scan).

The second section considers the primary mechanism contributing to the residual composite response at the Micro-scale of observation, namely the axial pull-out response of the embedded fibre. The experimental program, production method, test setup, procedure and results are outlined and discussed.

4.1 Experimental investigation at the Meso-scale

4.1.1 Specimen design

Selection of geometric parameter values

Based on the recommendations for specimen geometry provided in *Chapter 2*, a range of geometric parameters are investigated as tabulated in *Table 4.1*. The specimen shape is limited to a "dumbbell" shape as illustrated in *Fig. 4.1 (a)*. The geometric parameters include the gauge width (w_g), end width (w_e), thickness (t), gauge length (l_g), transition length (l_t) and transition radius (r).

Refinement of specimen geometry via numerical analysis in the elastic domain

The objective of the numerical analysis is to achieve, for the chosen parameter set, (1) a uniform maximum principal (tensile) stress distribution in the gauze zone (*Fig. 4.2*) and (2) minimise peak maximum principal (tensile) stresses in the transition zone (*Fig. 4.2*). The shape of the specimen and the loading configuration increases the likelihood of premature failure in the transition zone and therefore needs to be mitigated with an optimised design.

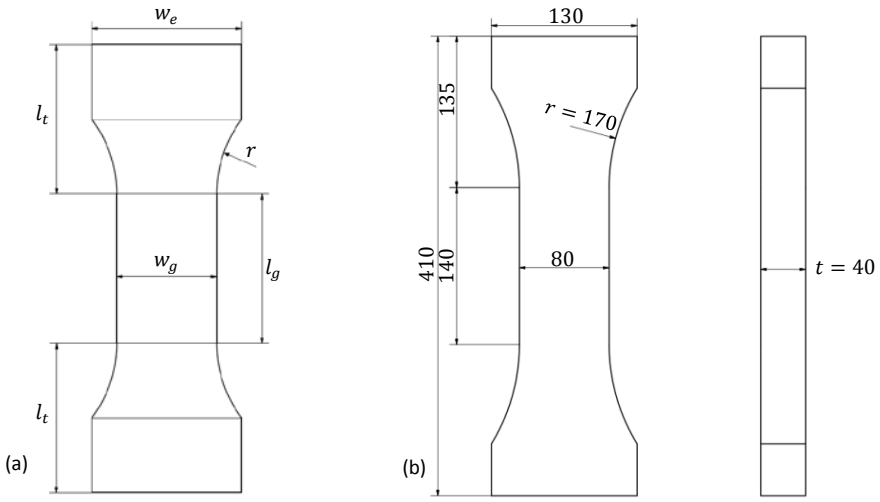

Fig. 4.1 – (a) UTT specimen geometry parameters; (b) Final specimen geometry (Dimensions in mm)

A total of 27 analyses are performed on three parameters with three parameter values each. They include the specimen end width, w_e= 120, 130 and 140 mm; specimen gauge length, l_g= 120, 140 and 160 mm and transition radius, r = 100 mm, an intermediate value and a maximum value utilising the entire transition length (l_t) for the radius. Analyses are performed in *Abaqus 6.10*. In addition to the geometry, the model input provided in *Table 4.2* is used.

The maximum principal (tensile) stresses are evaluated at the specimen edge (Line 1) and mid-section (Line 2) (see *Fig. 4.3*). *Table 4.3* shows the peak principal stress on Line 1 as a percentage of the principal stress at the middle of the specimen (on Line 1) for each analysis.

Considering first the effect of increasing the transition radius (r) for a fixed end width ($w_e = 120\ mm$) and gauge length ($l_g = 120\ mm$):

1. Specimen edge (Line 1):
   a. A reduction in peak principal stress is observed at the boundary of the transition/radial zone and gauge zone (*Fig. 4.4 (a)*). The same effect is observed for larger end widths ($w_e = 130\ \&\ 140\ mm$)
   b. An increase in the maximum principal stress is observed at the clamping/loading edge i.e. the boundary of the clamping and transition zone (*Fig. 4.4 (a)*). This is attributed to the reduction of the clamping area for a larger transition radius. The same effect is observed for larger end widths ($w_e = 130\ \&\ 140\ mm$)
2. Specimen mid-section (Line 2):
   a. Greater uniformity of principal stress distribution over specimen length (*Fig. 4.4 (b)*). The same effect is observed for larger end widths ($w_e = 130\ \&\ 140\ mm$)

Table 4.1 – Parameter values for specimen geometry

Parameter	**Parameter value(s)**	**Final value***	**Criteria used**
Gauge width, w_g	{80 mm}	80 mm	≥ 50 mm ≥ 3 x L_f = 105mm (L_f = 35 mm) ≥ 6 x a ≈ 80 mm (a_{max} = 13.2 mm) Aggregate particle size chosen as the determining factor.
End width, w_e	{120 mm, 130 mm & 140 mm}	130 mm	> 1.5 x w_g= 120 mm ≤ 140 mm (clamp width)
Thickness, t	{40 mm}	40 mm	> 0.5 x w_g = 40 mm > 3 x a ≈ 40 mm (a_{max} = 13.2 mm) Minimum of three aggregate particles over depth Maximum clamping opening = 50 mm
Gauge length, l_g	{120 mm, 140 mm & 160 mm}	140 mm	> 2-3 x minimum dimension Minimum dimension = 40 mm
Total length	{360 mm}	410 mm	Total specimen length used for all analyses is 360 mm Final length = 360 mm + 50 mm (25 mm added to each end in order to reduce wall-effects near clamping/transition zone boundary)
Total transition length, l_t (Transition zone + clamp zone)	{100 mm, 110 mm & 120 mm} for a 160, 140 and 120 mm gauge length respectively and fixed total length of 360 mm	135 mm	110 mm + 25 mm additional length (Refer to total length)
Transition radius, r	r = 100 mm – 370 mm Minimum = 100 mm Intermediate ≈ half of maximum radius Maximum = total transition length utilised for radius	170 mm	

*Based on results of numerical analysis

Secondly, the effect of the specimen end-width (w_e) can be summarised as follows:

A larger end width results in a smaller maximum transition radius and thus a larger clamp area, which reduces the peak stress observed at the specimen edge (Line 1) clamping-transition zone boundary. For a constant gauge length (l_g) and transition radius ($r = 100\ mm$), the end width has minimal or no effect on the peak principal stress values (see *Table 4.3*).

Thirdly, the effect of increasing the specimen gauge length (l_g) can be summarised as follows:

1. Overall, the behaviour observed for $l_g = 140\ \&\ 160\ mm$ is similar to that for $l_g = 120\ mm$ above.
2. An increase in the gauge length and the corresponding reduction in transition length (for a fixed total length), reduces the maximum transition radius.
3. For a fixed end width ($w_e = 120\ mm$) and transition radius ($r = 260\ mm$), the peak principal stress decreases at the gauge/transition zone boundary and increases at the clamping/transition zone boundary (*Fig. 4.5 (a)*). As before, this is attributed to the reduction of the available transition length and clamping area. The same effect is observed for larger end widths $w_e = 130\ \&\ 140\ mm$.
4. The stress distribution (Line 2) becomes less uniform near the centre of the mid-section for larger gauge lengths $l_g > 140\ mm$ (*Fig. 4.5 (b)*). The same effect is observed for larger end widths $w_e = 130\ \&\ 140\ mm$.

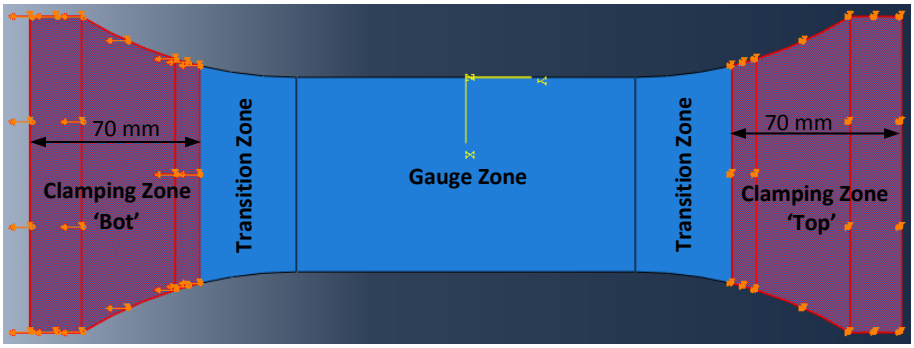

Fig. 4.2 – Boundary conditions (Specimen without 25 mm extension at each end, total length 360mm) [1]

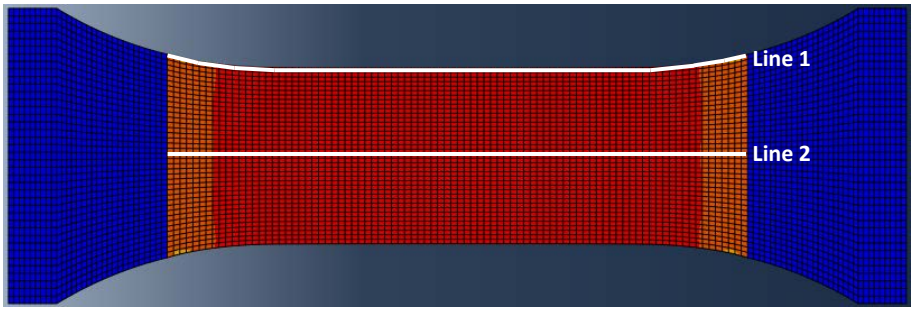

Fig. 4.3 – Maximum principal stress contour ($w_e = 130\ mm, l_g = 140\ mm, r = 170\ mm$) and data lines: Line 1 – Specimen edge, Line 2 – Specimen middle section[1]

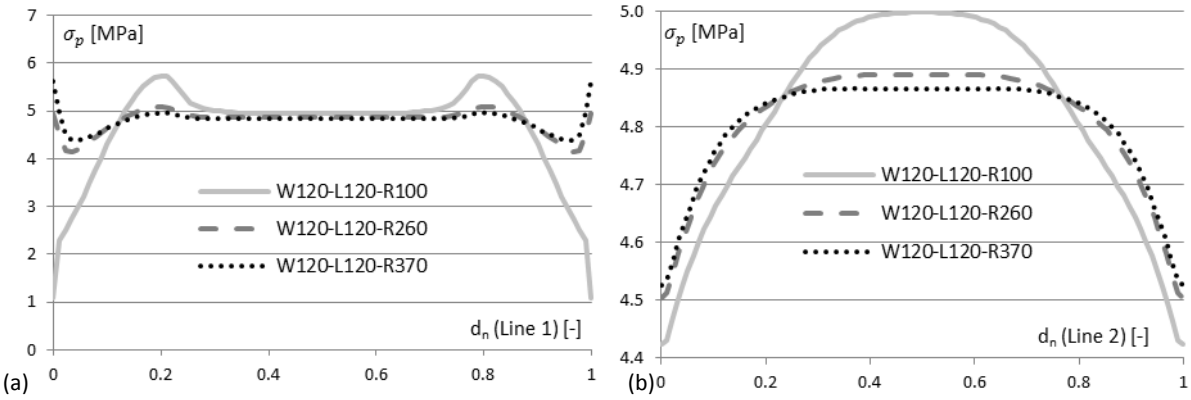

Fig. 4.4 – Maximum principal (tensile) stress (σ_p) vs normalised distance (d_n) on (a) Line 1 and (b) Line 2 for $w_e = 120\ mm$ and $l_g = 120\ mm$ (W = w_e, L = l_g, R = r)

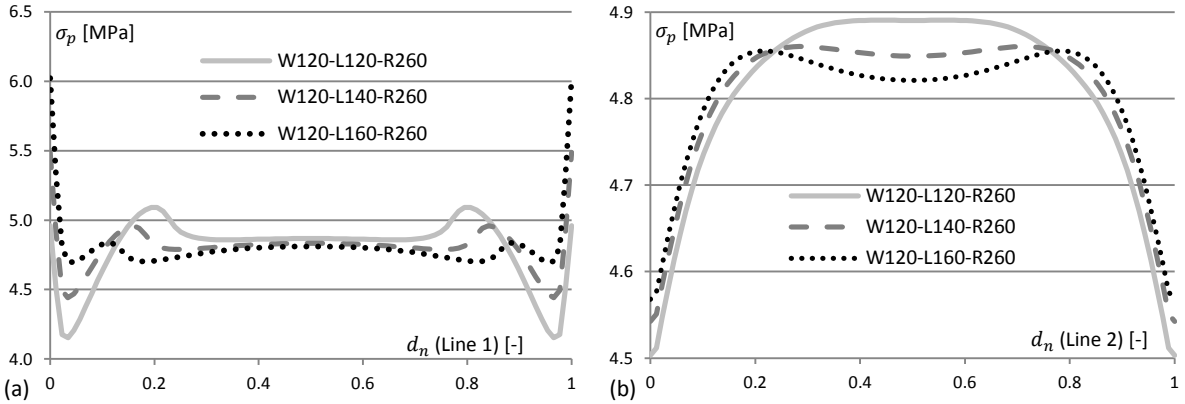

Fig. 4.5 – Maximum principal (tensile) stress (σ_p) vs normalised distance (d_n) on (a) Line 1 and (b) Line 2 for $w_e = 120\ mm$ and $r = 260\ mm$ (W = w_e, L = l_g, R = r)

Table 4.2 - Model input

Material definition/properties:	Elastic/Isotropic material Elastic modulus = 35 GPa Poisson's ratio = 0.2
Element and mesh definition:	Element type: Plane stress bilinear quadrilateral (CPS4) – no reduced integration Meshing algorithm(s): Structured and sweep Element size effect ranging from 1 to 10 mm investigated: An element size of 5 mm is deemed adequate from these results. An element size of 2.5 mm is however selected for all further analyses.
Boundary conditions (*Fig. 4.2*):	Clamping Zone 'Bot': Fixed against translation in the x-direction and fixed against rotation about the z-axis (out of plane); Prescribed displacement in the y-direction of -0.03 mm Note: Prescribed displacement based on a maximum tensile strength of 5 MPa, E-mod = 35 GPa and an initial length = 360 – 70 – 70 = 220 mm Clamping Zone 'Top': Fixed against all translation (X and Y direction) and rotation (about the Z axis)

In summary, the clamping area is the critical parameter influencing the peak principal stress at the clamping/transition zone boundary. A larger transition radius is beneficial in reducing the peak principal stress at the transition/gauge zone boundary. However, increasing the transition radius reduces the available clamping area, which increases the principal stresses at the clamping edge. Reducing the transition length (while keeping the transition radius constant) has the same effect. The final specimen geometry obtained from the numerical analysis, is presented in *Fig. 4.1 (b)*.

Despite the process of numerical refinement employed, a preliminary investigation shows that specimens, unreinforced within the transition zone are prone to failure outside the gauge zone, with failure occurring either at the clamping edge or within the transition zone. Apart from the limitations of a simplified elastic analysis, one conjecture could be that specimen pre-damage as a result of a combination of specimen shrinkage in the mould, handling, clamping and pre-loading, could cause specimen failure outside the gauge zone. An experimental investigation is conducted to determine the reinforcement required in the transition zone, to prevent premature failure in these areas. This is discussed further in *Section 4.1.2*.

In addition to reinforcing the specimen, a 4.5±0.5 mm saw-cut notch is also made in the middle of the specimen on both short sides (see *Fig. 4.7 (c)*). The notch reduces the section by 10 - 12.5% and forces the crack to initiate and propagate in the notched section. The use of a notch is suitable for the determination of the stress vs. crack-opening response and strain softening composites where localised failure is expected. It is important to note that as a consequence of introducing a notch in the specimen, the stress distribution at the fracture plane is no longer uniform. This only influences the elastic behaviour and peak stress values for some specimens, while producing reliable and consistent values for post-fracture toughness (refer to *Section 4.1.4*).

Table 4.3 – Peak principal stress on Line 1 as a percentage of principal stress observed at middle of specimen (on Line 1)

%	$w_e = 120$		
$l_g = 120$	$r = 100$	$r = 260$	$r = 370$
	116	**105**	**116**
$l_g = 140$	$r = 100$	$r = 260$	$r = 312.5$
	112	**114**	**120**
$l_g = 160$	$r = 100$	$r = 170$	$r = 260$
	109	**111**	**125**
	$w_e = 130$		
$l_g = 120$	$r = 100$	$r = 200$	$r = 300.5$
	116	**107**	**108**
$l_g = 140$	$r = 100$	$r = 170$	$r = 255$
	112	**106**	**113**
$l_g = 160$	$r = 100$	$r = 160$	$r = 212.5$
	107	**104**	**119**
	$w_e = 140$		
$l_g = 120$	$r = 100$	$r = 170$	$r = 255$
	116	**108**	**105**
$l_g = 140$	$r = 100$	$r = 160$	$r = 217$
	112	**106**	**106**
$l_g = 160$	$r = 100$	$r = 140$	$r = 182$
	109	**105**	**114**

4.1.2 Experimental program and production method

Research parameters

The research parameters considered for this part of the study include the fibre volume fraction (V_f) and average aggregate particle size, i.e. a self-consolidating concrete (SCC) as opposed to a self-consolidating mortar (SCM). The complete list of parameter values investigated is summarised in *Table 4.4*. A total of 8 test series are performed, with 6 specimens for each series. A total of 48 specimens are therefore tested.

Table 4.4 – Research parameters and parameter values for UTT

Research parameter	**Parameter values:**
Fibre volume fraction, V_f	0%, 0.5%. 0.75% & 1.0% of mortar/concrete volume
Fibre type	RC-65/35-BN ($L_f \approx$ 35mm, $L_f/d_f \approx$ 65, Low carbon, Hooked-end)
Mortar composition	Self-consolidating mortar (As developed in *Chapter 3*)
Average aggregate particle size, a	< 4.75 mm (mortar/no coarse aggregate) and 9.5 mm (Greywacke Hornfels)
Coarse aggregate content, V_a	0 kg/m^3 (mortar) and 450 kg/m^3 of concrete volume

Note: Sample size = 6

Specimen preparation

The respective mixture compositions and the mixing procedure are the same as described in *Chapter 3*. The base of each mould (*Fig.4.6 (a)*) is first coated with mould release oil and the mould sides treated with a thick grease to ease removal of the specimen from the mould after the specimen has set.

As discussed previously, unreinforced specimens failed prematurely, either within the transition zone or at the clamping end. A stainless steel 304 woven wire mesh (*Fig. 4.6 (b)*) with a 1.8 mm aperture size and 0.71 mm wire diameter is used to reinforce the UTT specimens. Two layers of reinforcing mesh, limiting the gauge length to 100 mm are sufficient to induce cracking in the middle of the specimen, even in the absence of a notch. A single layer of reinforcement is however insufficient, with cracking occurring outside or at the ends of the gauge area. Similar behaviour is observed for both an unreinforced (no fibre) and reinforced (V_f = 0.75%) mortar. In the case of measuring across the entire 140 mm gauge length, a single and double layer of reinforcement proves to be inadequate to reliably obtain a localised crack in the gauge zone. Two layers of reinforcing mesh for a 100 mm gauge length are therefore chosen for this investigation. The mesh is extended an additional 10 mm to limit the gauge length to only 80 mm (*Fig. 4.16*).

Specimens are cast in three layers in order to locate the two layers of mesh reinforcement at a 1/3 and 2/3 depth. Once cast, the specimens are moved to a climate controlled environment (Temp. ≈ 24$\pm$2°C & RH ≈ 65$\pm$2%) to set over a period of approximately 24-36 hrs. After this time, the specimens are de-moulded and transferred to a water curing tank (Temp. ≈ 24$\pm$2°C). 7 days prior to testing, the casting face of each specimen is ground level to ensure a proper clamping surface and a 4.5$\pm$0.5 mm notch is cut in the middle of the specimen on both short sides (See *Fig. 4.7 (c)*).

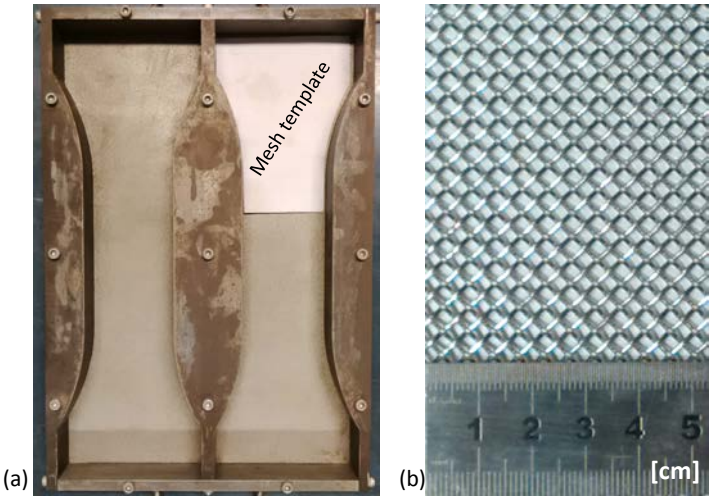

Fig. 4.6 – (a) UTT specimen mould (including mesh template), (b) woven wire mesh used to reinforce specimens in transition zones

The specimens are then returned to the curing tank until the day of testing. The tests are performed in a climate controlled room (Temp. ≈ 24 ±2°C & RH ≈ 65 ±2%).

4.1.3 Test setup and procedure

All tests are performed in a Zwick Z250 material testing machine. *Fig. 4.7 (a & b)* illustrates the test configuration and instrumentation. The specimen is clamped at both ends with hydraulic-pneumatic clamps (*Fig. 4.7b*), which provide a non-rotatable boundary condition. An extensometer is clamped and centred over the saw-cut notch with a gauge length of 80 mm. The extensometer measures the displacement on both sides of the specimen and records the average deformation. Each specimen is first preloaded to a 500 N tensile load at a rate of 1.0 mm/min via the machine crosshead position. The test rate is then controlled via the crosshead position of the testing machine at 0.15 mm/min. The test proceeds at this rate until a deformation (average extensometer reading) of 2 mm is achieved. *Fig. 4.7 (c)* shows a failed specimen.

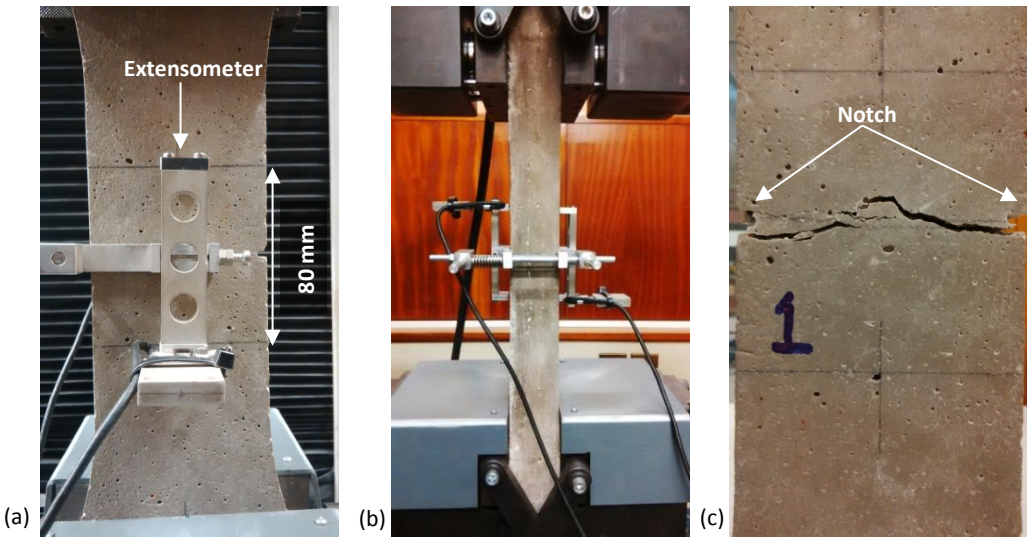

Fig. 4.7 – Test configuration and instrumentation (a) side view, (b) front view; (c) Failed specimen

4.1.4 Test results and discussion

Approximately 80% of the fiber-reinforced specimens failed in the notch. For the remainder, failure initiated outside the notch, but still within the gauge zone of the specimen. All V_f=0.5% specimens failed in the notch. 66% of the specimens that failed outside the notch where V_f=0.75%, the other 33% are V_f=1.0%

Stress-crack width response

The tensile stress-crack width response for SCC and SCM with fibre dosages of 0.5%, 0.75% and 1.0% are illustrated in *Figs. 4.9-11*. Both the sample and average responses are shown. With regard to the unreinforced (no fibre) composite, only crack-width data for the SCM is available (see *Fig. 4.8*). *Table 4.5* summarises the following data points: deformation w_m corresponding to the first peak or matrix cracking strength $\sigma_{t,m}$; the number of fibres N_f protruding from both sides of the fracture plane and the specific fracture energy G_f determined from the area underneath the average tensile load – crack width response and normalised with regard to the specimen cross-section at the fracture plane. The coefficient of variation (C.V.) is given for each data point. Note that for the determination of crack width and fracture energy, no compensation is made for elastic deformation over the 80 mm gauge length. Elastic deformation is considered insignificant for this test arrangement (refer to *Table 4.5*).

Fig. 4.12 plots the average response across the fibre range for both (a) SCM and (b) SCC. As anticipated, post-fracture toughness is increased for a larger fibre dosage. This is less evident for SCM and is attributed to the small difference between the fibre count for V_f = 0.75% ($N_f = 52$) and V_f = 1.0% ($N_f = 59$). Inspection of *Fig. 4.13* demonstrates the greater post-fracture toughness of SCM compared to SCC for the same fibre dosage V_f = 0.5% and 0.75%. The most likely explanation is the better consolidation observed for SCM compared to SCC and the impact of a larger coarse aggregate particle size distribution on the fibre distribution. This is confirmed by the lower fibre count for SCC for V_f = 0.5% and 0.75% (see *Table 4.5*). SCC and SCM have a similar average response for V_f = 1.0% (*Fig. 4.14 (a)*). *Fig. 4.14 (b)* plots the combined average response for both SCM and SCC for each fibre dosage, as well as the average response of all test samples.

Table 4.5 – Summary of UTT data

		SCM				SCC			
V_f	[%]	0*	0.5	0.75	1.0	0	0.5	0.75	1.0
w_m	[µm]	7.4	6.0	6.4	6.0	-	6.9	6.2	6.3
C.V.	[%]	11.8	29.4	-	39.3	-	8.8	16.0	29.3
$\sigma_{t,m}$	[MPa]	3.56	2.85	2.99	2.61	3.12	4.40	3.40	3.65
C.V.	[%]	7.7	30.8	-	38.8	18.5	5.1	24.8	17.1
N_f	[-]	-	35	52	59	-	25	45	63
C.V.	[%]	-	14	17	22	-	22	18	13
$G_f^{0.1mm}$	[N/mm]	-	0.22	0.23	0.22	-	0.31	0.26	0.32
$G_f^{0.3mm}$	[N/mm]	-	0.61	0.72	0.72	-	0.74	0.65	0.93
$G_f^{1.0mm}$	[N/mm]	-	2.05	2.34	2.30	-	1.58	1.89	2.54
$G_f^{2.0mm}$	[N/mm]	-	3.23	3.79	3.51	-	2.11	2.75	3.55
C.V. ($G_f^{2.0mm}$)	[%]	-	10.8	21.7	20.6	-	18.6	19.6	14.4

** Specimens were not notched*

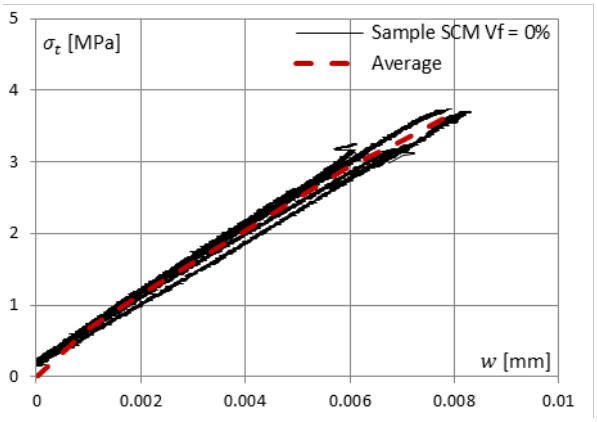

Fig. 4.8 – Tensile stress σ_t [MPa] vs. deformation w [mm] for SCM V_f = 0%

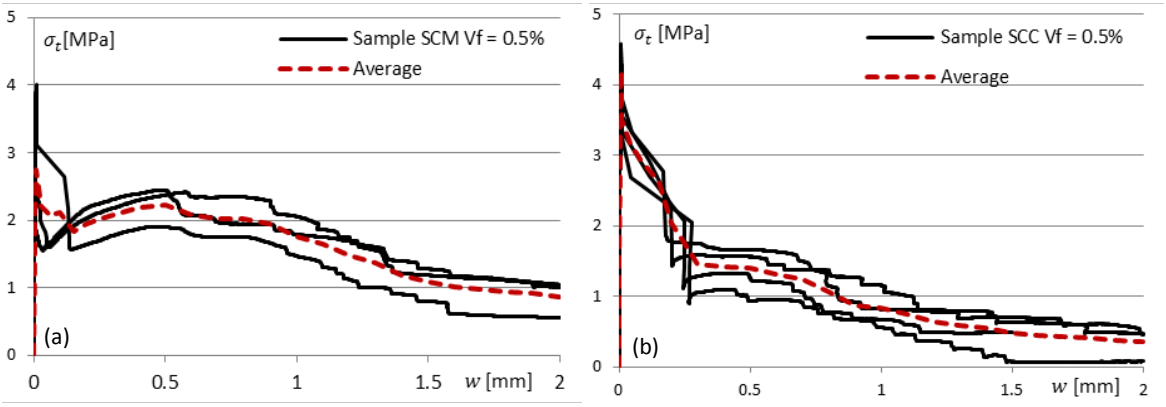

Fig. 4.9 – Tensile stress σ_t [MPa] vs. deformation w [mm] for (a) SCM V_f = 0.5% and (b) SCC V_f = 0.5%

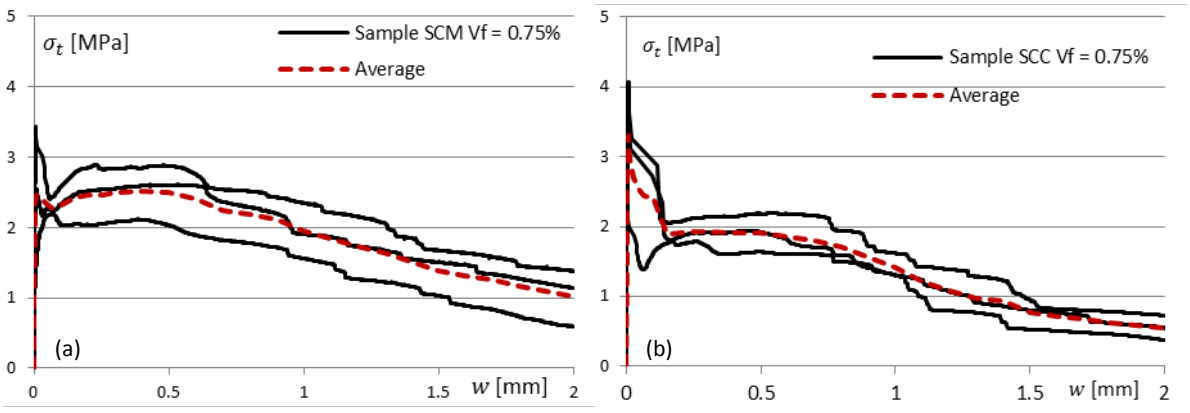

Fig. 4.10 – Tensile stress σ_t [MPa] vs. deformation w [mm] for (a) SCM V_f = 0.75% and (b) SCC V_f = 0.75%

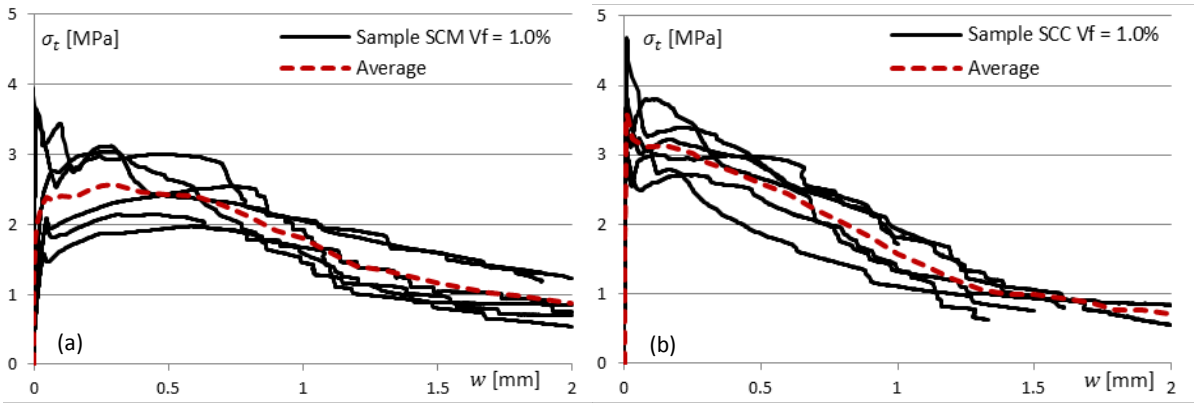

Fig. 4.11 – Tensile stress σ_t [MPa] vs. deformation w [mm] for (a) SCM V_f = 1.0% and (b) SCC V_f = 1.0%

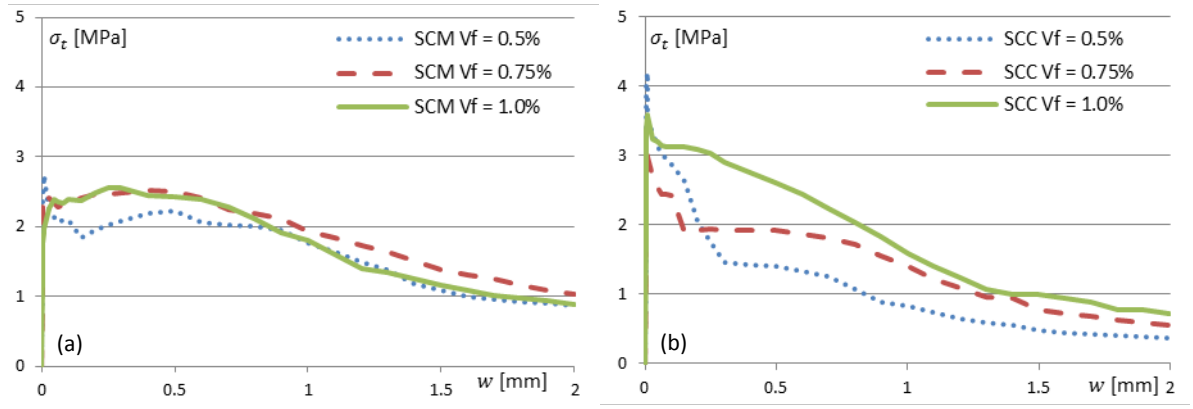

Fig. 4.12 – Tensile stress σ_t [MPa] vs. deformation w [mm] for (a) SCM and (b) SCC

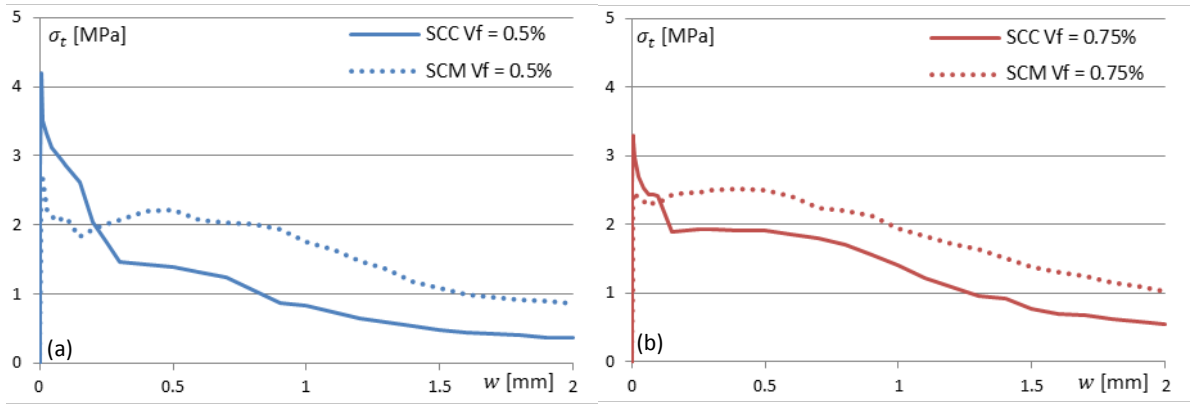

Fig. 4.13 – Average tensile stress σ_t [MPa] vs. deformation w [mm] for (a) V_f = 0.5% and (b) V_f = 0.75%

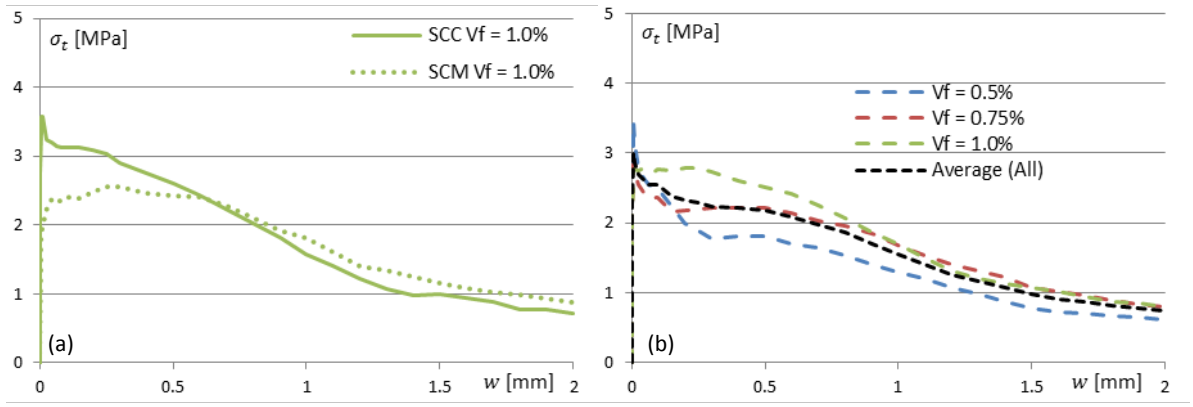

Fig. 4.14 – Average tensile stress σ_t [MPa] vs. deformation w [mm] for (a) V_f = 1.0% and (b) V_f = 0.5% - 1.0%

Fracture energy

The specific fracture energy determined from the average response for each composite is shown in *Fig. 4.15*. As with the stress-crack width data, the fracture energy corresponds well with the fibre count provided in *Table 4.5*. *Table 4.5* also compares the fracture energy up to a specified deformation/crack width $w = 0.1, 0.3, 1.0$ & $2.0\ mm$.

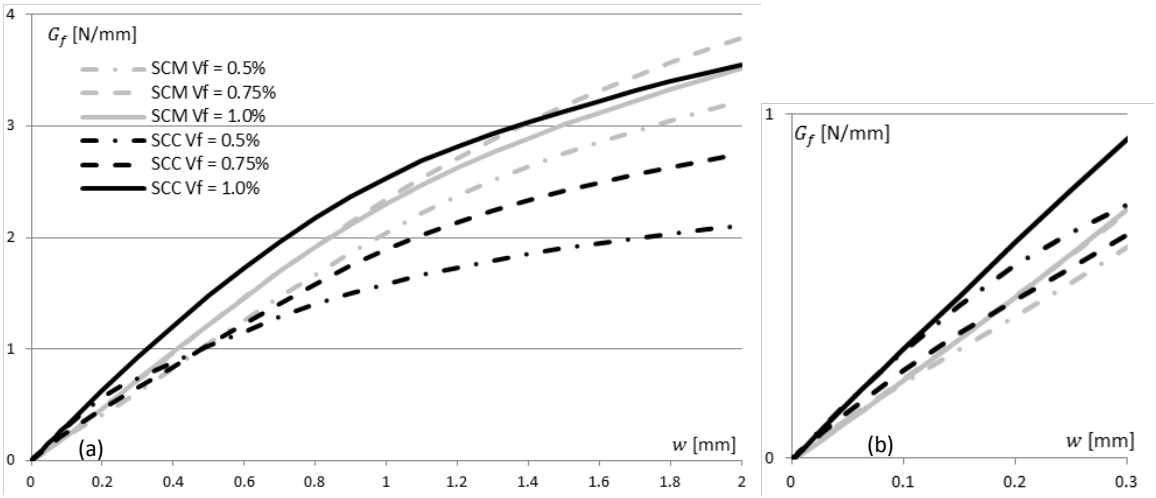

Fig. 4.15 – Specific fracture energy (a) up to $w = 2\ mm$ and (b) up to $w = 0.3\ mm$

Analysis of fibre distribution via Computed Tomography (CT-scan)

The CT (X-ray) Scanner Facility (*du Plessis et al., 2016*) which forms part of the Central Analytical Facilities (CAF) at Stellenbosch University is used to analyse the fibre distribution of three UTT specimens (from the SCC sample), namely one specimen for each fibre dosage V_f = 0.5%, 0.75% and 1.0%. Of interest to this study is the fibre count, orientation and embedded length.

The fibre count is determined by analysing the number of fibres intersecting three planes S1, S2 and S3 (*Fig.4.16*). The fibre count at each plane is given in *Table 4.6*. The average fibre count is compared to the manual fibre count found at the fracture plane for the individual specimens analysed. Close agreement is found between the two methods for V_f = 0.5% and 0.75%. A significant difference is

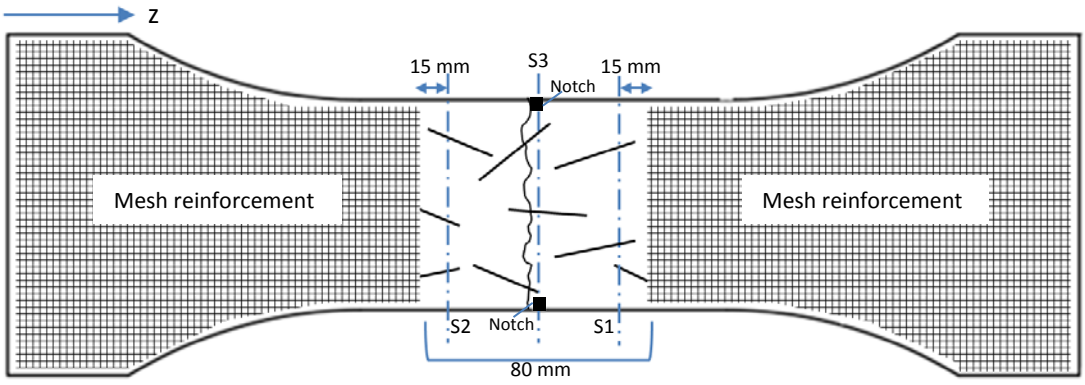

Fig. 4.16 – CT-scan data extraction method

however observed for V_f = 1.0%, with a 42% larger fibre count calculated by the CT-scan method compared to the manual counting method. A larger sample size is needed to properly compare the two methods. Given that the sample size for the manual count is 12 specimens (6 each for SCM and SCC) and only 1 for the CT-scan, the manual count is believed to more closely represent the actual fibre count.

The fibre orientation distribution (0 - 90°) is calculated within the gauge section volume relative to the longitudinal z-axis (*Fig. 4.16*). Six orientation intervals are used to plot the distribution in *Fig. 4.17*, these are 0-15°, 15-30°, 30-45°, 45-60°, 60-75° and 75-90°. All three fibre dosages provide similar fibre orientation distributions. The fibre orientation distribution is not fully uniform, with preferential fibre alignment present in the 15-45° intervals. Once again, this is a small sample size and may not be entirely representative of the actual fibre orientation distribution. *Figs. 4.18-20* show a contour image of the fibre orientation or deviation angle for each fibre dosage.

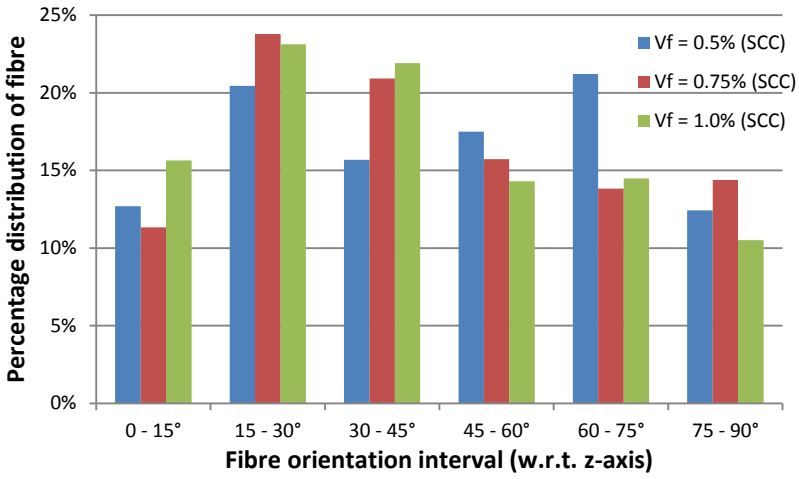

Fig. 4.17 – Fibre orientation distribution (SCC, V_f = 0.5%, 0.75% and 1.0%)

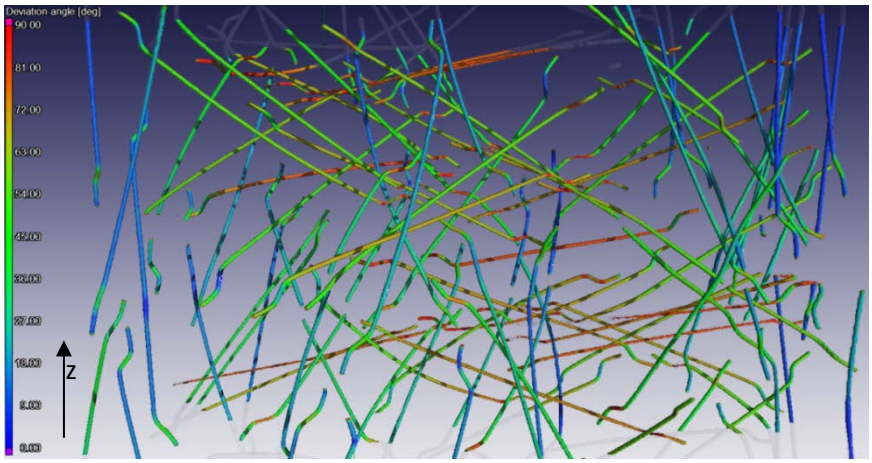

Fig. 4.18 – Contour image of fibre orientation (deviation angle from vertical z-axis), SCC, V_f = 0.5%

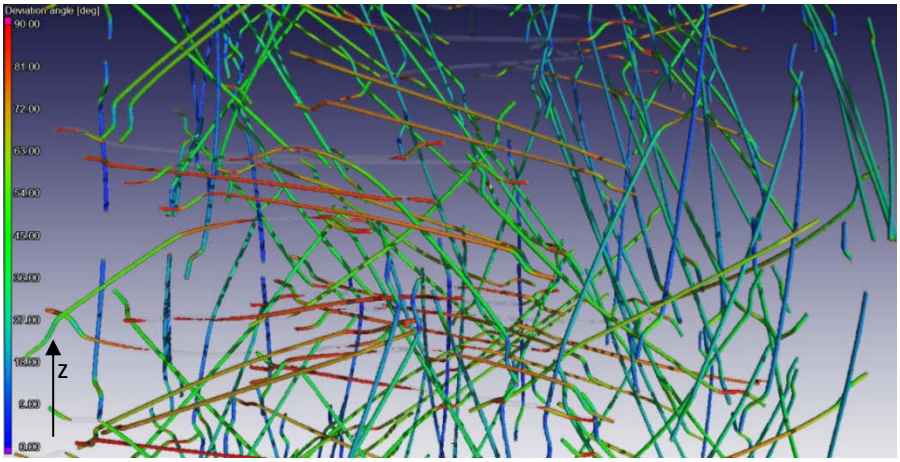

Fig. 4.19 – Contour image of fibre orientation (deviation angle from vertical z-axis), SCC, V_f = 0.75%

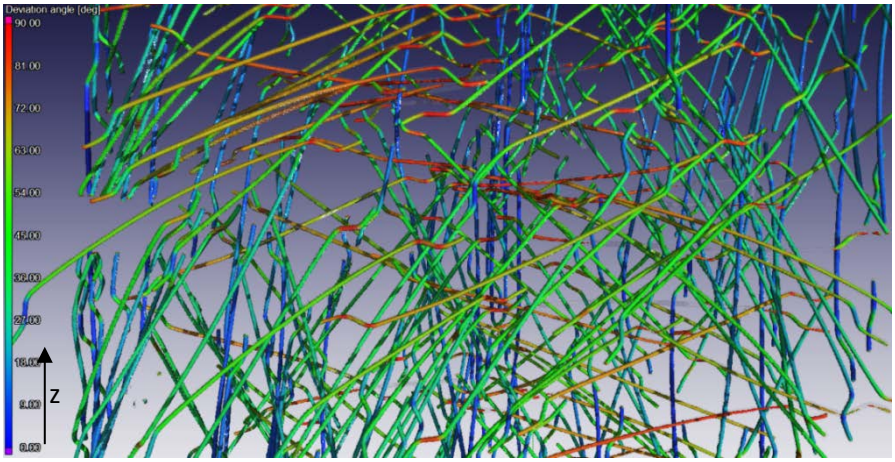

Fig. 4.20 – Contour image of fibre orientation (deviation angle from vertical z-axis), SCC, V_f = 1.0%

The average embedded length of fibres intersecting planes S1 and S2 is determined by calculating the combined volume of these intersecting fibres measured from the plane towards the centre of the specimen (*Table 4.7*). The average volume of fibres for plane S1 and S2 is then divided by the cross-sectional area (πr^2) of the fibre, giving the total embedded length of fibre. The difference between the actual fibre length and the projected fibre length (ignoring hooked-end geometry) is minimal (*Table 4.7*) and either length can be used to determine the embedded length. The average embedded length is determined by dividing the total length by the average fibre count according to the CT-scan (*Table 4.6*). In *Table 4.7*, the shorter embedded length is shown. The embedded length ranges between 9.8 mm and 11.8 mm, with an average of 11.0 mm for all three fibre dosages.

Table 4.6 – Fibre count (CT-scan)

V_f	0.5%	0.75%	1.0%
Middle (S3)	38	45	87
Top (S1)	39	49	70
Bottom (S2)	39	57	95
Average	**39**	**50**	**84**
Manual count (specimen)	33	52	59

Table 4.7 – Fibre embedded length

		V_f = 0.5%	V_f = 0.75%	V_f = 1.0%
Fibre volume (S1)	[mm^3]	255	322	345
Fibre volume (S2)	[mm^3]	179	283	582
Fibre volume (Avg.)	[mm^3]	217	303	464
Fibre length (total)	[mm]	913	1273	1951
Fibre length (projected)	[mm]	908	1267	1940
Embedded length (short side)	[mm]	**11.4**	**9.8**	**11.8**

Average embedded length (short) = **11.0 mm**

4.2 Experimental investigation at the Micro-scale

This section experimentally investigates the axial pull-out response of the *RC-65/35-BN* fibre embedded in the self-consolidating mortar (SCM) developed in this study. The experimental program, production method, test setup, procedure and results are outlined and discussed.

4.2.1 Experimental program and production method

Experimental program

The parameters affecting the axial pull-out response of a fibre embedded in a cement-based matrix include: the properties of the fibre (material and geometry), fibre embedded length (L_{fe}), fibre orientation/inclination with respect to the pull-out direction (θ), and the properties of the matrix in which the fibre is embedded. The parameters investigated in this study are summarised in *Table 4.8* and defined in *Fig. 4.21*. A total of 45 specimens are tested in this series.

Table 4.8 – Research parameters for fibre axial pull-out response

Fibre type	**End anchorage**	L_{fe} **[mm]**	θ **[°]**	**Matrix**
RC-65/35-BN	With	$L_f/4$	0°	SCM
	Without		30°	
			60°	

Production method

The specimen dimensions are provided in *Fig. 4.21*. A wooden mould is fabricated for this purpose as shown in *Fig. 4.22 (a)*. In order to position the fibre at the required embedded length and inclination, the fibre is wedged between two wooden blocks as shown in *Fig.4.22 (b)*. Prior to casting, the inner mould surface is coated with mould release oil. The surface from which the fibre protrudes is coated

with grease to facilitate de-moulding. The self-consolidating mortar is then poured into the mould and levelled with a trowel. No additional external compaction or vibration is applied to the specimen. The specimens are then moved to a climate controlled room (Temp. = 24 ±2°C and relative humidity = 65±2%) and allowed to set for 24-36 hours. At the end of this period, the specimens are carefully removed from their moulds and are allowed to cure at an ambient room temperature (24±2°C) and humidity (50±5%) for 28 days. During preliminary tests, specimens were submerged in water (Temp. = 24 ±2°C) for 28 days, however, the majority of specimens could not be used, because the fibres had corroded quite severely. Due to time constraints it was decided to store the specimens at room temperature and humidity to mitigate the likelihood of corrosion. *Section 4.2.3* compares the results of the water-cured specimens (only two specimens each for fibre inclination angles 0° and 30°) and the room-cured specimens. Neutral curing of specimens (e.g. wrapping specimens with tinfoil or cling wrap), with no loss or gain of moisture is recommended for future studies.

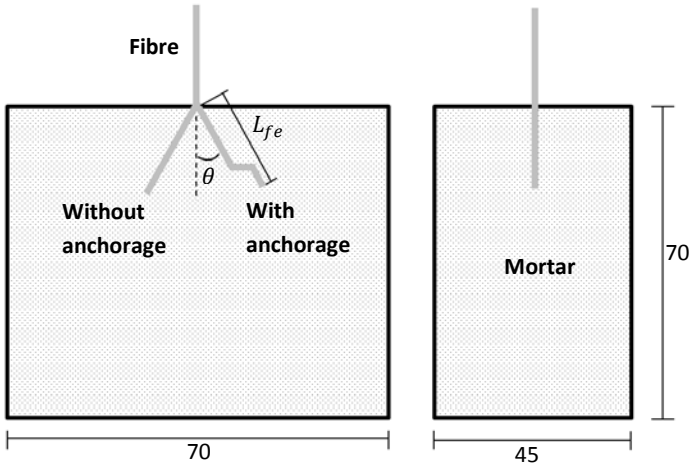

Fig. 4.21 – Specimen dimensions (in [mm]) and definition of fibre embedded length L_{fe} and inclination angle θ

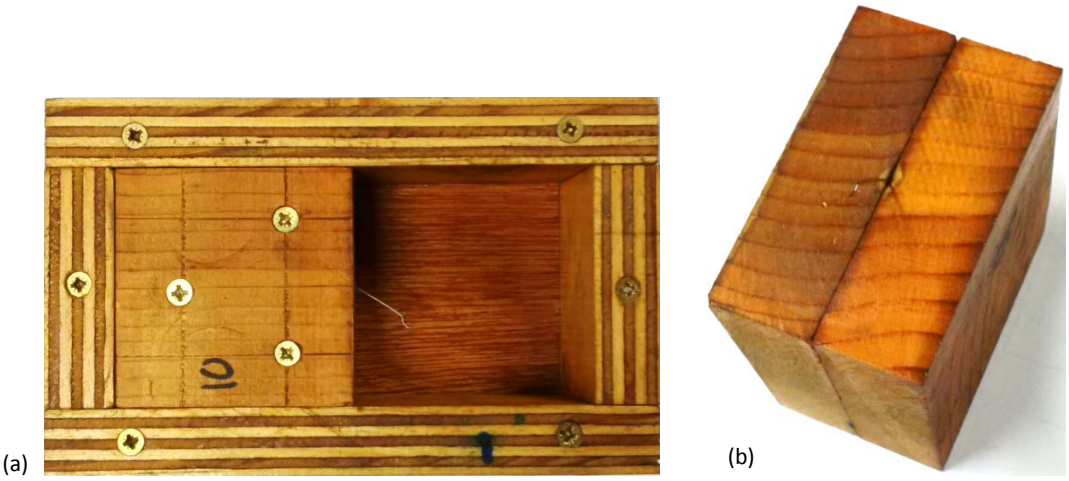

Fig. 4.22 – (a) Specimen mould and (b) fibre wedged between two wooden blocks

4.2.2 Test setup and procedure

The test configuration is illustrated in *Fig.4.23*. All tests are executed in a Zwick Z250 materials testing machine. The specimen with the embedded fibre is positioned in the centre of the bottom clamping faces. The top clamping faces hold the rig to which a load cell and two LVDTs are connected. The load cell records the fibre pull-out load and the two LVDTs record the fibre pull-out deformation/displacement. The load and deformation/displacement data is synchronised and recorded via a data logger at a rate of 10Hz (0.1s interval).

The test procedure is as follows: First the specimen is more or less centred (without being clamped) with respect to the fibre-end clamping mechanism; the bottom clamp and specimen are then raised and the position of the specimen is adjusted accordingly, so that the straight fibre end enters the clamping mechanism; the specimen is then clamped between the two clamping faces; the load cell is balanced; the fibre-end is clamped via a set screw (*Fig.4.23 (b)*) and the LVDTs are balanced. The test is then initiated and proceeds with a test rate of 0.015 mm/s of the machine crosshead position, until the fibre is completely pulled out of the surrounding mortar matrix.

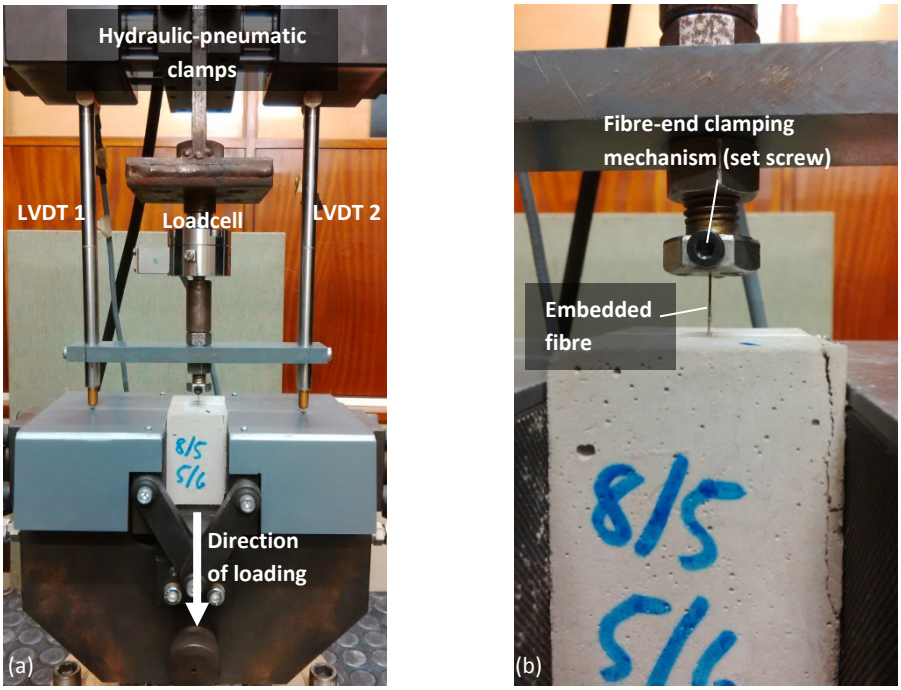

Fig. 4.23 – (a) Test configuration and (b) fibre clamping mechanism

4.2.3 Test results and discussion

Fig. 4.24 and *4.25(a)* show the sample and average fibre (with anchorage) pull-out load vs. pull-out deformation/displacement for the fibre inclination angles 0°, 30° and 60°. It is evident from *Fig. 4.25 (b)* that increasing the fibre inclination angle from 0° to 30°, marginally increases the peak and residual pull-out resistance. However, a larger inclination angle of 60° drastically diminishes the pull-out resistance. This is attributed to the spalling failure of the surrounding mortar, which results in the fibre bond and anchorage not being fully engaged.

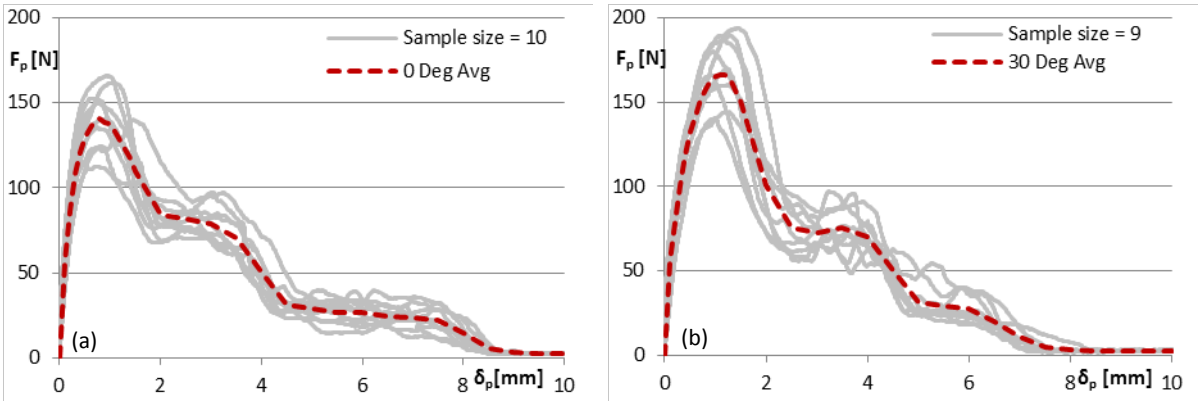

Fig. 4.24 – Fibre pull-out load F_p [N] vs. pull-out displacement δ_p [mm] for inclination angle (a) 0° and (b) 30° (With anchorage)

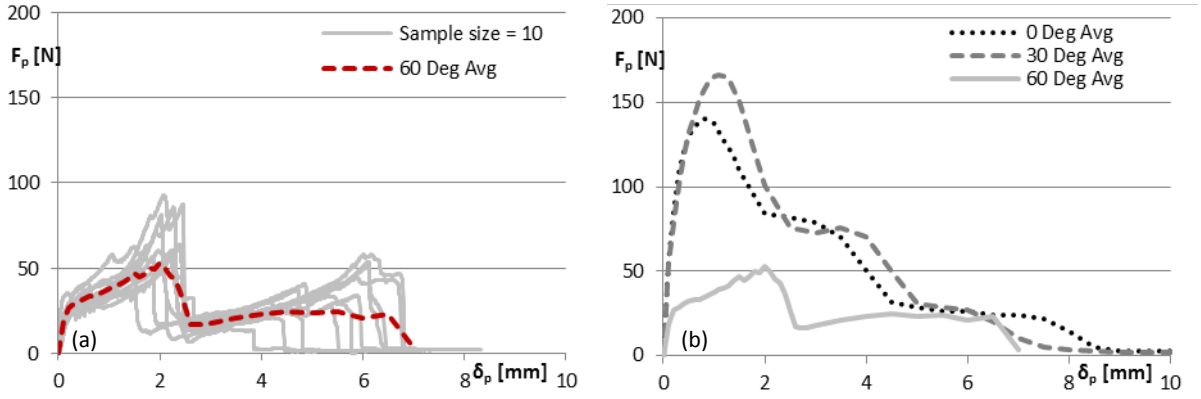

Fig. 4.25 – (a) Fibre pull-out load F_p [N] vs. pull-out displacement δ_p [mm] for inclination angle 60° and (b) average response for each inclination angle 0°, 30° and 60° (With anchorage)

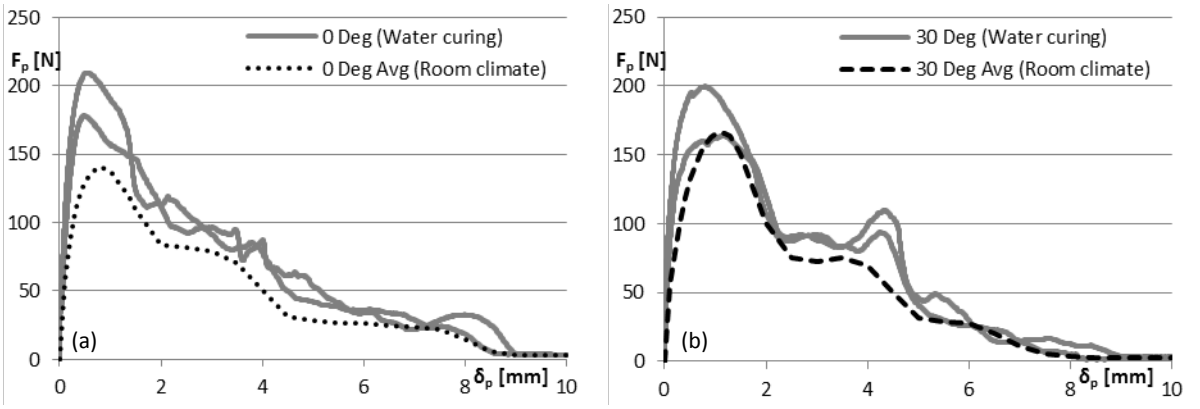

Fig. 4.26 – Influence of curing method on fibre pull-out load F_p [N] vs. pull-out displacement δ_p [mm] for inclination angle (a) 0° and (b) 30°

Fig. 4.26 demonstrates the influence of the curing method on the pull-out response. Greater peak and residual pull-out resistance is observed for water cured specimens, compared to air-cured specimens stored at room temperature and humidity. This anticipated result is attributed to the formation of more hydration products in a moisture rich environment, facilitating improved bond

between the fibre and surrounding matrix. As mentioned in *Section 4.2.1*, only two water-cured specimens could be salvaged for θ = 0° and 30°, and are therefore only indicative and not representative.

Fig.4.27 and *4.28 (a)* show the sample and average fibre (without anchorage) pull-out load vs. pull-out deformation/displacement for the fibre inclination angles 0°, 30° and 60°. In the case of an embedded fibre without end-anchorage, the fibre inclination has a more prominent effect, as illustrated in *Fig.4.28 (b)*, compared to a fibre with anchorage. Increasing the fibre inclination angle from 0° to 30°, increases the peak and residual pull-out resistance. Increasing the inclination angle further to 60°, shifts the peak pull-out resistance to occur at a larger pull-out displacement. In addition, a greater pull-out resistance is observed, but is accompanied by a reduction in ductility.

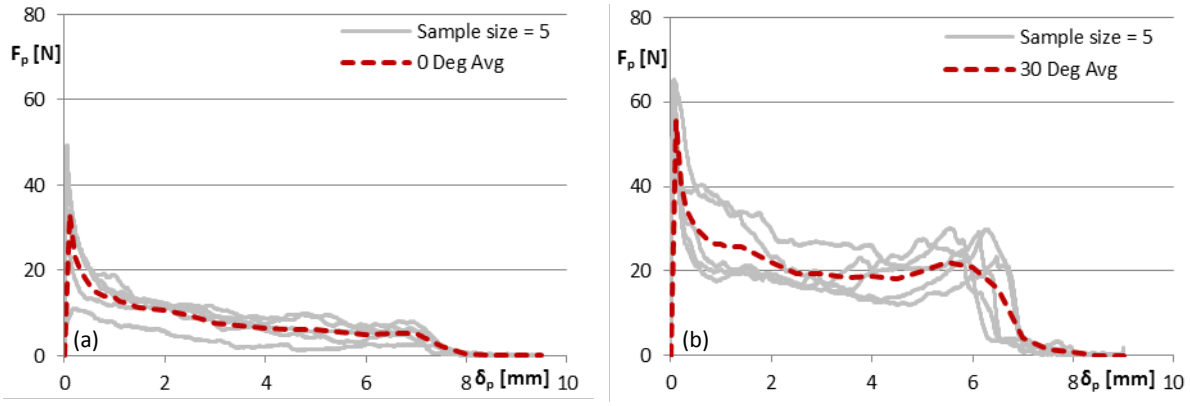

Fig. 4.27 – Fibre pull-out load F_p [N] vs. pull-out displacement δ_p [mm] for inclination angle (a) 0° and (b) 30° (Without anchorage)

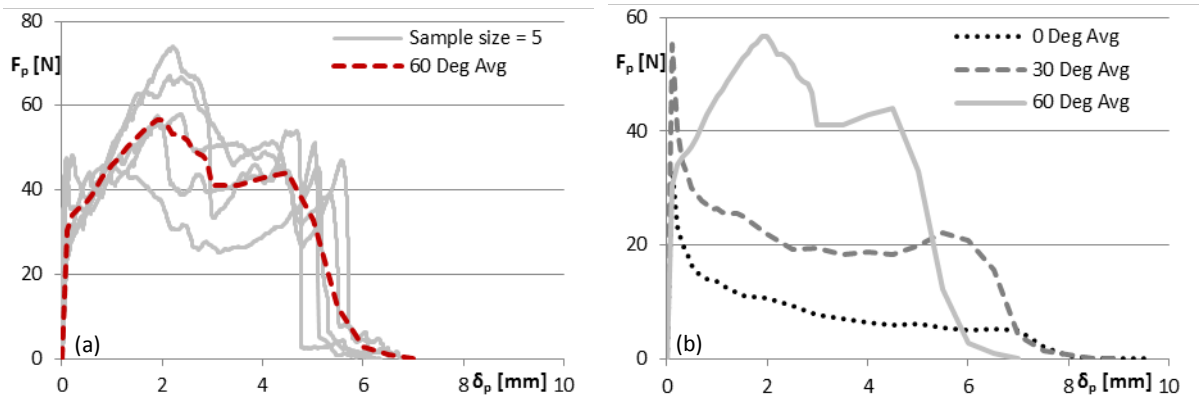

Fig. 4.28 – (a) Fibre pull-out load F_p [N] vs. pull-out displacement δ_p [mm] for inclination angle 60° and (b) average response for each inclination angle 0°, 30° and 60° (Without anchorage)

The fibre end-anchorage constitutes a significant portion of the total pull-out resistance for fibre inclination angles 0° and 30°, as can be seen in *Fig.4.29*. This is not the case for an inclination angle of 60° (see *Fig.4.30*). Up to a pull-out displacement of approximately 2 mm, the average response is

similar, after which the pull-out resistance drops drastically for the fibre with end-anchorage, compared to the fibre without end-anchorage. It is likely that the end-anchorage is influential in the spalling effect that is present for this fibre inclination angle, especially at larger pull-out displacements, where the end-anchorage is engaged. A more detailed investigation could characterise the effect of fibre inclination, end-anchorage and 3D orientation of end-anchorage on the spalling effect.

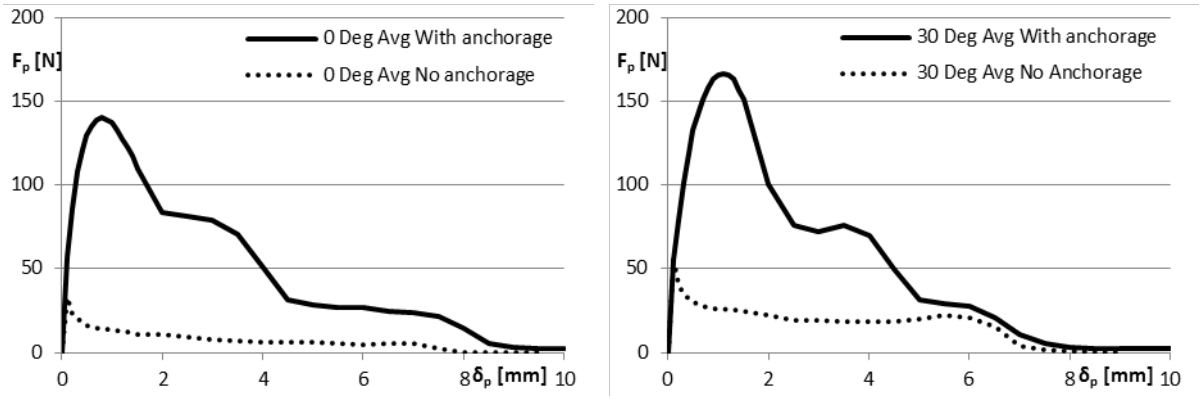

Fig. 4.29 – Comparison of average response: with anchorage vs. without anchorage for inclination angle (a) 0° and (b) 30°

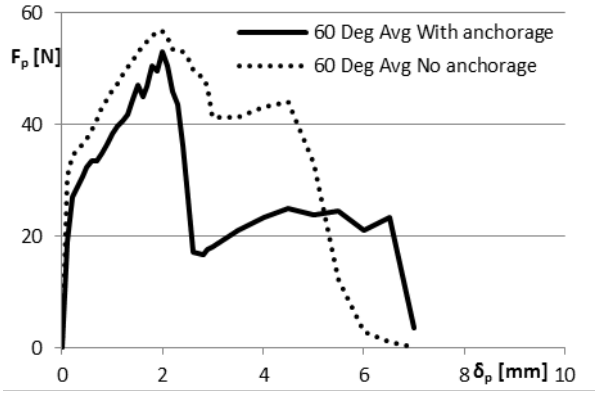

Fig. 4.30 – Comparison of average response: with anchorage vs. without anchorage for inclination angle 60°

Summary and conclusions

Meso-scale investigation

The first objective of the specimen design phase is to produce a specimen geometry that complies with the size-effect criteria for the fibre and aggregate dimensions used in this study. In so doing, a uniform 2D fibre orientation distribution can be achieved. However, an analysis of the fibre orientation distribution shows that a degree of preferential fibre alignment is present. This preferential fibre alignment is attributed to the composite rheology and casting method and not just specimen geometry. With regard to the casting method, recall that specimens had to be cast in three layers in order to locate the reinforcing mesh. Ignoring any clamping restrictions, the following

specimen geometry is suggested to reduce preferential fibre alignment for this composite: $w_g = 100\ mm$ and $t = 50\ mm$.

The second objective is to achieve a uniform maximum principal tensile stress distribution in the gauge zone and minimise any peak stresses outside the gauge zone, which would result in cracking/failure in these zones. The process of numerical refinement gives some insight into the effect of geometric parameters on the stress distribution. However, it is less successful in producing a specimen geometry which would reliably fail in the gauge zone. The specimen has to be reinforced and notched to ensure failure in the gauge zone. Only then can repeatable data be obtained. Given this outcome, a more efficient geometry would simply be a prismatic specimen with a 100 x 50 mm section. The specimen will still have to be reinforced outside the gauge zone and depending on the nature of the material (strain hardening or softening), a notch may also be required.

Micro-scale investigation

The test setup and procedure adopted in this study, provides repeatable data and is recommended for future research. The *RC-65/35-BN* fibre used, was found to be susceptible to corrosion during water-curing. A neutral curing method, with no loss or gain of moisture, should prevent corrosion and is also believed to be representative of the conditions of an embedded fibre at a Meso or Macro-scale. Only a limited parameter set is investigated in this study and can be expanded to fully characterise the axial pull-out response in terms of fibre type, embedded length, inclination angle, anchorage and matrix composition. CT-scans of single embedded fibres at different stages of pull-out displacement could also aid in characterising the underlying mechanisms.

Chapter 5

Meso and Micro-mechanical investigation of Mode II fracture

The Iosipescu shear test method (*Iosipescu, 1967*), introduced in *Chapter 2*, is adapted via finite element refinement in the elastic domain, to investigate the composite (Meso-scale) shear behaviour of a fibre-reinforced self-consolidating mortar (SCM) and concrete (SCC). Three fibre volume fractions are investigated: V_f = 0.5%, 0.75% and 1.0% of composite volume. Two initial crack widths w_i ≈ 0.1 mm and 0.3 mm are also investigated and induced prior to shear testing. To achieve this, the test program is divided into three phases. *Phase I*: In order to accurately determine the maximum crack width for each fibre volume, which would result in a residual (unloaded) crack width in the region of 0.1 mm and 0.3 mm, four specimens of each fibre dosage are subjected to cyclic tensile loading/unloading until a maximum crack width of 0.5 mm is achieved. (This was only done for the SCM group). *Phase II*: The data from phase I is then used to determine the maximum crack width for each fibre dosage and target residual crack width. Four to six specimens are pre-cracked, at 28-day strength, for each target residual crack width and fibre dosage. *Phase III*: All specimens, including those subjected to cyclic loading are tested in shear at 28-35 days. The fibre distribution including the fibre count, orientation and embedded length is analysed for a number of tested specimens, via X-ray CT-scanning.

An experimental investigation is also performed in order to characterise the transverse pull-out response (Micro-scale) of the hooked-end steel fibre embedded in the SCM. The parameters include the fibre inclination/orientation with regard to the loading configuration and the embedded length of fibre.

5.1 Experimental investigation at the Meso-scale

5.1.1 Specimen design

The basic configuration for the Iosipescu shear test is illustrated in *Fig. 5.1(a)*. Simple beam mechanics and numerical/FE refinement in the elastic domain is performed in order to optimise the specimen geometry. Two criteria are used for this process, namely (1) for failure to occur within the shear plane and (2) to achieve as far as possible a uniform shear stress distribution in the shear plane. *Fig. 5.1(b)* illustrates the simplified loading, shear and moment diagrams. Theoretically, a uniform shear force is applied between the inner supports and a zero moment occurs within the shear plane. The possible failure modes that can occur include: (1) shear-dominant failure in the shear plane at the location of zero bending moment, (2) flexure-dominant failure at the location of maximum bending moment or (3) shear-flexure failure between the position of maximum flexure and the shear plane.

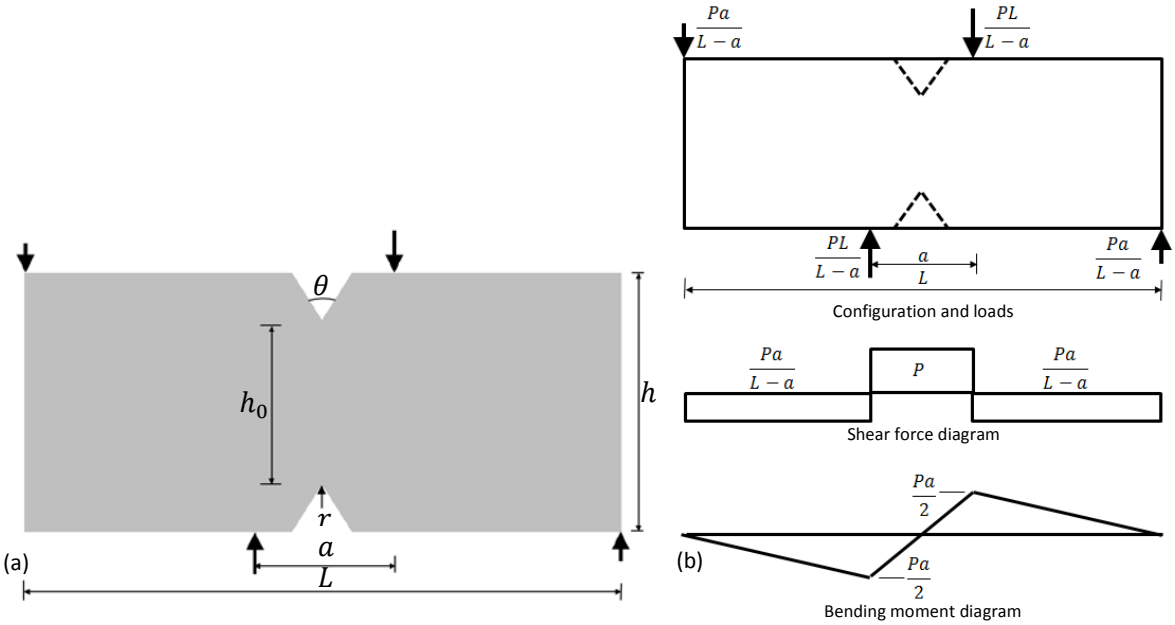

Fig. 5.1 – (a) Basic configuration for Iosipescu shear test and (b) internal forces (*Shang & van Zijl, 2007*)

Selection of geometric parameter values

Several factors need to be considered for the determination of the global dimensions, including restrictions with respect to the testing equipment as well as consideration of a representative fibre volume and production method: (1) Thickness, t – The maximum opening width of the clamping system used to pre-crack the specimen is 50 mm. The specimen thickness is therefore limited to 45 mm, which is believed to still be adequate for a maximum coarse aggregate particle size of 10-13 mm in future studies, but may result in a 2D preferential fibre alignment. Even though it was not done for this study, it is recommended that the contact stress and the potential for compressive splitting failure at the points of load application also be considered. (2) Height, h: The width of the clamping system is 140 mm. The specimen height is therefore chosen only slightly larger at 150 mm. (3) Shear plane height, h_0 – A height of at least twice the fibre length (L_f = 35 mm) is chosen to limit preferential fibre alignment in the region of the shear plane. (4) An inner support separation (a) of

70 mm, outer support separation (L) of 200 mm and overall length of 300 mm is chosen for practical execution.

If linear elasticity is assumed together with brittle failure in either shear or flexure, the following requirement for failure in the notch can be deduced (see *Eq. 5.1* and *Shang & van Zijl (2007)*). *Eq. 5.1* is based on the ratio of maximum applied shear and flexural stress and the ratio of maximum shear and flexural resistance. Substituting a conservative value for τ_u/σ_{tu} = 1.5 (where $\tau_u$and σ_{tu} are the ultimate shear and tensile resistance of the material respectively) and a and h equal to 70 mm and 150 mm respectively, it follows that the shear plane height, h_0 < 71.4 mm. A shear plane height of 70 mm ($\sim 2 \cdot L_f$) is therefore selected.

$$h_0 < \frac{h^2}{3a\left(\tau_u/\sigma_{tu}\right)} \tag{5.1}$$

Refinement of specimen geometry via numerical analysis in the elastic domain

A process of numerical refinement within the elastic domain is performed in order to optimise the notch geometry. Commercial FE software *Abaqus 6.10* is used. The criteria for geometrical refinement, includes the uniformity of the shear stress distribution in the shear plane (Line 1 in *Fig. 5.2 (a)*), the location of maximum principal stress along the perimeter of the notch (Line 2) and the maximum principal stress distribution (Line 1) when the specimen is subjected to uniaxial tension (during pre-cracking). The parameters varied in the analysis are the notch angle (θ), notch tip radius (r) and notch depth (d) (see *Fig. 5.2 (b)*).

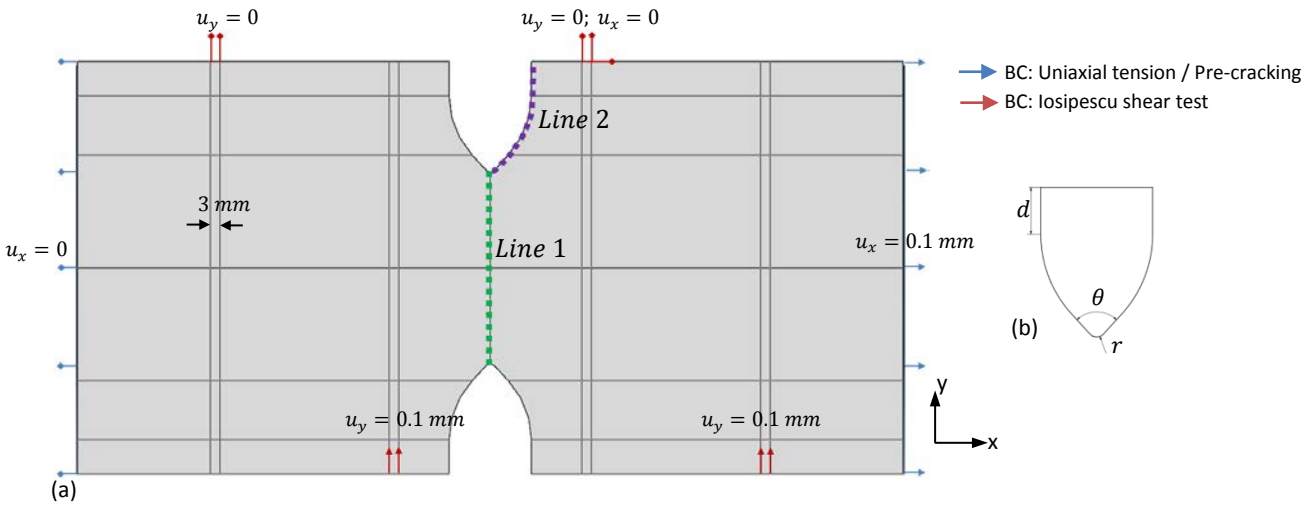

Fig. 5.2 – (a) FE model (*Abaqus 6.10*) indicating boundary conditions and positions (Line 1 & 2) monitored for stress distributions (b) Parameters for notch geometry

Model parameters:
The fixed and variable geometric parameters are shown in *Table 5.1*. Three notch angles (θ = 80°, 90° and 100°), three notch radii (r = 0, 2.5 and 3.5 mm) and three notch depths (d = 10, 15 and 20 mm) are investigated. A linear elastic material is considered with an elastic modulus and Poisson's ratio of 30 GPa and 0.2 respectively. The element type(s) used for all analyses included a 6-node quadratic plane stress triangle and an 8-node biquadratic plane stress quadrilateral. An average global element size of approximately 2 mm is used throughout.

Table 5.1 – Geometric parameter values for numerical analysis

Fixed parameters	Parameter values
Specimen height, h [mm]	150
Shear plane height, h_0 [mm]	70
Thickness, t [mm]	45
Inner support separation, a [mm]	70
Outer support separation, L [mm]	200
Total length [mm]	300
Variable parameters	
Notch angle, θ [deg.]	80°, 90°, 100°
Notch tip radius, r [mm]	0, 2.5, 3.5
Notch depth, d [mm]	10, 15, 20

Boundary and loading conditions:
The boundary conditions for both loading configurations (pre-cracking and shear) are shown in *Fig. 5.2 (a)*. In the case of the shear test, all points of load application are distributed over a width of 3 mm, to simulate the contact surface area of the roller supports on the specimen.

Criteria for geometric refinement:
Fig. 5.3 shows the typical stress contours analysed. Failure of brittle materials, such as concrete, initiates at the position of maximum principal stress (SMax). It is evident from *Fig. 5.3 (a)* that the peak maximum principal stresses are localised at the notch perimeter. The objective is to locate the position of peak maximum principal stress as close to the shear plane as possible. As mentioned, the other two criteria for evaluating the chosen geometry include, the uniformity of the shear stress (S12) distribution in the shear plane (Line 1) and the maximum principal stress distribution (Line 1) when the specimen is subjected to uniaxial tension.

Analysis results and discussion:
Influence of model parameters on shear stress (S12) distribution in the shear plane (Line 1):

The shear stress (S12) distribution in the shear plane (Line 1) is illustrated in *Figs. 5.4* and *5.5 (a)* for θ = 90° and r = 2.5 mm. The results of the analyses of the other parameters are included in *Appendix D.6*. Increasing the notch tip radius (r), angle (θ) and depth (d), marginally improves the uniformity of the shear stress distribution. The effect is more prominent at the notch tip, especially for a notch tip radius larger than 2.5 mm.

Influence of model parameters on maximum principal stress distribution in notch perimeter (Line 2):

The maximum principal stress distribution at the notch perimeter (Line 2) is illustrated in *Figs. 5.5 (b)* and *5.6* for θ = 90° and r = 2.5 mm. The results of the analyses of the other parameters are included

in *Appendix D.6*. The peak maximum principal stress (SMax) observed at the perimeter of the notch (Line 2) increases with the introduction of a notch tip radius, however the stress observed at the notch apex is reduced. The peak maximum principal stress is reduced for a larger notch angle. The position of the peak maximum principal stress remains more or less the same for the different parameter values considered. The maximum principal stress increases away from the shear plane for larger values of the notch angle and depth. Given the objective to maximise the peak maximum principal stress in the vicinity of the notch apex and shear plane, a smaller to intermediate notch angle and depth of 85° and 12.5 mm respectively are proposed.

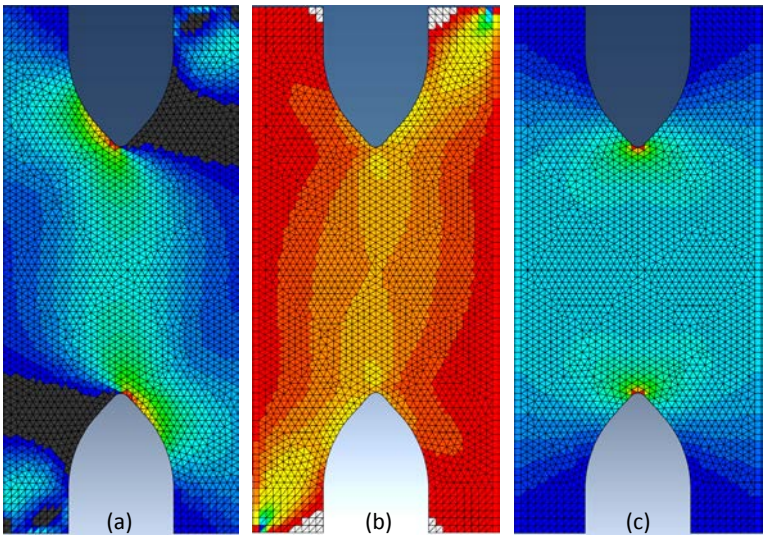

Fig. 5.3 – Typical stress contours for (a) maximum principal stress (SMax) during shear loading, (b) shear stress (S12) during shear loading and (c) maximum principal stress (SMax) during tensile/pre-crack loading (*Abaqus 6.10*)

Influence of model parameters on maximum principal stress distribution (for tensile loading/pre-cracking) in shear plane (Line 1):

The results for these analyses are not presented here and are included in *Appendix D.6*. The notch tip radius has negligible effect on the stress distribution, apart from reducing the peak stress observed at the notch for larger values of the notch tip radius i.e. r = 3.5 mm. The notch angle has little or no effect on stress distribution. Notch depth also has a minimal effect; however peak maximum principal stress at the notch does increase for a notch depth larger than 10 mm.

Based on the findings above, an intermediate notch tip radius and a smaller-to-intermediate notch angle and depth is chosen i.e. r = 2.5 mm, θ = 85° and d = 12.5 mm.

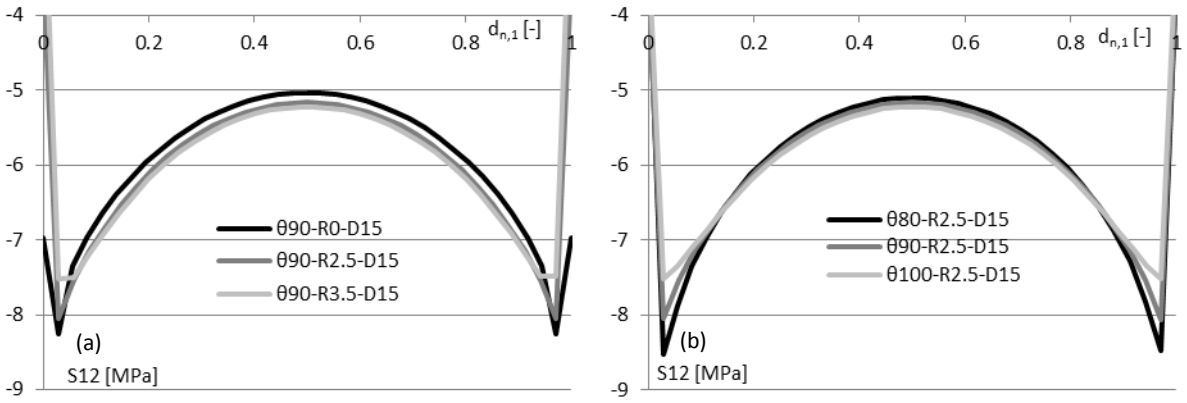

Fig. 5.4 – Shear stress (S12) distribution on Line 1 (normalised distance) (a) θ = 90°, d = 15 mm and r variable (b) r = 2.5 mm, d = 15 mm and θ variable

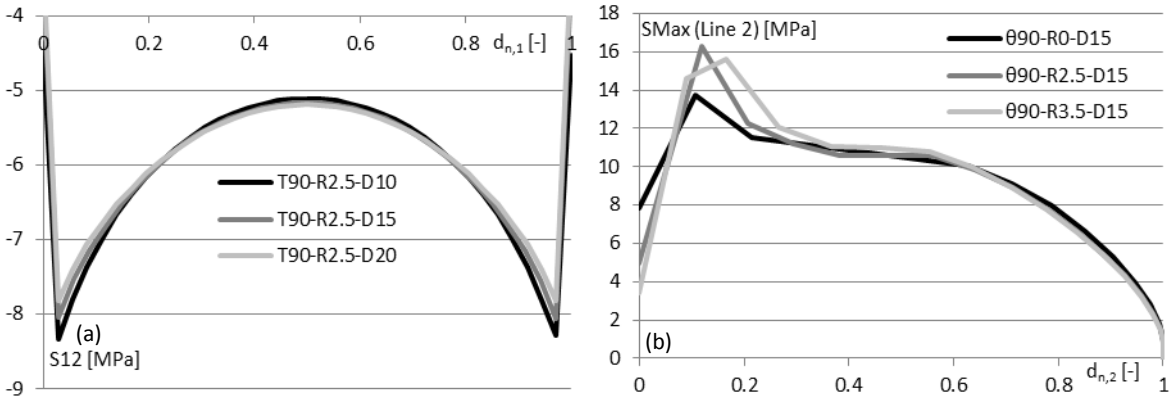

Fig. 5.5 – (a) Shear stress (S12) distribution on Line 1 (normalised distance) θ = 90°, r = 2.5 mm and d variable (b) Maximum principal stress (SMax) distribution on Line 2 (normalised distance) θ = 90°, d = 15 mm and r variable

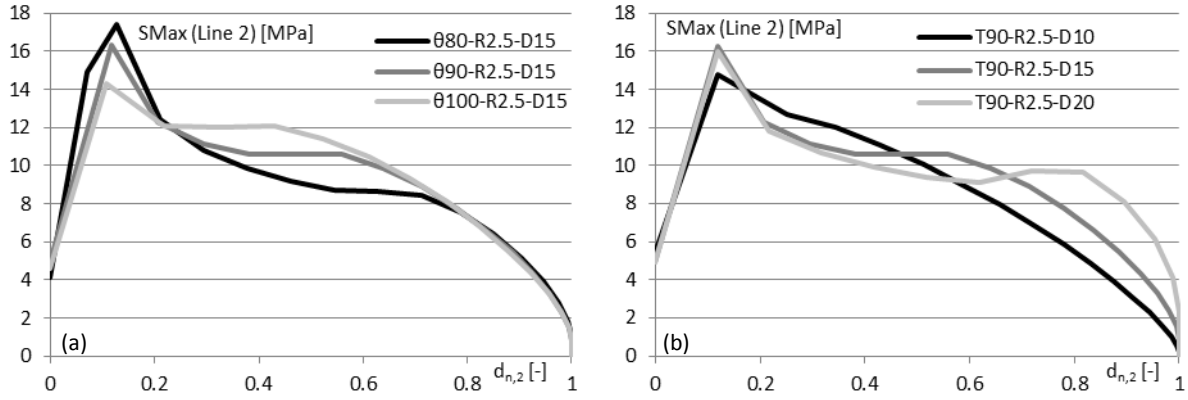

Fig. 5.6 – (a) Maximum principal stress (SMax) distribution on Line 2 (normalised distance) (a) r = 2.5 mm, d = 15 mm and θ variable (b) θ = 90°, r = 2.5 mm and d variable

5.1.2 Experimental program and production method

Research parameters

The experimental program is summarised in *Table 5.2* for a total of 84 tests. The three composites, SCM, SCC-450 and SCC-600, developed in *Chapter 3* are investigated. Three fibre volume fractions, V_f = 0.50%, 0.75% and 1.00% and two initial crack widths $w_i \approx 0.1$ mm and 0.3 mm are also investigated.

Table 5.2 – Experimental program (Number of specimens indicated in brackets)

Composite	V_f = 0.50%			V_f = 0.75%			V_f = 1.00%		
SCM	Cyclic (4)	w_i = 0.1 (4)	w_i = 0.3 (4)	Cyclic (4)	w_i = 0.1 (4)	w_i = 0.3 (4)	Cyclic (4)	w_i = 0.1 (4)	w_i = 0.3 (4)
SCC-450		w_i = 0.1 (6)	w_i = 0.3 (6)		w_i = 0.1 (6)	w_i = 0.3 (6)		w_i = 0.1 (6)	w_i = 0.3 (6)
SCC-600		w_i = 0.1 (6)	w_i = 0.3 (6)						

SCC-450 = 450 kg/m^3 (Greywacke 9.5mm); SCC-600 = 600 kg/m^3 (Greywacke 9.5mm)

Specimen preparation

Wooden moulds (*Fig. 5.7 (a)*) are fabricated according to the specimen dimensions determined. Twelve specimens are cast for each composite and fibre dosage. Prior to casting, a thin layer of grease is applied to the notch area instead of standard mould release oil, to facilitate the removal of the wedge notches once the specimen has hardened. After casting, the specimens are stored at 24±2°C and 65±2% RH for 24-36 hrs, at which time, the specimens are de-moulded and transferred to water curing tanks with a temperature of 24±2°C.

Preliminary tests show that specimens do not reliably fail in the shear plane. Compression splitting failure at the points of load application induced diagonal cracking between the two inner supports. The shear plane (Line 1) is therefore weakened with a saw-cut notch, to ensure failure in this zone. After 21 days of water curing, the casting face of each specimen is ground level (to facilitate clamping during pre-cracking) and a 2.5 mm saw-cut notch is made on both sides of the shear plane (see *Fig. 5.8(b)*). The specimens are then returned to the curing tank until testing.

(a) 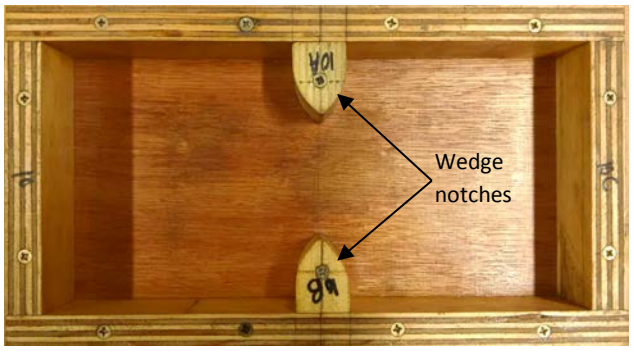

(b) 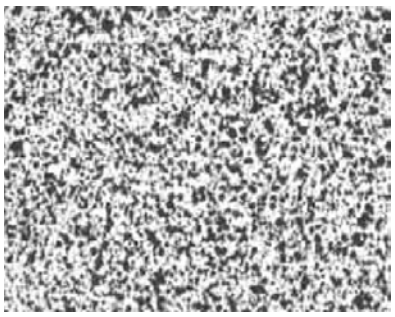

Fig. 5.7 – (a) Specimen mould and (b) sprinkle pattern for Digital Image Correlation (DIC)

Digital Image Correlation (DIC) via an *Aramis (GOM)* system is used to measure the deformation of the surface of the specimen during testing. As discussed in *Chapter 2*, characteristics observed for each facet of each image are used to determine the deformation in each stage (image) relative to a reference stage (image). In the case of a homogeneous surface, such as that of concrete, the measuring surface needs to be prepared. The application of a stochastic or sprinkle pattern, such as the one illustrated in *Fig. 5.7 (b)*, on the surface of the specimen provides identifiable characteristics. Before testing, the surface of each specimen is first prepared by applying a thin limestone coating (ground limestone mixed with water). A sprinkle pattern is then sprayed onto the dried limestone surface with black aerosol spray paint.

5.1.3 Test setup and procedure

Phase I: Cyclic tensile loading
The test arrangement for cyclic tensile loading is illustrated in *Fig. 5.8 (a)*. The specimen is clamped at both ends with hydraulic-pneumatic grips, which provide a non-rotatable boundary condition. An extensometer is clamped and centred over the saw-cut notch with a gauge distance of 80 mm. The extensometer measures the displacement on both sides and the average deformation is recorded. Each specimen is subjected to 20 cycles of loading and complete unloading, with a displacement (extensometer) increment of 0.025 mm. The rate of the test is controlled via the crosshead position of the Zwick Z250 testing machine at 0.25 mm/min. The test is stopped at an extensometer reading of 0.50 mm. After analysis of the data, the average maximum crack width for each target residual crack width and fibre dosage is determined.

Phase II: Pre-cracking
The test arrangement for the pre-cracking phase is identical to the cyclic tests performed previously. The average maximum crack width obtained from phase I is used as input and each specimen is loaded to this value and then unloaded to achieve the average residual crack width. Four to six specimens are tested for each target residual crack width (w_i = 0.1 mm and 0.3 mm) and fibre dosage (V_f = 0.5%, 0.75% and 1.0%). The rate of the test is controlled via the machine crosshead position at 0.05 mm/min.

Phase III: Iosipescu shear test
Each of the pre-cracked specimens is tested as illustrated in *Fig. 5.8 (b)*. The specimen is centred with respect to the shear plane, with an anti-symmetric inner load separation of 70 mm and outer support separation of 200 mm. The specimen is loaded through rollers that allow free rotation and horizontal translation. A LVDT is mounted centrally on one side of the specimen (see *Fig. 5.9 (d)*) in order to correlate the normal displacement across the shear plane with the optical measurement (*Fig. 5.9 (a)*). The test rate is controlled via the machine crosshead position with an initial rate of 0.3 mm/min until a crosshead displacement of 3 mm is reached. The test rate is then increased to 0.5 mm/min until a crosshead displacement of 5 mm.

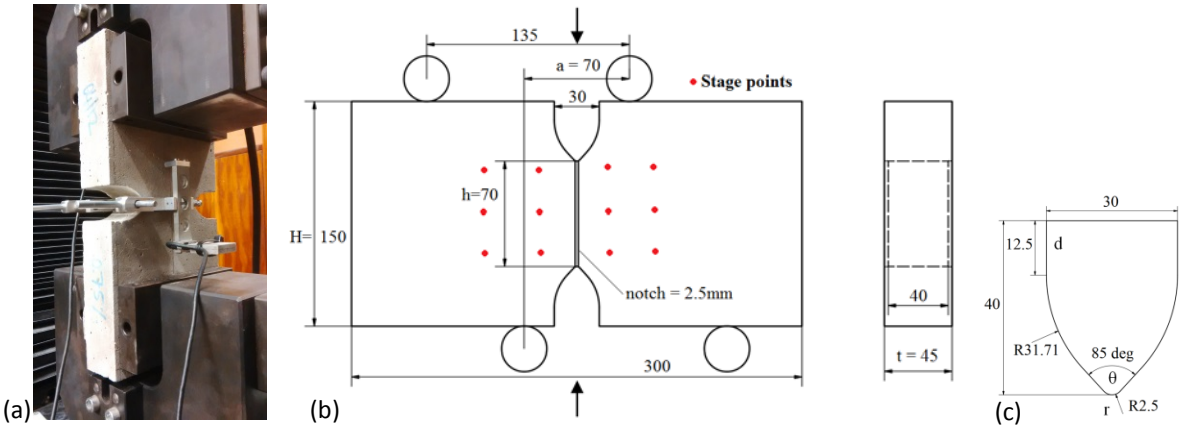

Fig. 5.8 – (a) Cyclic and pre-crack setup, (b) Test configuration showing load application and stage points used in DIC, (c) Notch detail (*Zeranka & van Zijl, 2015*)

Fig. 5.9 – Test setup: (a) Front view, (b) Back view (c) Front (close-up) and (d) LVDT measuring normal displacement

5.1.4 Test results and discussion

Phase I: Cyclic tensile loading

The cyclic tensile loading/unloading phase is only applied to the SCM composite. The tensile load-crack width response is shown in *Fig. 5.10* for each fibre dosage V_f = 0.50%, 0.75% and 1.00%. *Table 5.3* provides the average maximum crack width that needs to be applied in order to achieve the chosen residual/unloaded crack width of 0.1 mm and 0.3 mm for each fibre dosage. These maximum crack widths are implemented in Phase II. The coefficient of variation (*C.V.*) in *Table 5.3* gives an indication of the variability of the data. The average residual crack widths for the specimens tested in this phase ($w_{c,res}$ in *Table 5.3*) are considered to be close enough to the required target 0.3 mm residual crack width. These specimens are therefore included in the $w_{c,res}$ = 0.3 mm sample in Phase III. The complete data set for *Table 5.3* is provided in *Appendix D.5.1* (*Table D.1-3*).

Phase II: Pre-cracking

The average residual/unloaded crack widths obtained in the pre-cracking phase are tabulated in *Table 5.4*. The complete data set is provided in *Appendix D.5.2* (*Table D.4-6*). Deviation from the target residual crack width ranges from 0.001 mm to 0.035 mm, with a coefficient of variation in the range 1.8 - 12.0%. *Fig. 5.11 (a-g)* illustrates the pre-cracking stage (tensile load, F_t[kN] vs. deformation, w_c [mm]) for each composition and fibre dosage.

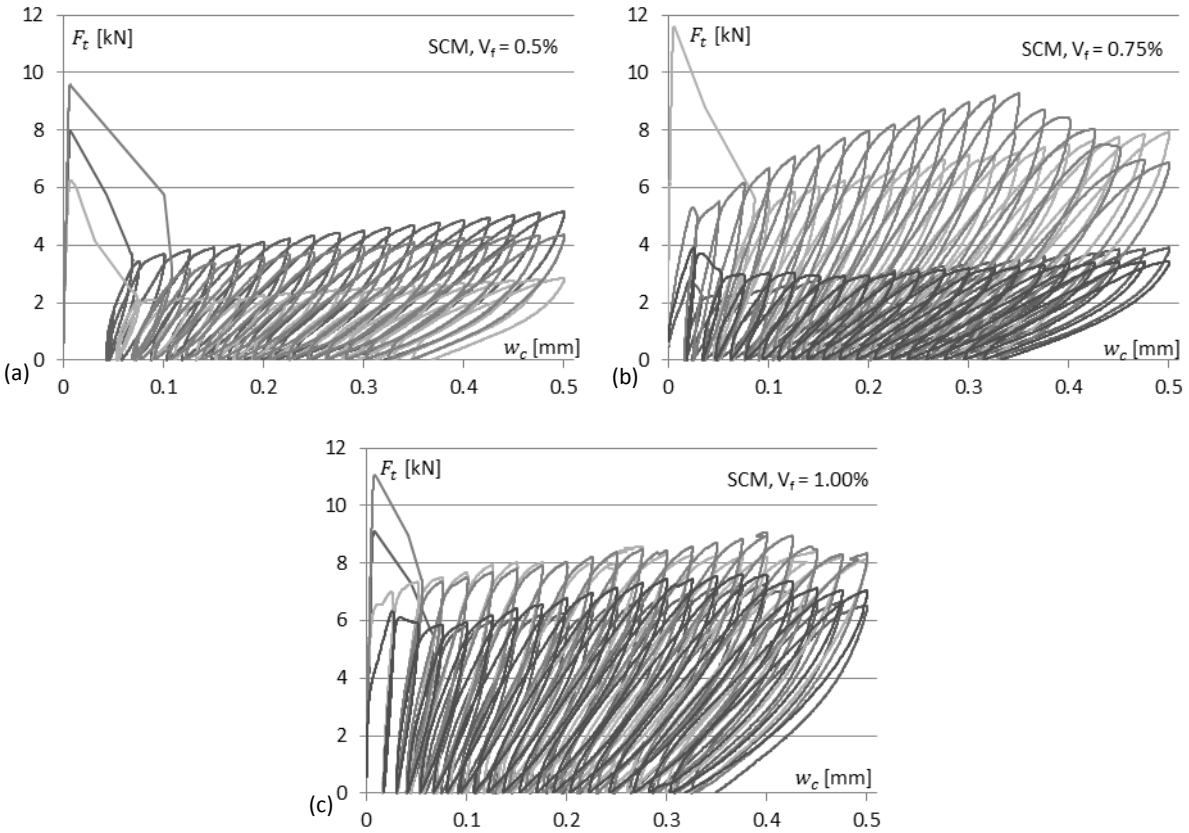

Fig. 5.10 – Cyclic tensile load (F_t $[kN]$) – extensometer displacement (w_c $[mm]$) response for SCM, V_f = (a) 0.5%, (b) 0.75% and (c) 1.00%

Table 5.3 – Average maximum crack width for corresponding target residual crack width (SCM only)

$w_{c,max}$	V_f = 0.50%	V_f = 0.75%	V_f = 1.00%
$w_{c,res}^{target}$ = 0.1 mm	0.163*	0.182	0.176
C.V.	13.5%	6.8%	5.7%
$w_{c,res}^{target}$ = 0.3 mm	0.446†	0.466	0.459
C.V.	7.1%	2.7%	3.8%
$w_{c,res}$	0.346	0.324	0.330
C.V.	6.9%	2.5%	4.0%

* Value used for pre-cracking = 0.150 mm
† Value used for pre-cracking = 0.450 mm

Table 5.4 – Average residual/unloaded crack widths obtained in the pre-cracking phase

	V_f = 0.50%		V_f = 0.75%		V_f = 1.00%	
SCM	w_i = 0.1 mm	w_i = 0.3 mm	w_i = 0.1 mm	w_i = 0.3 mm	w_i = 0.1 mm	w_i = 0.3 mm
Average	0.097	0.322	0.113	0.301	0.104	0.295
C.V.	11.0%	4.6%	7.2%	1.8%	5.9%	5.8%
SCC-450						
Average	0.098	0.319	0.112	0.335	0.103	0.317
C.V.	6.3%	5.2%	9.0%	4.2%	5.3%	2.0%
SCC-600						
Average	0.096	0.310				
C.V.	12.0%	5.1%				

It is postulated that the variability in the initial peak strength may be attributed to the combination of the cast-in wedge notch and the saw-cut notch, which may not be conducive to a uniform stress distribution in the vicinity of the shear plane and notch apex. The significant variability in the post-cracking capacity is largely attributed to the high variability in fibre count for some of the composites, with a maximum coefficient of variation of 36.6% (*Appendix D.5.4*). The fibre orientation and embedded length distribution can also be influential. However, consistent residual crack widths are obtained and in most cases, a uniform crack could be achieved in the shear plane, which is ultimately the objective.

Phase III: Iosipescu shear test

Twelve points arranged in four columns (two columns on either side of the shear plane) and three rows (over the height of the specimen) are monitored via the DIC system, as illustrated in *Fig. 5.8 (b)*. The 'stage' points are centred and equidistant with respect to the shear plane. These 12 points allow the measurement of the rotation over the height of the specimen on both sides of the shear plane and consequently the displacement parallel and normal to the rotating shear plane, and the correct shear load component (which is also a function of the specimen rotation) is determined.

The effect of the parameters, including fibre dosage (V_f), initial crack width (w_i) and coarse aggregate fraction (SCM, SCC-450 and SCC-600) is discussed. *Table 5.5* provides the average peak shear stress achieved for each composition, fibre dosage and initial crack width. The complete data set for *Table 5.5* is provided in *Appendix D.5.3* (*Table D.7-9*).

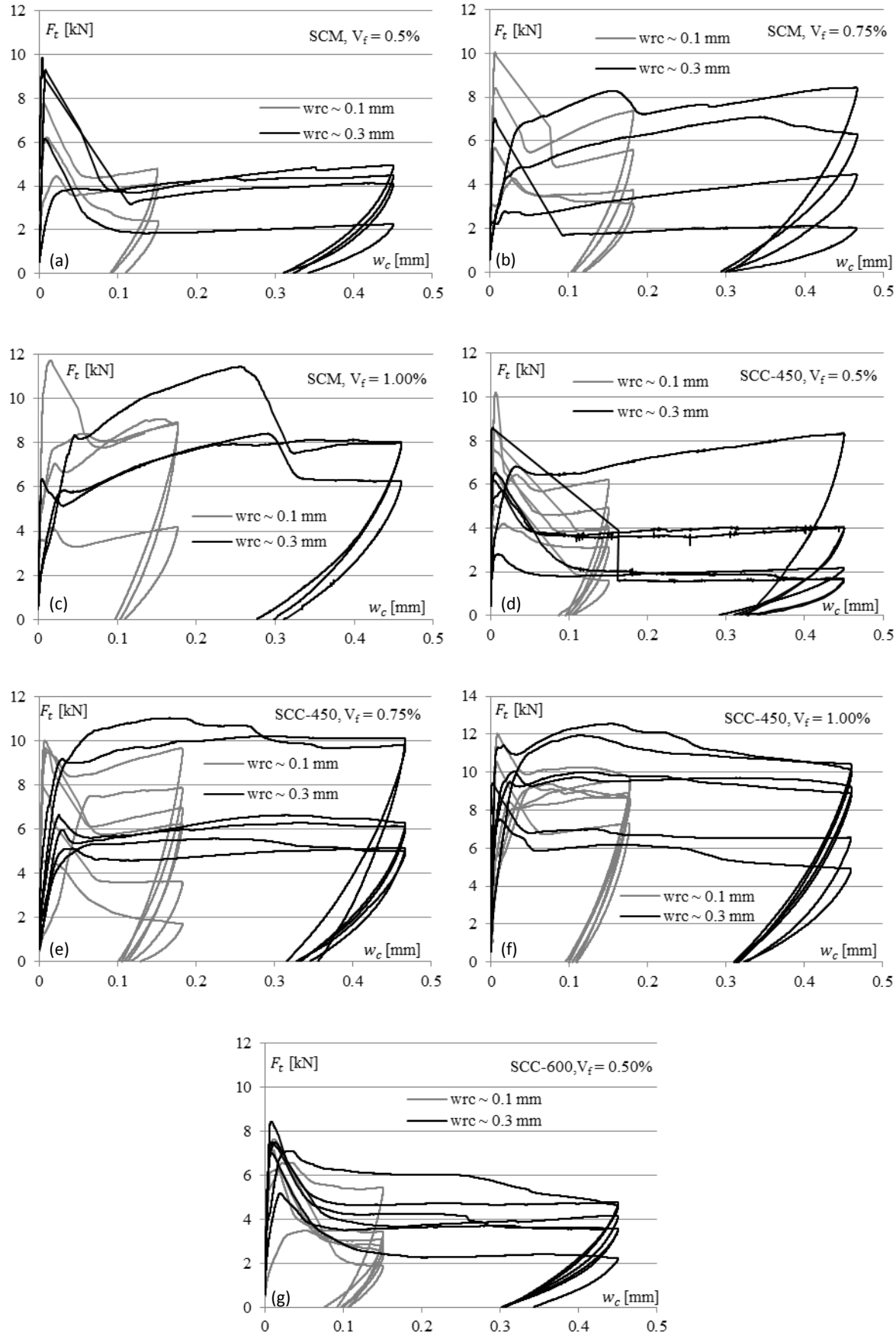

Fig. 5.11 – Tensile load ($F_t[kN]$) vs. extensometer displacement (w_c $[mm]$) for SCM, V_f = (a) 0.5%, (b) 0.75%, (c) 1.0%; SCC-450, V_f = (d) 0.5%, (e) 0.75%, (f) 1.0% and SCC-600, V_f = (g) 0.5%

Table 5.5 – Average peak shear stress achieved for each composition, fibre dosage and initial crack width

	V_f = 0.50%		V_f = 0.75%		V_f = 1.00%	
w_i	0.1 mm	0.3 mm/Cyc.	0.1 mm	0.3 mm/Cyc.	0.1 mm	0.3 mm/Cyc.
SCM						
τ_{avg}^{max} [MPa]	7.73	4.48	9.50	5.19	9.99	7.70
C.V.	24.1%	26.7%	17.4%	39.8%	34.4%	23.1%
SCC-450						
τ_{avg}^{max} [MPa]	7.14	4.03	8.16	6.54	12.39	9.31
C.V.	35.6%	31.6%	34.3%	29.4%	6.9%	34.1%
SCC-600						
τ_{avg}^{max} [MPa]	6.04	5.89				
C.V.	34.8%	16.5%				

Note: "Cyc." are the specimens subjected to cyclic testing for the SCM composition and are added to the data sample where the initial crack width, $w_i \approx 0.3$ mm.

Effect of fibre dosage (V_f):

Table 5.6 summarises the effect of fibre dosage on the composite response. In general, the peak shear strength increases with increasing fibre dosage. Considering the increase in peak shear strength relative to the peak shear strength for V_f = 0.5%, fibre reinforcement is more beneficial at a larger (0.3 mm) initial crack width and coarse aggregate fraction (SCC-450). The increase in peak shear strength is 23% (for V_f = 0.75%) and 29% (for V_f = 1.0%) for SCM (w_i = 0.1 mm), whereas the increase in peak shear strength is 62% (for V_f = 0.75%) and 131% (for V_f = 1.0%) for SCC-450 (w_i = 0.3 mm). *Fig. 5.12* illustrates this effect. The effect of fibre dosage on the crack width-shear displacement response is marginal for SCM at both initial crack widths (w_i = 0.1 mm & 0.3 mm). In the case of SCC-450 however, the larger fibre dosage of 0.75% and 1.0% are effective at reducing the crack width for a given shear displacement (see *Fig. 5.13*). As anticipated, the fracture energy also increases with increasing fibre dosage (see *Fig. 5.14*). The complete data set is provided in *Appendix D.2*.

However, any comparison between the composites SCM and SCC-450 needs to take into account the difference in fibre count between SCM and SCC-450. The average manual fibre count is: 24 & 30 (V_f = 0.5%), 35 & 50 (V_f = 0.75%) and 52 & 82 (V_f = 1.0%) for SCM and SCC-450 respectively (*Appendix D.5.4*). SCC-450 on average has a significantly higher fibre count compared to SCM, especially for V_f = 0.75% and 1.0%.

Table 5.6 - Effect of fibre dosage on the composite response (SCM and SCC-450)

SCM	w_i = 0.1 mm	w_i = 0.3 mm
$F_v - \delta_v$	Peak shear strength: ↑ (23-29 %)	Peak shear strength: ↑ (16-72%)
$w_c - \delta_v$	Marginal effect	Marginal effect
G_f	↑ (Lower contribution for V_f = 1.00%)	↑ (Lower contribution for V_f = 0.75%)
SCC-450	w_i = 0.1 mm	w_i = 0.3 mm
$F_v - \delta_v$	Peak shear strength: ↑ (14 – 73%)	Peak shear strength: ↑ (62 – 131%)
$w_c - \delta_v$	Larger crack widths observed for smaller fibre dosage at same shear displacement Marginal difference between 0.75% & 1.00%	Larger crack widths observed for smaller fibre dosage at same shear displacement Marginal difference between 0.75% & 1.00%
G_f	↑	↑

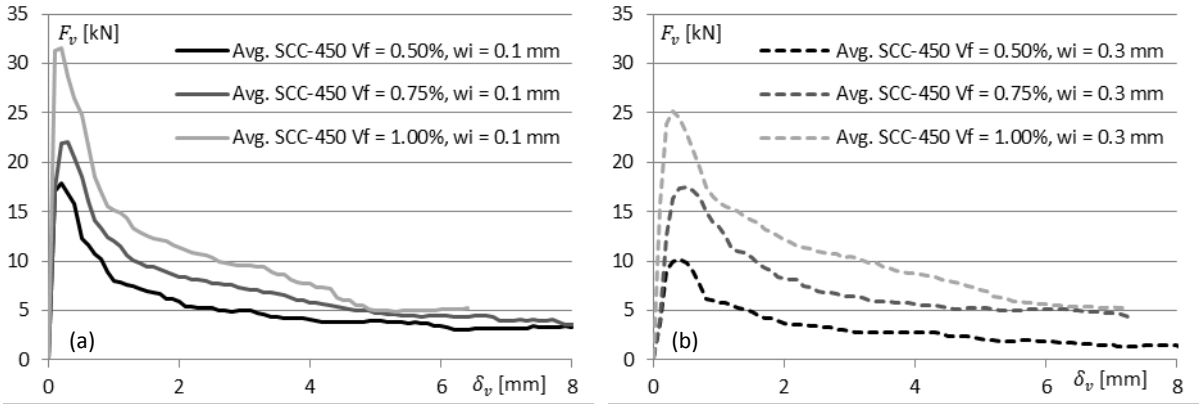

Fig. 5.12 – Shear load, F_v [kN] vs. shear displacement, δ_v [mm] for SCC-450 V_f = 0.50-1.00% (a) w_i = 0.1 mm (b) w_i = 0.3 mm

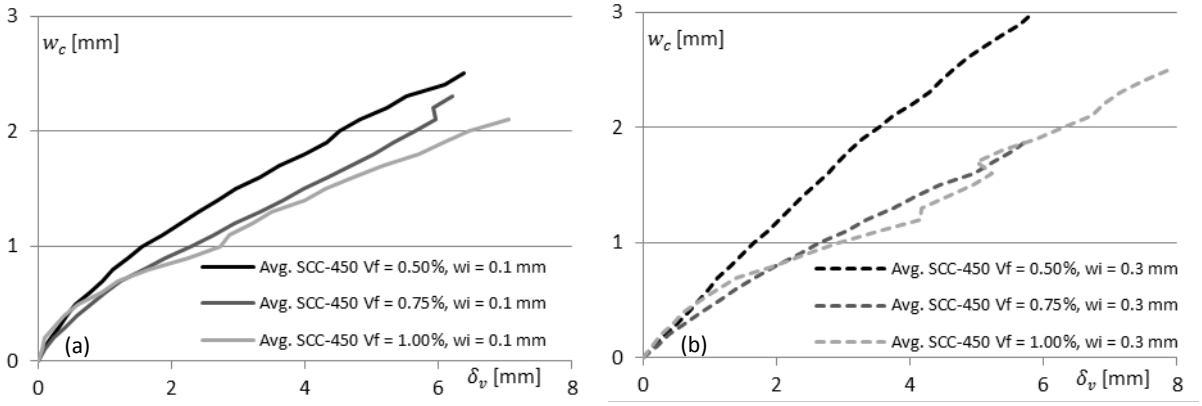

Fig. 5.13 – Crack width, w_c [mm] vs. shear displacement, δ_v [mm] for SCC-450 V_f = 0.50-1.00% (a) w_i = 0.1 mm (b) w_i = 0.3 mm

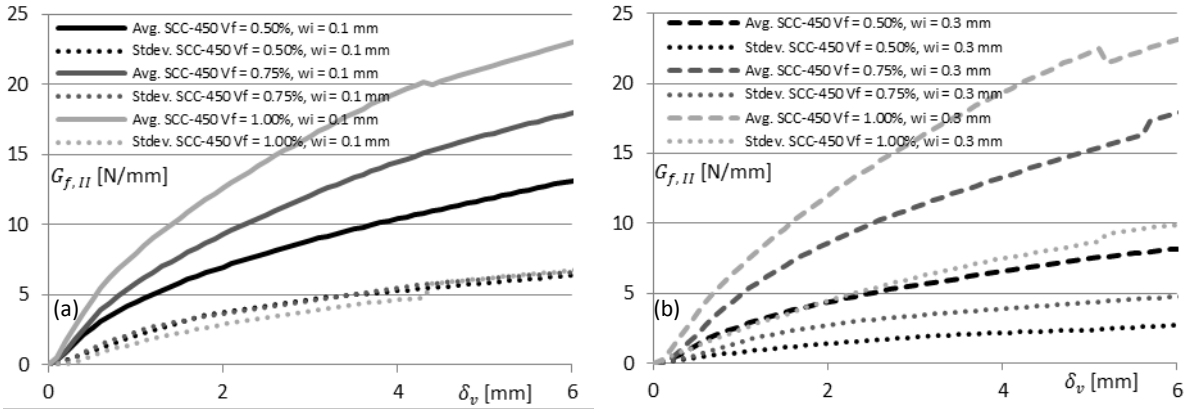

Fig. 5.14 – Fracture energy, $G_{f,II}$ [N/mm] vs. shear displacement, δ_v [mm] for SCC-450 V_f = 0.50-1.00% (a) w_i = 0.1 mm (b) w_i = 0.3 mm

Effect of initial crack width (w_i):

Table 5.7 summarises the effect of the initial crack width (w_i) on the composite response. As expected, a reduction in the peak shear strength is observed for a larger initial crack width (*Fig. 5.15*). The drop in peak shear strength is reduced at a larger fibre dosage (V_f = 1.00% for SCM and $V_f \geq$ 0.75% for SCC-450). Increasing the initial crack width from 0.1 mm to 0.3 mm has a marginal effect on the peak shear strength for SCC-600 (V_f = 0.5%). It is evident from this result that fibre reinforcement and aggregate interlock/shear interface roughness synergise well to limit the effect of initial crack width or cracking in general. Initial crack width appears to have a marginal influence on the crack width – shear displacement response. The effect on the fracture energy is similar to that of the peak shear strength. The fracture energy drops at a larger initial crack width (*Fig. 5.16*), but the drop is diminished for a larger fibre dosage and increased coarse aggregate fraction. The complete data set is provided in *Appendix D.3*.

Table 5.7 – Effect of the initial crack width (w_i) on the composite response

SCM	V_f = 0.5%	V_f = 0.75%	V_f = 1.00%
$F_v - \delta_v$	Peak shear strength: ↓ 42%	Peak shear strength: ↓ 45%	Peak shear strength: ↓ 23%
$w_c - \delta_v$	---	---	---
G_f	↓	↓	---
SCC-450			
$F_v - \delta_v$	Peak shear strength: ↓ 44%	Peak shear strength: ↓ 20%	Peak shear strength: ↓ 25%
$w_c - \delta_v$	---	---	---
G_f	↓	---	---
SCC-600			
$F_v - \delta_v$	Peak shear strength: ↓ 3%		
$w_c - \delta_v$	---		
G_f	---		

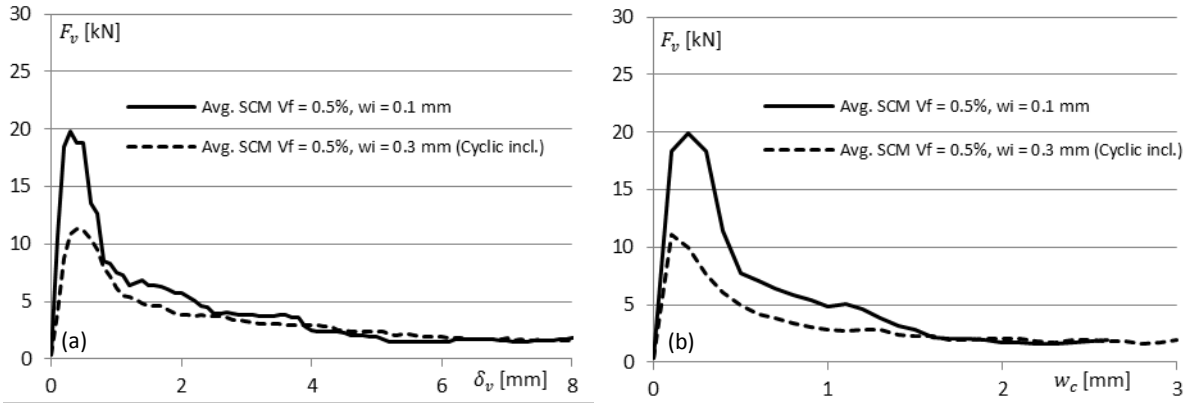

Fig. 5.15 – SCM V_f = 0.50%, Shear load, F_v [kN] vs. (a) shear displacement, δ_v [mm] and (b) crack width, w_c [mm]

Effect of aggregate fraction (coarse aggregate content and size):

The effect of the aggregate fraction on the composite response is summarised in *Table 5.8*. The percentage increase or decrease in peak shear strength (F_p) is measured relative to the corresponding value obtained for SCM (no coarse aggregate). For a 0.5% fibre dosage, a reduction

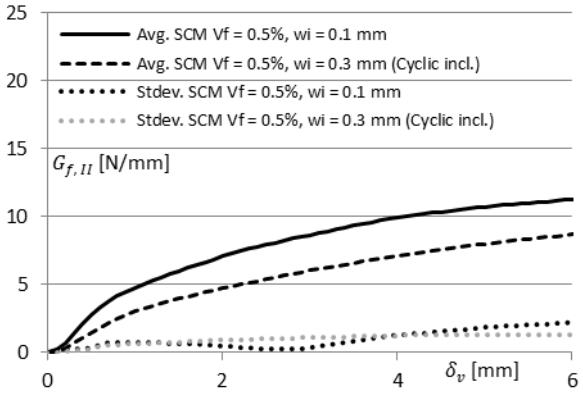

Fig. 5.16 – Fracture energy, $G_{f,II}$ [N/mm] vs. shear displacement, δ_v [mm] for SCM V_f = 0.50%

(- 8-10%) in peak shear strength is observed for SCC-450 compared to corresponding SCM. SCC-600 with w_i = 0.3 mm (Fibre count = 35) shows an increase (+31%) in peak shear strength compared to corresponding SCM (Fibre count = 24). For SCC-450 (V_f = 0.75%), a reduction (-14%) in peak shear strength is obtained for w_i = 0.1 mm (Fibre count = 41 vs. 38 for SCM) and an increase (+26%) for w_i= 0.3 mm (Fibre count = 58 vs. 34 for SCM). In the case of SCC-450 with V_f = 1.0%, an increase (+21-24%) in peak shear strength is observed for both initial crack widths (Fibre count = 82 vs 52 for SCM). Given this result, the peak shear strength decreases for a larger coarser aggregate fraction, but only for lower fibre dosage (V_f= 0.5-0.75%) and smaller initial crack width (w_i= 0.1 mm). For the larger coarse aggregate fraction (SCC-450 and SCC-600), larger fibre dosage (V_f = 0.75-1.00%) and initial crack width w_i= 0.3 mm, peak shear strength increases in the range 21 – 31%. See *Fig. 5.17*.

In terms of the post-peak response, SCC-450 and SCC-600 show greater residual capacity at a given crack width (See *Fig. 5.18*). Larger crack widths are observed for SCC-450 & 600 compared to SCM for a specified shear displacement (*Fig. 5.19*). This is true for V_f = 0.5% and w_i = 0.1 mm, but for w_i = 0.3 mm, only a marginal difference is seen between SCC-450 and SCC-600. This effect is marginal for higher fibre dosages (V_f = 0.75% and 1.00%), for both w_i = 0.1 mm and 0.3 mm.

For V_f = 0.5%, the effect of the coarse aggregate fraction on the fracture energy is marginal, with only SCC-600 (w_i= 0.3 mm) showing an increase in fracture energy compared to SCM. At V_f = 0.75%, the fracture energy increases for SCC-450 (for both w_i = 0.1 mm and 0.3 mm). See *Fig. 5.20*. Due to the scatter in the data, SCC-450 (w_i = 0.1 mm) could possibly show a marginal effect only. At V_f = 1.00%, the fracture energy increases for SCC-450 (for both w_i = 0.1 mm and 0.3 mm). Due to the scatter in the data, SCC-450 (w_i = 0.3 mm) could possibly show a marginal effect only. The complete data set is provided in *Appendix D.4*.

In conclusion, the differences observed between the composites: SCM, SCC-450 and SCC-600 are attributed to the differences in fibre count. If the fibre count were to be balanced out between the composites, it is hypothesised that the responses are similar; further work is needed to confirm this. As discussed in *Chapter 3*, the coarse aggregate content and size for SCC-450 and SCC-600 is relatively low compared to what is typically used and recommended in practice, even for SCC. A small contribution by shear interface roughness or aggregate interlock is therefore not too surprising. Achieving an adequate mortar and concrete workability for each fibre dosage, to facilitate the fibre mechanism, is of higher priority for this study.

Table 5.8 – Effect of aggregate fraction on composite response

V_f = 0.5%	SCC-450		SCC-600	
w_i	0.1 mm	0.3 mm	0.1 mm	0.3 mm
$F_v - \delta_v$	F_p -8%	F_p-10%	F_p-22%	F_p+31%
$w_c - \delta_v$	Slope increase for larger particle size & content	Slope increase for larger particle size & content	Slope increase for larger particle size & content	Slope increase for larger particle size & content; Marginal difference between 450 & 600
G_f	---	---	---	↑
V_f = 0.75%				
$F_v - \delta_v$	F_p-14%	F_p+26%		
$w_c - \delta_v$	Reduction in difference between SCM & 450; Marginal difference	Reduction in difference between SCM & 450; Marginal difference		
G_f	↑ or Marginal given standard deviation	↑		
V_f = 1.00%				
$F_v - \delta_v$	F_p+24%	F_p+21%		
$w_c - \delta_v$	Marginal	Marginal		
G_f	↑	↑ or Marginal given standard deviation		

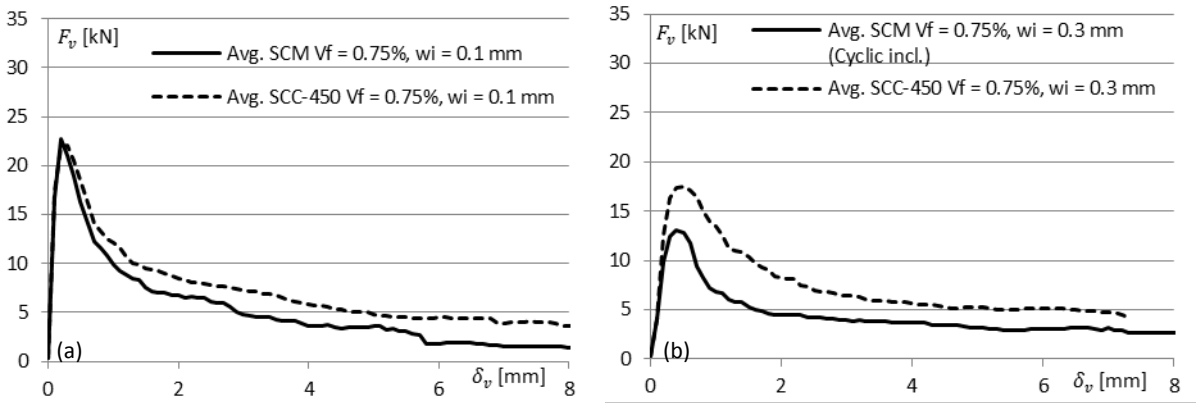

Fig. 5.17 – Shear load, F_v [kN] vs. shear displacement, δ_v [mm] for V_f = 0.75% (a) w_i = 0.1 mm (b) w_i = 0.3 mm

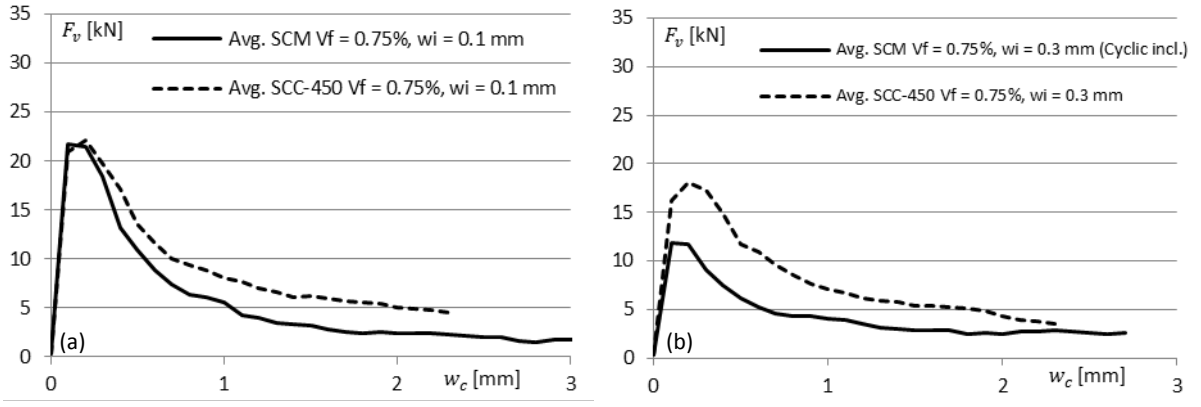

Fig. 5.18 – Shear load, F_v [kN] vs. crack width, w_c [mm] for V_f = 0.75% (a) w_i = 0.1 mm (b) w_i = 0.3 mm

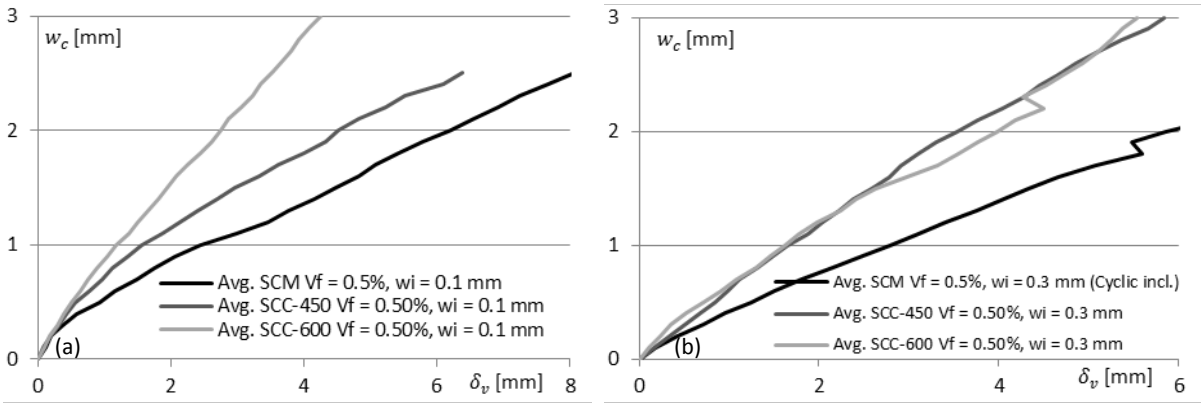

Fig. 5.19 – Crack width, w_c [mm] vs. shear displacement, δ_v [mm] for V_f = 0.50% (a) w_i = 0.1 mm (b) w_i = 0.3 mm

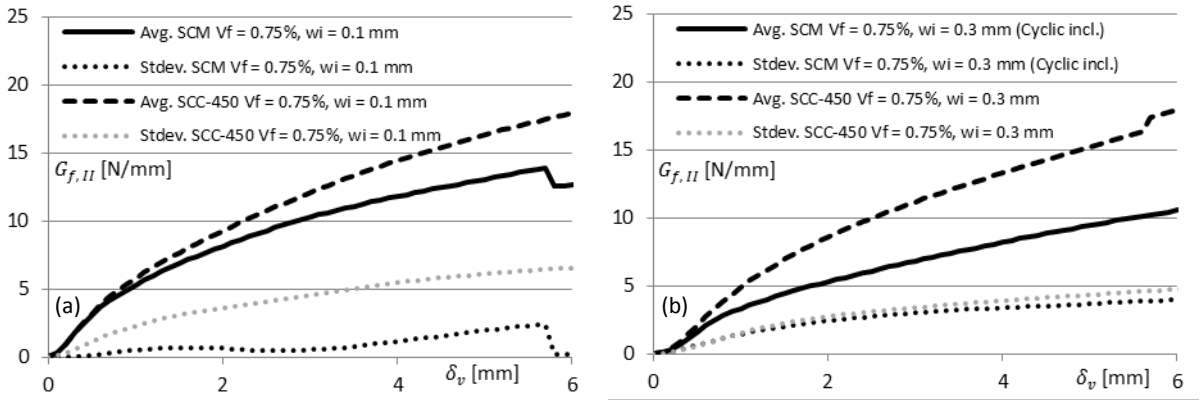

Fig. 5.20 – Fracture energy, G_f [N/mm] vs. shear displacement, δ_v [mm] for V_f = 0.75% (a) w_i = 0.1 mm (b) w_i = 0.3 mm

5.1.5 Analysis of fibre distribution via Computed Tomography (CT-scan)

Fibre count

The fibre count is determined by analysing (via X-ray CT-scanning as discussed in *Chapter 4*) the number of fibres intersecting plane S3 (see *Fig. 5.21*). *Table 5.9* provides the fibre count for plane S3. Only the SCC-450 composite is selected for scanning and only one specimen for each fibre dosage (V_f = 0.5%, 0.75% and 1.0%) is scanned. Note that scans are performed on specimens that have already been tested/fractured. Comparison of the CT-scan count and the manual count (for the specimen and sample average) shows similar values in most cases. *Appendix D.5.4* (*Table D.16-18*) provides the complete data set for the manual fibre count.

Table 5.9 – Fibre count for SCC-450 (CT-scan and manual count)

V_f		0.5%	0.75%	1.0%
Scan ID		*CT-11*	*CT-12*	*CT-9*
CT-scan count – S3		27	56	76
Manual count – S3 (specimen)		30	38	76
Manual count – S3 (average)		30	50	82
1D Aligned fibres (*Hannant, 1978*)	$N = \frac{V_f}{\pi r^2}$	59	88	118
2D Random (*Hannant, 1978*)	$N = \frac{2}{\pi}\frac{V_f}{\pi r^2}$	38	**56**	**75**
3D Random (*Hannant, 1978*)	$N = \frac{1}{2}\frac{V_f}{\pi r^2}$	**29**	44	59

r = 0.55 mm (RC-65/35-BN)

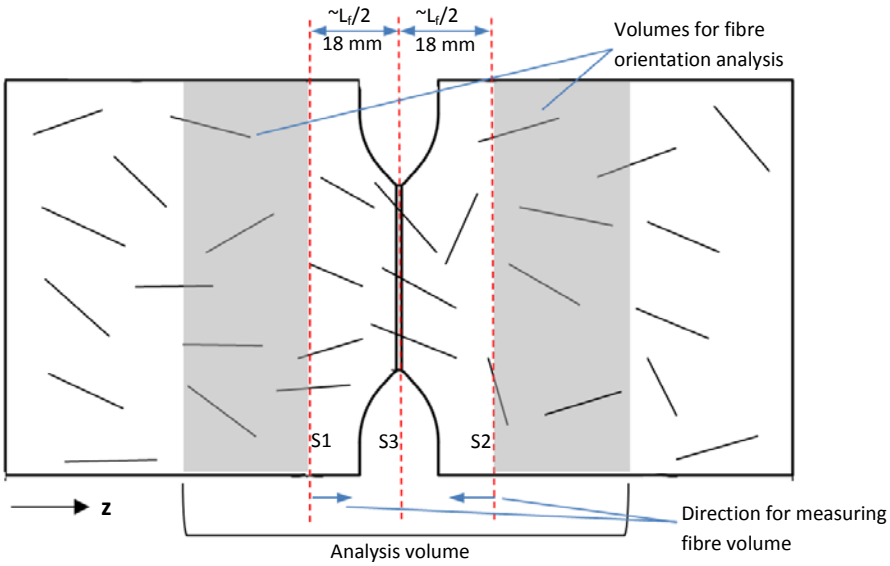

Fig. 5.21 – CT-scan analysis and data extraction method

According to the criteria proposed by *Hannant (1978)* in *Table 5.9*, the fibre count achieved for a fibre dosage of V_f = 0.5%, indicates a 3D-random fibre distribution. The fibre count for V_f = 0.75% and 1.0%, suggests a 2D-random fibre distribution. In the case of SCM, the fibre count is indicative of a 3D-random fibre distribution for each fibre dosage up to V_f = 1.0%. SCC-600 V_f = 0.5% is also 3D-random.

Fibre orientation

The fibre orientation distribution (0 - 90°) relative to the longitudinal z-axis is calculated for two section volumes on either side of the shear plane (see *Fig. 5.21*). Because CT-scans are performed on tested specimens, fibres are deformed within the vicinity of the crack and should not form part of the orientation analysis. Six orientation intervals are used to plot the distribution in *Fig. 5.22*, these are 0-15°, 15-30°, 30-45°, 45-60°, 60-75° and 75-90°. A lower percentage of fibres have extreme orientations (0-15° and 75-90°), with a more or less uniform distribution of fibres in the range 15-75°. Note that this is a small sample size and may not be entirely representative of the actual fibre orientation distribution. *Figs. 5.23-25* show a contour image of the fibre orientation or deviation angle for each fibre dosage.

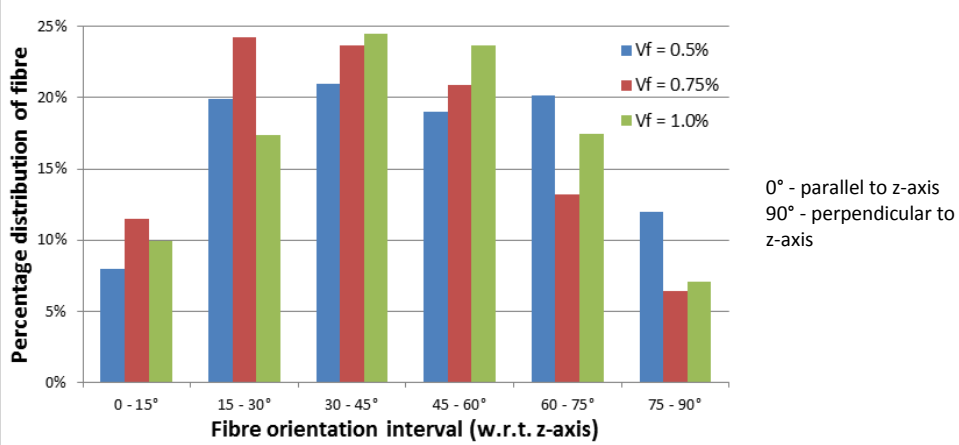

Fig. 5.22 – Fibre orientation distribution (SCC-450, V_f = 0.5%, 0.75% and 1.0%)

Fibre embedded length

The average embedded length of fibres intersecting planes S1 and S2 is determined by calculating the combined volume of these intersecting fibres measured from the plane towards the centre of the specimen S3 (*Table 5.10*). The average volume of fibres for plane S1 and S2 is then divided by the cross-sectional area (πr^2) of the fibre, giving the total embedded length of fibre. The difference between the actual fibre length and the projected fibre length (ignoring hooked-end geometry) is minimal (*Table 5.10*) and either length can be used to determine the embedded length. The average embedded length is determined by dividing the total length by the average fibre count of plane S1 and S2, according to the CT-scan (*Table 5.10*). The average embedded length ranges from 16.4mm (~0.47L_f) to 26.4mm (~0.75L_f) for V_f=0.5% to 1.0% respectively. Once again, this is a small sample size and should be interpreted carefully. An average embedded length closer to 0.5L_f seems likely for the given composite and specimen geometry. It must be noted that in the case of a higher fibre volume (V_f ≥0.75%), the fibres intersecting planes S1 and S2 are more likely to make contact or touch other fibres in the volume. These non-intersecting fibres that touch the intersecting fibres are included in the fibre volume calculation and hence the average embedded length is overestimated, as may be the case for V_f=1.0%, even though an embedded length ratio of 0.25:0.75 is generally considered typical. Further post-processing of the CT-scan images is needed in order to validate this point.

Table 5.10 – Fibre embedded length (SCC-450)

		V_f = 0.5%	V_f = 0.75%	V_f = 1.0%
Fibre volume (S1)	[mm^3]	216	251	707
Fibre volume (S2)	[mm^3]	155	451	652
Fibre volume (Avg.)	[mm^3]	186	351	680
Fibre length (total)	[mm]	781	1477	2860
Fibre length (projected)	[mm]	774	1468	2846
Fibre count (S1)	[-]	50	83	112
Fibre count (S2)	[-]	45	63	105
Embedded length	[mm]	**16.4 (~0.47L_f)**	**20.2 (~0.58L_f)**	**26.4(~0.75L_f)**
Embedded length (**shorter side**)	[-]	**0.47L_f**	**0.42L_f**	**0.25L_f**

5.2 Experimental investigation at the Micro-scale

5.2.1 Experimental program, specimen design and production method

The Ohno-beam (*Arakawa & Ohno, 1957*) shear test method is adapted to investigate the transverse pull-out response of a single hooked-end steel fibre. Five fibre orientations are investigated as defined in *Fig. 5.26 (b)*. Two fibre embedded lengths (L_{fe}) are considered, $L_f/4$ and $L_f/2$ (L_f – fibre length). $L_f/4$ is selected here to be representative of the average embedded length and the data for this embedded length will be used in an empirical model in *Section 6.7*.

The specimen dimensions are 140 x 70 x 45 mm (*Fig. 5.26 (a)*). The same mould used for the single fibre axial tests in *Section 4.2* is used here again. Specimen casting consists of two stages. In the first stage the fibre is wedged between two wooden blocks at the chosen fibre orientation and embedded length and placed inside the wooden mould. The self-consolidating mortar (SCM) is then poured into the other half of the mould with the protruding fibre and allowed to harden at a room temperature and relative humidity of 24±2°C and 65±2% respectively. The specimen is de-moulded

24 hrs later with the position and orientation of the fibre fixed by the hardened mortar. To avoid bond between the two halves of the specimen, the shear plane surface of the specimen is covered with a thin layer of thick grease. Mortar is then poured into the second half of the mould and the specimen is once again allowed to harden over 24 hrs. Specimens are then water-cured for up to 28 days at 24±2°C. No fibre corrosion took place as was observed in *Section 4.2*. Both sides of the fibre are fully embedded in the surrounding mortar and due to the treatment of the shear plane with grease, there is no water penetration. On the day of testing the specimens are prepared for optical measurement as with the Meso-scale tests in *Section 5.1*.

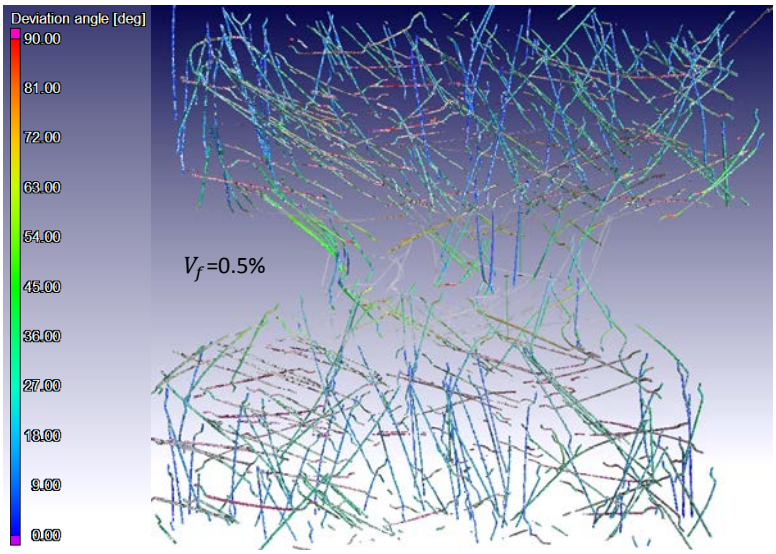

Fig. 5.23 – Contour image of fibre orientation (deviation angle from vertical z-axis), SCC-450, V_f = 0.5%

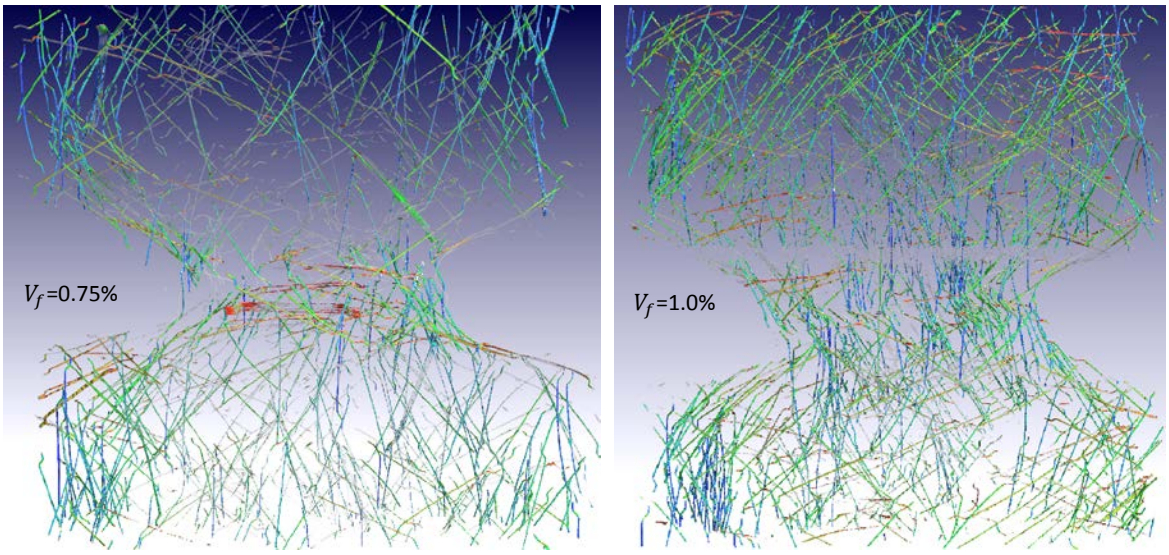

Fig. 5.24-25 – Contour image of fibre orientation (deviation angle from vertical z-axis), SCC-450, V_f = 0.75% & 1.0%

5.2.2 Test setup and procedure

The test configuration is illustrated in *Fig. 5.26 (a)*. The specimen is centred with respect to the shear plane, with an anti-symmetric inner load separation of 30 mm and outer support separation of 110 mm. The specimen is loaded through rollers that allow free rotation and translation.

All specimens are tested in the Zwick Z250 materials testing machine. In order to improve the resolution on the load data, a smaller 10 kN load cell is used. In addition to the optical measurement of displacement on the one side of the specimen, a LVDT with a nominal range of 10 mm is mounted on the other side at mid-height of the specimen, in order to correlate the normal displacement across the shear plane (see *Fig. 5.26 (c)*). The arrangement of the DIC cameras is identical to that of the Meso-scale tests. The test rate is controlled via the machine crosshead position with an initial rate of 0.15 mm/min until a crosshead displacement of 3 mm is reached. The test rate is then increased to 0.6 mm/min until fibre pull-out or rupture.

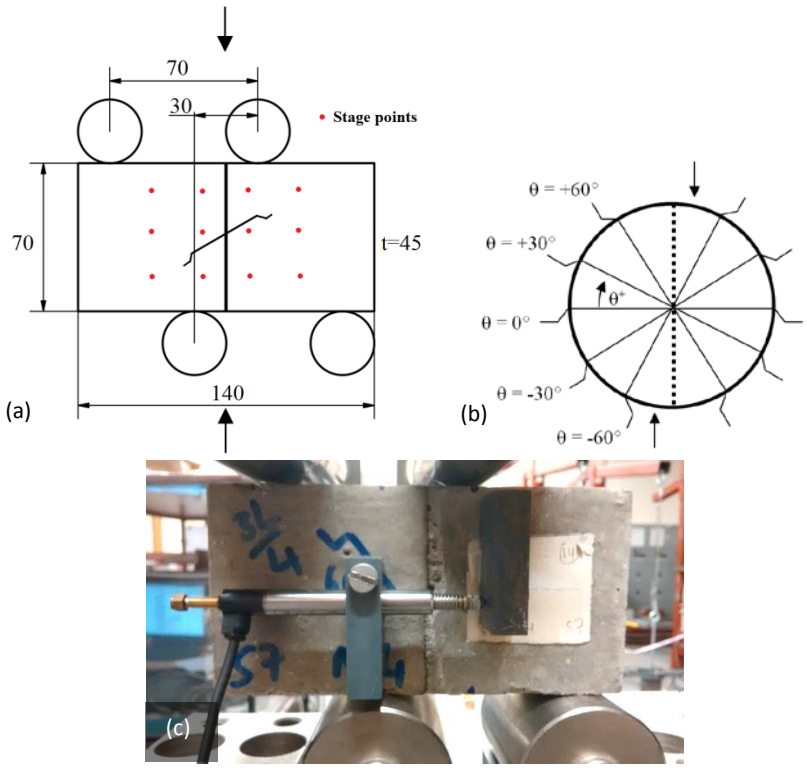

Fig. 5.26 – (a) Experimental configuration of Micro-scale (single fibre) test including stage point definition for DIC (*Zeranka & van Zijl, 2015*), (b) Definition of fibre orientation, θ with respect to loading configuration (*Zeranka & van Zijl, 2015*), (c) LVDT mounting to measure normal displacement across shear plane

5.2.3 Test results and discussion

Transverse pull-out load vs. transverse displacement

For each orientation angle, the shear or transverse pull-out load (F_{pt}) in Newton is plotted against the shear or transverse pull-out displacement (δ_{pt}) as determined by the optical measurement. The results for θ = +60°, +30°, 0°, -30° and -60° and embedded length of $L_f/4$ are illustrated in *Figs. 5.27-29 (a)* respectively, with a summary of the average response provided in *Fig. 5.29 (b)*. Two failure

modes are observed, either fibre pull-out or fibre rupture. In general the behaviour observed for the different fibre orientations is similar to tests conducted using the shear push-off (*Lee & Foster, 2006*) and shear push-through (*Soetens & Matthys, 2012*) methods as discussed in *Section 2.5*.

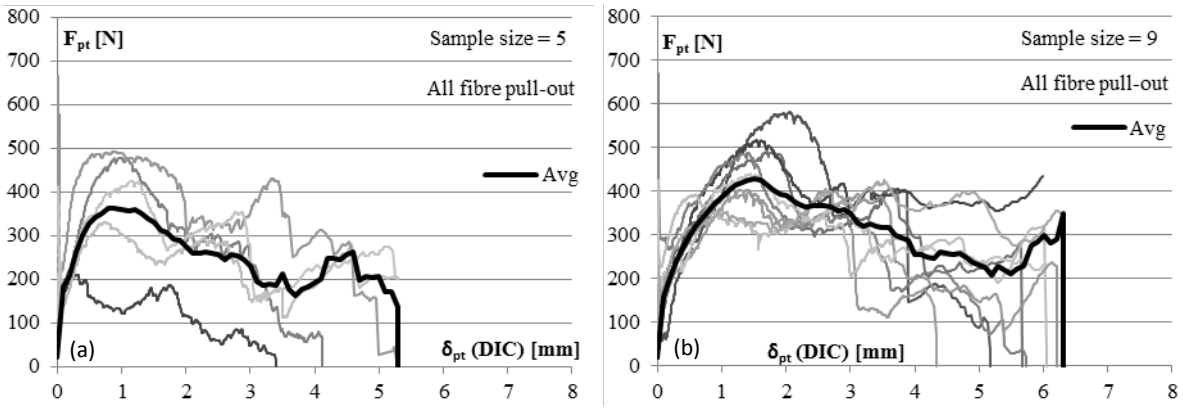

Fig. 5.27 – Transverse pull-out load (F_{pt}) vs. transverse pull-out displacement (δ_{pt}) for (a) θ = +60°, $L_{fe} = L_f/4$ and (b) θ = +30°, $L_{fe} = L_f/4$

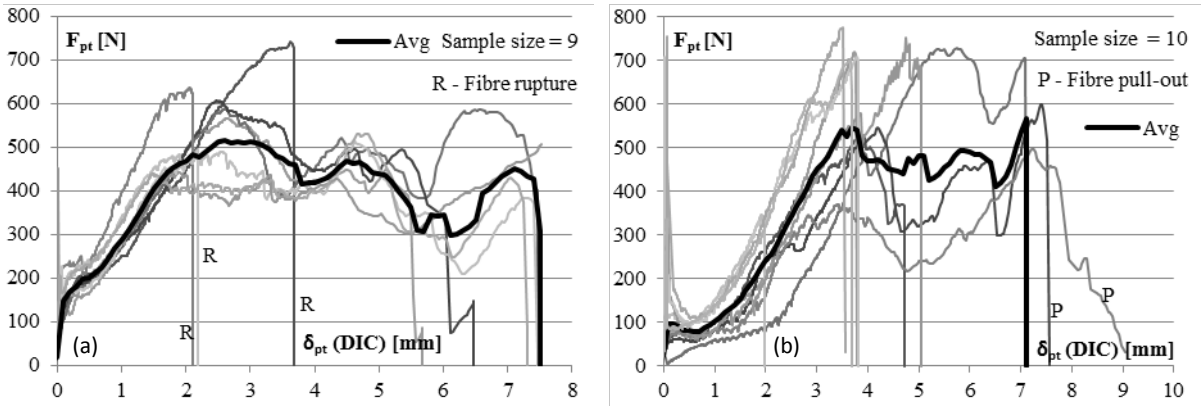

Fig. 5.28 – Transverse pull-out load (F_{pt}) vs. transverse pull-out displacement (δ_{pt}) for (a) θ = 0°, $L_{fe} = L_f/4$ and (b) θ = -30°, $L_{fe} = L_f/4$

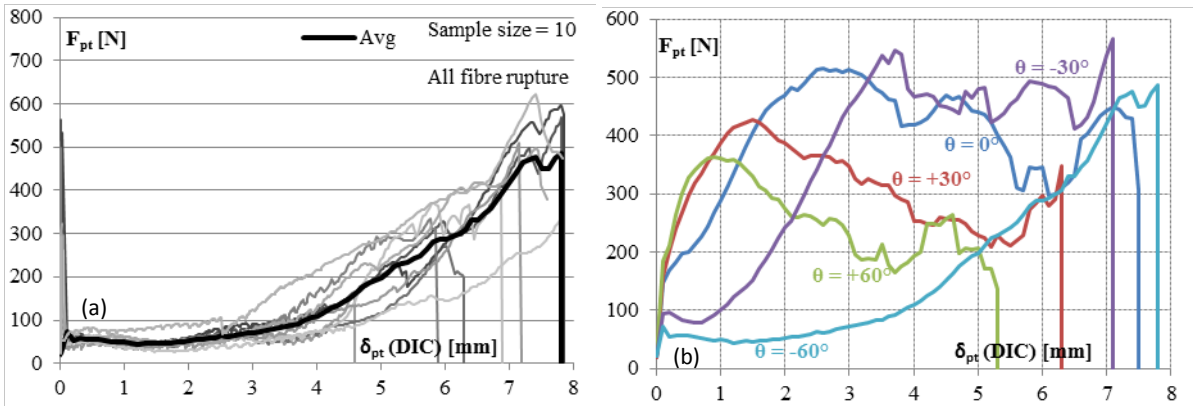

Fig. 5.29 – Transverse pull-out load (F_{pt}) vs. transverse pull-out displacement (δ_{pt}) for (a) θ = -60°, $L_{fe} = L_f/4$ and (b) average response for θ = -60° to +60°, $L_{fe} = L_f/4$

Positive fibre orientations (θ = +30° and +60°) exhibit pull-out failure exclusively as illustrated in *Fig. 5.27*. For negative fibre orientations (θ = -30° and -60°), substantial transverse displacement occurs before the fibre is fully engaged (see *Fig. 5.28 (b)* and *5.29 (a)*). This is attributed to the snubbing effect as also observed by *Lee & Foster (2006)* and *Soetens & Matthys (2012)*. Fibre rupture in conjunction with snubbing or pull-out is the predominant mode of failure in this case. A fibre orientation in the region of θ = 0° (*Fig. 5.28 (a)*), represents a transition zone between fibre pull-out and fibre rupture and both failure modes are likely to occur. Three of the nine specimens tested, failed by fibre rupture and the rest by fibre pull-out.

As explained in more detail by *Lee & Foster (2006)*, the difference in the behaviour between the positive (> +30°) and negative (< -30°) fibre orientations is attributed to the different bending deformations that the fibre undergoes. In the case of negative fibre orientations, the bending stresses in the fibre predominates the overall behaviour, whereas for positive orientations, the pull-out mechanism governs the behaviour. The test results for an embedded length of $L_f/2$ are provided in *Appendix D.7.1*. A comparison of the two embedded lengths ($L_f/4$ and $L_f/2$) follows at the end of this section.

Transverse pull-out load vs. normal displacement

The transverse pull-out load (F_{pt}) vs. normal pull-out displacement (n_{pt}) response is given in *Figs. 5.30-32*. As the fibre orientation changes from positive to negative and the resistive mechanism changes from fibre bond and mechanical anchorage to fibre bending and dowel action, the corresponding normal displacement is reduced. In the case of θ= -60°, an initial increase in normal displacement is followed by a reduction of normal displacement (open-close effect). This reduction of normal displacement is accompanied with an increase in transverse pull-out load. This is attributed to the snubbing effect, where on both sides of the shear plane, the fibre is bent beyond the normal or horizontal alignment with the shear plane, which causes the opening between the two shear planes to close again.

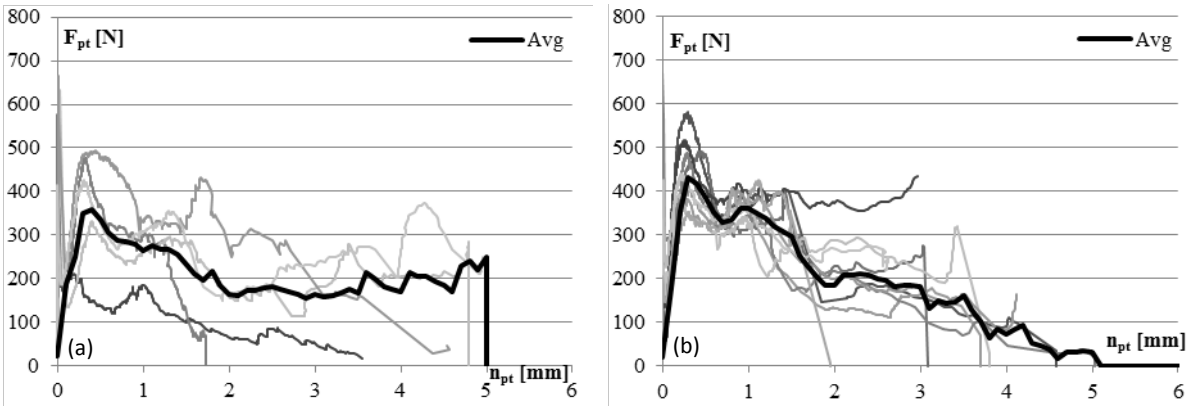

Fig. 5.30 – Transverse pull-out load (F_{pt}) vs. normal pull-out displacement (n_{pt}) for (a) θ = +60°, L_{fe} = $L_f/4$ and (b) θ = +30°, L_{fe} = $L_f/4$

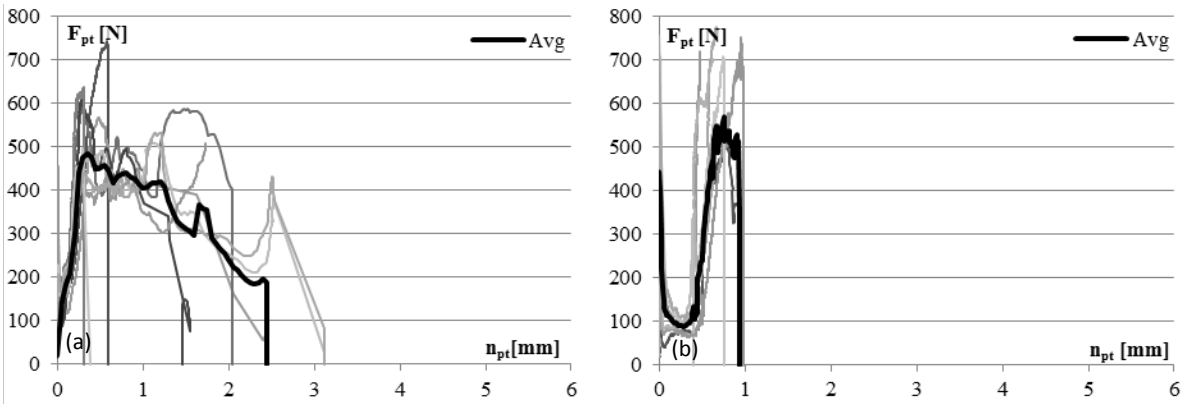

Fig. 5.31 – Transverse pull-out load (F_{pt}) vs. normal pull-out displacement (n_{pt}) for (a) θ = 0°, L_{fe} = $L_f/4$ and (b) θ = -30°, L_{fe} = $L_f/4$

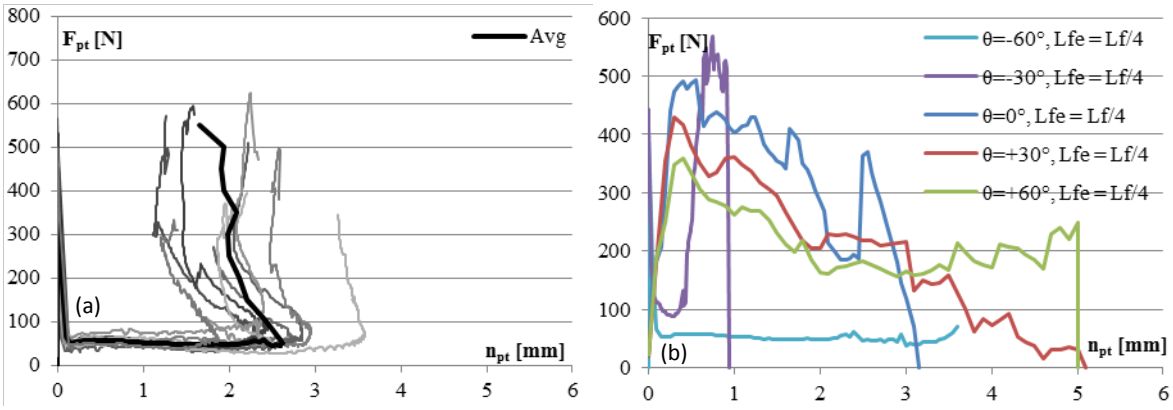

Fig. 5.32 – Transverse pull-out load (F_{pt}) vs. normal pull-out displacement (n_{pt}) for (a) θ = -60°, L_{fe} = $L_f/4$ and (b) average response for θ = -60° to +60°, L_{fe} = $L_f/4$

Effect of embedded length ($L_f/4$ and $L_f/2$):

Figs. 5.33-35 compare the transverse pull-out response of the embedded lengths $L_f/4$ and $L_f/2$, for each fibre orientation. If the variability of the data is taken into account, only marginal differences are observed between the two embedded lengths. Where fibre pull-out is dominant (θ = +30° and +60°), end anchorage is believed to be the primary resistive mechanism (as found in axial pull-out tests performed in *Chapter 4*), because peak pull-out resistances are similar for $L_f/4$ and $L_f/2$. However, a longer embedded length does result in more ductility due to the longer fibre channel and frictional pull-out resistance still present. Where fibre bending and eventual fibre rupture is present (θ = -30° and -60°), embedded length is believed to be negligible, because the failure mechanism is localised dowel action, fibre yielding and rupture in the vicinity of the shear plane and not fibre pull-out.

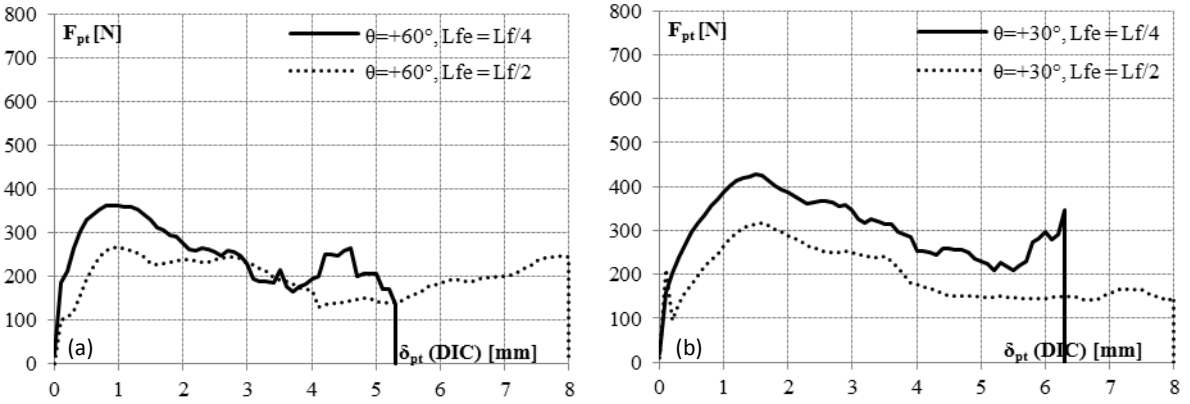

Fig. 5.33 – Transverse pull-out load (F_{pt}) vs. transverse pull-out displacement (δ_{pt}) for (a) θ = +60°, L_{fe} = $L_f/4$ and $L_f/2$ (b) θ = +30°, L_{fe} = $L_f/4$ and $L_f/2$

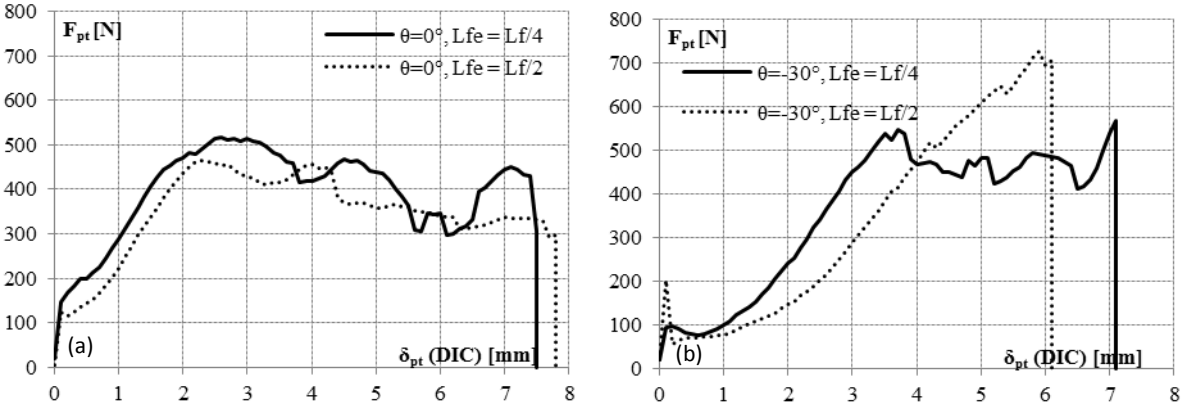

Fig. 5.34 – Transverse pull-out load (F_{pt}) vs. transverse pull-out displacement (δ_{pt}) for (a) θ = 0°, L_{fe} = $L_f/4$ and $L_f/2$ (b) θ = -30°, L_{fe} = $L_f/4$ and $L_f/2$

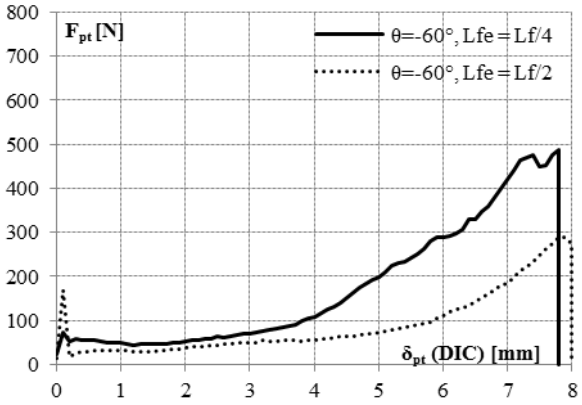

Fig. 5.35 – Transverse pull-out load (F_{pt}) vs. transverse pull-out displacement (δ_{pt}) for θ = -60°, L_{fe} = $L_f/4$ and $L_f/2$

Summary and conclusions

At the Meso-scale:

(1) Specimen design:

(1.1) It can be argued that the refinement of the specimen notch geometry via numerical analysis in the elastic domain is not necessary, considering the introduction of a saw cut notch on both sides of the shear plane after the fact. The saw cut notch likely invalidates the analysis results. As long as the same shear plane height (h_0) is used, a simplified notch geometry e.g. triangular or saw-cut, could be used. Experimental trials on different notch geometries are recommended. Future studies should also consider the effect a cast-in-notch has on the casting procedure and consequently the fibre dispersion and orientation.

(1.2) Preliminary tests showed that specimens did not reliably fail in the shear plane. Compression splitting failure at the points of load application induced diagonal cracking between the two inner supports. This failure mode should not be overlooked in future studies. The introduction of the above-mentioned saw-cut notch and pre-cracking in the shear plane is however sufficient to localise shear failure to the shear plane.

(1.3) Analysis of the specimen fibre count suggests a 2D-random fibre distribution for SCC-450 V_f = 0.75% and 1.0%. All other composites have a 3D-random distribution. The specimen dimensions, especially the specimen depth and shear plane size need to be increased for increased aggregate content and size, as well as for a fibre dosage V_f > 0.75%.

(2) Experimental program and production method:

(2.1) The specimens tested in this study are all pre-cracked prior to shear testing. Un-notched and uncracked specimen did not fail in pure shear. Shear testing of uncracked specimens will therefore require modifications to the specimen geometry.

(2.2) Emphasis is placed on the fibre component and mechanism. The composites developed in this study including SCM, SCC-450 and SCC-600, all have relatively low coarse aggregate contents. Future studies should incorporate larger coarse aggregate contents and sizes to investigate the potential synergy between fibre reinforcement and shear interface roughness.

(3) Test setup and procedure:

(3.1) The cyclic tensile loading and pre-cracking phases are successful in producing the target unloaded crack widths and this method is recommended.

(3.2) The non-contact measurement method (Aramis DIC) proved invaluable in determining the specimen shear displacement and rotation. Careful consideration should be given to the instrumentation used in the test when designing the specimen and test configuration. It must be noted that a significant amount of post-processing is required to extract the desired data when using this method.

(4) Analysis of fibre distribution via CT-scanning:

(4.1) The CT-scanning facility provides valuable insight into the fibre distribution and the ability to analyse and quantify the fibre orientation distribution is a powerful tool.

(4.2) A larger sample size is recommended in future studies to better characterise the fibre distribution.

At the Micro-scale:

(5) Experimental program, specimen design and production method

(5.1) The results from this study match well with work done by other researchers (*Lee & Foster (2006)* & *Soetens & Matthys (2012)*), using different test methods.

(5.2) Additional fibre orientations (e.g. θ = ±15°, ±45° and ±75°) and embedment lengths (e.g. $L_f/6$ and $L_f/8$) should be investigated to characterise the transverse pull-out response even further.

(5.3) The nature of the test configuration can be restrictive due to excessive rotation of the specimen at large shear displacements, specifically for a larger fibre embedded length. It may therefore not be possible to test the complete pull-out or fibre rupture response. In some cases for the embedded length $L_f/2$, undue specimen rotation would occur, which would influence the result at large displacements. This needs to be mitigated by restricting the fibre length, modifying the test or using an alternative method where specimen rotation is less, such as the shear push-off (*Lee & Foster, 2006*) or push-through (*Soetens & Matthys, 2012*) methods.

Chapter 6
Constitutive model and numerical verification

Abaqus is a finite element program which provides an interface (UMAT) for connecting a user-defined constitutive model to its source code. The objective of this chapter is to develop a user-defined constitutive model that incorporates the Meso-scale data obtained in *Chapters 4* and *5*. The constitutive model is verified by modelling the Meso-scale Iosipescu shear test.

The modelling concept and analytical formulation of the constitutive model is discussed first, and is followed by the outline of the numerical procedure as programmed in FORTRAN. It is essential that the material model is first verified for a single finite element, testing model performance for different boundary conditions and ensuring that the material model is objective with respect to element size i.e. mesh objectivity. The model is calibrated with the experimental data in *Chapters 4* and *5* and the material parameter values are determined for each composite. Finally, the Meso-scale Iosipescu shear test is modelled in Abaqus and the constitutive model is verified with respect to the calibrated models and experimental data. In the final section of this chapter an empirical link/model is developed between the Micro and Meso-scale data for the Iosipescu shear test.

6.1 Modelling concept

In the smeared crack concept, a cracked solid remains a continuum and the effect of the crack(s) is distributed or "smeared" over the entire element area. This concept was originally proposed by *Rashid (1968)*. Isotropy is assumed prior to cracking with orthotropic behaviour after crack formation. The total strain ε is decomposed into two components, the strain in the uncracked material ε_c and the strain in the crack ε_{cr} (*Eq. 6.1*). The uncracked material and the crack are assumed to work in series (*Fig. 6.1*).

$$\{\varepsilon\} = \{\varepsilon_c\} + \{\varepsilon_{cr}\} \tag{6.1}$$

The membrane element in *Fig. 6.2* is subject to general in-plane stresses. In the uncracked stage (*Fig. 6.2a*) the axes of the local coordinate system (I-II) are coincident with the principal stress directions, oriented with an angle φ with respect to the global coordinate system xy. As soon as the maximum principal tensile stress exceeds the concrete tensile strength, crack formation occurs perpendicular to the principal tensile stress direction. At this point the crack orientation is assumed to be fixed according to the smeared-fixed crack concept. The axes of orthotropy (local coordinate system 1-2) are normal and parallel to the crack surface (*Fig. 6.2b*).

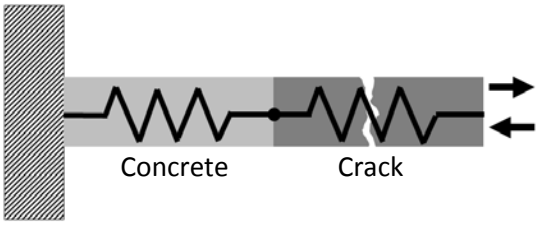

Fig. 6.1 – Uncracked concrete and crack working in series (*Bernardi et al., 2012*)

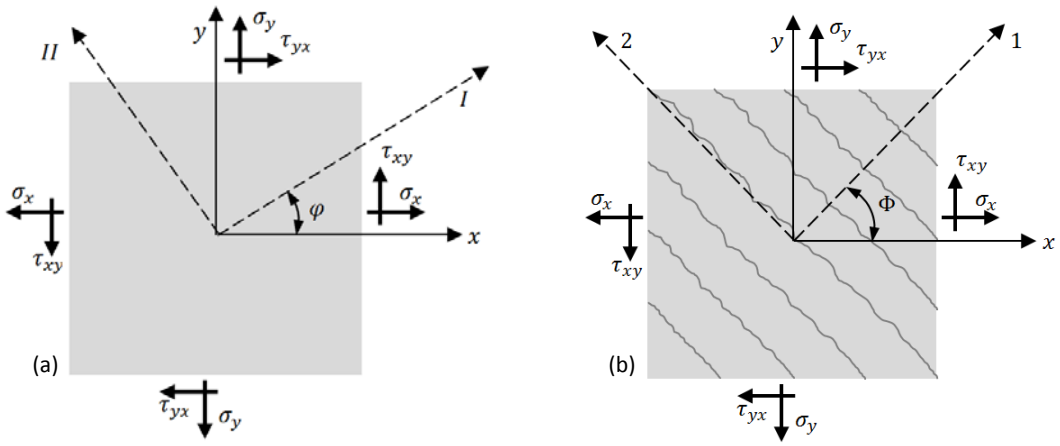

Fig. 6.2 – Plane stress element (a) Uncracked, (b) Cracked

Crack evolution and the formation of secondary cracks can be treated in different ways:

- Fixed crack: The crack retains the original orientation upon initial cracking throughout the entire loading sequence.
- Rotating crack: The crack rotates with the principal strain direction
- Rotate-fixed crack: The crack is allowed to rotate up to a specified point, at which stage it is fixed for the remainder of the analysis.
- Fixed multi-directional: The initial crack direction is fixed, however a secondary crack can form at the same integration point, provided certain criteria are met. The criteria typically include a threshold angle between the first and second crack, as well as the fracture criteria for the second crack to occur.

In this study, the fixed crack concept will be implemented in the model, as this reflects the behaviour of the predefined crack in the Iosipescu shear test

6.2 Analytical formulation of material model

Prior to cracking, the material is assumed to be isotropic linear elastic. The only parameters for this state are the Young's modulus (E) and Poisson's ratio (v). At crack initiation, when the positive principal tensile stress is equal to or exceeds the tensile strength of the material at an integration point, the formulation changes from isotropic to orthotropic in the local crack coordinate system (1-2), which remains fixed for the duration of the analysis.

According to *Eq. 6.1*, the strain increment is decomposed into its uncracked and crack portions. The uncracked material is assumed to remain isotropic linear elastic. The crack traction increment Δt^{cr} is related to the crack strain increment $\Delta\varepsilon_{12}^{cr}$ via the crack tangent stiffness matrix D^{cr}. *Eq. 6.2* is derived in *Subsection 6.3.4* to follow.

$$\Delta t^{cr} = D^{cr}\Delta\varepsilon_{12}^{cr} \tag{6.2}$$

The crack tangent stiffness matrix is assumed to take the form:

$$D^{cr} = \begin{bmatrix} D^{I} & 0 \\ 0 & D^{II} \end{bmatrix}, \tag{6.3}$$

where D^{I} and D^{II} are the Mode I and II stiffness moduli respectively.

The assumption of zero off-diagonal terms in *Eq. 6.3* implies that direct shear-normal coupling is ignored. This effect can be obtained indirectly, by relating the shear modulus D^{II} to the crack normal strain. The implication of this simplification will be discussed in the analysis output and chapter conclusions.

6.2.1 Mode I parameters

Strength parameters and fracture initiation

A simple Rankine-type tension-cut off condition (*Fig. 6.3a*) is assumed in the principal stress space. Only one strength parameter, namely the uniaxial tensile strength f_{ct} is therefore needed to represent this model. This assumption requires the following to be true (*Rots, 1989*): tensile cracking is not accompanied by significant lateral compression (justified according to *Kupfer et al. (1969)*). With regard to crack initiation, the crack is assumed to be orientated perpendicular to the direction of the major principal tensile stress only in the absence of significant lateral compression.

Fracture propagation

Several Mode I fracture softening functions have been proposed in the literature e.g. *Hillerborg et al. (1976)* and *Bazant & Oh (1983)* (as well as *Fig. 6.3b*). The parameters, which are assumed to be fixed material properties, include the fracture energy, G_{ft}, which is the amount of energy required to create one unit of area of a Mode I crack and the shape of the softening diagram e.g. linear, multi-linear, exponential or some other nonlinear function. An exponential function, such as the one illustrated in *Fig. 6.3b (iii)* is used. For smeared cracks, the facture is assumed to be distributed over a crack band width h (*Bazant & Oh, 1983*). The crack band width is related to the specific FE configuration. It is assumed that the energy is released over this width in order to obtain results that are objective with regard to mesh refinement. A uniform strain distribution is assumed over the crack band. The local Mode I crack traction-strain ($t_1^{cr} - \varepsilon_1^{cr}$) relation has the form given by *Eq. 6.4*. The fracture energy G_{ft}/h corresponds to the area under the softening curve for a discrete crack. This can be verified by the definite integral (*Eq. 6.5*).

$$t_1^{cr} = f_{ct}e^{-\frac{f_{ct}h}{G_{ft}}\varepsilon_1^{cr}} \tag{6.4}$$

$$\int_0^{\infty} f_{ct}e^{-\frac{f_{ct}h}{G_{ft}}\varepsilon_1^{cr}} = f_{ct}\cdot\frac{G_{ft}}{f_{ct}h} = \frac{G_{ft}}{h} \tag{6.5}$$

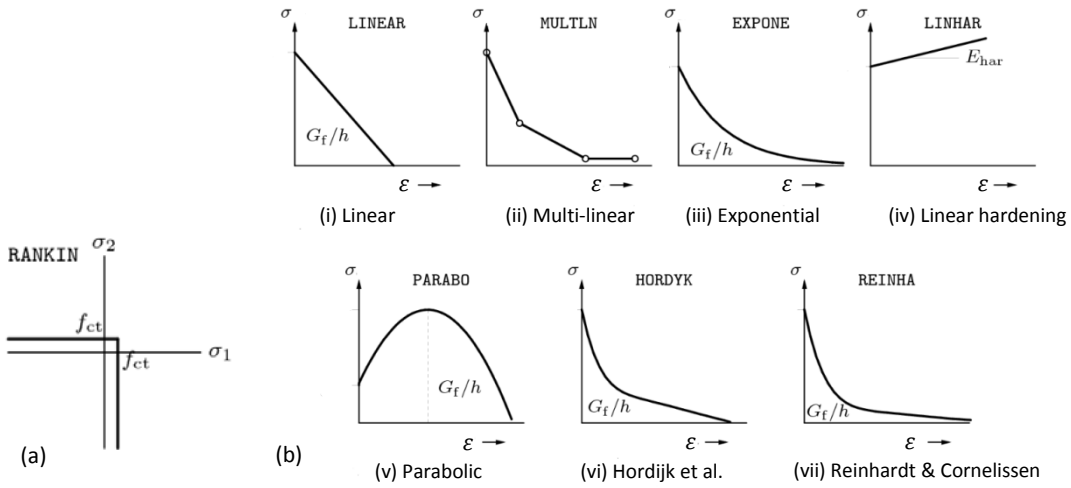

Fig. 6.3 – (a) Rankine-type tension cut-off model; (b) Mode I fracture softening functions (i-vii) (*Diana FEA Manual 2017*)

Crack (tangent) stiffness modulus

The crack tangent stiffness is the derivate of the softening function and is therefore also expressed in terms of the strength and energy parameters, as well as the shape of the softening diagram (*Eq. 6.6*).

$$D^I = \frac{d}{d\varepsilon_1^{cr}}(t_1^{cr}) = \frac{-{f_{ct}}^2 h}{G_{ft}} e^{-\frac{f_{ct}h}{G_{ft}}\varepsilon_1^{cr}} \tag{6.6}$$

Below is an implementation of the material model using random material properties (*Fig. 6.4*):

$$f_{ct} = 3; h = 20;\ G_{ft} = 50$$

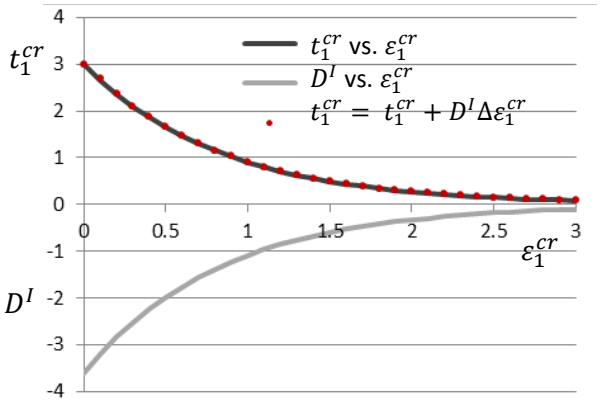

Fig. 6.4 – Mode I model implementation

Unloading and reloading

Linear unloading and reloading is assumed for the Mode I response. Two unloading/reloading stiffnesses (D_u^I) are defined, each linked to a maximum loading state and unloaded state observed experimentally (*Chapter 5 – Cyclic tension and pre-crack data*). The average maximum and unloaded crack width corresponding to a target unloaded crack width of 0.1 mm and 0.3 mm is shown in *Table 6.1*.

Table 6.1 – Average maximum and unloaded crack widths (mm)

Target unloaded crack width	**0.1**	**0.3**
Avg. maximum crack width	0.169	0.458
Avg. unloaded crack width	0.105	0.315

The unloading/reloading stiffness is calculated from the Mode I limit function as follows (*Eq. 6.7-8*). Note that the maximum and unloaded cracks widths are determined from the Iosipescu specimen loaded in tension. An assumption is therefore made that these values are transferable to the uniaxial tensile specimen, data of which is used to calibrate the Mode I limit function. To generalise an unload/reload Mode I stiffness, more characterisation unloading-reloading data should be generated, in order to accurately reflect the reduced reloading stiffness upon increased crack width. In the absence of characterising data, no attempt to generalisation is made here.

Unload/Reload stiffness Mode I ($w \leq 0.3mm$):

$$D_u^I = \frac{h f_{ct} e^{\frac{-f_{ct} \cdot 0.169}{G_{ft}}}}{0.169 - 0.1045} \tag{6.7}$$

Unload/Reload stiffness Mode I ($w > 0.3mm$):

$$D_u^I = \frac{h f_{ct} e^{\frac{-f_{ct} \cdot 0.458}{G_{ft}}}}{0.458 - 0.3148} \tag{6.8}$$

The Mode I traction is the lesser of the limit function value at the end of the increment and the summation of the Mode I traction at the start of the increment and the linear unloading or reloading value.

6.2.2 Mode II parameters

The Mode II response has a limit function of the same type as for Mode I, namely

$$t_{12}^{cr} = f_{cs} e^{-\frac{f_{cs} h}{G_{fs}} \gamma_{12}^{cr}} \tag{6.9}$$

The shear stiffness for initial Mode II loading as well as unloading and reloading is a function of the normal strain in the crack (*Eq. 6.10*). The crack width therefore determines the initial shear stiffness and hence the peak shear stress reached. Loading along the limit function is a function of shear strain only (*Eq. 6.9*). Stated differently, the crack shear stress is a function of the crack normal and shear strain during loading and unloading. Once the Mode II limit function is reached, the shear stress and tangent stiffness is only a function of the crack shear strain.

$$D^{II} = \max\left(\left[1 - \frac{\varepsilon_1^{cr} h}{w_m}\right] G \cdot f_i, G_{min}\right) \cdot h \tag{6.10}$$

where

t_{12}^{cr} = crack shear traction
γ_{12}^{cr} = crack shear strain
f_{cs} = peak shear stress on limit function (where $\varepsilon_1^{cr} = 0, \gamma_{12}^{cr} = 0$)
G_{fs} = shear fracture energy
w_m = calibrated model parameter
G = elastic shear modulus

f_i = calibrated model parameter
G_{min} = minimum shear modulus

6.2.3 Normal stress parallel to crack

The normal stress parallel to the crack is computed from the global cracked stiffness matrix and strain increment, and transformed to the local crack coordinate system. In the Meso-scale model, the corresponding stiffness (D^{c2}) is reduced (*Eq. 6.11*), similar to D^{II}. This stress component is not directly accounted for by the other material models and is not supported by experimental data from this study. The objective is therefore to minimise this stress component and hence limit its impact on the stress distribution across the shear interface.

$$D^{c2} = \max\left(\left[1 - \frac{\varepsilon_1^{cr} h}{w_m}\right]\frac{E}{1-\nu^2} \cdot 0.05, c_{min}\right) \tag{6.11}$$

where

Constant = 0.05 is a model parameter
c_{min} = minimum stiffness (model parameter)

6.3 Numerical procedure

6.3.1 Overview of the procedure: Input and Output

User subroutine UMAT is called for each integration point at each iteration of every increment. It is provided with the material state at the start of the increment (stress, solution-dependent state variables, temperature, and any predefined field variables) and with the increments in temperature, predefined state variables, strain, and time.

Input

In more detail, Abaqus supplies the following information to the UMAT at the beginning of each increment:

- An array $\{\varepsilon\}_{xy}^{a}$ denoted *STRAN (Abaqus)*, containing the total global strains at the beginning of the increment, where the superscript a denotes the start of an increment and the subscript xy denotes the global coordinate system.
- Abaqus also supplies an array of strain increments $\{\Delta\varepsilon\}_{xy}^{a}$ denoted *DSTRAN (Abaqus)*.
- An array $\{\sigma\}_{xy}^{a}$ or *STRESS (Abaqus)* passed in as the stress tensor at the beginning of the increment and which must be updated in the UMAT routine to be the stress tensor at the end of the increment.
- An array *STATEV (Abaqus)* containing the solution-dependent state variables; these are passed in as the values at the beginning of the increment. In all cases *STATEV* must be returned as the values at the end of the increment.
- A user-specified array *PROPS (Abaqus)* of material constants associated with this user material. The material constants are input via the Abaqus user interface.

Output

- In addition to updating the stresses and the solution-dependent state variables to their values at the end of the increment, subroutine UMAT must also provide the material

tangent stiffness $[D]_{xy}^{tangent}$ or *DDSDDE* (*Abaqus*) matrix. $[D]_{xy}^{tangent}$ is the tangent stiffness matrix of the constitutive model, $\partial\Delta\sigma/\partial\Delta\varepsilon$, where $\Delta\sigma$ are the stress increments and $\Delta\varepsilon$ are the strain increments. *DDSDDE*(I,J) defines the change in the I_{th} stress component at the end of the time increment caused by an infinitesimal perturbation of the J_{th} component of the strain increment array.

Fig.6.5 illustrates the above input and output:

Input passed to UMAT from ABAQUS at the beginning of the increment T_a

$$\{\varepsilon\}_{xy}^{a} = \begin{bmatrix} \varepsilon_x^a \\ \varepsilon_y^a \\ \gamma_{xy}^a \end{bmatrix};\ \{\Delta\varepsilon\}_{xy}^{a} = \begin{bmatrix} \Delta\varepsilon_x^a \\ \Delta\varepsilon_y^a \\ \Delta\gamma_{xy}^a \end{bmatrix};\ \{\sigma\}_{xy}^{a} = \begin{bmatrix} \sigma_x^a \\ \sigma_y^a \\ \tau_{xy}^a \end{bmatrix};\ \{STATEV\}^{a} = \begin{bmatrix} s_1^a \\ s_2^a \\ \vdots \\ s_n^a \end{bmatrix};\ \{PROPS\} = \begin{bmatrix} p_1 \\ p_2 \\ \vdots \\ p_n \end{bmatrix}$$

STRAN *DSTRAN* *STRESS* *STATEV* *PROPS*

↓

Output passed to ABAQUS from UMAT at the end of the increment T_b

$$\{\sigma\}_{xy}^{b} = \begin{bmatrix} \sigma_x^b \\ \sigma_y^b \\ \tau_{xy}^b \end{bmatrix};\ \{STATEV\}^{b} = \begin{bmatrix} s_1^b \\ s_2^b \\ \vdots \\ s_n^b \end{bmatrix};\ [D]_{xy}^{tangent}$$

STRESS *STATEV* *DDSDDE*

Fig. 6.5 – Numerical procedure: Input to and output from UMAT

6.3.2 Determining and storing the material state: uncracked or cracked

The positive principal tensile strain governs the material state. The first task is therefore to compute the principal strain values from the given total global strain. Abaqus passes an array containing the total strains at the beginning of the increment (*STRAN)* and an array of strain increments (*DSTRAN*) to the user material. The total global strain at the end of the increment is therefore the summation of *STRAN* and *DSTRAN (Eq.6.12)*.

$$STRAN^{i} = STRAN^{i-1} + DSTRAN^{i} \tag{6.12}$$

With the updated global strains, the principal strains can be computed as follows

$$\varepsilon_{max}, \varepsilon_{min} = \frac{\varepsilon_{xx}+\varepsilon_{yy}}{2} \pm \sqrt{\left(\frac{\varepsilon_{xx}-\varepsilon_{yy}}{2}\right)^2 + \left(\frac{\gamma_{xy}}{2}\right)^2} \tag{6.13}$$

The cracking criterion is defined via the cracking strain, which is computed as

$$\varepsilon_{cr} = {}^{f_{ct}}/_{E} \tag{6.14}$$

If the positive principal tensile strain is less than the specified cracking strain, linear elastic isotropy is assumed. However, if this is not the case, the material is considered to be cracked or damaged and nonlinear orthotropic behaviour is assumed. Because this material model considers strain reversals accompanied with unloading, it is important to establish a state variable which remembers the cracked state of the material. The treatment of the elastic domain, crack domain and unloading (and reloading) will be discussed in more detail next.

6.3.3 Elastic domain (Linear elastic isotropy)

Provided the positive principal tensile strain does not equal or exceed the prescribed strain at which cracking initiates and the state variable which tracks the status of the material, does not equate to a "cracked" status, the material will be treated as a linear elastic isotropic material.

This is simple to implement numerically. The first step is to assemble the elastic stiffness matrix or *DDSDDE* (*Eq.6.15*) as defined by the Abaqus UMAT interface. The tangent stiffness matrix remains constant as long as the material remains elastic. The next step is to update the stress tensor for the strain increment provided by Abaqus. The current stress tensor is therefore equal to the stress tensor at the end of the previous strain increment added to the product of the tangent stiffness matrix and the current strain increment (*Eq. 6.16*).

$$DDSDDE = \frac{E}{1-v^2}\begin{bmatrix} 1 & v & 0 \\ v & 1 & 0 \\ 0 & 0 & \frac{1-v}{2} \end{bmatrix} \tag{6.15}$$

where

E = Young's modulus of elasticity
v = Poisson's ratio

$$\{STRESS\}^i = \{STRESS\}^{i-1} + [DDSDDE]^i * \{DSTRAN\}^i \tag{6.16}$$

6.3.4 Cracked domain: Derivation of stress-strain relation

An incremental strain formulation is used in the derivation of the stress-strain relation in the cracked domain (*Rots, 1989*). As stated before, the total strain of the cracked material is decomposed into the strain in the crack and the strain in the uncracked material. Expressed in incremental form this is

$$\Delta\varepsilon_{xy} = \Delta\varepsilon_{xy}^{cr} + \Delta\varepsilon_{xy}^{co} \tag{6.17}$$

where

$\Delta\varepsilon_{xy}$ – total strain of cracked material (in global coordinates)
$\Delta\varepsilon_{xy}^{cr}$ – strain in crack (in global coordinates)
$\Delta\varepsilon_{xy}^{co}$ – strain of uncracked material (in global coordinates)

Considering the strain increment in the local crack coordinates 1-2,

$$\Delta\varepsilon_{12}^{cr} = [\Delta\varepsilon_1^{cr}\ \Delta\gamma_{12}^{cr}]^T \tag{6.18}$$

where
$\Delta\varepsilon_1^{cr}$ – local strain normal to the crack (Mode I)
$\Delta\gamma_{12}^{cr}$ – local shear strain parallel to the crack (Mode II)

The generalised transformation equations for stress can be written as

$$\sigma_1 = \sigma_x \cos^2 \Phi + \sigma_y \sin^2 \Phi + 2\tau_{xy} \sin \Phi \cos \Phi \tag{6.19a}$$
$$\sigma_2 = \sigma_x \sin^2 \Phi + \sigma_y \cos^2 \Phi - 2\tau_{xy} \sin \Phi \cos \Phi \tag{6.19b}$$
$$\tau_{12} = (\sigma_y - \sigma_x) \sin \Phi \cos \Phi + \tau_{xy}(\cos^2 \Phi - \sin^2 \Phi) \tag{6.19c}$$

In matrix form

$$\begin{bmatrix} \sigma_1 \\ \sigma_2 \\ \tau_{12} \end{bmatrix} = \begin{bmatrix} c^2 & s^2 & 2sc \\ s^2 & c^2 & -2sc \\ -sc & sc & c^2 - s^2 \end{bmatrix} \begin{bmatrix} \sigma_x \\ \sigma_y \\ \tau_{xy} \end{bmatrix} \tag{6.20}$$

Or alternatively this can be written in the form

$$\begin{bmatrix} \sigma_x \\ \sigma_y \\ \tau_{xy} \end{bmatrix} = \begin{bmatrix} c^2 & s^2 & -2sc \\ s^2 & c^2 & 2sc \\ sc & -sc & c^2 - s^2 \end{bmatrix} \begin{bmatrix} \sigma_1 \\ \sigma_2 \\ \tau_{12} \end{bmatrix} \tag{6.21}$$

where $c = \cos\varphi$ and $s = \sin\varphi$

Eliminating the second row in the first instance gives the local normal and shear stress as a function of the global stress.

$$\begin{bmatrix} \sigma_1 \\ \tau_{12} \end{bmatrix} = \begin{bmatrix} c^2 & s^2 & 2sc \\ -sc & sc & c^2 - s^2 \end{bmatrix} \begin{bmatrix} \sigma_x \\ \sigma_y \\ \tau_{xy} \end{bmatrix} \tag{6.22}$$

Eliminating the second column in the second instance gives the global stress as a function of the local normal and shear stress.

$$\begin{bmatrix} \sigma_x \\ \sigma_y \\ \tau_{xy} \end{bmatrix} = \begin{bmatrix} c^2 & -2sc \\ s^2 & 2sc \\ sc & c^2 - s^2 \end{bmatrix} \begin{bmatrix} \sigma_1 \\ \tau_{12} \end{bmatrix} \tag{6.23}$$

Define T_σ^{12} as the stress transformation matrix for global to local stress

$$\begin{bmatrix} \sigma_1 \\ \tau_{12} \end{bmatrix} = [T_\sigma^{12}] \begin{bmatrix} \sigma_x \\ \sigma_y \\ \tau_{xy} \end{bmatrix} \tag{6.24}$$

$$T_\sigma^{12} = \begin{bmatrix} c^2 & s^2 & 2sc \\ -sc & sc & c^2 - s^2 \end{bmatrix} \tag{6.25}$$

Similarly define T_σ^{xy} as the stress transformation matrix for local to global stress

$$\begin{bmatrix} \sigma_x \\ \sigma_y \\ \tau_{xy} \end{bmatrix} = [T_\sigma^{xy}] \begin{bmatrix} \sigma_1 \\ \tau_{12} \end{bmatrix} \tag{6.26}$$

$$T_{\sigma}^{xy} = \begin{bmatrix} c^2 & -2sc \\ s^2 & 2sc \\ sc & c^2 - s^2 \end{bmatrix} \tag{6.27}$$

The same procedure can be followed for strain:

The generalised transformation equations for strain can be written as

$$\varepsilon_1 = \varepsilon_x \cos^2 \Phi + \varepsilon_y \sin^2 \Phi + \gamma_{xy} \sin \Phi \cos \Phi \tag{6.28a}$$
$$\varepsilon_2 = \varepsilon_x \sin^2 \Phi + \varepsilon_y \cos^2 \Phi - \gamma_{xy} \sin \Phi \cos \Phi \tag{6.28b}$$
$$\gamma_{12} = 2(\varepsilon_y - \varepsilon_x) \sin \Phi \cos \Phi + \gamma_{xy}(\cos^2 \Phi - \sin^2 \Phi) \tag{6.28c}$$

In matrix form

$$\begin{bmatrix} \varepsilon_1 \\ \varepsilon_2 \\ \gamma_{12} \end{bmatrix} = \begin{bmatrix} c^2 & s^2 & sc \\ s^2 & c^2 & -sc \\ -2sc & 2sc & c^2 - s^2 \end{bmatrix} \begin{bmatrix} \varepsilon_x \\ \varepsilon_y \\ \gamma_{xy} \end{bmatrix} \tag{6.29}$$

Or alternatively this can be written in the form

$$\begin{bmatrix} \varepsilon_x \\ \varepsilon_y \\ \gamma_{xy} \end{bmatrix} = \begin{bmatrix} c^2 & s^2 & -sc \\ s^2 & c^2 & sc \\ 2sc & -2sc & c^2 - s^2 \end{bmatrix} \begin{bmatrix} \varepsilon_1 \\ \varepsilon_2 \\ \gamma_{12} \end{bmatrix} \tag{6.30}$$

Eliminating the second row in the first instance gives the local normal and shear strain as a function of the global strains.

$$\begin{bmatrix} \varepsilon_1 \\ \gamma_{12} \end{bmatrix} = \begin{bmatrix} c^2 & s^2 & sc \\ -2sc & 2sc & c^2 - s^2 \end{bmatrix} \begin{bmatrix} \varepsilon_x \\ \varepsilon_y \\ \gamma_{xy} \end{bmatrix} \tag{6.31}$$

Eliminating the second column in the second instance gives the global strains as a function of the local normal and shear strain.

$$\begin{bmatrix} \varepsilon_x \\ \varepsilon_y \\ \gamma_{xy} \end{bmatrix} = \begin{bmatrix} c^2 & -sc \\ s^2 & sc \\ 2sc & c^2 - s^2 \end{bmatrix} \begin{bmatrix} \varepsilon_1 \\ \gamma_{12} \end{bmatrix} \tag{6.32}$$

Define T_{ε}^{12}as the strain transformation matrix for global to local strain

$$\begin{bmatrix} \varepsilon_1 \\ \gamma_{12} \end{bmatrix} = [T_{\varepsilon}^{12}] \begin{bmatrix} \varepsilon_x \\ \varepsilon_y \\ \varepsilon_{xy} \end{bmatrix} \tag{6.33}$$

$$T_{\varepsilon}^{12} = \begin{bmatrix} c^2 & s^2 & sc \\ -2sc & 2sc & c^2 - s^2 \end{bmatrix} \tag{6.34}$$

Similarly define T_{ε}^{xy} as the strain transformation matrix for local to global strain

$$\begin{bmatrix} \varepsilon_x \\ \varepsilon_y \\ \gamma_{xy} \end{bmatrix} = [T_{\varepsilon}^{xy}] \begin{bmatrix} \varepsilon_1 \\ \gamma_{12} \end{bmatrix} \tag{6.35}$$

$$T_{\varepsilon}^{xy} = \begin{bmatrix} c^2 & -sc \\ s^2 & sc \\ 2sc & c^2 - s^2 \end{bmatrix} \tag{6.36}$$

Noting that $\left[T_{\varepsilon}^{xy}\right] = [T_{\sigma}^{12}]^T$, the expressions that follow can be simplified by equating $\left[T_{\varepsilon}^{xy}\right]$ to $[N]$ i.e.

$$N = \begin{bmatrix} c^2 & -sc \\ s^2 & sc \\ 2sc & c^2 - s^2 \end{bmatrix} \tag{6.37}$$

The local crack strains can be expressed in the global coordinate system xy.

$$\Delta\varepsilon_{xy}^{cr} = N\Delta\varepsilon_{12}^{cr} \tag{6.38}$$

In the same way, the incremental tractions on the crack surface can be expressed as

$$\Delta t^{cr} = [\Delta t_1^{cr}\ \Delta t_{12}^{cr}]^T \tag{6.39}$$

where

Δt_1^{cr} – Mode I normal traction increment

Δt_{12}^{cr} – Mode II shear traction increment

The relationship between the global stress increment and the local traction increment is

$$\Delta t^{cr} = N^T\Delta\sigma \tag{6.40}$$

where

$\Delta\sigma$ is the total global stress increment

To complete the system of equations, a constitutive model for the uncracked material (between cracks) is needed, as well as traction-strain/displacement relations for the smeared cracks i.e.

$$\Delta\sigma = D^{co}\Delta\varepsilon^{co} \tag{6.41a}$$
$$\Delta t^{cr} = D^{cr}\Delta e^{cr} \tag{6.41b}$$

where

D^{co} is the tangent stiffness matrix for the uncracked material
D^{cr} is the tangent stiffness matrix for the cracked material

The overall stress-strain relation for the cracked material with respect to the global coordinate system can now be derived. First substitute the relation for the global crack strain increment in terms of the local crack strain increment into the decomposition relation i.e.

- Substitute $\Delta\varepsilon_{xy}^{cr} = N\Delta\varepsilon_{12}^{cr}$ into $\Delta\varepsilon = \Delta\varepsilon^{cr} + \Delta\varepsilon^{co}$,
- which yields $\Delta\varepsilon = N\Delta\varepsilon_{12}^{cr} + \Delta\varepsilon^{co}$
- Substitute $\Delta\varepsilon = N\Delta\varepsilon_{12}^{cr} + \Delta\varepsilon^{co}$ into $\Delta\sigma = D^{co}\Delta\varepsilon^{co}$,
- which yields $\Delta\sigma = D^{co}(\Delta\varepsilon - N\Delta\varepsilon_{12}^{cr})$
- Pre-multiplying with N^T yields

- $N^T \Delta\sigma = N^T D^{co}(\Delta\varepsilon - N\Delta\varepsilon_{12}^{cr})$
- With $\Delta t^{cr} = D^{cr}\Delta\varepsilon_{12}^{cr}$ and $\Delta t^{cr} = N^T\Delta\sigma$ substituted into the LHS of above, yields
- $D^{cr}\Delta\varepsilon_{12}^{cr} = N^T D^{co}(\Delta\varepsilon - N\Delta\varepsilon_{12}^{cr})$
- which provides the link between local crack strain and total global strain
- $(D^{cr} + N^T D^{co} N)\Delta\varepsilon_{12}^{cr} = N^T D^{co}\Delta\varepsilon$
- $\Delta\varepsilon_{12}^{cr} = (D^{cr} + N^T D^{co} N)^{-1} N^T D^{co}\Delta\varepsilon$
- Finally, the overall relation between global stress and strain by substituting above into
- $\Delta\sigma = D^{co}(\Delta\varepsilon - N\Delta\varepsilon_{12}^{cr})$, which yields
- $\Delta\sigma = D^{co}(\Delta\varepsilon - N(D^{cr} + N^T D^{co} N)^{-1} N^T D^{co}\Delta\varepsilon)$
- $\Delta\sigma = (D^{co} - D^{co} N(D^{cr} + N^T D^{co} N)^{-1} N^T D^{co})\,\Delta\varepsilon$
- Finally, this can be written as :
- $\Delta\sigma = D^{crco}\,\Delta\varepsilon$, where
- $D^{crco} = D^{co} - D^{co} N(D^{cr} + N^T D^{co} N)^{-1} N^T D^{co}$ is the total stiffness matrix for the cracked material

6.3.5 Cracked domain: Procedure

The positive principal tensile strain is greater than or equal to the cracking strain or the state variable which tracks the material state is set to a “cracked” state. The first step in the cracked state is to determine the crack orientation. The crack orientation is only determined once at the onset of cracking and is then stored.

Compute and store initial crack orientation

The principal strain orientation can be determined from the following equation:

$$\tan(2\theta_p) = \frac{\gamma_{xy}}{\varepsilon_{xx} - \varepsilon_{yy}} \tag{6.42}$$

Given the global strain tensor in matrix form

$$[\varepsilon] = \begin{bmatrix} \varepsilon_{xx} & \varepsilon_{xy} \\ \varepsilon_{yx} & \varepsilon_{yy} \end{bmatrix} \tag{6.43}$$

The transformation matrix Q (to transform the global strains into the principal directions) is:

$$[Q] = \begin{bmatrix} \cos\theta_p & \sin\theta_p \\ -\sin\theta_p & \cos\theta_p \end{bmatrix} \tag{6.44}$$

The principal strain tensor can be calculated from:

$$[\varepsilon_{12}] = [Q][\varepsilon_{xy}][Q]^T \tag{6.45}$$

The strain value entry (1, 1) or ε_{11} in $[\varepsilon_{12}]$ corresponds to the value of θ_p. The value for θ_p must correspond to $\varepsilon_{11} = \varepsilon_{p,max}$ (positive maximum principal strain). If $\varepsilon_{11} \neq \varepsilon_{p,max}$, then $\theta_p = \theta_p + \pi/2$. The cosine and sine of θ_p are then saved as state variables in the UMAT.

Compute incremental and total local strain

The material model implemented, is expressed in terms of the local total strains, as well as the local strain increment, in the case of unloading or reloading. The next step in the procedure is therefore

to transform the global total strain tensor *STRAN* and the global strain increment *DSTRAN*, to the crack basis using the following transformations as expressed previously in *Eq. 6.29*.

$$\begin{bmatrix} \varepsilon_1 \\ \varepsilon_2 \\ \gamma_{12} \end{bmatrix} = \begin{bmatrix} c^2 & s^2 & sc \\ s^2 & c^2 & -sc \\ -2sc & 2sc & c^2 - s^2 \end{bmatrix} \begin{bmatrix} \varepsilon_x \\ \varepsilon_y \\ \gamma_{xy} \end{bmatrix}$$

$$\begin{bmatrix} \Delta\varepsilon_1 \\ \Delta\varepsilon_2 \\ \Delta\gamma_{12} \end{bmatrix} = \begin{bmatrix} c^2 & s^2 & sc \\ s^2 & c^2 & -sc \\ -2sc & 2sc & c^2 - s^2 \end{bmatrix} \begin{bmatrix} \Delta\varepsilon_x \\ \Delta\varepsilon_y \\ \Delta\gamma_{xy} \end{bmatrix}$$

Compute local stress components and corresponding tangent stiffness from material model
Compute the local stresses and corresponding local tangent stiffness as per material model defined in *Section 6.2*, then assemble the global tangent stiffness matrix for cracked material as per *Subsection 6.3.4*. Transform local stresses to global basis and return stress and cracked material tangent stiffness matrix to Abaqus. The FORTRAN code for the UMAT is provided in the *Appendix E*.

6.4 Model verification for a single finite element

Testing and validation of the user subroutine first has to be done for a single element, where the only complex part of the model is the UMAT and the boundary conditions can be isolated easily.

6.4.1 Material input parameters

The following material parameters (*Table 6.2*) are used in the single finite element analysis.

Table 6.2 – Material input parameters for single element validation

Young's modulus [MPa]	E	30,000
Poisson's ratio [-]	v	0.2
Peak tensile stress [MPa]	f_{ct}	2.85
Mode I fracture energy [N/mm]	G_{ft}	3.23
Peak shear stress (w_i = 0.1mm) [MPa]	f_{cs}	9
Mode II fracture energy (w_i = 0.1mm) [N/mm]	G_{fs}	14.12
Shear stiffness model parameter (w_i = 0.1mm) [mm]	w_m	0.5
Shear stiffness model parameter (w_i = 0.1mm) [-]	f_i	0.005

w_i = initial crack width [mm]

6.4.2 Element type and dimensions

A 4-node bilinear plane stress quadrilateral is used in all cases. Two element sizes 1x1mm and 10x10mm are tested to ensure that the UMAT is objective with respect to the element size. The plane stress thickness is 1 in both cases.

6.4.3 Boundary conditions

The boundary conditions tested are illustrated in *Fig. 6.6*. The element is first subjected to uniaxial tensile loading (*Fig. 6.6a*) and repeated unloading (*Fig. 6.6b*) and reloading. In the unloading step, the prescribed displacement is removed linearly over the step time, while the other boundary conditions are retained. These two boundary conditions serve to test and validate the Mode I material model directly, as well as the unloading and reloading functions of the Mode I response. The next boundary condition tested is the Mode II response without initial loading in Mode I

(*Fig. 6.6d*). Even though this load case is not implemented in the Meso-scale test, it demonstrates the case for a diagonal crack in the element. An equation constraint is applied to the two loading nodes to ensure that both nodes undergo the same horizontal displacement. This way the element edges remain parallel and the strains and stresses observed for all four integration points in the element remain uniform.

The final boundary condition to be tested executes Mode I loading (*Fig. 6.6a*), Mode I unloading (*Fig. 6.6b*), followed by Mode II loading only (*Fig. 6.6c*). In this case the crack is fixed vertically in the Mode I step and is subjected to shear loading.

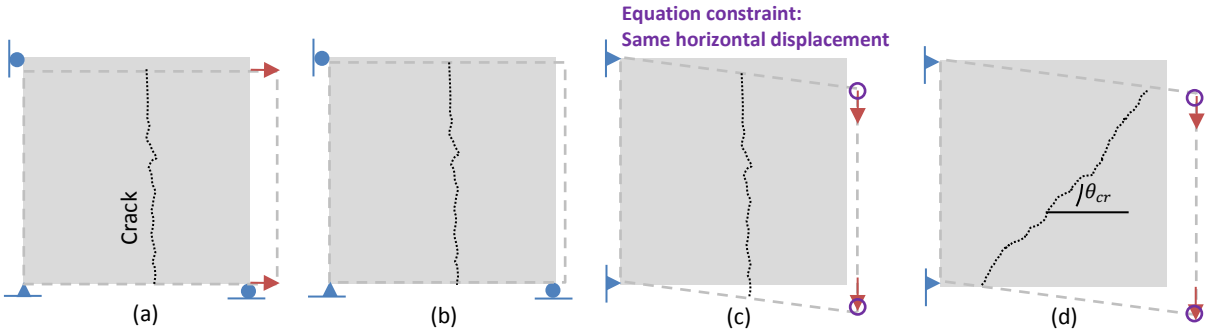

Fig. 6.6 – Single element test boundary conditions (a) tensile loading, followed by (b) tensile unloading and (c) shear loading; (d) Shear/Mode II loading only (diagonal cracking)

6.4.4 Analysis output

Fig. 6.7 defines the global and local stresses in the element. For the purpose of analysing the Abaqus output, the notation for global stresses according to Abaqus will be used i.e. S_{11}, S_{22} and S_{12}. The local crack stresses are redefined as well to S_n and S_t, which are the crack normal stresses, normal and parallel to the crack respectively. S_{nt} is the local shear stress parallel to the crack.

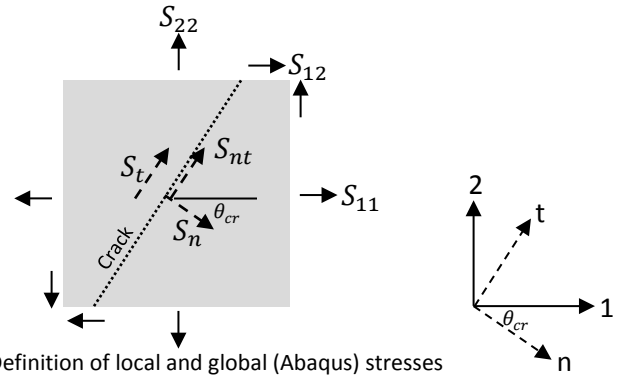

Fig. 6.7 – Definition of local and global (Abaqus) stresses

Mode I Loading and repeated Unloading and Reloading

Fig. 6.8 demonstrates the UMAT performance when subjected to two cycles of loading, unloading, and reloading in Mode I (*Fig. 6.6a & b*). The Abaqus output stress S_{11} agrees with the model limit function and the stress unloads to the correct crack width $w \cong 0.1mm$ and $w \cong 0.3mm$ ($w \cong \varepsilon_{11} h$) for the given unloading displacement (maximum displacement at the end of the reloading/loading step).

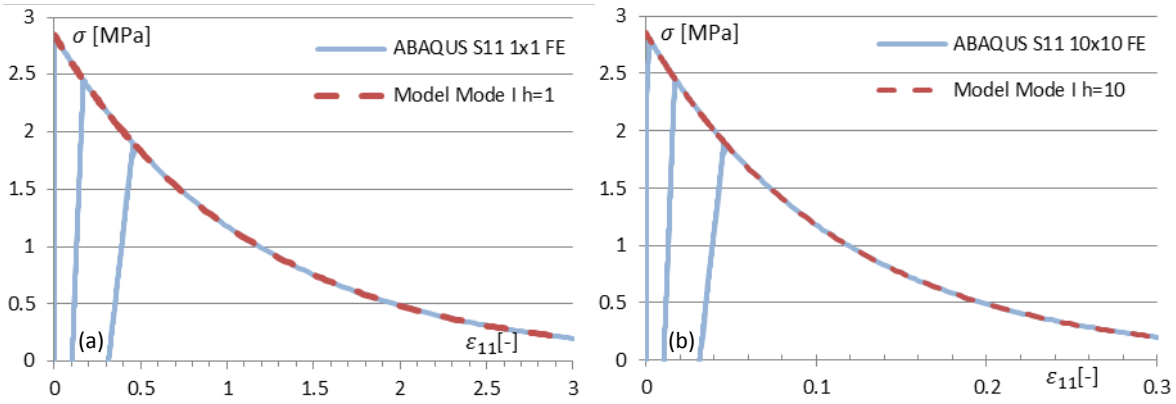

Fig.6.8 – Mode I loading, followed by repeated unloading and reloading (a) 1x1 element, (b) 10x10 element

Mode II Loading only

The local normal stress to the crack (S_n) follows the prescribed Mode I model as shown in *Fig. 6.9*. The global normal stress S_{11} remains zero. Similarly the local shear stress (S_{nt}) also adheres to the prescribed Mode II model (*Fig. 6.10*). In each case the local or global stress is plotted against the corresponding strain.

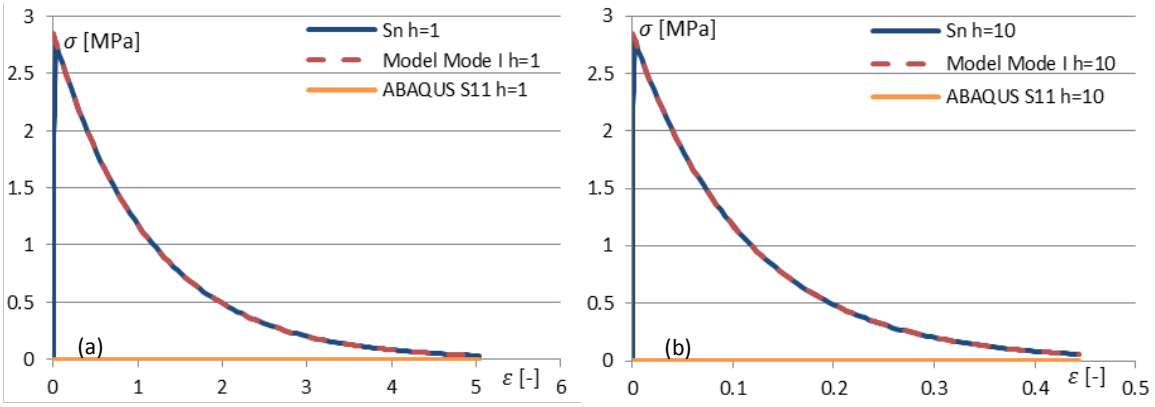

Fig. 6.9 – Mode II only load case: Local (S_n) and global (S_{11}) normal stress for element size (a) 1x1 and (b) 10x10

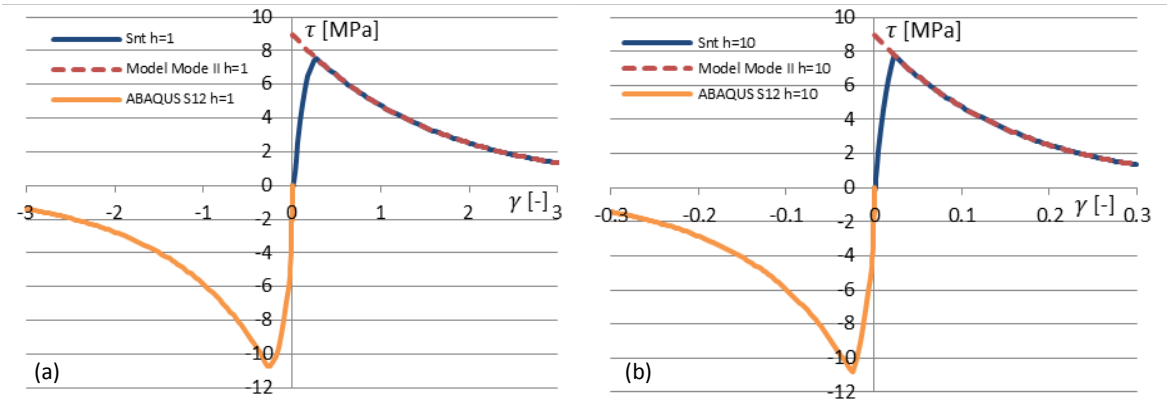

Fig. 6.10 – Mode II only load case: Local (S_{nt}) and global (S_{12}) shear stress for element size (a) 1x1 and (b) 10x10

Mode I Loading and Unloading, followed by Mode II Loading

Fig. 6.11 demonstrates the Abaqus stress S_{11} output for this load case. Recall that the crack in this case is vertical and the local coordinates system therefore coincides with the global system. The normal stress S_{11} adheres to the Mode I model during loading along the limit function and unloading produces the prescribed permanent deformation. Notice that the strain normal to the crack does not increase again in the shear/Mode II step and hence no reloading takes place normal to the crack. This is anticipated for this model where the Mode I and Mode response are decoupled and dilatancy is not accounted for. The only link between the Mode I and Mode II response is the shear stiffness during initial shear loading, as well as shear unloading and reloading, where the shear stiffness is a function of the crack width. This effect can be observed in *Fig. 6.12*. Increasing the initial crack width reduces the initial shear stiffness and consequently also the peak shear stress. The global shear stress S_{12} adheres to the Mode II model.

In conclusion, the Mode I and Mode II material models are successfully validated by the single element test for the boundary conditions considered. The material model is also objective with respect to element size.

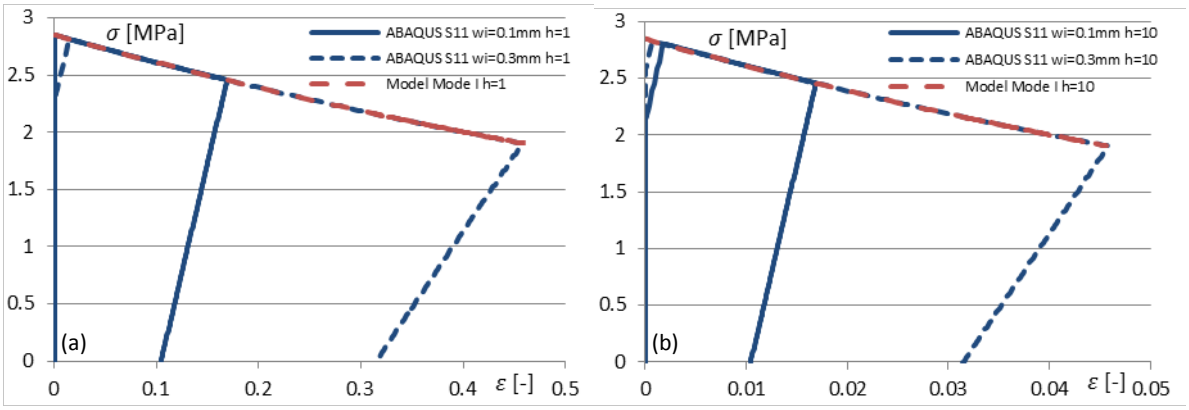

Fig. 6.11 – Mode I LU and Mode II L load case: Global (S_{11}) normal stress for element size (a) 1x1 and (b) 10x10

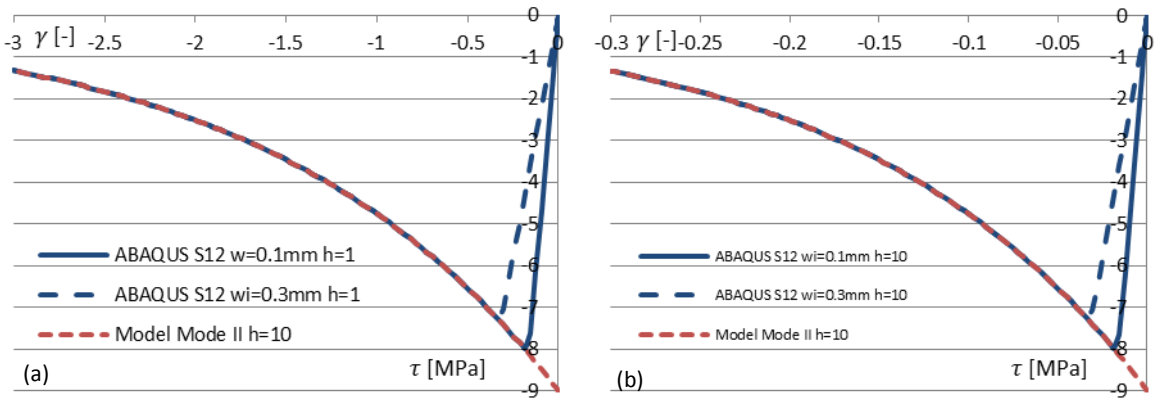

Fig. 6.12 – Mode I LU and Mode II L load case: Global (S_{12}) shear stress for element size (a) 1x1 and (b) 10x10

6.5 Model calibration with Meso-scale data

6.5.1 Calibration of Mode I model

Only two materials parameters are required for the Mode I material model, namely the peak tensile strength f_{ct} and the Mode I fracture energy G_{ft}. These parameters are obtained from the experimental data as outlined in Chapter 4 and is summarised in the *Table 6.3*. *Figs. 6.13* plot the calibrated model (*Eq. 6.4*) with the sample and average uniaxial tensile response determined experimentally. Given the simplicity of the model, it adequately represents the experimental data.

Table 6.3 – Mode I material parameter values

Composite:	SCM			SCC		
V_f [%]	0.5%	0.75%	1.0%	0.5%	0.75%	1.0%
f_{ct} [N/mm^2]	2.85	2.99	2.61	4.40	3.40	3.65
G_{ft} [N/mm]	3.23	3.79	3.51	2.11	2.75	3.55

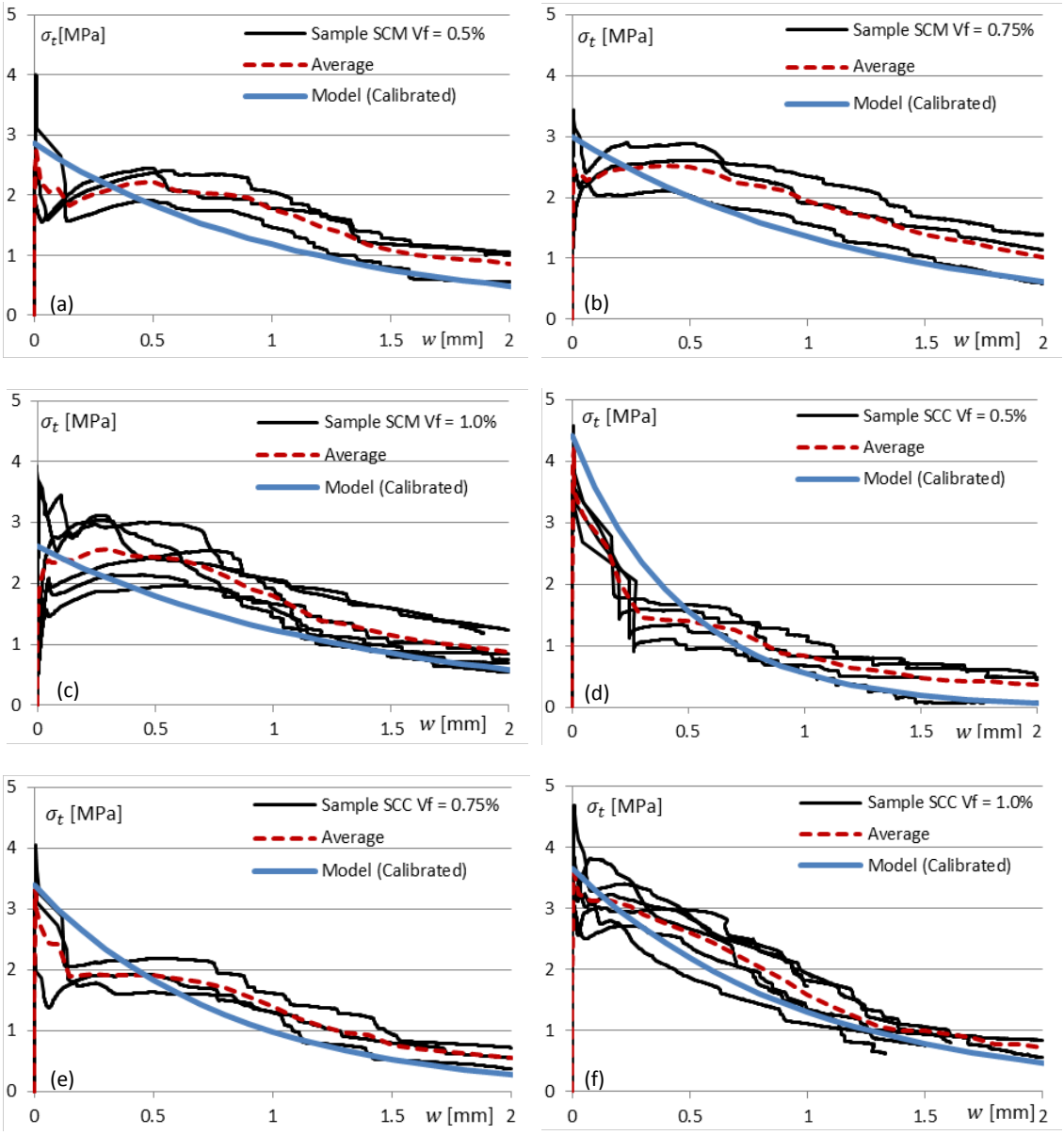

Fig. 6.13 – Mode I model calibration (a)-(f)

6.5.2 Calibration of Mode II model

Four parameters are used to describe and calibrate the Mode II material model. The calibrated values are provided in *Table 6.4* for each composite type, fibre dosage and pre-crack value. Apart from the shear fracture energy G_{fs}, which is the average from the experimental data outlined in *Chapter 5*, the other parameters f_{cs}, w_m and f_i are adjusted to fit the experimental average data. Some of the calibrated curves are shown in *Figs. 6.14*. The rest of the data set is provided in *Addendum F.1*. Again, given the simplicity of the model, it adequately represents the experimental data.

Table 6.4 – Mode II material parameter values

Composite:	SCM						SCC-450						SCC-600	
V_f [%]	0.5%		0.75%		1.0%		0.5%		0.75%		1.0%		0.5%	
w_i [mm]	0.1	0.3	0.1	0.3	0.1	0.3	0.1	0.3	0.1	0.3	0.1	0.3	0.1	0.3
f_{cs} [N/mm^2]	9.0	4.0	9.5	6.0	10.0	8.0	7.0	4.3	8.7	7.2	12.2	10.2	6.0	6.0
G_{fs} [N/mm]	14.12	10.90	13.95	12.47	16.10	21.74	15.94	7.87	21.24	18.78	25.91	24.06	14.64	13.84
w_m [mm]	0.50	0.48	0.60	0.55	0.50	0.65	0.60	0.65	0.60	0.60	0.52	0.60	0.55	0.56
f_i [-]	0.005	0.018	0.007	0.006	0.007	0.006	0.007	0.0035	0.007	0.0065	0.015	0.015	0.006	0.014

Note that w_m and f_i are currently defined as model parameters and not material parameters. Although it is likely that these parameters have physical significance, this will not be investigated further in this study. The values of w_m and f_i are also not unique, but can vary in certain ranges. All that can be said of these parameter values is that the specific combination given in *Table 6.4* adequately calibrates the model for the experimental average data.

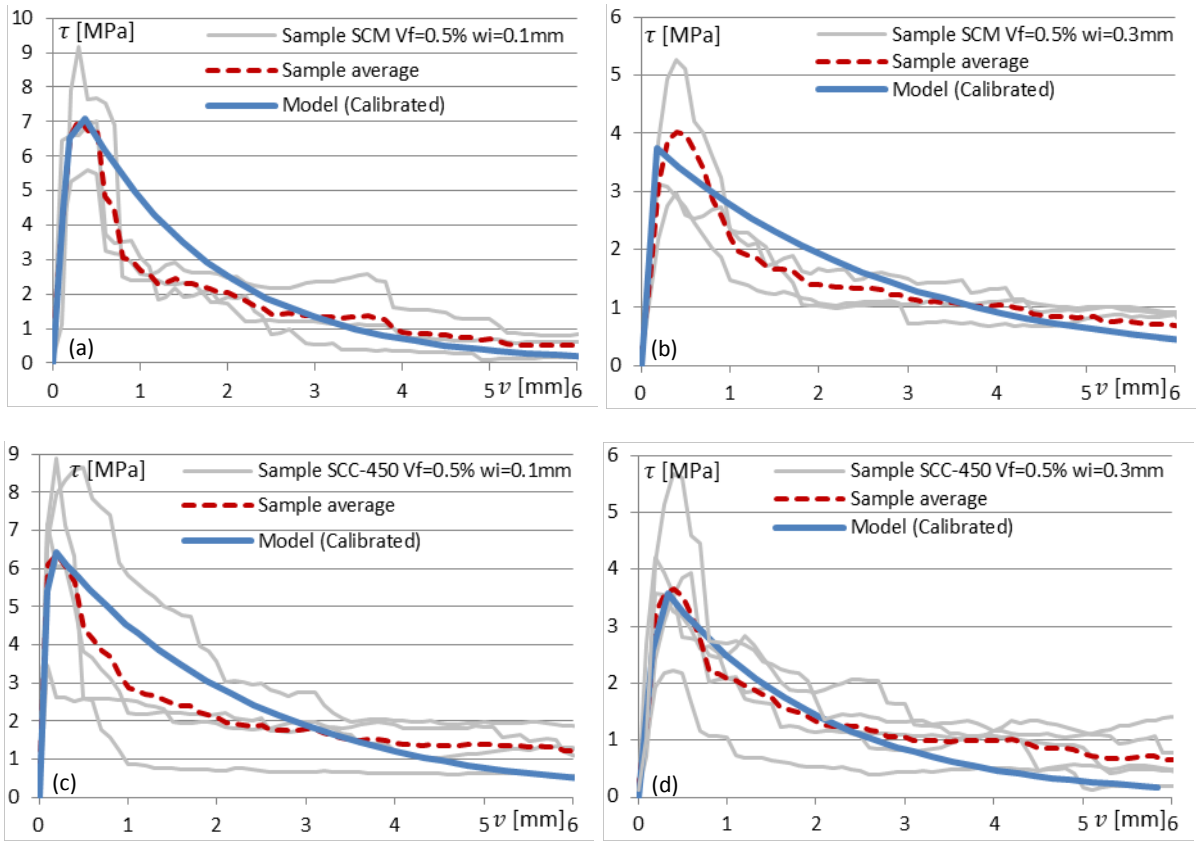

Fig. 6.14 – Mode II model calibration: Shear stress τ vs. shear displacement v (a)-(d)

6.6 Model verification via Meso-scale Iosipescu shear test

6.6.1 Model details

Model dimensions

The model dimensions are shown in *Fig. 6.15a*. The wedge notch geometry is simplified to a rectangular notch. The impact of this simplification is believed to be minimal. All other dimensions are the same as the experimental specimen. The roller supports are assumed to bear over a width of 3mm. The region outside the notch is assumed to remain linear elastic, with the same elastic properties as the notch.

Boundary conditions

The boundary conditions (BC1) applied in the tension and shear step are shown in *Fig. 6.15b* & *c* respectively. The inner supports are restrained against horizontal translation during the shear step in all analyses. An alternative boundary condition (BC2) where only one inner support is restrained against horizontal translation is also discussed in terms of the deformed shape and analysis output.

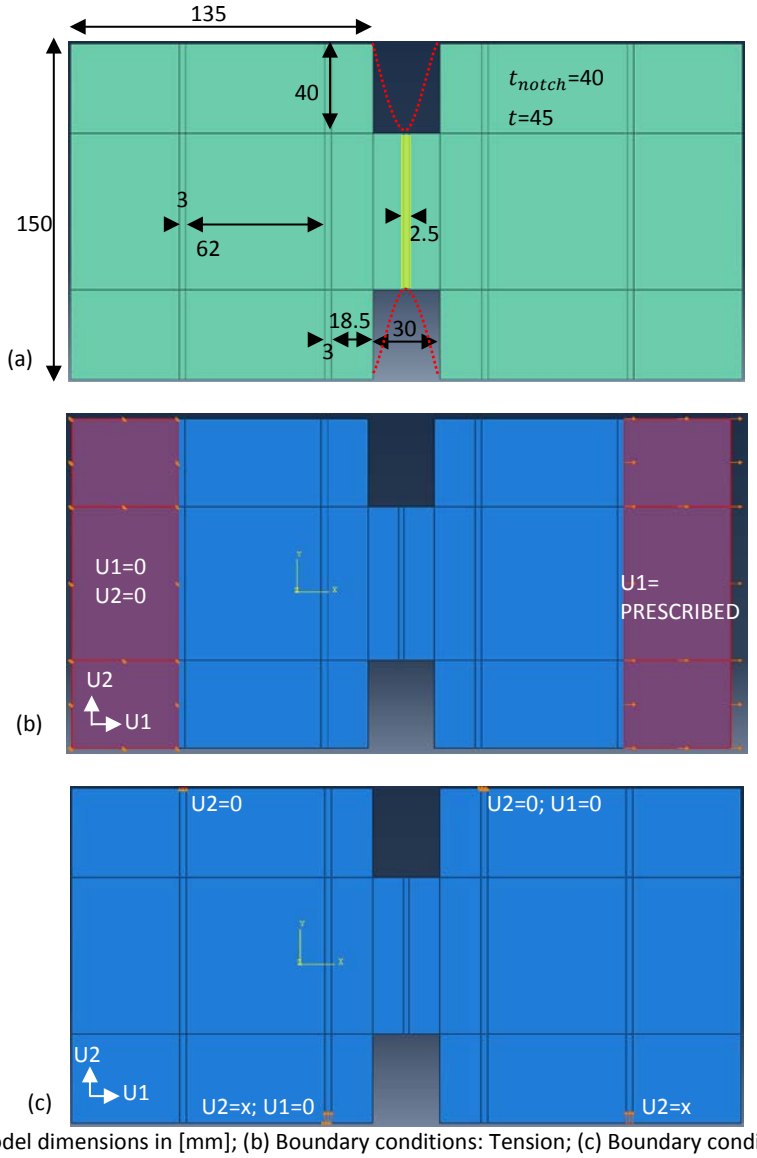

Fig. 6.15 – (a) Model dimensions in [mm]; (b) Boundary conditions: Tension; (c) Boundary condition: Shear (Both inner supports restrained against horizontal translation)

Mesh configuration

The mesh layout is shown in *Fig. 6.16*. As for the single element test, a 4-node bilinear plane stress quadrilateral is used in all analyses. Each element in the notch is 2.5x2.5mm. There are 28 elements over the height of the notch.

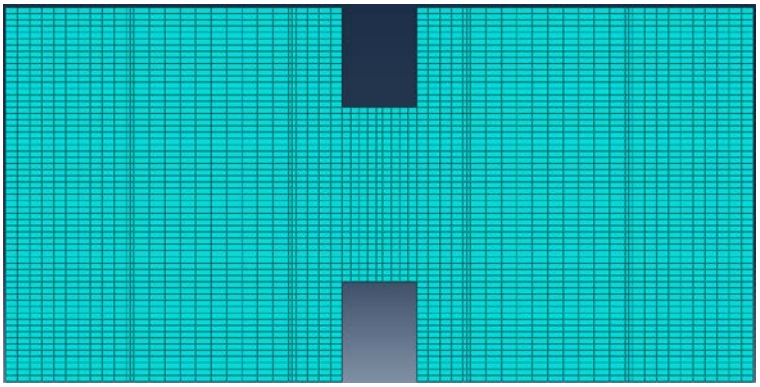

Fig. 6.16 – Mesh configuration

Analysis details

The automatic incrementation scheme in *Table 6.5* is used for all analyses:

Table 6.5 – Incrementation scheme

Max. no. of increments	1000
Increment size:	
Initial	1E-015 to 1E-005
Minimum	1E-015
Maximum	0.01

6.6.2 Analysis output

Deformed shape

The typical deformed shape is given in *Fig. 6.17a* and *b* for the model (with both inner supports restrained against horizontal translation) and experiment respectively. It is clear from the comparison between the two deformed shapes, that the model overestimates the crack opening. This is attributed to the choice of boundary conditions. From the experiment it is also clear that horizontal translation does occur at the inner supports, which is assumed to be zero in the model. If one of the inner supports is allowed to translate freely in the horizontal direction (BC2), the deformed shape in *Fig. 6.18* is obtained.

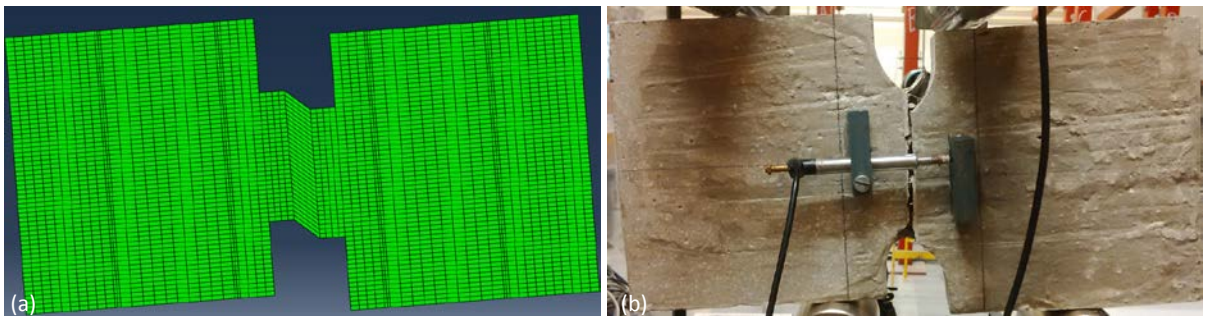

Fig. 6.17 – Deformed shape: (a) Typical analysis (Both inner supports restrained against horizontal translation), (b) Experiment

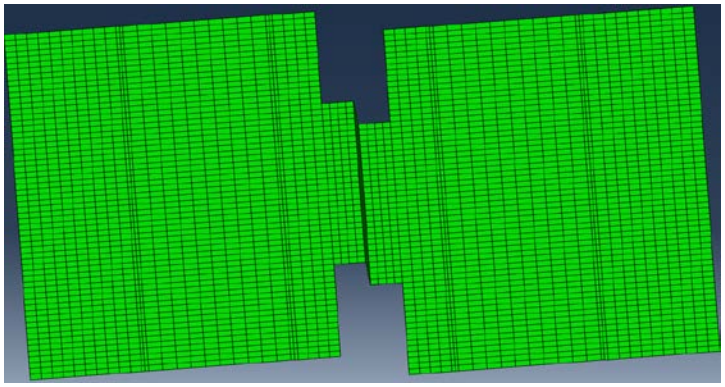

Fig. 6.18 – Deformed shape: Only one inner support restrained against horizontal translation

Fig. 6.18 has a closer resemblance to *Fig. 6.17b* and the associated boundary condition is believed to be a better approximation compared to that of *Fig. 6.17a*. However, some issues arise when using this boundary condition with a material model where the Mode I and Mode II responses are decoupled and dilatancy is not accounted for. This will be addressed in the analysis of the Abaqus output that follows.

All stresses are the average centroid element stresses of all 28 elements over the height of the notch.

ABAQUS output S11:
In the case of a vertical crack, the crack coordinate system coincides with the global coordinate system and the global stress S11 matches the local normal stress. *Fig. 6.19* illustrates the model performance. In all cases, after initial loading and unloading in Mode I, reloading in Mode I occurs during the Iosipescu shear step. This is contrary to what is observed for a single element, where no further crack opening is observed or expected for a vertical crack subjected to pure shear loading. This increased crack widening is not due to the material model, as dilatancy is not accounted for and the Mode I and Mode II actions are decoupled. Due to the simulated boundary conditions of the Iosipescu shear test, the crack width continues to increase during shear loading. As observed for the deformed shape in *Fig. 6.17a*, the crack width is overestimated in all cases (also see *Fig. 6.23b*). The complete data set is provided in *Addendum F.2*.

The alternative boundary condition (BC2, *Fig. 6.18*) results in the normal crack strain becoming negative and no reloading takes place normal to the crack during the shear step.

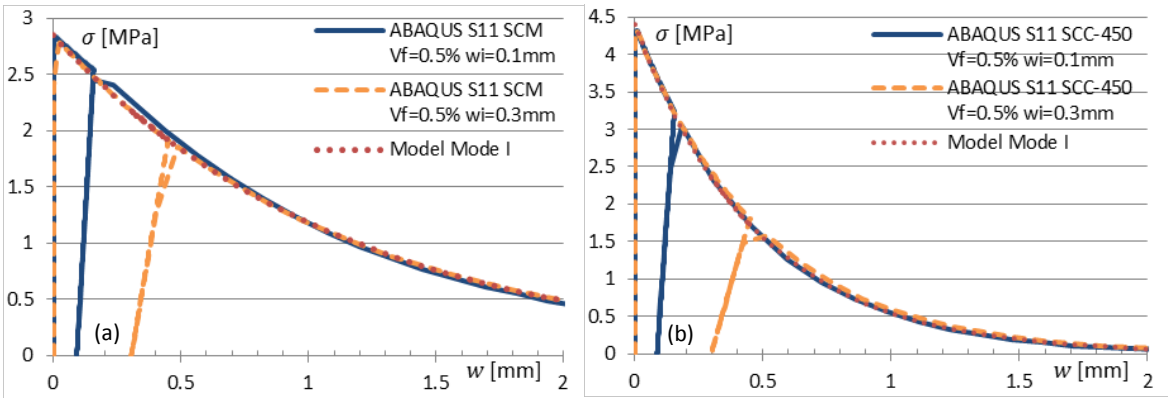

Fig. 6.19 – S11 vs crack width, w for w_i=0.1 and 0.3mm (a) SCM Vf=0.5%; (b) SCC-450 Vf=0.5%

ABAQUS output S12:

In all analyses, the Abaqus global shear stress S12 matches the calibrated model. The only discrepancy that occurs between the calibrated model and the Abaqus output, is in the computation of the initial shear stiffness and consequently the peak shear stress. This is attributed to the fact that the initial shear stiffness is a function of the crack width, which is overestimated by the Abaqus model. As a result a softer response occurs initially, as can be seen in the typical results in *Figs. 6.20-21*. This error is less prevalent for the smaller initial crack width $w_i = 0.1mm$, which is expected. The complete data set is provided in *Appendix F.2*.

A comparison is made between the two boundary conditions analysed in *Fig. 6.22* for one composite. Recall that 'BC2' is the boundary condition where only one of the inner supports is restrained against horizontal translation. 'BC2' gives a better approximation of the peak shear stress compared to 'BC1', but at larger shear displacements, the shear stress increases again and deviates from the material model. This phenomenon has been characterised by *Rots (ICF7, 1989)* as "stress-locking", which occurs in continuum and smeared crack modelling when fixed cracks with significant shear retention lead to stress rebuild.

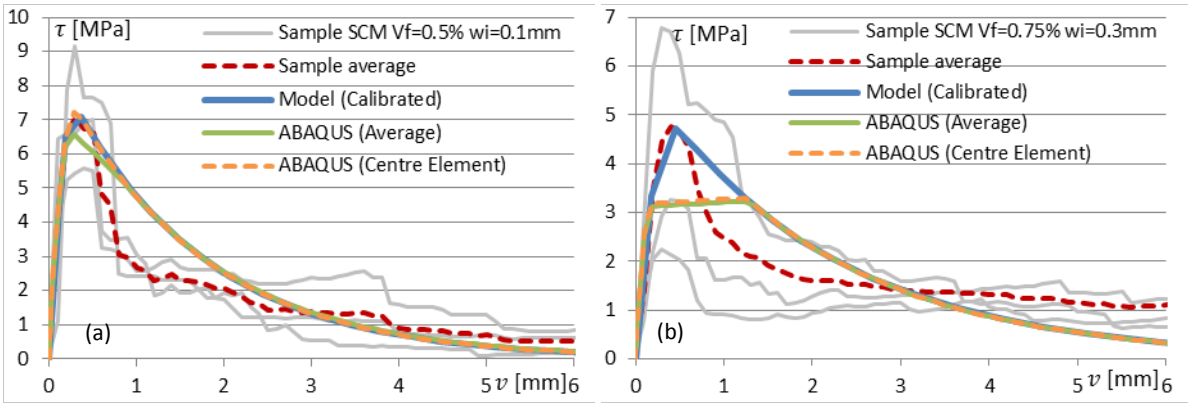

Fig. 6.20 – S12 vs v for (a) SCM Vf=0.5% wi=0.1mm and (b) SCM Vf=0.75% wi=0.3mm

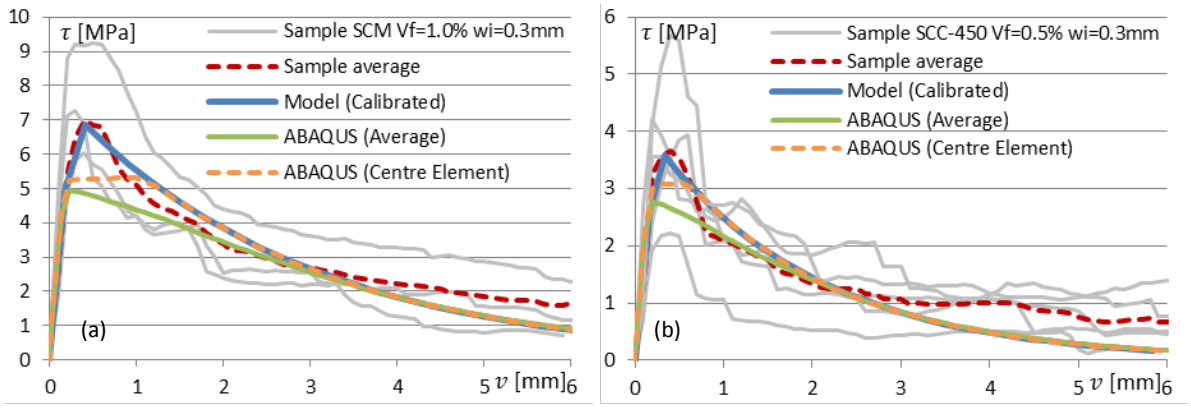

Fig. 6.21 – S12 vs v for (a) SCM Vf=1.0% wi=0.3mm and (b) SCC-450 Vf=0.5% wi=0.3mm

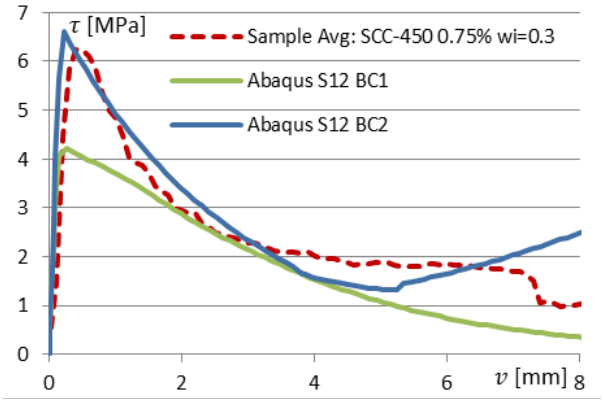

Fig. 6.22 – S12 vs *v* for BC1 (Both inner supports restrained horizontally) and BC2 (One inner support restrained horizontally)

Typical results for ABAQUS output S22 and v-w:

The softening model employed for the normal stress parallel to the crack is successful in minimising the corresponding stress as can be seen in *Fig. 6.23a*. *Fig. 6.23b* shows the typical discrepancy between the experimental and Abaqus shear vs. crack opening displacement. In the case of the alternative boundary condition (BC2), the normal strain and stress parallel to the crack becomes unrealistically high. Recall that the softening of the corresponding stiffness (D^{c2} in *Eq. 6.11*) is a function of the crack width, which becomes negative during the shear step and is therefore not reliable in this case *Rots (ICF7, 1989)*.

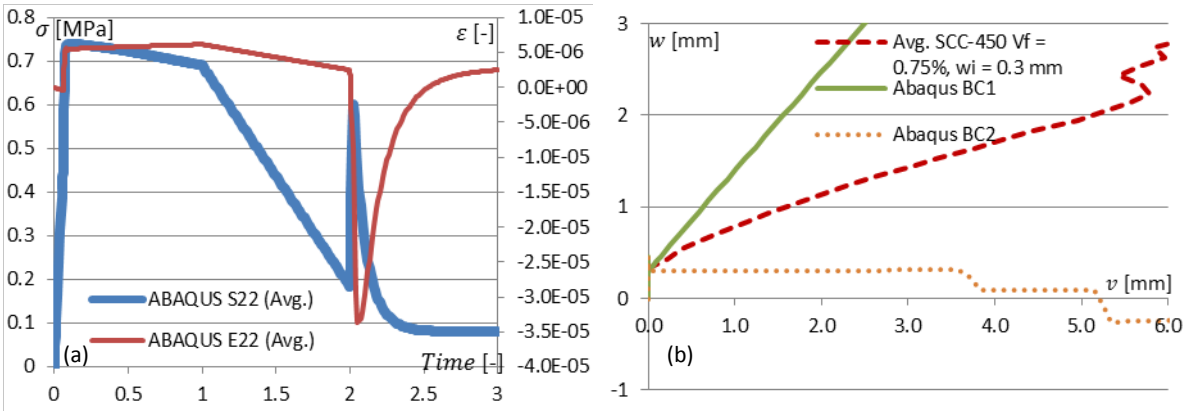

Fig. 6.23 – (a) S22-E22 and (b) w-v (Abaqus BC1 and BC2 vs Average sample data)

6.7 Empirical link between Micro and Meso-scale data

An empirical model which utilises the data obtained at the Micro and Meso-scale of observation, as well as the analysis of the fibre distribution, simulates the fibre component of the composite Mode II response.

6.7.1 Model description

A simple empirical model can be derived from the experimental data obtained at the Meso and Micro-scale of observation. The main principle of the model is to superimpose/reconcile and validate the fibre mechanisms (Micro-scale) and the composite (Meso-scale) fracture response. Given the total fibre count and fibre orientation distribution, the number of fibres that fall inside each defined orientation interval can be determined. The average transverse pull load vs. normal displacement response (*Fig. 5.32b*) from *Chapter 5* and shown here again in (*Fig. 6.24*) for each fibre orientation (θ = -60°, -30°, 0°, +30° and +60°) is then multiplied by the number of fibres in each corresponding orientation interval defined in *Table 6.6* and added together to estimate the total fibre contribution to the composite response (in the form of total shear load vs. normal displacement/crack opening). Finally, for each composite and fibre volume fraction, the average shear displacement (δ_v) - crack width (w_c) relation at the Meso-scale is used to estimate the shear load vs. shear displacement relation.

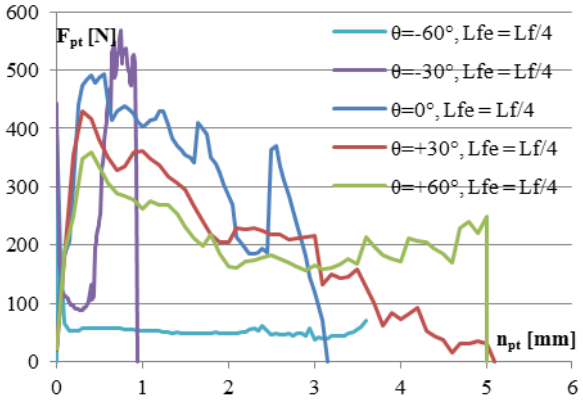

Fig. 6.24 – Transverse pull-out load (F_{pt}) vs. normal pull-out displacement (n_{pt}) for average response θ = -60° to +60°, $L_{fe} = L_f/4$

A note on the fibre orientation distribution: The fibre orientation distribution as shown in *Fig. 5.22* is the total 3D/volumetric orientation distribution and a distinction is not made between 2D "positive" or "negative" fibre orientations as defined in *Fig. 5.26*. Each fibre orientation is therefore assigned an orientation interval in the range [0° to 90°], as defined in *Fig. 5.22* and *Table 6.6*. The following simplifications are assumed: The fibre orientations θ = -30° and +30° share the 3D orientation interval [15°-45°] equally i.e. θ = -30° accounts for 50% of the fibres in this interval and θ = +30° accounts for the other 50%. The same is assumed for θ = -60° and θ = +60° for the interval [45°-75°]. Fibre orientation θ = 0° accounts for the interval [0°-15°]. The interval [75°-90°] is assumed to not contribute to the pull-out resistance.

Also recall that the orientation analyses are done in regions away from the shear plane (*Fig. 5.21*). Due to the change in geometry (notches) at the shear plane, the fibre orientation will be different within the vicinity of the shear plane compared to regions away from the shear plane (see *Figs. 5.23-25*). Future studies should analyse the fibre orientation distribution in the shear plane before fracturing the specimens, to avoid this discrepancy.

Table 6.6 – Fibre orientation interval definition

Fibre orientation, θ	2D interval	3D interval	% of fibre count for interval
Total range	[-90°; +90°]	[0°; 90°]	
-60°	[-45°; -75°]	[45°; 75°]	50%
-30°	[-15°; -45°]	[15°; 45°]	50%
0°	[-15°; +15°]	[0°; 15°]	100%
+30°	[+15°; +45°]	[15°; 45°]	50%
+60°	[+45°; +75°]	[45°; 75°]	50%
Other	[-75°; -90°], [+75°; +90°]	[75°; 90°]	No contribution assumed

6.7.2 Model input

The model requires the following input:

1. The shear/transverse pull-out load (F_{pt}) vs. normal displacement (n_{pt}) for each of the fibre orientations considered (*Fig. 6.24*). Only the results from the embedded length $L_f/4$ are used. $L_f/4$ is assumed to be representative of the average embedded length.
2. The fibre count, i.e. the number of fibres in the shear plane of the Meso-scale test. The fibre count is determined from destructive and non-destructive (CT-scan) methods (see *Table 5.9* for SCC-450)
3. The fibre orientation distribution for each fibre dosage (V_f = 0.5%, 0.75% & 1.0%), as determined for SCC-450 (*Fig. 5.22*)
4. The shear displacement (δ_v) - crack width (w_c) relation at the Meso-scale for each composite (SCM, SCC-450 and SCC-600) and fibre dosage (V_f = 0.5%, 0.75% and 1.0%)

6.7.3 Model validation

Figs. 6.25-27 compares the model of the composite Micro-scale fibre mechanism to the actual composite response at the Meso-scale. Only V_f = 0.75% is shown for the composite SCM and SCC-450. The complete data set can be found in *Addendum G*. The model is validated with respect to the shear load (F_v) vs. normal displacement/crack opening (w_c) and shear displacement (δ_v), for both initial crack widths $w_i \approx$ 0.1 mm and 0.3 mm. As mentioned, the fibre orientation distribution is determined from the CT-scan data (*Figs. 5.23-25*). Comparisons are made in terms of peak shear load, residual response, initial stiffness (prior to peak load) and composite type i.e. SCM, SCC-450 and SCC-600.

Peak shear load

In general, a better approximation is made for an initial crack width, $w_i \approx$ 0.3 mm. Recall that the model only considers the fibre component. It is therefore postulated that at smaller initial crack width, $w_i \approx$ 0.1 mm, shear interface cohesion and roughness/friction is still present, contributing to peak shear load. As the crack width, w_c increases, the model closely simulates the Meso-scale response, as the majority of the shear interface cohesion and friction is no longer present. Only the fibre mechanism provides resistance at this stage.

Residual/tail end response

In general, the fibre only model simulates the residual/tail end response reasonably well.

Initial stiffness (before and at peak shear load)

The model does not simulate the initial stiffness before and up to peak shear load. The stiffness is underestimated and in most cases, the modelled peak shear load is offset from the actual peak shear load with a significant margin. This is however to be expected for a model that only simulates the fibre component and does not account for the composite stiffness provided by the shear interface cohesion and shear interface roughness or aggregate interlock.

Effect of composite parameters i.e. SCM vs SCC-450 vs. SCC-600

The fibre orientation distribution is determined for SCC-450 only and is used for SCM and SCC-600. This may account for differences in model performance for each composite. In the case of SCC-600 V_f = 0.5%, the peak shear load is underestimated, even for w_i = 0.3 mm. The larger coarse aggregate content of SCC-600 likely accounts for a larger contribution of shear interface roughness that is not incorporated in the model.

6.7.4 User-defined fibre orientation analysis and discussion

A total of 9 user defined fibre orientation distributions (*Table 6.7* (*Zeranka & van Zijl, 2015*)) are created and compared to the composite SCC-450 V_f = 0.75% in *Fig. 6.28*. This serves to demonstrate the range of the model for w_i = 0.1 mm and 0.3 mm.

The empirical 'fibre-only' model can be improved with a larger sample size at the Micro and Meso-scale. The fibre pull-out response should also be investigated for other fibre orientations and embedment lengths. With respect to the fibre distribution (fibre count and orientation distribution) determined via CT-scanning, a larger sample size is also recommended. In this instance the fibre orientation distribution is only analysed for three specimens, one for each fibre dosage, from the SCC-450 composite. As mentioned, CT-scanning was only performed after the specimens were fractured, consequently the fibre orientation distribution is analysed in regions away from the shear plane, where the fibres are not disturbed from their original orientation. In future, the fibre orientation distribution should be analysed in the vicinity of the shear plane, before the specimens are fractured.

Table 6.7 – Fibre orientation distributions (as a percentage of fibre count) (*Zeranka & van Zijl, 2015*)

%	θ = +60°	θ = +30°	θ = 0°	θ = -30°	θ = -60°
1	20	20	20	20	20
2	15	25	20	25	15
3	10	30	20	30	10
4	5	35	20	35	5
5	0	40	20	40	0
6	15	27.5	15	27.5	15
7	10	35	10	35	10
8	5	42.5	5	42.5	5
9	0	50	0	50	0

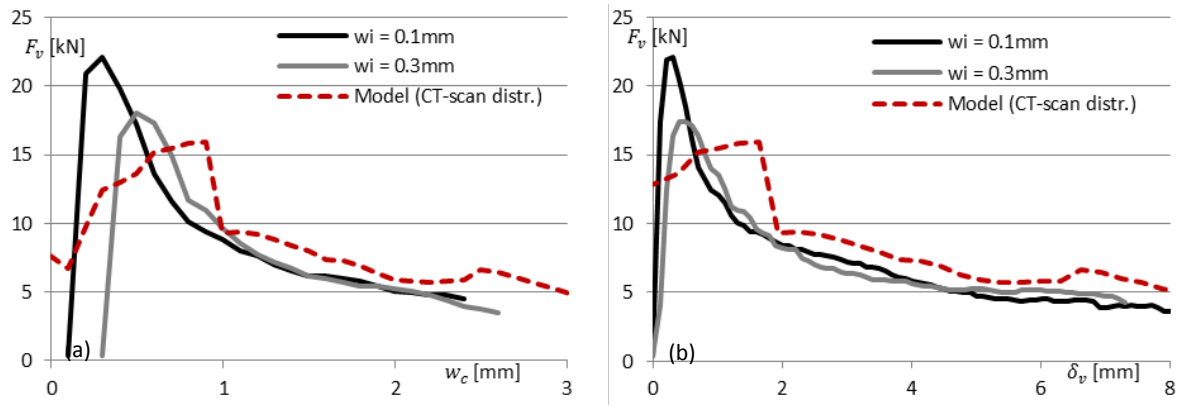

Fig. 6.25 – Shear load (F_v [kN]) vs. (a) normal displacement/crack opening (w_c [mm]) and (b) shear displacement (δ_v [mm] for SCC-450 V_f = 0.75%

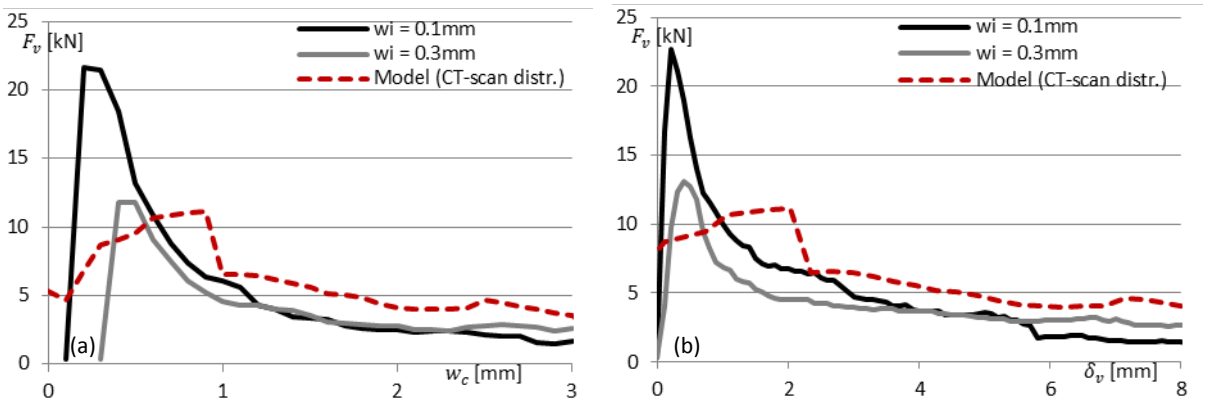

Fig. 6.26 – Shear load (F_v [kN]) vs. (a) normal displacement/crack opening (w_c [mm]) and (b) shear displacement (δ_v [mm] for SCM V_f = 0.75%

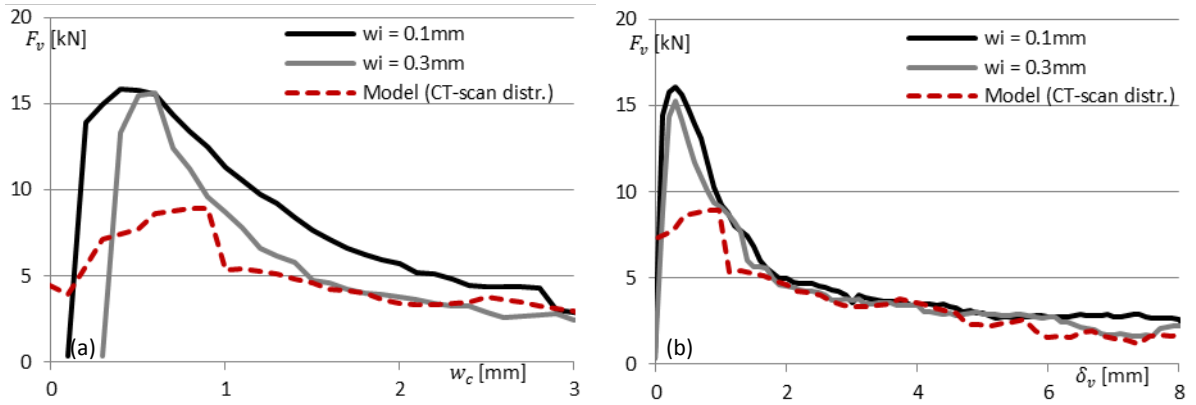

Fig. 6.27 – Shear load (F_v [kN]) vs. (a) normal displacement/crack opening (w_c [mm]) and (b) shear displacement (δ_v [mm] for SCC-600 V_f = 0.5%

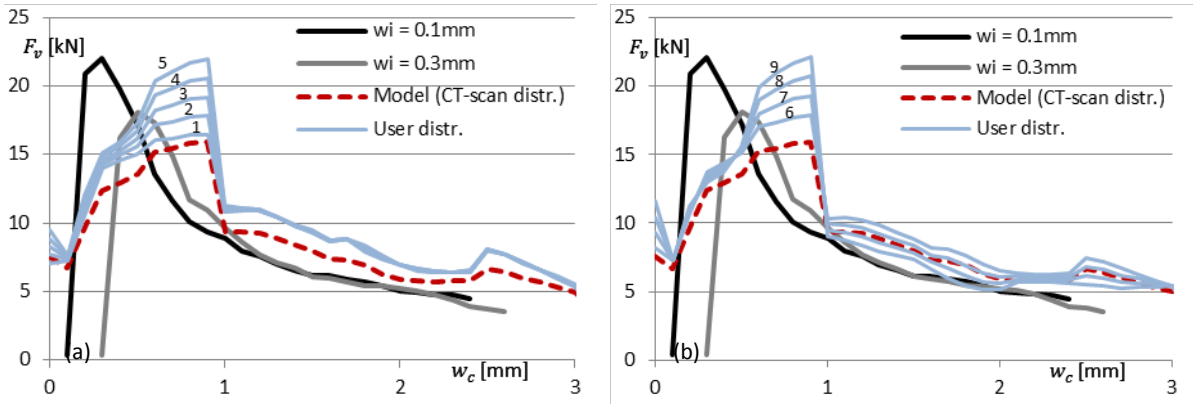

Fig. 6.28 – Shear load (F_v [kN]) vs. normal displacement/crack opening (w_c [mm]) for SCC-450 V_f = 0.75%: User-defined fibre orientation distribution (a) Distribution 1-5 (b) Distribution 6-9 (*Table 6.7*)

Summary and conclusions

The numerical and empirical models developed simulate the composite response well, given their relative simplicity and limited experimental data. In structural applications, continuum elements are the most appropriate for analysis. Limitations are however encountered for continuum elements and this particular application due to unstable/unreliable results at larger shear-slip (observed for BC2). This behaviour is mitigated in this instance by choosing different boundary conditions (BC1). Alternatively, this can also be resolved via the use of discrete/interface elements and a corresponding interface material model instead of continuum elements. However, the general application of discrete elements requires complex and computational demanding re-meshing algorithms to be implemented correctly. Future research should attempt to link the Mode I and Mode II response and account for dilatancy and confinement across the shear interface.

Chapter 7

Conclusions and Recommendations

Conventionally reinforced concrete is prone to cracking and liable to reduce the durability and serviceability of the structure. One solution is to reinforce and strengthen, in terms of residual strength and ductility, the concrete composite itself.

Today steel fibre reinforcement is utilised commercially for both non-structural and structural applications and has the potential to partially or totally replace conventional reinforcement. Methods for material characterisation, constitutive modelling and design must be improved in order to achieve greater structural application of SFRC. Analogous to existing numerical tools for RC membrane elements, research towards a constitutive material model and numerical procedure for the analysis of SFRC membrane elements is essential. A direct and rational approach to model the generic material response also has the potential to allow for tailoring and optimisation in material and structural design.

The first outcome of this dissertation is the adaptation of a composite design procedure for SCC in order to develop a SFR-SCC. The composite is then classified in terms of standard performance indicators and testing procedures. The primary outcome of this dissertation is to characterise the Mode I and Mode II fracture at the Micro and Meso-scale of observation. This required the design, fabrication and execution of experimental tests. The data gathered from the characteristic tests are used as input and validation for the development of a constitutive model. The constitutive model is implemented in a numerical procedure via a user-material interface, denoted *UMAT* in Abaqus. A FE representation of the Iosipescu shear test is used to validate the material model. Finally, an empirical model is also developed which reconciles the Micro and Meso-scales for Mode II fracture.

This chapter summarises the main conclusions and recommendations from *Chapter 2* to *Chapter 6* and concludes this dissertation.

7.1 Conceptual and methodological framework

A large database of experimental data and empirical models on scaled or full-scale shear-critical structural beams has accumulated. It is concluded from a literature survey that material-level characterisation and constitutive modelling are more beneficial in facilitating the demand for greater structural application of SFRC. Consequently, the primary mechanisms governing the fundamental behaviour of SFRC need to be characterised in order to produce a direct definition of the material's constitutive model.

Limited work has been done on the direct shear response of fibre reinforced concretes. Even fewer investigations attempt to link the Micro-scale (i.e. the transverse pull-out of steel fibres) to the Meso-scale for Mode II fracture. At the time of publication of *Soetens & Matthys (2012)*, only one study, *Lee & Foster (2006)* was known that applies this method for investigating the Mode II fracture of SFRC. *Soetens & Matthys (2012)* and *Lee & Foster (2006)* observed similar characteristic behaviour, despite using different testing methods.

7.2 Composite design and classification

The composite design method optimises the composite performance at the level of the paste, mortar, concrete and fibre-reinforcement.

7.2.1 Compressive strength development

The average 28-day compressive strength ranges between 50 MPa and 60 MPa, with an average of 56 MPa across all test series. Steel fibre addition in the range of 0.5-1.0% of concrete volume marginally increases compressive strength compared to the unreinforced mortar or concrete developed in this research. On average, 70-75 MPa 112 day strength is achieved.

7.2.2 Elastic compression modulus

For the moderate fibre volume (0.5-1.0% of concrete volume) used in this dissertation, fibre reinforcement has minimal or no effect on the elastic modulus and an average elastic modulus of 41.2 GPa is obtained across all fibre dosages. The test setup used is believed to over-estimate the stiffness of the composite by 3 – 4 GPa (compared to *Tab. 5.1-7 fib Model Code 2010*). Future studies using this particular setup should take the necessary steps to improve the experimental setup in terms of instrumentation and specimen alignment.

7.2.3 Wedge-splitting test

As anticipated, the ductility, residual capacity and fracture energy increases for a larger fibre dosage. Based on the wedge splitting test, an optimum fibre dosage for this mix design is 0.75%. Increasing the fibre volume fraction beyond 0.75% to 1.0% has no significant benefit for mechanical response.

7.2.4 Flexural response

ASTM C1609

During initial trials, the *RC-65/35-BN* fibre performed the best overall, as may be expected for a fibre with higher aspect ratio. In general, a fibre dosage greater than 1.0% becomes less effective. This is especially evident for the *RL-45/35-BN* fibre type. Apart from the *RL-45/35-BN* with V_f = 0.5%, all trial mixes considered meet the minimum performance requirements ($f_{300}^D/f_1 \geq 90\%$ and $f_{150}^D/f_1 \geq 75\%$) for structural shear design as outlined in *ACI 318-08 (5.6.6.2)*. The *RC-65/35-BN* fibre is chosen for all experimental programs and given the material performance and workability requirements for SCC, a maximum fibre dosage of 1.0% is proposed.

For the final SFR-SCC design (*Table 3.3*, Fibre type = *RC-65/35-BN*, V_a = 450 kg/m^3, a = 9.5mm) only the 1.0% fibre dosage complies with the recommended performance requirements. This is directly attributed to the greater first peak strength (f_1) achieved for this higher compressive strength class of concrete compared to the preliminary mix design (*Tables 3.2 & 3.13*). It is important to recognise that the compressive strength of the composite still increases significantly beyond the 28-day strength, with 70+ MPa achieved at 112-day age (*Fig. 3.9 (a)*). Future studies that follow on this work should be cognisant of the effect the compressive strength has on the embrittlement of the fibre-reinforced composite. Unfortunately no further time could be allotted to optimise the composite further.

EN 14651 (RC-65/35-BN only)

As observed for the wedge-splitting test and to some extent also the *ASTM C1609* data, material performance does not improve significantly for a fibre dosage larger than 0.75%. In some cases a higher fibre dosage of 1.0% performs worse than 0.75%. This may be attributed to poorer consolidation for larger fibre dosages. Increasing the fibre dosage does however reduce the amount of scatter/variability in the data. Based on the average values (not the characteristic values), the 0.5%, 0.75% and 1.0% composite is classified as “5b”, “6b” and “6b” respectively. *Eqs. 3.4-5* are also satisfied on the basis of the average values given in *Table 3.15*, making this material appropriate for structural use according to *fib Model Code 2010*.

7.3 Meso and Micro-mechanical investigation of Mode I fracture

7.3.1 Experimental investigation at the Meso-scale

Specimen design

Despite the process of numerical refinement employed, a preliminary investigation shows that specimens, unreinforced within the transition zone are prone to failure outside the gauge zone, with failure occurring either at the clamping edge or within the transition zone. Apart from the limitations of a simplified elastic analysis, one conjecture could be that specimen pre-damage as a result of a combination of specimen shrinkage in the mould, handling, clamping and pre-loading, could cause specimen failure outside the gauge zone. An experimental investigation is conducted to determine the reinforcement required in the transition zone, to prevent premature failure in these areas.

In addition to reinforcing the specimen, a 4.5±0.5 mm saw-cut notch is also made in the middle of the specimen on both short sides. The notch reduces the section by 10 - 12.5% and forces the crack

to initiate and propagate in the notched section. The use of a notch is suitable for the determination of the stress vs. crack-opening response and strain softening composites where localised failure is expected. It is important to note that as a consequence of introducing a notch in the specimen, the stress distribution at the fracture plane is no longer uniform. Given this outcome, a more efficient geometry would simply be a prismatic specimen with a 100 x 50 mm section. The specimen will still have to be reinforced outside the gauge zone and depending on the nature of the material (strain hardening or softening), a notch may also be required.

Test results and discussion
As anticipated, post-fracture toughness is increased for a larger fibre dosage. This is less evident in the absence of coarse aggregate (SCM) and is attributed to the small difference between the fibre count for V_f = 0.75% ($N_f = 52$) and V_f = 1.0% ($N_f = 59$). Greater post-fracture toughness is observed for SCM compared to SCC for the same fibre dosage V_f = 0.5% and 0.75%. The most likely explanation is the better consolidation observed for SCM compared to SCC and the impact of a larger coarse aggregate particle size distribution on the fibre distribution. This is confirmed by the lower fibre count for SCC for V_f = 0.5% and 0.75%. SCC and SCM have a similar average response for V_f = 1.0%. As with the stress-crack width data, the fracture energy corresponds well with the fibre count.

7.3.2 Experimental investigation at the Micro-scale

Increasing the fibre inclination angle from 0° to 30°, marginally increases the peak and residual pull-out resistance. However, a larger inclination angle of 60° drastically diminishes the pull-out resistance. This is attributed to the spalling failure of the surrounding mortar, which results in the fibre bond and anchorage not being fully engaged.

In the case of an embedded fibre without end-anchorage, the fibre inclination has a more prominent effect, compared to a fibre with anchorage. Increasing the fibre inclination angle from 0° to 30°, increases the peak and residual pull-out resistance. Increasing the inclination angle further to 60°, shifts the peak pull-out resistance to occur at a larger pull-out displacement. In addition, a greater pull-out resistance is observed, but is accompanied by a reduction in ductility.

The fibre end-anchorage constitutes a significant portion of the total pull-out resistance for fibre inclination angles 0° and 30°. This is not the case for an inclination angle of 60°. Up to a pull-out displacement of approximately 2 mm, the average response is similar, after which the pull-out resistance drops drastically for the fibre with end-anchorage, compared to the fibre without end-anchorage. It is likely that the end-anchorage is influential in the spalling effect that is present for this fibre inclination angle, especially at larger pull-out displacements, where the end-anchorage is engaged. A more detailed investigation could characterise the effect of fibre inclination, end-anchorage and 3D orientation of end-anchorage on the spalling effect.

The test setup and procedure adopted in this study provide repeatable data and are recommended for future research. The *RC-65/35-BN* fibre used, was found to be susceptible to corrosion during water-curing. A neutral curing method, with no loss or gain of moisture, should prevent corrosion and is also believed to be representative of the conditions of an embedded fibre at a Meso or Macro-scale. Only a limited parameter set is investigated in this study and can be expanded to fully characterise the axial pull-out response in terms of fibre type, embedded length, inclination angle,

anchorage and matrix composition. CT-scans of single embedded fibres at different stages of pull-out displacement could also aid in characterising the underlying mechanisms.

7.4 Meso and Micro-mechanical investigation of Mode II fracture

7.4.1 Experimental investigation at the Meso-scale

Specimen design

Preliminary Iosipescu shear tests showed that specimens do not reliably fail in the shear plane. Compression splitting failure at the points of load application induced diagonal cracking between the two inner supports. It is recommended that the contact stress and the potential for compressive splitting failure at the points of load application also be considered. The introduction of a saw-cut notch and pre-cracking in the shear plane is however sufficient to localise shear failure to the shear plane.

It can be argued that the refinement of the specimen notch geometry via numerical analysis in the elastic domain is not necessary, considering the introduction of a saw cut notch on both sides of the shear plane after the fact. The saw cut notch likely invalidates the analysis results. As long as the same shear plane height (h_0) is used, a simplified notch geometry e.g. triangular or saw-cut, could be used. Experimental trials on different notch geometries are recommended. Future studies should also consider the effect a cast-in-notch has on the casting procedure and consequently the fibre dispersion and orientation. Future studies should include the degree of constraint across the shear interface as a parameter for both the single fibre and composite tests. The Ohno beam and Iosipescu shear test only represent an unconstrained condition, where free dilatancy is permitted. The push-through method as used by *Soetens & Matthys (2012)* is considered to be a fully constrained condition.

Experimental program and production method

The specimens tested in this study are all pre-cracked prior to shear testing. Un-notched and uncracked specimen did not fail in pure shear. Shear testing of uncracked specimens will therefore require modifications to the specimen geometry.

Emphasis is placed on the fibre component and mechanism. The composites developed in this study including SCM, SCC-450 and SCC-600, all have relatively low coarse aggregate contents. Future studies should incorporate larger coarse aggregate contents and sizes to investigate the potential synergy between fibre reinforcement and shear interface roughness.

Test setup and procedure

The cyclic tensile loading and pre-cracking phases are successful in producing the target unloaded crack widths and this method is recommended.

The non-contact measurement method (Aramis DIC) proved invaluable in determining the specimen shear displacement and rotation. Careful consideration should be given to the instrumentation used in the test when designing the specimen and test configuration. It must be noted that a significant amount of post-processing is required to extract the desired data when using this method.

Conclusions and recommendations

Test results and discussion: Pre-cracking

It is postulated that the variability in the initial peak strength may be attributed to the combination of the cast-in wedge notch and the saw-cut notch, which may not be conducive to a uniform stress distribution in the vicinity of the shear plane and notch apex at initial cracking. The significant variability in the post-cracking capacity is largely attributed to the high variability in fibre count for some of the composites, with a maximum coefficient of variation of 36.6%. However, consistent residual crack widths are obtained and in most cases, a uniform crack could be achieved in the shear plane, which is ultimately the objective.

Test results and discussion: Iosipescu shear test

Effect of fibre dosage: In general, the peak shear strength increases with increasing fibre dosage. Considering the increase in peak shear strength relative to the peak shear strength for V_f = 0.5%, fibre reinforcement is more beneficial at a larger (0.3 mm) initial crack width and coarse aggregate fraction (SCC-450). The effect of fibre dosage on the crack width-shear displacement response is marginal for SCM at both initial crack widths (w_i = 0.1 mm & 0.3 mm). In the case of SCC-450 however, the larger fibre dosage of 0.75% and 1.0% are effective at reducing the crack width for a given shear displacement. As anticipated, the fracture energy also increases with increasing fibre dosage.

However, any comparison between the composites SCM and SCC-450 needs to take into account the difference in fibre count between SCM and SCC-450. The average manual fibre count is: 24 & 30 (V_f = 0.5%), 35 & 50 (V_f = 0.75%) and 52 & 82 (V_f = 1.0%) for SCM and SCC-450 respectively. SCC-450 on average has a significantly higher fibre count compared to SCM, especially for V_f = 0.75% and 1.0%.

Effect of initial crack width: As expected, a reduction in the peak shear strength is observed for a larger initial crack width. The drop in peak shear strength is reduced at a larger fibre dosage (V_f = 1.00% for SCM and $V_f \geq$ 0.75% for SCC-450). Increasing the initial crack width from 0.1 mm to 0.3 mm has a marginal effect on the peak shear strength for SCC-600 (V_f = 0.5%). It is evident from this result that fibre reinforcement and aggregate interlock/shear interface roughness synergise well to limit the effect of initial crack width or cracking in general. The effect on the fracture energy is similar to that of the peak shear strength. The fracture energy drops at a larger initial crack width, but the drop is diminished for a larger fibre dosage and increased coarse aggregate fraction.

Effect of aggregate fraction: The differences observed between the composites: SCM, SCC-450 and SCC-600 are attributed to the differences in fibre count. If the fibre count were to be balanced out between the composites, it is believed that the responses would be similar. As discussed in *Chapter 3*, the coarse aggregate content and size for SCC-450 and SCC-600 are relatively low compared to what is typically used and recommended in practice, even for SCC. A small contribution by shear interface roughness or aggregate interlock is therefore not too surprising. Achieving an adequate mortar and concrete workability for each fibre dosage, to facilitate the fibre mechanism, is of higher priority for this study.

Analysis of fibre distribution via CT-scanning

The CT-scanning facility provides valuable insight into the fibre distribution and the ability to analyse and quantify the fibre orientation distribution is a powerful tool. A larger sample size is recommended in future studies to better characterise the fibre distribution.

Analysis of the specimen fibre count suggests a 2D-random fibre distribution for SCC-450 V_f = 0.75% and 1.0%. All other composites have a 3D-random distribution. Again, a larger sample size is needed to confirm this. The specimen dimensions, especially the specimen depth and shear plane size need to be increased for increased aggregate content and size, as well as for a fibre dosage V_f > 0.75%.

7.4.2 Experimental investigation at the Micro-scale

One of two failure modes is observed, either fibre pull-out or fibre rupture. In general the behaviour observed for the different fibre orientations is similar to tests conducted using the shear push-off (*Lee & Foster, 2006*) and shear push-through (*Soetens & Matthys, 2012*) methods.

Positive fibre orientations (θ = +30° and +60°) exhibit pull-out failure exclusively. For negative fibre orientations (θ = -30° and -60°), substantial transverse displacement occurs before the fibre is fully engaged. This is attributed to the snubbing effect as also observed by *Lee & Foster (2006)* and *Soetens & Matthys (2012)*. Fibre rupture in conjunction with snubbing or pull-out is the predominant mode of failure in this case. A fibre orientation in the region of θ = 0°, represents a transition zone between fibre pull-out and fibre rupture and both failure modes are likely to occur.

The following was found when comparing the transverse pull-out response of the embedded lengths $L_f/4$ and $L_f/2$, for each fibre orientation. If the variability of the data is taken into account, only marginal differences are observed between the two embedded lengths. Where fibre pull-out is dominant (θ = +30° and +60°), end anchorage is believed to be the primary resistive mechanism (as found in axial pull-out tests performed in *Chapter 4*), because peak pull-out resistances are similar for $L_f/4$ and $L_f/2$. However, a longer embedded length does result in more ductility due to the longer fibre channel and frictional pull-out resistance still present. Where fibre bending and eventual fibre rupture is present (θ = -30° and -60°), the effect of embedded length is believed to be negligible, because the failure mechanism is localised dowel action, fibre yielding and rupture in the vicinity of the shear plane and not fibre pull-out.

Additional fibre orientations (e.g. θ = ±15°, ±45° and ±75°) and embedment lengths (e.g. $L_f/6$ and $L_f/8$) should be investigated to characterise the transverse pull-out response even further.

The nature of the test configuration can be restrictive due to excessive rotation of the specimen at large shear displacements, specifically for a larger fibre embedded length. A DIC system, such as the one used in this study is needed in order to capture the specimen rotation. Even if DIC is used, it may still not be possible to test the complete pull-out or fibre rupture response. In some cases for the embedded length $L_f/2$, undue specimen rotation would occur, which would influence the result at large displacements. This needs to be mitigated by restricting the fibre length, modifying the test or using an alternative method where specimen rotation is less, such as the shear push-off (*Lee & Foster, 2006*) or push-through (*Soetens & Matthys, 2012*) methods.

7.5 Constitutive model and numerical verification

Continuum FE modelling is utilised to model the cracked SFRC. A smeared fixed-crack approach is considered as a first choice. Research that follows on this work should investigate other crack-modelling strategies and compare modelling performance.

The Mode I and Mode II material models are successfully verified by the single element test for the boundary conditions considered. The material model is also objective with respect to element size. Mixed mode behaviour is not addressed in this study. Mode I and Mode II fracture is therefore decoupled and no interaction is considered for the most part. The influence of dilatancy and confinement across the shear interface is therefore also ignored. An empirical model which reconciles the fibre component (Micro-scale) with the composite (Meso-scale) response for Mode II fracture is also produced.

7.5.1 Model verification via Meso-scale Iosipescu shear test

In all analyses, the Abaqus global shear stress S12 matches the calibrated model. The only discrepancy that occurs between the calibrated model and the Abaqus output, is in the computation of the initial shear stiffness and consequently the peak shear stress. This is attributed to the fact that the initial shear stiffness is a function of the crack width, which is overestimated by the Abaqus model. As a result the shear stiffness and peak shear stress is underestimated. This error is less prevalent for the smaller initial crack width w_i = 0.1 mm, which is expected.

A comparison is made between the two boundary conditions analysed, 'BC1' and 'BC2'. 'BC2' gives a better approximation of the peak shear stress compared to 'BC1', but at larger shear displacements, the shear stress increases again and deviates from the material model. This phenomenon has been characterised by *Rots (ICF7, 1989)* as "stress-locking", which occurs in continuum and smeared crack modelling when fixed cracks with significant shear retention lead to stress rebuild. In addition to improvements to the material model, such as consideration of Mode I & II interaction, alternative numerical methods, including the use of other element types (e.g. cross-triangles) should be tested first to alleviate this problem.

7.5.2 Empirical link between Micro and Meso-scale

The quantification of the fibre orientation distribution within the composite allows for the superimposition of the single fibre transverse pull-out responses at different fibre orientation angles. In this way, the fibre reinforcement component of the composite can be extracted and analysed.

In general, a better approximation is made for an initial crack width, $w_i \approx 0.3$ mm. Recall that the model only considers the fibre component. It is therefore postulated that at smaller initial crack width, $w_i \approx 0.1$ mm, shear interface cohesion and roughness/friction is still present, contributing to peak shear load. As the crack width, w_c increases, the model closely simulates the Meso-scale response, as the majority of the shear interface cohesion and friction is no longer present. Only the fibre mechanism provides resistance at this stage. Further study is needed to characterise and model the aggregate interlock component and confirm this postulation.

The empirical 'fibre-only' model can be improved with a larger sample size at the Micro and Meso-scale. The fibre pull-out response should also be investigated for other fibre orientations and embedment lengths. With respect to the fibre distribution (fibre count and orientation distribution) determined via CT-scanning, a larger sample size is also recommended. In this instance the fibre orientation distribution is only analysed for three specimens, one for each fibre dosage, from the SCC-450 composite. As mentioned, CT-scanning was only performed after the specimens were fractured, consequently the fibre orientation distribution is analysed in regions away from the shear plane, where the fibres are not disturbed from their original orientation. In future, the fibre

orientation distribution should be analysed in the vicinity of the shear plane, before the specimens are fractured.

Summary

The numerical and empirical models developed simulate the composite response well, given their relative simplicity and limited experimental data. In structural applications, continuum elements are the most appropriate for analysis. Limitations are however encountered for continuum elements and this particular application due to unstable/unreliable results at larger shear-slip (observed for BC2). This behaviour is mitigated in this instance by choosing different boundary conditions (BC1), but the model then overestimates the crack opening displacement. Alternatively, this can also be resolved via the use of discrete/interface elements and a corresponding interface material model instead of continuum elements. However, the general application of discrete elements requires complex and computational demanding re-meshing algorithms to be implemented correctly. Future research should attempt to link the Mode I and Mode II response and account for dilatancy and confinement across the shear interface. Finally, the material model needs to be validated on the Macro-scale/structural level.

References

Abaqus 6.10 Finite Element Analysis software, SIMULIA™ by Dassault Systèmes ®

ACI 544.1R-96, Report on fiber reinforced concrete, Farmington Hills, Michigan: American Concrete Institute, 1996.

ACI Committee 318, 2008. *Building code requirements for structural concrete (ACI 318-08) and commentary (ACI-318R-08)*, MI: Farmington Hills.

Adebar, P., Mindess, S., St.-Pierre, D. & Olund, B., 1997. Shear tests of fiber concrete beams without stirrups. *ACI Structural Journal*, January-February, 94(1), pp. 68-76.

Al-Ta'an, S. A. & Al-Feel, J. R., 1990. Evaluation of shear strength of fibre-reinforced concrete beams. *Cement & Concrete Composites*, Volume 12, pp. 87-94.

Arakawa, T. & Ohno, K. (1957). Shear Tests of Reinforced Concrete Beams by Special Type of Loading (In Japanese), *Transactions of the Architectural Institute of Japan*, 57: 581-584.

Aramis v6.1 User Manual – Software, 2008. GOM Optical Measuring Techniques, www.gom.com

Ashour, S. A., Hasanain, G. S. & Wafa, F. F., 1992. Shear behavior of high-strength fiber reinforced concrete beams. *ACI Structural Journal*, March-April, 89(2), pp. 176-184.

ASTM C 1609/C 1609M-07, 2007. Standard Test Method for Flexural Performance of Fiber-Reinforced Concrete (Using Beam with Third-point Loading. ASTM International, United States.

Bazant, Z. P. & Oh, B. H., 1983. Crack band theory for fracture of concrete. *Materials and Construction,* May, 16(3), pp. 155-177.

Bekaert Dramix®: Reference sheet – Park Oceanographic, www.bekaert.com/building.

Bernardi P., Cerioni R., Michelini E., 2012. Prediction of post-cracking behaviour in SFRC elements under in-plane stresses. *Proceedings: 4th International conference on crack paths (CP 2012)*, Gaeta, Italy. pp. 651 – 659

Boulekbache, B., Hamrat, M., Chemrouk, M. & Amziane, S., 2012. Influence of yield stress and compressive strength on direct shear behaviour of steel fibre-reinforced concrete. *Construction and Building Materials*, Volume 27, pp. 6-14.

Brühwiler, E. & Wittmann, F.H., 1990. The wedge splitting test, a new method of performing stable fracture mechanics tests. *Engineering Fracture Mechanics* 35.1, pp. 117–125.

BS EN 14651:2005+A1:2007. Test method for metallic fibre concrete – Measuring the flexural tensile strength (limit of proportionality (LOP), residual). *BSI Standards Publication*.

BS EN 12390-13:2013. Testing hardened concrete. Determination of secant modulus of elasticity in compression. *BSI Standards Publication*.

Cho, S. & Kim, Y., 2003. Effects of steel fibers on short beams loaded in shear. *ACI Structural Journal*, November-December, 100(6), pp. 765-774.

Cucchiara, C., Mendola, L. L. & Papia, M., 2004. Effectiveness of stirrups and steel fibres as shear reinforcement. *Cement & Concrete Composites*, Volume 26, pp. 777-786.

de Oliveira, F. L., 2010. Design-oriented constitutive model for steel fiber reinforced concrete. PhD-thesis, Universitat Politècnica de Catalunya.

de Villiers, J. P., 2015. Bond behaviour of deformed steel reinforcement in lightweight foamed concrete. M-thesis, Stellenbosch University.

Diana FEA. Manual. www.dianafea.com (Accessed on 08/2017)

Ding, Y., You, Z. & Jalali, S., 2011. The composite effect of steel fibres and stirrups on the shear behaviour of beams using self-consolidating concrete. *Engineering Structures*, Volume 33, pp. 107-117.

Ding, Y., Zhang, F., Torgal, F. & Zhang, Y., 2012. Shear behaviour of steel fibre reinforced self-consolidating concrete beams based on the modified compression field theory. *Composite Structures*, Volume 94, pp. 2440-2449.

Dinh, H. H., Parra-Montesinos, G. J. & Wight, J. K., 2010. Shear behaviour of steel fiber-reinforced concrete beams without stirrup reinforcement. *ACI Structural Journal*, September-October, 107(5), pp. 597-606.

Dinh, H. H., Parra-Montesinos, G. J. & Wight, J. K., 2011. Shear strength model for steel fiber reinforced concrete beams without stirrup reinforcement. *ASCE Journal of Structural Engineering*, October, 137(10), pp. 1039-1051.

du Plessis, A., le Roux, S.G. and Guelpa, A., 2016. The CT Scanner Facility at Stellenbosch University: an open access X-ray computed tomography laboratory. Nuclear Instruments and Methods in Physics Research Section B: Beam Interactions with Materials and Atoms, 384, pp.42-49.

EFNARC, 2002. *Specification and Guidelines for Self-Compacting Concrete*, February 2002, www.efnarc.org.

Eurocode 2, 2003. *Design of concrete structures*, prEN 1992 Ver. December 2003.

FIB Model Code, 2010. Fibre reinforced concrete. Draft Ver.

Furlan Jr., S. & de Hanai, J. B., 1997. Shear behaviour of fiber reinforced concrete beams. *Cement and Concrete Composites*, Volume 19, pp. 359-366.

Grünewald, S., 2004. Performance-based design of self-compacting fibre reinforced concrete, PhD-thesis, Technical University of Delft.

Hannant, D. J., 1978. Fibre cements and fibre concretes. Wiley, Chichester, UK.

Hillerborg, A., Modéer, M., Petersson, P. E., 1976. Analysis of crack formation and crack growth in concrete by means of fracture mechanics and finite elements. *Cement Concrete Res*, 6, pp. 773-782.

Hsu, T. T. C., Mau, S. T. & Chen, B., 1987. Theory of shear transfer strength of reinforced concrete. *ACI Structural Journal*, 84(2), pp. 149-160.

Iosipescu, N., 1967. New accurate method for single shear testing of metals, *J. Materials*, 2(3): 537-566.

JSCE-SF6, 1990. Method of test for shear strength of steel fiber reinforced concrete (SFRC), Tokyo: Japan Society of Civil Engineers.

JSCE-G 553-1999. 2005. Test method for shear strength of steel fiber reinforced concrete. Standard Specifications for Concrete Structures, Test Methods and Specifications, Japan Society of Civil engineers (JSCE), Tokyo.

Juárez, C., Valdez, P., Durán, A. & Sobolev, K., 2007. The diagonal tension behaviour of fiber reinforced concrete beams. *Cement & Concrete Composites*, Volume 29, pp. 402-408.

Jůn, P. (2011): Behaviour of strain-hardening cement-based composites (SHCC) under monotonic and cyclic tensile loading, PhD-thesis, Technical University of Dresden.

Kim, K. S., Lee, D. H., Hwang, J. & Kuchma, D. A., 2012. Shear behavior model for steel fiber-reinforced concrete members without transverse reinforcements. *Composites: Part B*, Volume 43, pp. 2324-2334.

Kong, F. K. & Evans, R. H., 1987. *Reinforced and pre-stressed concrete*. 3rd ed. Wokingham, England: Van Nostrand Reinhold

Kupfer, H., Hilsdorf, H. K., and Rusch, H., 1969. Behaviour of concrete under biaxial stresses. *ACI Journal*, 66(8), pp. 656-666.

Kwak, Y., Eberhard, M. O., Kim, W. & Kim, J., 2002. Shear strength of steel fiber-reinforced concrete beams without stirrups. *ACI Structural Journal*, July-August, 99(4), pp. 530-538.

Lee, D. H. et al., 2012. Nonlinear finite element analysis of steel fiber-reinforced concrete members using direct tension force transfer model. *Finite Elements in Analysis and Design*, Volume 50, pp. 266-286.

Lee, G. G. & Foster, S. J., 2006. *Behaviour of steel fibre reinforced mortar in shear I: direct shear testing*, UNICIV Report R-444, Sydney.

Lim, D. H. & Oh, B. H., 1999. Experimental and theoretical investigation on the shear of steel fibre reinforced concrete beams. *Engineering Structures*, Volume 21, pp. 937-944.

Li, V. C., Ward, R. & Hamza, A. M., 1992. Steel and synthetic fibres as shear reinforcement. *ACI Materials Journal*, September-October, 89(5), pp. 499-508.

Malatesta, S. C. & Contreras, M. C., 2009. Shear behaviour of steel fiber reinforced concretes. *Revista Ingeniería de Construcción*, April, 24(1), pp. 79-94.

Mansur, M. A., Ong, K. C. G. & Paramasivam, P., 1986. Shear strength of fibrous concrete beams without stirrups. *ASCE Journal of Structural Engineering*, September, 112(9), pp.2066-2079.

Mattock, A.H., & Hawkins, N.M., 1972. Research on the shear transfer in reinforced concrete. *PCI Journal*, 17(2):55–75, March-April.

Mechtcherine, V. 2007. Testing Behaviour of Strain Hardening Cement-Based Composites in Tension - Summary of Recent Research. *High Performance Fiber Reinforced Cement Composites (HPFRCC5)* Mainz, Germany - July 10-13, 2007.

Meda, A., Minelli, F., Plizzari, G. A. & Riva, P., 2005. Shear behaviour of steel fibre reinforced concrete beams. Materials and Structures, April, Volume 38, pp. 343-351.

Minelli, F. & Plizzari, G. A., 2008. Shear design of FRC members with little or no conventional shear reinforcement. *Tailor Made Concrete Structures*, pp. 605-610.

Minelli, F. & Vecchio, F. J., 2004. Compression field modelling of fibre reinforced concrete: preliminary numerical study. *RILEM PRO 39*, September, pp. 885-894.

Minelli, F. & Vecchio, F. J., 2006. Compression field modelling of fiber-reinforced concrete members under shear loading. *ACI Structural Journal*, March-April, 103(2), pp. 244-252.

Mirsayah, A. & Banthia, N., 2002. Shear strength of steel fiber reinforced concrete. *ACI Material Journal*, Volume 99, pp. 473-479.

Naaman A.E., Fischer G., Krstulovic-Opara N. (2007) Measurement of tensile properties of fibre reinforced concrete: Draft submitted to ACI Committee 544. HPFRCC5, Mainz, Germany

Narayanan, R. & Darwish, I. Y. S., 1987. Use of steel fibers as shear reinforcement. *ACI Structural Journal*, May-June, 84(3), pp. 216-227.

Noghabai, K., 2000. Beams of fibrous concrete in shear and bending: experiment and model. *Journal of Structural Engineering ASCE*, February, 126(2), pp. 243-251.

Nooru-Mohamed M.B. Mixed-mode fracture of concrete: An experimental approach. PhD thesis, Delft University of Technology, 1992.

Okamura, H., Ouchi, M., 1999. Self-Compacting Concrete. Development, Present Use and Future. *First Int. Symposium on SCC*, Stockholm, Edited by Skarendahl and Petersson, RILEM publications PRO 7, Cachan, pp. 3-14.

Parra-Montesinos, G. J., 2006. Shear strength of beams with deformed steel fibers - Evaluating an alternative to minimum transverse reinforcement. *Concrete International*, November. pp. 57-66.

Rashid, Y. R., 1968. Analysis of prestressed concrete pressure vessels. *Nuclear Engineering and Design*, 7(4), pp. 334-344.

RILEM TC 162-TDF, 2001. Test and design methods for steel fibre reinforced concrete: Uniaxial tension test for steel fibre reinforced concrete – Recommendations, *Materials and Structures*, 34:3-6.

RILEM TC 162-TDF, 2002. Test and design methods for steel fibre reinforced concrete – Bending test: Final Recommendation. *Material and Structures*, Volume 35, pp. 579-582.

RILEM TC 162-TDF, 2002. Test and design methods for steel fibre reinforced concrete - sigma-w method (principles and applications). *Material and Structures*, Volume 35, pp. 262-278.

RILEM TC 162-TDF, 2003. Test and design methods for steel fibre reinforced concrete - sigma-epsilon design method (final recommendation). *Materials and Structures*, October, Volume 36, pp. 560-567.

Roberts, T. M. & Ho, N. L., 1982. Shear failure of deep fibre reinforced concrete beams. *The International Journal of Cement Composites and Lightweight Concrete*, August, 4(3), pp. 145-152.

Rots, J. G., 1989. Crack models for concrete: Discrete or smeared? Fixed, multi-directional or rotating? *Heron*, Vol. 34 no.1.

Rots, J. G., 1989. Various crack concepts for curved fracture in concrete. *ICF7*, Houston (USA).

SANS 201: 2008: *Sieve analysis fines, content and dust content of aggregates*. Pretoria: South African Bureau of Standards.

SANS 50197-1: 2013: *Cement, Part 1: Composition, specifications and conformity criteria for common cements*. Pretoria: South African Bureau of Standards.

SANS 50450-1: 2014: *Fly ash for concrete, Part 1: Definition, specifications and conformity criteria*. Pretoria: South African Bureau of Standards.

SCCEP Group, 2005. The *European Guidelines for Self-Compacting Concrete: Specification, Production and Use*, May 2005, www.efca.info or www.efnarc.org.

Sertillanges, A. D., 1978. The Intellectual Life: Its Spirits, Conditions and Methods. Dublin: Mercier Press, translated by Mary Ryan, p. 145.

Shang, Q., & van Zijl, G.P.A.G., 2007. Characterising the shear behaviour of strain hardening fibre-reinforced cement-based composites. *Journal of the South African Institution of Civil Engineering*, Volume 49 No.2, pp.16-23.

Sharma, A. K., 1986. Shear strength of steel fiber reinforced concrete beams. *ACI Journal, Proceedings*, July-August, 83(4), pp. 624-628.

Slater, E., Moni, M. & Alam, M. S., 2012. Predicting the shear strength of steel fiber reinforced concrete beams. *Construction and Building Materials*, Volume 26, pp. 423-436.

Soetens, T., Matthys, S. (2012) A semi-analytical model to simulate the direct shear pull-out behaviour of hooked-end steel fibres. In: *Proceedings Fibre reinforced concrete BEFIB2012* (pp. 1-12), eds. J. Barros et al.

Soltani M., An X., Maekawa K. (2003) Computational model for post cracking analysis of RC membrane elements based on local stress-strain characteristics. *Engineering Structures 25* (pp.993-1007)

References

Sun C. & Jin Z. (2012) *Fracture mechanics*. Academic Press. p.26

Swamy, R. N. & Bahia, H. M., 1985. The effectiveness of steel fibers as shear reinforcement. *Concrete International*, March. pp. 35-40.

Tan, K. H. & Mansur, M. A., 1990. Shear transfer in reinforced fiber concrete. *Journal of Materials in Civil Engineering*, November, 2(4), pp. 202-214.

Tan, K. H., Murugappan, K. & Paramasivam, P., 1993. Shear behavior of steel fiber reinforced concrete beams. *ACI Structural Journal*, January-February, 90(1), pp. 3-11.

Vecchio, F. J. & Collins, M. P., 1986. Modified compression field theory for reinforced concrete elements subjected to shear. *ACI Journal Proceedings*, 83(2), pp. 219-231.

Watanabe, K., Kimura, T. & Niwa, J., 2010. Synergetic effect of steel fibers and shear-reinforcing bars on the shear resistance mechanisms of RC linear members. *Construction and Building Materials*, Volume 24, pp. 2369-2375.

Wight, J. K. & MacGregor, J. G., 2009. *Reinforced concrete - mechanics & design*. 5th ed. New Jersey: Pearson Prentice Hall.

Zeranka S. & van Zijl G.P.A.G. (2013) A review of the shear behaviour of reinforced steel fibre concrete, 5th International Conference on Structural Engineering, Mechanics & Computation, Cape Town, South Africa, pp.567 - 568.

Zeranka S. & van Zijl G.P.A.G. (2015) Multi-scale characterisation of the shear-dominant fracture in a steel fibre-reinforced cement-based composite. 5th International Conference on Construction Materials (ConMat'15), Whistler, BC, Canada

Addenda

A List of abbreviations

A.1 Chapter 1

RC	Reinforced Concrete
SCC	Self-Consolidating Concrete
FRC	Fibre-Reinforced Concrete
SFRC	Steel Fibre-Reinforced Concrete
SFR-SCC	Steel Fibre-Reinforced Self-Consolidating Concrete
SHCC	Strain-Hardening Cement-based Composite
FE	Finite Element

A.2 Chapter 2

R-SFRC	Reinforced Steel Fibre-Reinforced Concrete
MCFT	Modified Compression Field Theory
FEA	Finite Element Analysis
DSFM	Disturbed Stress Field Model
VMA	Viscosity Modifying Admixture

A.3 Chapter 3

UTT	Uniaxial Tensile Test
SCM	Self-Consolidating Mortar
SFPO	Single Fibre (Axial) Pull-out
SFTP	Single Fibre Transverse Pull-out
COD	Crack Opening Displacement
LVDT	Linear Variable Displacement Transducer
CMOD	Crack Mouth Opening Displacement
LOP	Limit of proportionality
MTM	Materials Testing Machine
RH	Relative Humidity

A.4 Chapter 4

CT	Computed Tomography

A.5 Chapter 5

SMAX	Abaqus: Maximum principal stress
S12	Abaqus: Global shear stress
SCC-450	Self-Consolidating Concrete with coarse aggregate content V_a=450kg/m^3 (a=9.5 mm)
SCC-600	Self-Consolidating Concrete with coarse aggregate content V_a=600kg/m^3 (a=9.5 mm)
DIC	Digital Image Correlation

A.6 Chapter 6

UMAT	User-Material
STRAN	Abaqus UMAT: Array of total global strains at the beginning of the increment
DSTRAN	Abaqus UMAT: Array of strain increments
DDSDDE	Abaqus UMAT: Material tangent stiffness matrix of the constitutive model
STRESS	Abaqus UMAT: Global stress tensor at the beginning of the increment
STATEV	Abaqus UMAT: Array containing solution-dependent state variables

PROPS	Abaqus UMAT: Array of material constants
BC	Boundary condition

B List of notations and symbols

B.1 Chapter 1-2

F	Fibre factor
L_f	Fibre length
d_f	Fibre diameter
V_f	Fibre volume
D_f	Fibre bond efficiency factor
V_d	Shear transferred by dowel action of longitudinal reinforcement
V_c	Shear transferred by uncracked concrete in compression zone
V_s	Shear transferred by tension in stirrups
V_a	Shear transferred by aggregate interlock
a_v	Shear span

B.2 Chapter 3

w/p	Volumetric water-powder ratio
f_c	Concrete compressive cube strength
V_a	Volume of coarse aggregate
a	Nominal coarse aggregate particle size
F_v	Wedge splitting test: Vertical load
F_h	Wedge splitting test: Splitting force
a_w	Wedge splitting test: Wedge angle
f	ASTM 1609: flexural strength
P	ASTM 1609: applied load
L	ASTM 1609: span length
b	ASTM 1609: average width of the specimen at location of fracture
d	ASTM 1609: average depth of the specimen at location of fracture
δ_1	ASTM 1609: net deflection at first peak
f_1	ASTM 1609: flexural stress at first peak
δ_p	ASTM 1609: net deflection at peak (maximum)
f_p	ASTM 1609: flexural stress at peak (maximum)
f_{600}^D	ASTM 1609: flexural stress at a net deflection of $L/600$
f_{300}^D	ASTM 1609: flexural stress at a net deflection of $L/300$
f_{150}^D	ASTM 1609: flexural stress at a net deflection of $L/150$
$f_{R,j}$	EN 14651: residual flexural tensile strength corresponding to $CMOD = CMOD_j$
F_j	EN 14651: load corresponding to $CMOD = CMOD_j$
l	EN 14651: span length;
b	EN 14651: specimen width;
h_{sp}	EN 14651: distance between the notch tip and the top of the specimen (125 mm)
f_L	EN 14651: limit of proportionality

B.3 Chapter 4

w_g	UTT specimen gauge width
w_e	UTT specimen end width
t	UTT specimen thickness
l_g	UTT specimen gauge length
l_t	UTT specimen transition length

r UTT specimen transition radius
w_m UTT specimen deformation corresponding to the first peak or matrix cracking strength
$\sigma_{t,m}$ UTT specimen first peak or matrix cracking strength
N_f UTT specimen number of fibres protruding from both sides of the fracture plane
G_f UTT specimen specific fracture energy
L_{fe} Fibre embedded length
θ Fibre orientation/inclination with respect to the pull-out direction
F_p Fibre (axial) pull-out loading
δ_p Fibre (axial) pull-out displacement

B.4 Chapter 5

w_i Initial crack width of Iosipescu shear test specimens (Meso-scale)
θ Iosipescu (Meso-scale) specimen design: notch angle
r Iosipescu (Meso-scale) specimen design: notch tip radius
d Iosipescu (Meso-scale) specimen design: notch depth
F_{pt} Single fibre transverse pull-out load
δ_{pt} Single fibre transverse pull-out displacement
n_{pt} Single fibre normal pull-out displacement

B.5 Chapter 6

ε Total strain
ε_c Strain in uncracked material
ε_{cr} Strain in the crack
φ Orientation of principal stress direction
Δt^{cr} Crack traction increment
$\Delta\varepsilon_{12}^{cr}$ Crack strain increment
D^{cr} Crack tangent stiffness matrix
D^{I} Local Mode I stiffness modulus
D^{II} Local Mode II stiffness modulus
f_{ct} Uniaxial tensile strength of composite
G_{ft} Mode I fracture energy
h Characteristic element length representing the crack band width
t_1^{cr} Local Mode I crack traction
ε_1^{cr} Local Mode I crack strain
D_u^I Mode I unloading/reloading stiffness
w Crack width
t_{12}^{cr} Local Mode II crack shear traction
γ_{12}^{cr} Local Mode II crack shear strain
f_{cs} Peak shear stress on limit function (where $\varepsilon_1^{cr} = 0, \gamma_{12}^{cr} = 0$)
G_{fs} Mode II fracture energy
w_m Calibrated model parameter
G Elastic shear modulus
f_i Calibrated model parameter
G_{min} Minimum shear modulus
D^{c2} Local stiffness parallel to crack
E Elastic modulus (Isotropic)
v Poisson's ratio
c_{min} Minimum stiffness of D^{c2} (model parameter)
ε_{max} Maximum principal strain
ε_{min} Minimum principal strain
ε_{xx} Global normal strain in x-direction

ε_{yy} Global normal strain in y-direction
γ_{xy} Global shear strain
ε_{cr} Strain at which crack initiates

C Trial self-consolidating mortar designs (Chapter 3)

Parameter values:

Water/powder ratio, w/p (volume):	[0.85, 0.90, 0.95, 1.0, and 1.05]
Cement type:	[CEM I and CEM II]
Cement extender type:	Fly Ash (Durapozz)
Percentage fly ash replacement (mass):	[40%, 45%, 50%, 55%, 60%]
Percentage of fine aggregate (volume):	[45% and 50%]
Fine aggregate types:	Malmesbury Sand & Philippi sand
Fine aggregate composition (mass)	Malmesbury : Philippi [100 : 0] & [70 : 30]
Mix sizes:	3 and 12 litres
Test method (rheology)	Flow spread (small scale)
Test method (mechanical)	Cube crushing strength (100 mm) (7-, 14- and 28-day)
Superplasticiser	SP1 (MAPEI)
VMA	None
Target flow spread	240 – 260 mm
Target average compressive strength:	40 – 50 MPa

Mix ID	w/p[1]	Cement[2]	Fly Ash %[3]	Fine Agg. %[4]	M : P[5]	SP1 [3ℓ][6]	SF [3ℓ][7]	VI[8]	SP1 [12ℓ]	SF [12ℓ]	VI	7-day[9]	14-day[10]	28-day[11]
1	0.9	II	50%	50%	100 : 0	0.20	235-235	NS				23.18	26.32	46.13
2	0.9	II	50%	50%	70 : 30	0.27	245-250	GC, SSS	0.25	245-260	SSS	24.86	29.98	46.76
3	0.9	II	50%	45%	100 : 0	0.20	245-245	SSS, SL				21.02	31.15	38.61
4	0.9	II	50%	45%	70 : 30	0.20	260-270	SSS, SL	-	-	-	-	-	-
5	0.9	I	60%	45%	70 : 30	0.20	230-230	GC, VSSS	-	-	-	19.85	-	-
6	0.9	II	40%	50%	100 : 0	0.22	245-255	GC, NS	-	-	-	24.18	-	-
7	0.9	II	40%	50%	70 : 30	0.26	245-250	GC, NS	0.26	240-240	VSSS	30.57	43.47	48.61
8	0.9	II	40%	45%	100 : 0	0.18	265-270	SSS	-	-	-	30.46	-	-
9	0.9	II	40%	45%	70 : 30	0.22	270-270	SSS	-	-	-	31.77	-	-
10	0.9	I	50%	50%	100 : 0	0.24	240-245	VSSS	-	-	-	32.70	-	-
11	0.9	I	50%	50%	70 : 30	0.28	250-255	NS	0.34	240-245	VSSS	34.49	38.94	54.37
12	0.9	I	50%	45%	100 : 0	0.22	235-240	SSS	-	-	-	32.09	-	-
13	0.9	I	50%	45%	70 : 30	0.24	235-245	SSS	-	-	-	35.05	-	-
14	0.9	I	40%	50%	100 : 0	0.28	260-265	VSSS	-	-	-	45.14	-	-
15	0.9	I	40%	50%	70 : 30	0.36	285-290	SS	-	-	-	48.40	-	-
16	0.9	I	40%	45%	100 : 0	0.24	245-250	VSSS	-	-	-	-	55.83	-
17	0.9	I	40%	45%	70 : 30	0.26	245-250	VSSS	-	-	-	-	51.69	-
18	1.05	I	45%	50%	100 : 0	0.20	235-240	SSS	-	-	-	27.24	-	-
19	1.05	I	45%	50%	70 : 30	0.26	245-250	SSS	-	-	-	27.96	-	-
20	1.05	I	45%	45%	100 : 0	0.16	245-250	SSS, SIS	-	-	-	28.04	-	-
21	1.05	I	45%	45%	70 : 30	0.18	245-250	SSS, SIS	-	-	-	24.78	-	-
22	0.95	II	50%	50%	70 : 30	0.22	265-270	SSS, SIS	0.22	245-250	SSS, SIS	24.41	32.89	40.38
23	1.0	II	50%	50%	70 : 30	0.18	245-250	SSS, SIS	0.16	230-240	SSS, SIS	20.23	26.66	36.23
24	0.85	II	55%	50%	70 : 30	0.28	285-290	SSS, SIS	0.24	240-245	SSS	25.67	32.58	43.61
25	0.9	II	55%	50%	70 : 30	0.24	265-270	SSS, SIS	0.22	240-240	SSS, SIS	20.57	31.03	38.02
26	0.95	I	50%	50%	70 : 30	0.26	250-255	VSSS, NIS	0.28	220-230	SSS, NIS	32.17	41.75	54.81
27	0.9	I	55%	50%	70 : 30	0.28	245-245	VSSS	0.28	250-250	VSSS	29.21	38.49	48.67
28	0.95	I	55%	50%	70 : 30	0.26	240-250	VSSS	0.26	240-245	SSS	23.51	35.35	47.87
29	0.9	I	60%	50%	70 : 30	0.24	250-255	VSSS	0.28	240-245	SSS	22.12	31.66	42.15
30	0.85	I	60%	50%	70 : 30	0.26	270-270	SSS	0.28	240-240	VSSS	23.97	33.92	45.33

Table key: 1: water/powder ratio; 2: cement type; 3: percentage fly-ash replacement; 4: fine aggregate volume percentage; 5: fine aggregate composition [Malmesbury (M) : Philippi (P)]; 6: superplasticiser dosage [L/100 kg binder]; 7: slump-flow spread diameter; 8: visual inspection (NS – no segregation, GC – good consistency, SSS – slight surface segregation, SL – superplasticiser limit, VSSS – very slight surface segregation, SS – surface segregation, SIS – slight internal segregation, NIS – no internal segregation; 9, 10, 11: 7, 14 and 28-day compressive strength [MPa] respectively.

Addendum D

Meso and Micro-mechanical investigation of Mode II fracture

D.1 Meso-scale: Sample data and average response

D.1.1 SCM, V_f = 0.5%, w_i = 0.1 mm & 0.3 mm

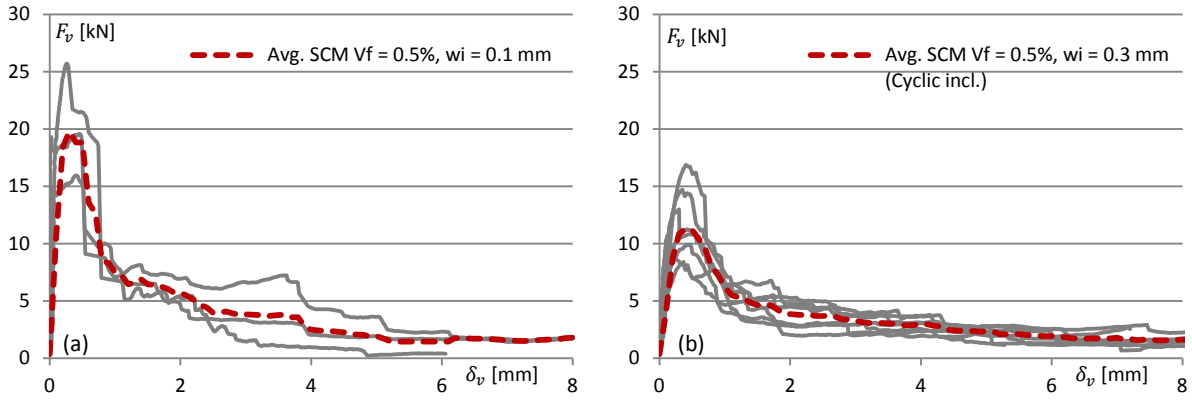

Fig.D.1 – Shear load, F_v [kN] vs. shear displacement, δ_v [mm] for SCM V_f = 0.5% (a) w_i = 0.1 mm (b) w_i = 0.3 mm

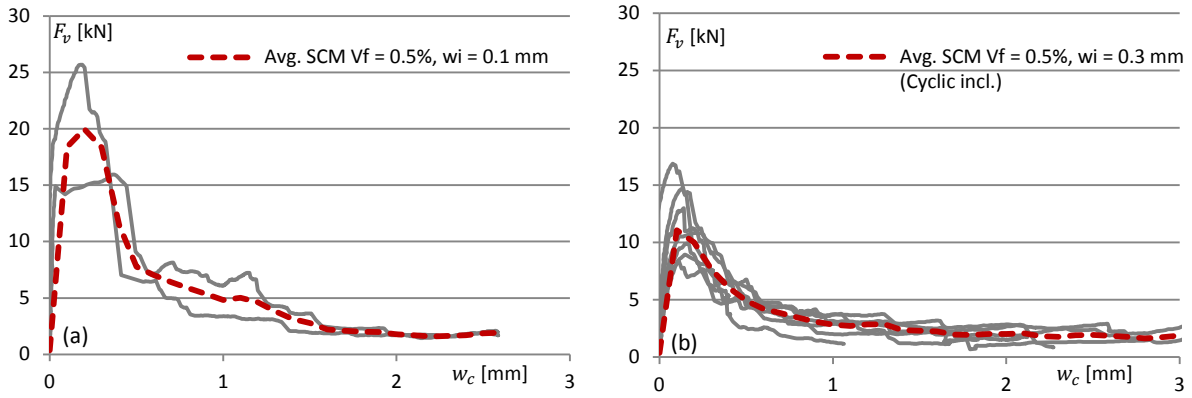

Fig.D.2 – Shear load, F_v [kN] vs. crack width, w_c [mm] for SCM V_f = 0.5% (a) w_i = 0.1 mm (b) w_i = 0.3 mm

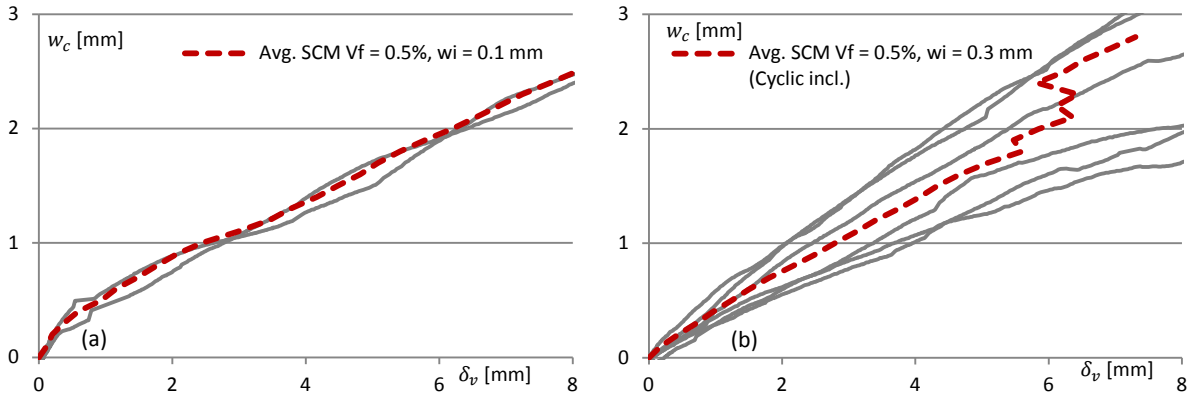

Fig.D.3 – Crack width, w_c [mm] vs. shear displacement, δ_v [mm] for SCM V_f = 0.5% (a) w_i = 0.1 mm (b) w_i = 0.3 mm

D.1.2 SCM, V_f = 0.75%, w_i = 0.1 mm & 0.3 mm

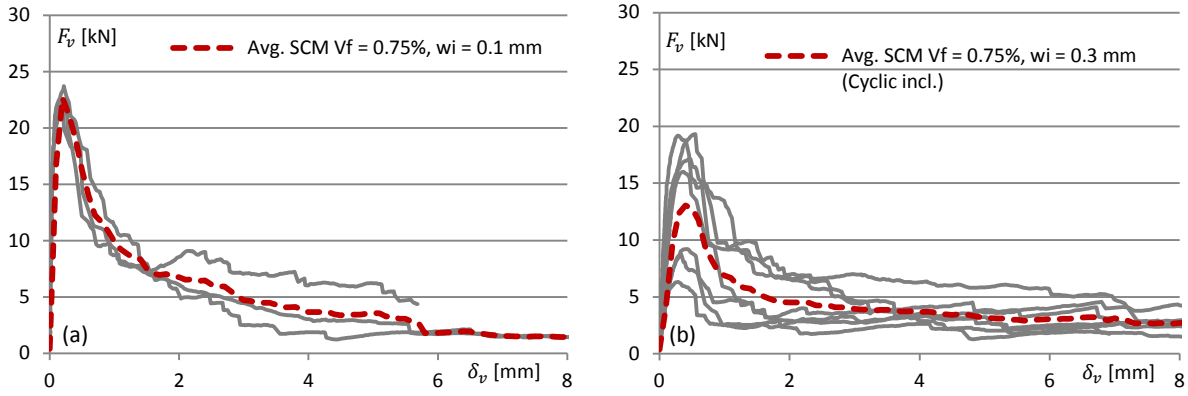

Fig.D.4 – Shear load, F_v [kN] vs. shear displacement, δ_v [mm] for SCM V_f = 0.75% (a) w_i = 0.1 mm (b) w_i = 0.3 mm

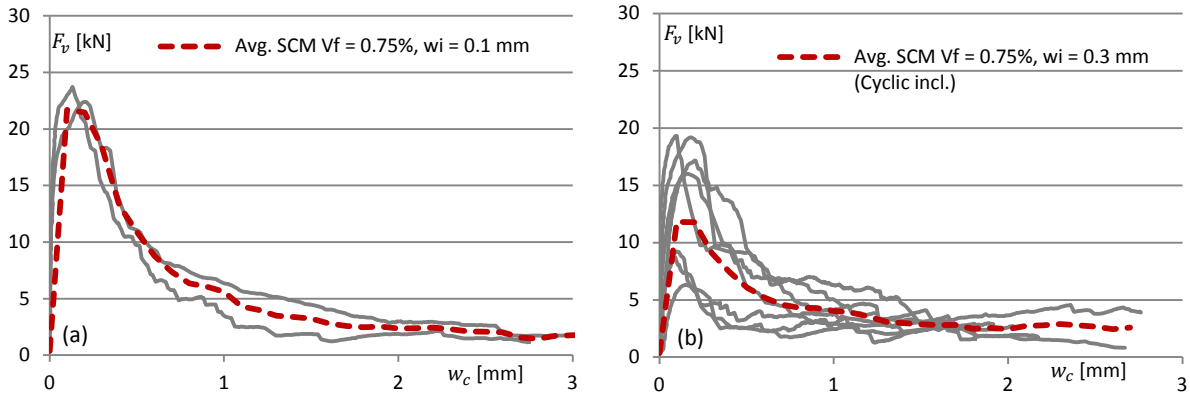

Fig.D.5 – Shear load, F_v [kN] vs. crack width, w_c [mm] for SCM V_f = 0.75% (a) w_i = 0.1 mm (b) w_i = 0.3 mm

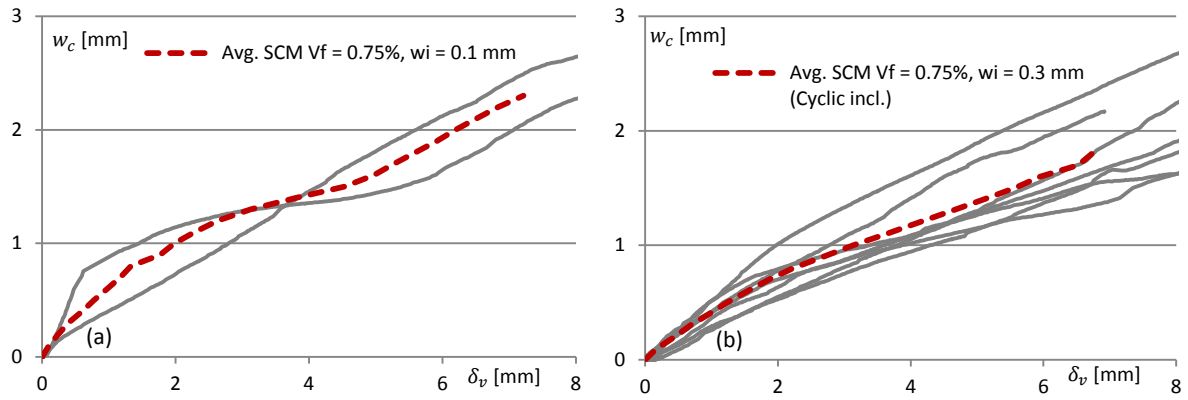

Fig.D.6 – Crack width, w_c [mm] vs. shear displacement, δ_v [mm] for SCM V_f = 0.75% (a) w_i = 0.1 mm (b) w_i = 0.3 mm

D.1.3 SCM, V_f = 1.00%, w_i = 0.1 mm & 0.3 mm

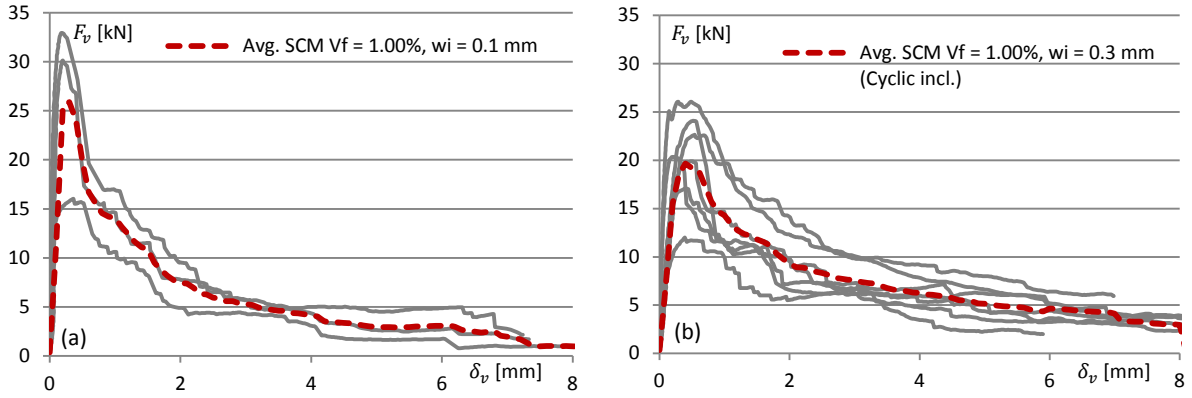

Fig.D.7 – Shear load, F_v [kN] vs. shear displacement, δ_v [mm] for SCM V_f = 1.00% (a) w_i = 0.1 mm (b) w_i = 0.3 mm

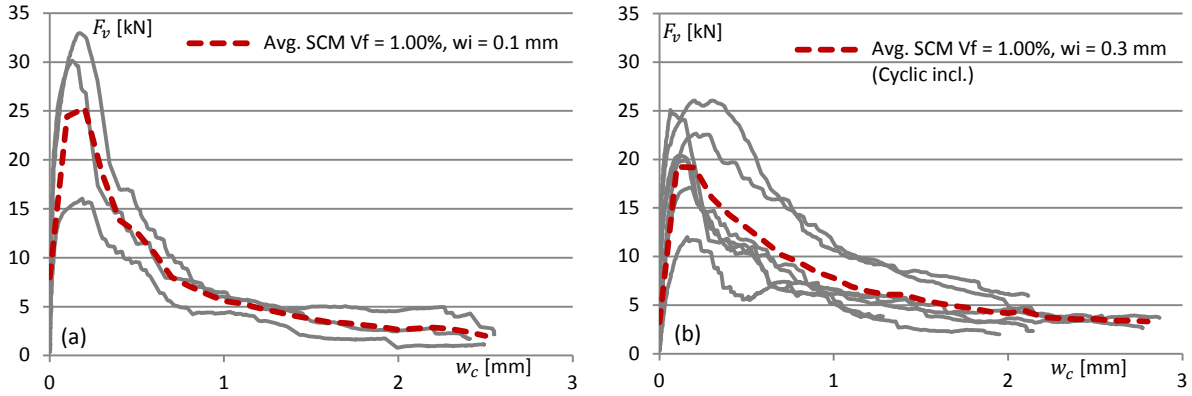

Fig.D.8 – Shear load, F_v [kN] vs. crack width, w_c [mm] for SCM V_f = 1.00% (a) w_i = 0.1 mm (b) w_i = 0.3 mm

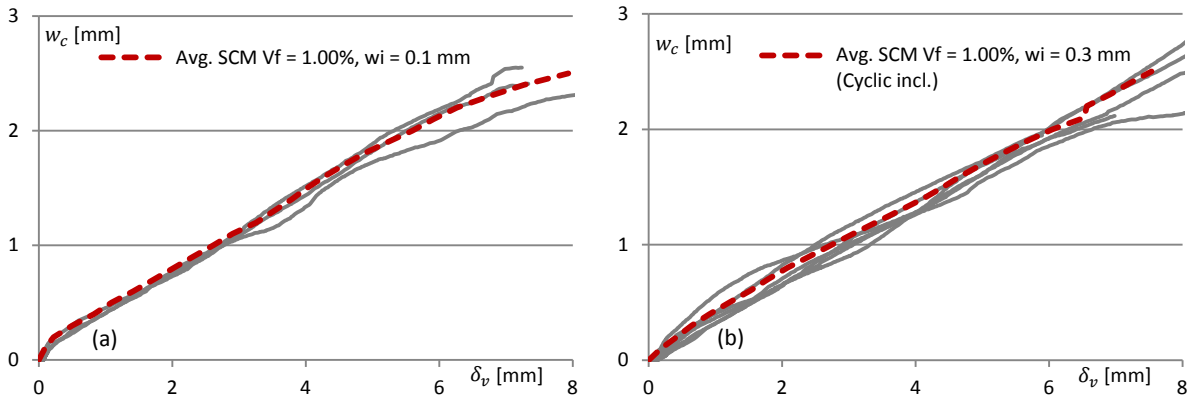

Fig.D.9 – Crack width, w_c [mm] vs. shear displacement, δ_v [mm] for SCM V_f = 1.00% (a) w_i = 0.1 mm (b) w_i = 0.3 mm

D.1.4 Fracture energy, G_f (SCM, V_f = 0.50 – 1.00%, w_i = 0.1 mm & 0.3 mm)

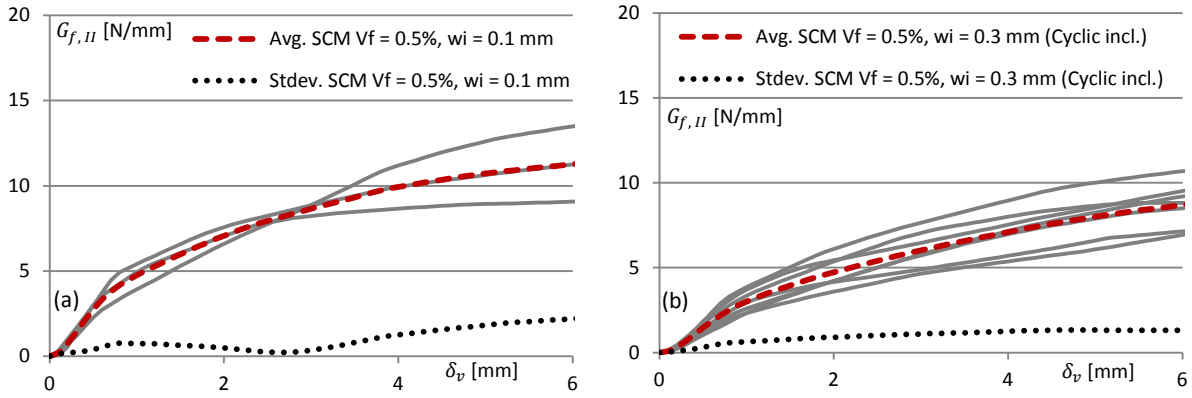

Fig.D.10 – Fracture energy, G_f [N/mm] vs. shear displacement, δ_v [mm] for SCM V_f = 0.50% (a) w_i = 0.1 mm (b) w_i = 0.3 mm

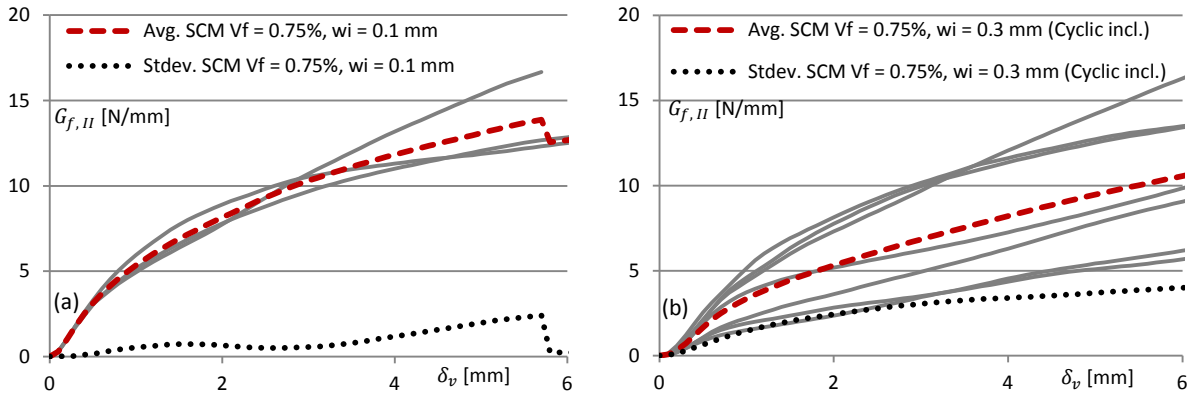

Fig.D.11 – Fracture energy, G_f [N/mm] vs. shear displacement, δ_v [mm] for SCM V_f = 0.75% (a) w_i = 0.1 mm (b) w_i = 0.3 mm

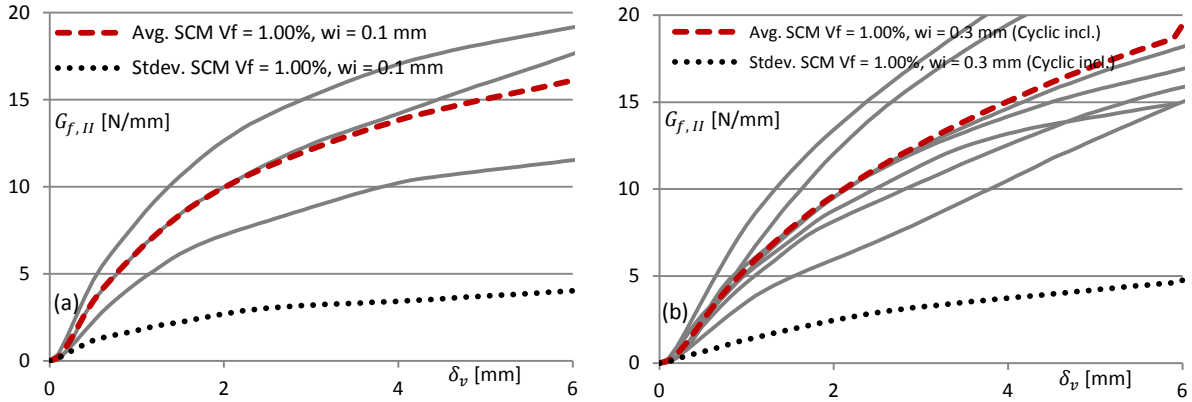

Fig.D.12 – Fracture energy, G_f [N/mm] vs. shear displacement, δ_v [mm] for SCM V_f = 1.00% (a) w_i = 0.1 mm (b) w_i = 0.3 mm

D.1.5 SCC-450, V_f = 0.50%, w_i = 0.1 mm & 0.3 mm

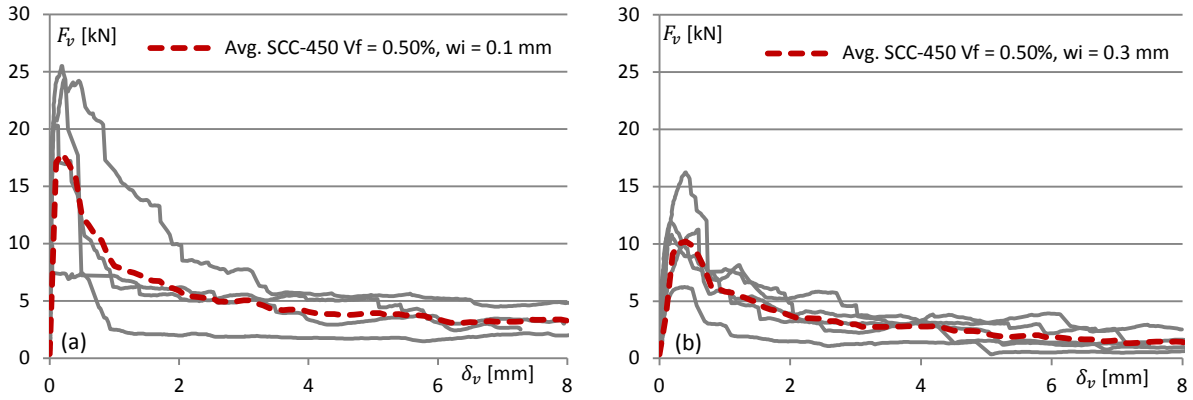

Fig.D.13 – Shear load, F_v [kN] vs. shear displacement, δ_v [mm] for SCC-450 V_f = 0.50% (a) w_i = 0.1 mm (b) w_i = 0.3 mm

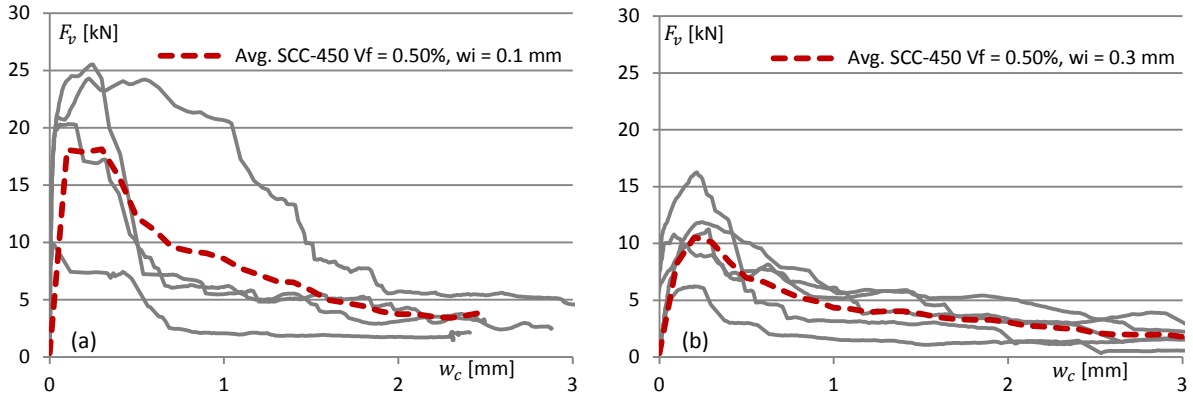

Fig.D.14 – Shear load, F_v [kN] vs. crack width, w_c [mm] for SCC-450 V_f = 0.50% (a) w_i = 0.1 mm (b) w_i = 0.3 mm

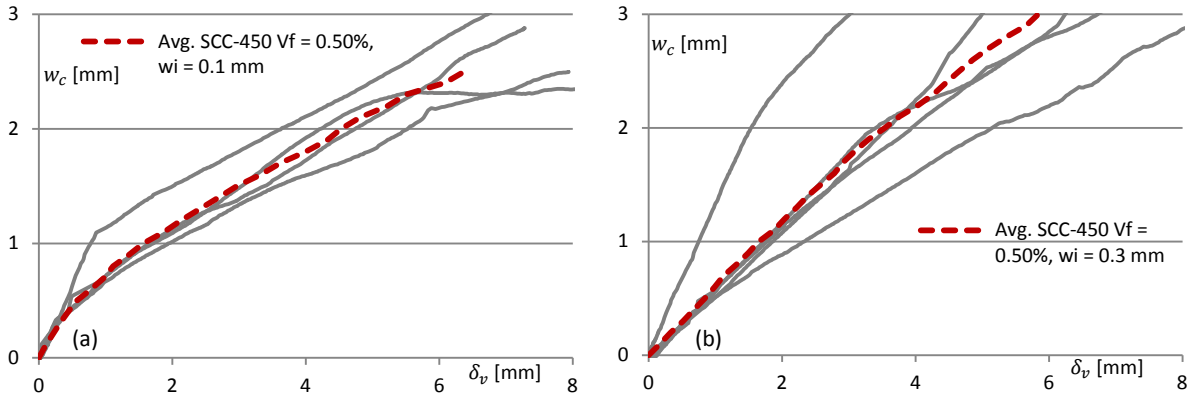

Fig.D.15 – Crack width, w_c [mm] vs. shear displacement, δ_v [mm] for SCC-450 V_f = 0.50% (a) w_i = 0.1 mm (b) w_i = 0.3 mm

D.1.6 SCC-450, V_f = 0.75%, w_i = 0.1 mm & 0.3 mm

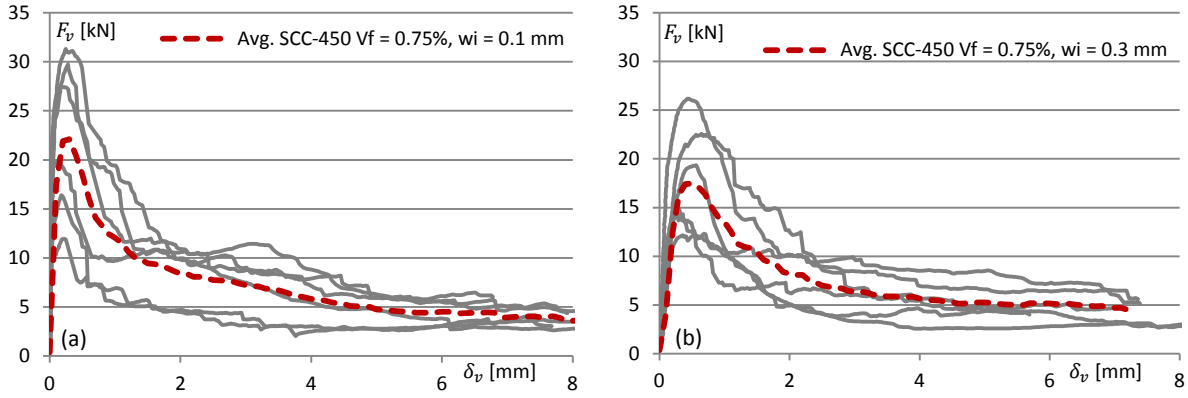

Fig.D.16 – Shear load, F_v [kN] vs. shear displacement, δ_v [mm] for SCC-450 V_f = 0.75% (a) w_i = 0.1 mm (b) w_i = 0.3 mm

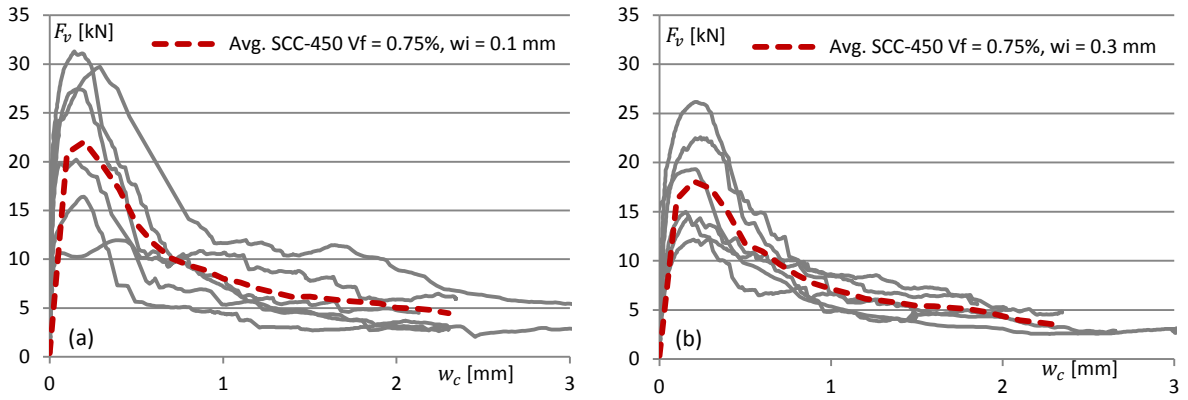

Fig.D.17 – Shear load, F_v [kN] vs. crack width, w_c [mm] for SCC-450 V_f = 0.75% (a) w_i = 0.1 mm (b) w_i = 0.3 mm

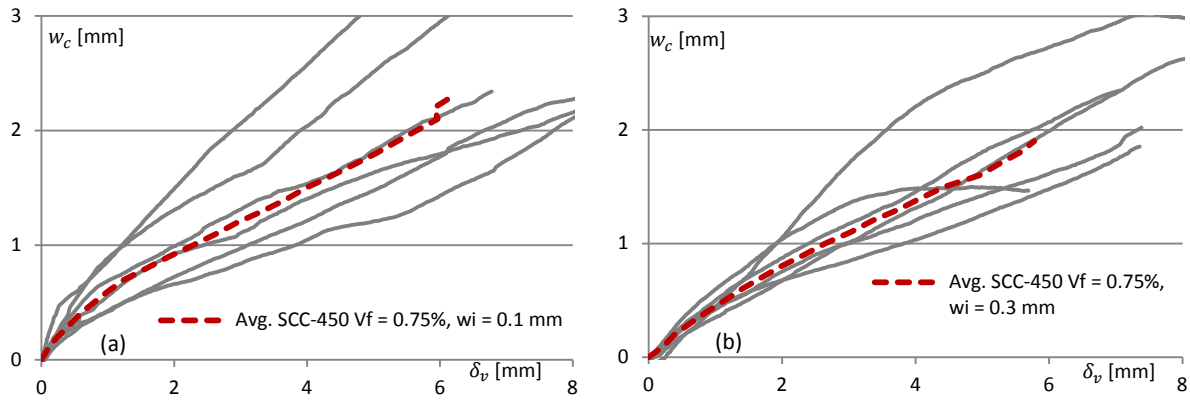

Fig.D.18 – Crack width, w_c [mm] vs. shear displacement, δ_v [mm] for SCC-450 V_f = 0.75% (a) w_i = 0.1 mm (b) w_i = 0.3 mm

D.1.7 SCC-450, V_f = 1.00%, w_i = 0.1 mm & 0.3 mm

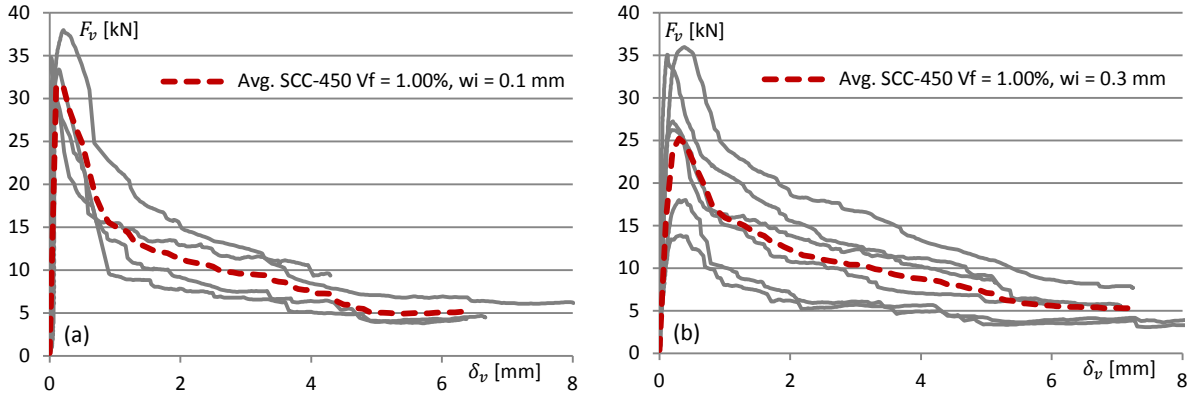

Fig.D.19 – Shear load, F_v [kN] vs. shear displacement, δ_v [mm] for SCC-450 V_f = 1.00% (a) w_i = 0.1 mm (b) w_i = 0.3 mm

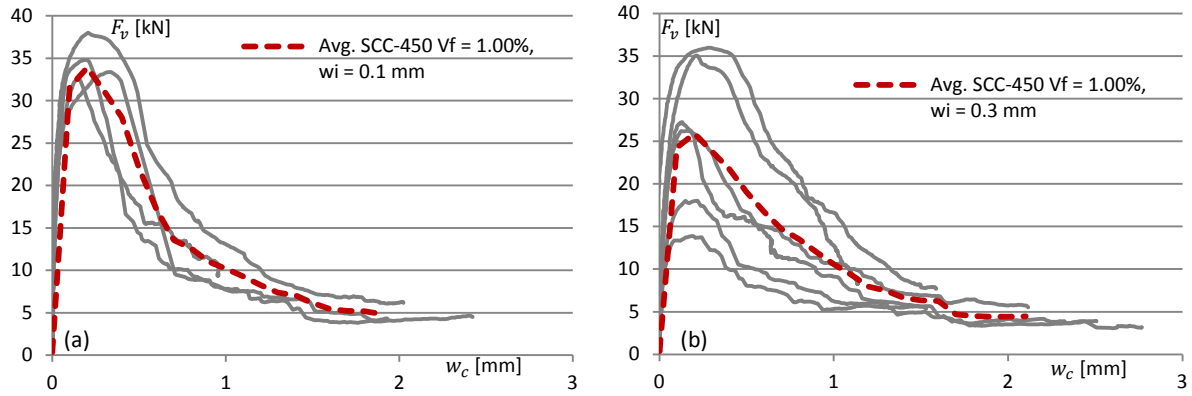

Fig.D.20 – Shear load, F_v [kN] vs. crack width, w_c [mm] for SCC-450 V_f = 1.00% (a) w_i = 0.1 mm (b) w_i = 0.3 mm

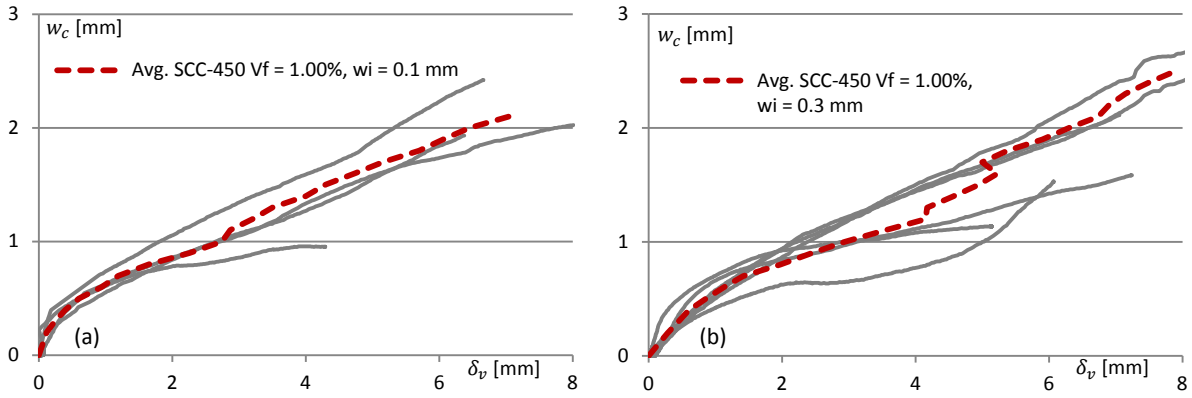

Fig.D.21 – Crack width, w_c [mm] vs. shear displacement, δ_v [mm] for SCC-450 V_f = 1.00% (a) w_i = 0.1 mm (b) w_i = 0.3 mm

D.1.8 Fracture energy, G_f (SCC-450, V_f = 0.50 – 1.00%, w_i = 0.1 mm & 0.3 mm)

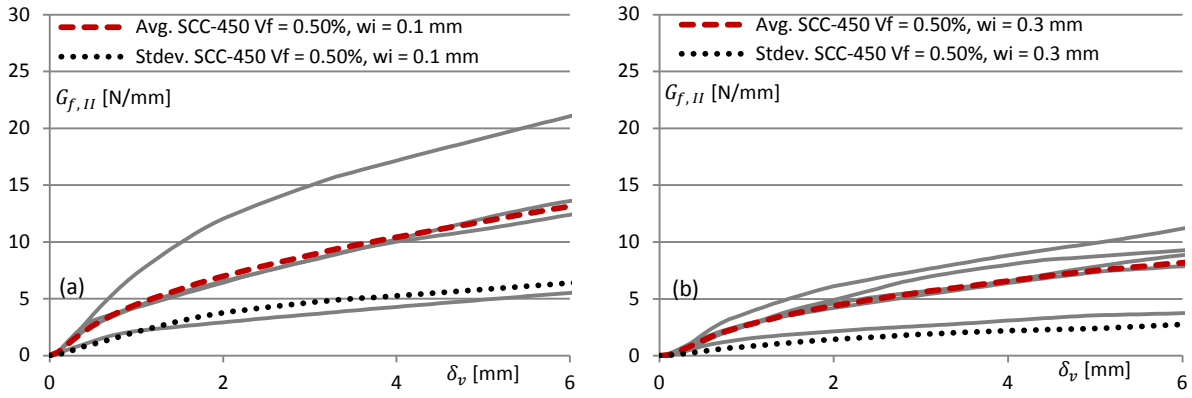

Fig.D.22 – Fracture energy, G_f [N/mm] vs. shear displacement, δ_v [mm] for SCC-450 V_f = 0.5% (a) w_i = 0.1 mm (b) w_i = 0.3 mm

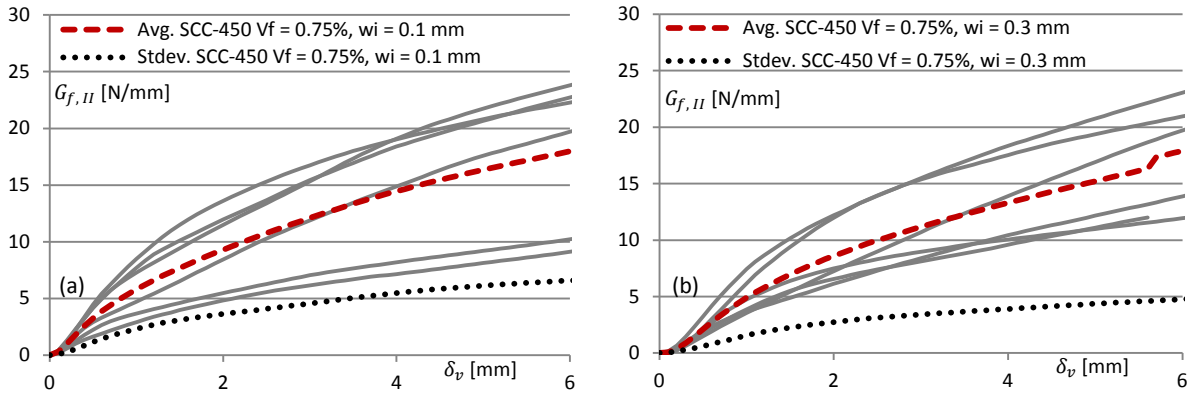

Fig.D.23 – Fracture energy, G_f [N/mm] vs. shear displacement, δ_v [mm] for SCC-450 V_f = 0.75% (a) w_i = 0.1 mm (b) w_i = 0.3 mm

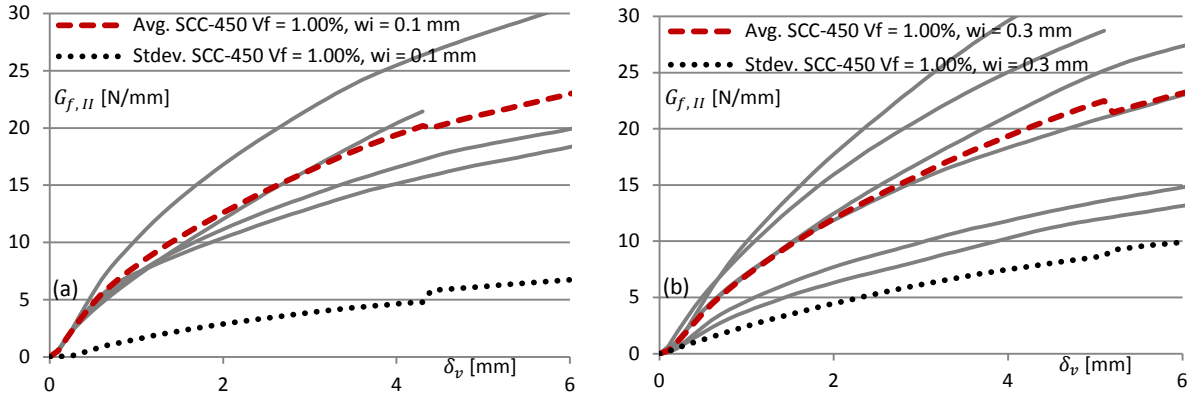

Fig.D.24 – Fracture energy, G_f [N/mm] vs. shear displacement, δ_v [mm] for SCC-450 V_f = 1.00% (a) w_i = 0.1 mm (b) w_i = 0.3 mm

D.1.9 SCC-600, V_f = 0.50%, w_i = 0.1 mm & 0.3 mm

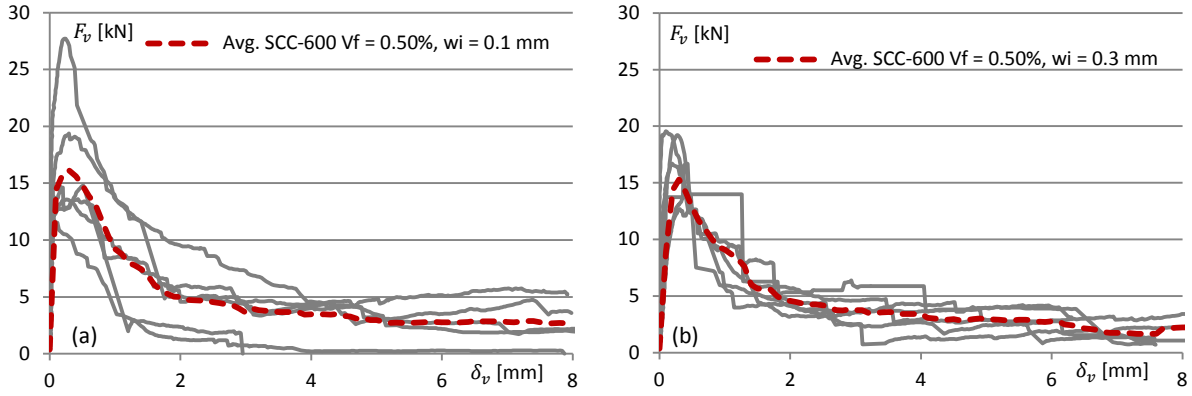

Fig.D.25 – Shear load, F_v [kN] vs. shear displacement, δ_v [mm] for SCC-600 V_f = 0.50% (a) w_i = 0.1 mm (b) w_i = 0.3 mm

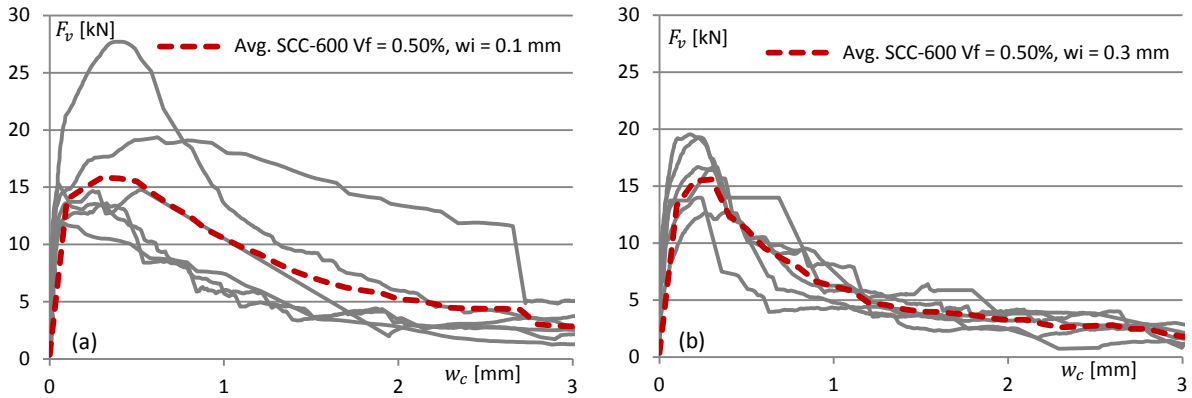

Fig.D.26 – Shear load, F_v [kN] vs. crack width, w_c [mm] for SCC-600 V_f = 0.50% (a) w_i = 0.1 mm (b) w_i = 0.3 mm

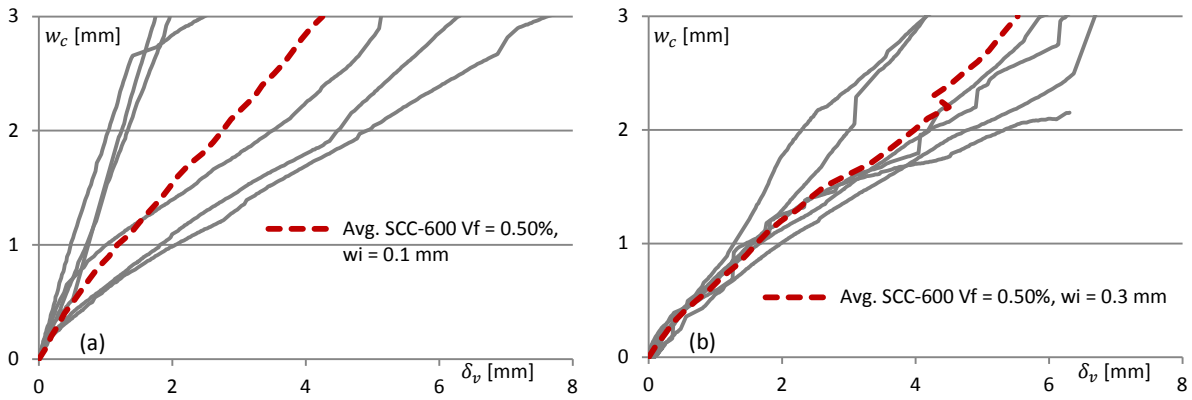

Fig.D.27 – Crack width, w_c [mm] vs. shear displacement, δ_v [mm] for SCC-600 V_f = 0.50% (a) w_i = 0.1 mm (b) w_i = 0.3 mm

D.1.10 Fracture energy, G_f (SCC-600, V_f = 0.50%, w_i = 0.1 mm & 0.3 mm)

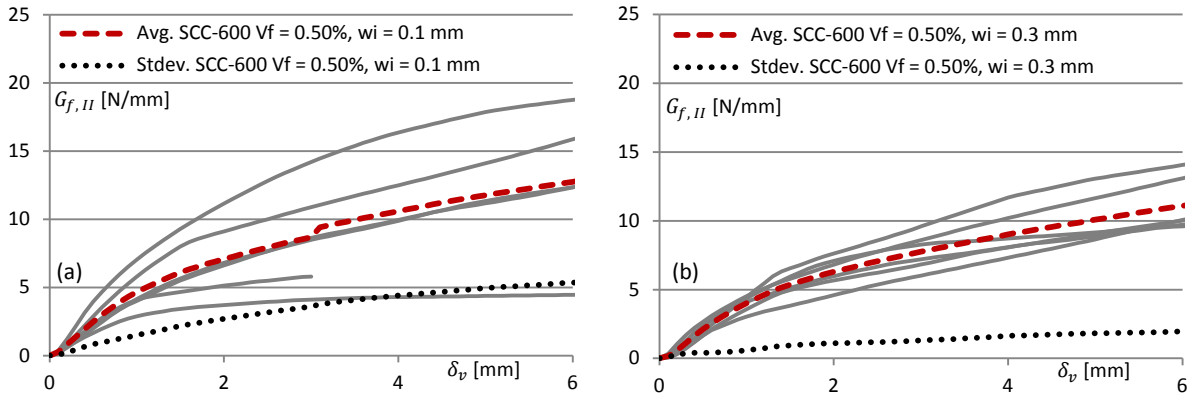

Fig.D.28 – Fracture energy, G_f [N/mm] vs. shear displacement, δ_v [mm] for SCC-600 V_f = 0.5% (a) w_i = 0.1 mm (b) w_i = 0.3 mm

D.2 Effect of fibre dosage (V_f) on (average) composite response

D.2.1 Self-consolidating mortar (SCM)

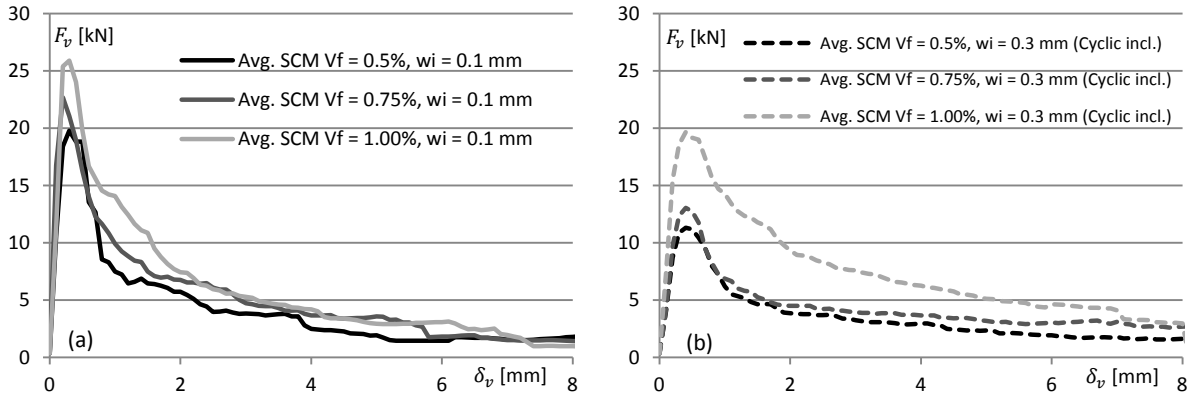

Fig.D.29 – Shear load, F_v [kN] vs. shear displacement, δ_v [mm] for SCM V_f = 0.50-1.00% (a) w_i = 0.1 mm (b) w_i = 0.3 mm

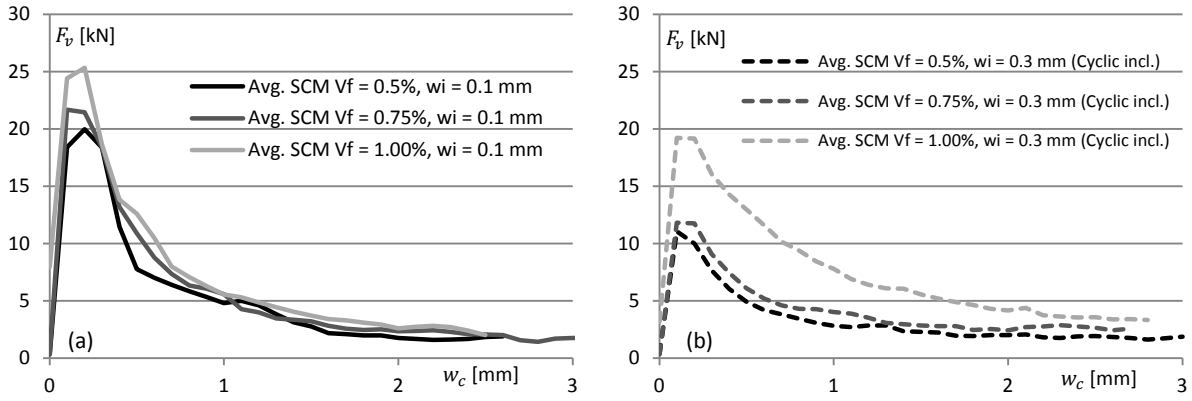

Fig.D.30 – Shear load, F_v [kN] vs. crack width, w_c [mm] for SCM V_f = 0.50-1.00% (a) w_i = 0.1 mm (b) w_i = 0.3 mm

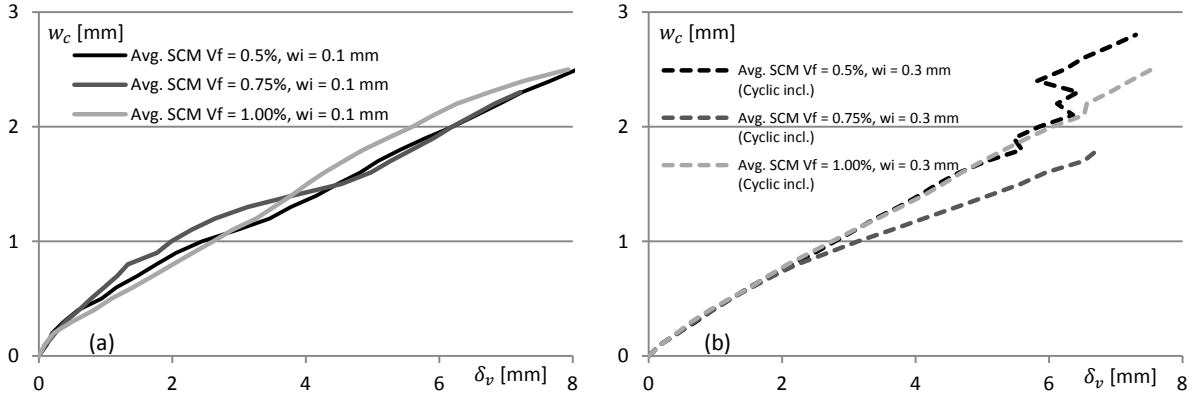

Fig.D.31 – Crack width, w_c [mm] vs. shear displacement, δ_v [mm] for SCM V_f = 0.50-1.00% (a) w_i = 0.1 mm (b) w_i = 0.3 mm

D.2.2 Self-consolidating concrete V_a = 450 kg/m^3 (SCC-450)

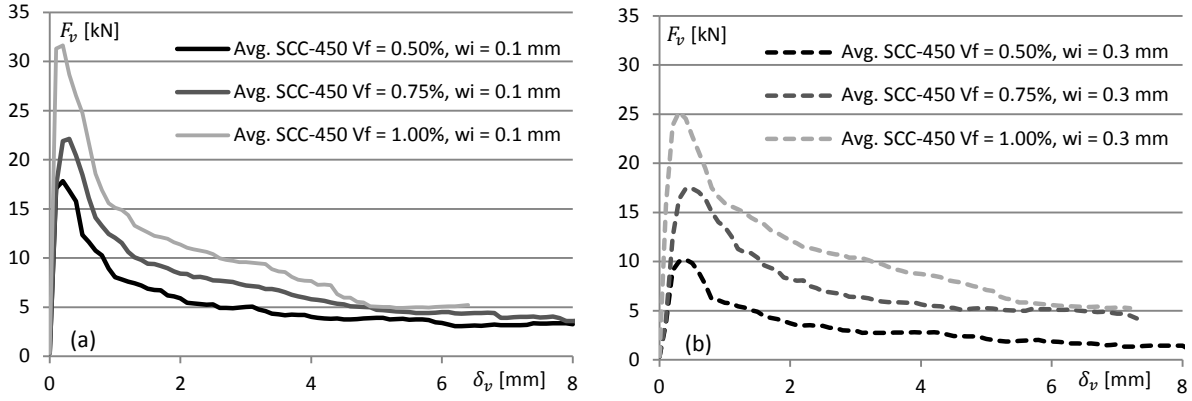

Fig.D.32 – Shear load, F_v [kN] vs. shear displacement, δ_v [mm] for SCC-450 V_f = 0.50-1.00% (a) w_i = 0.1 mm (b) w_i = 0.3 mm

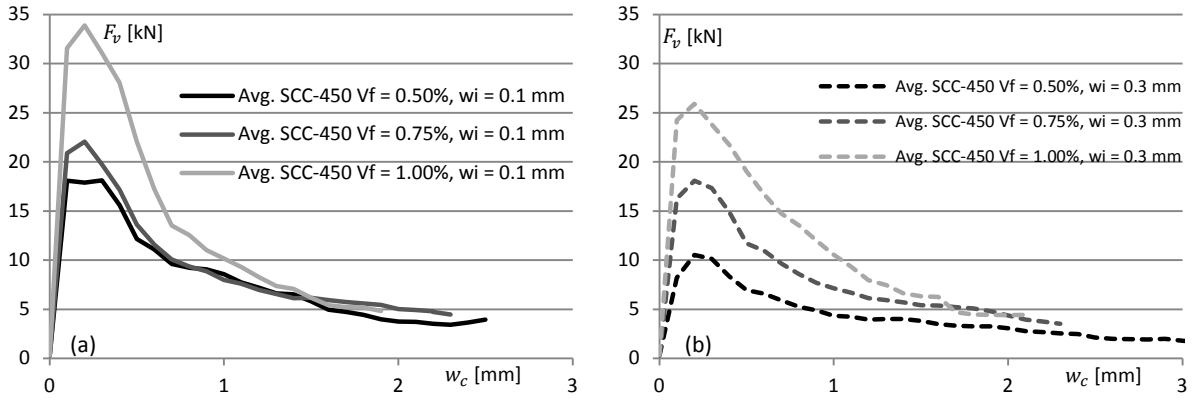

Fig.D.33 – Shear load, F_v [kN] vs. crack width, w_c [mm] for SCC-450 V_f = 0.50-1.00% (a) w_i = 0.1 mm (b) w_i = 0.3 mm

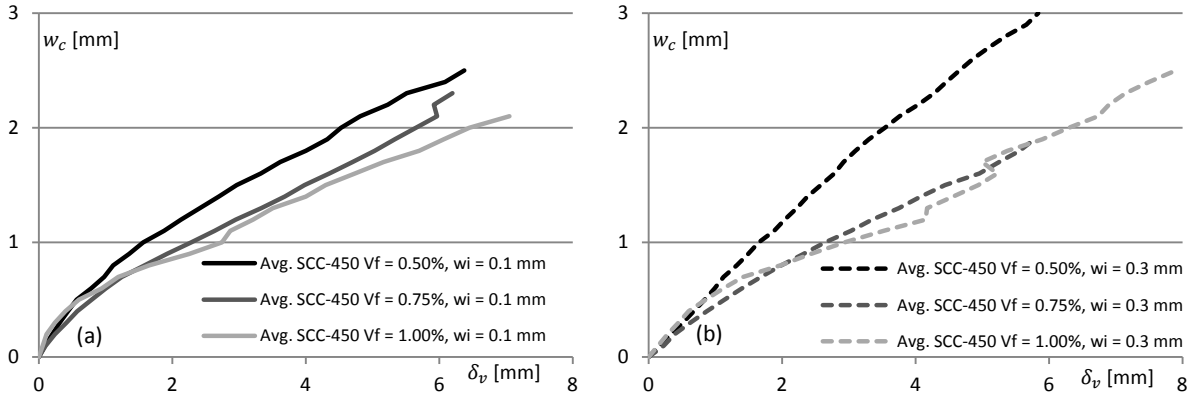

Fig.D.34 – Crack width, w_c [mm] vs. shear displacement, δ_v [mm] for SCC-450 V_f = 0.50-1.00% (a) w_i = 0.1 mm (b) w_i = 0.3 mm

D.2.3 Fracture energy

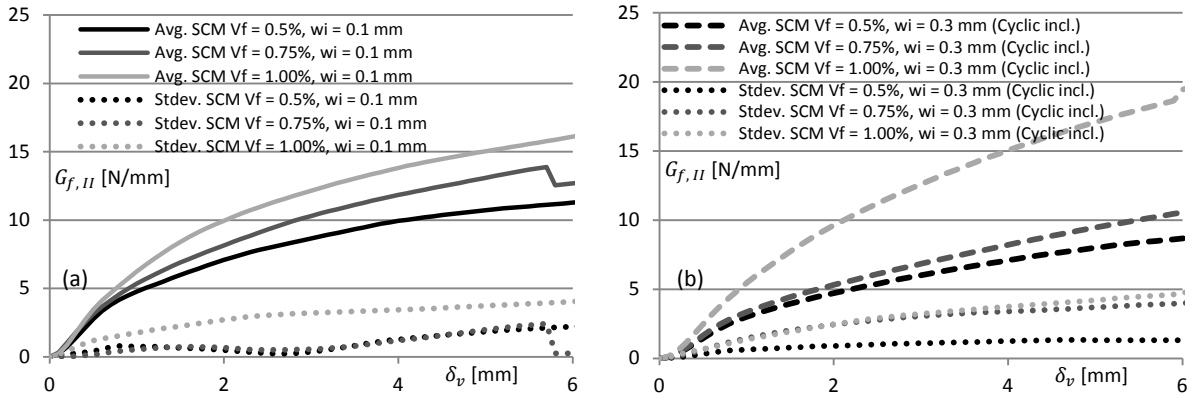

Fig.D.35 – Fracture energy, G_f [N/mm] vs. shear displacement, δ_v [mm] for SCM V_f = 0.50-1.00% (a) w_i = 0.1 mm (b) w_i = 0.3 mm

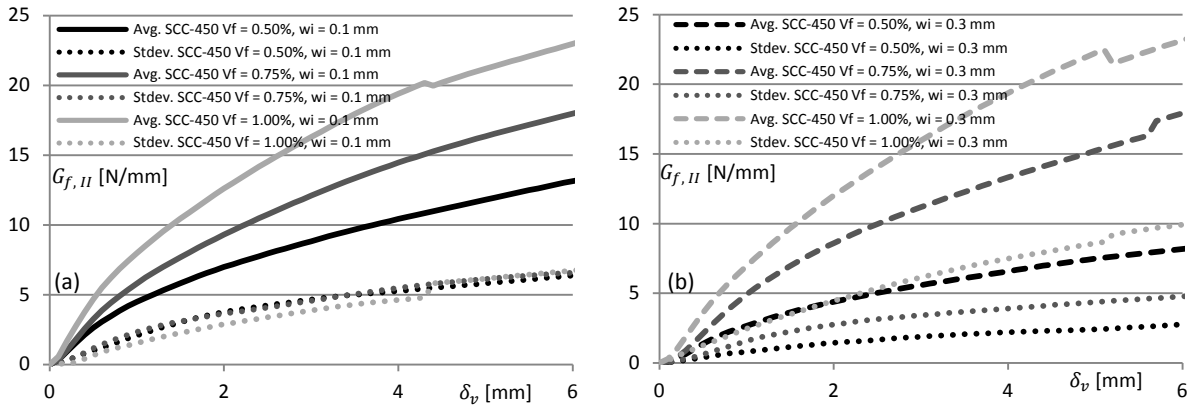

Fig.D.36 – Fracture energy, G_f [N/mm] vs. shear displacement, δ_v [mm] for SCC-450 V_f = 0.50-1.00% (a) w_i = 0.1 mm (b) w_i = 0.3 mm

D.3 Effect of initial crack width (w_i) on (average) composite response

D.3.1 Self-consolidating mortar (SCM)

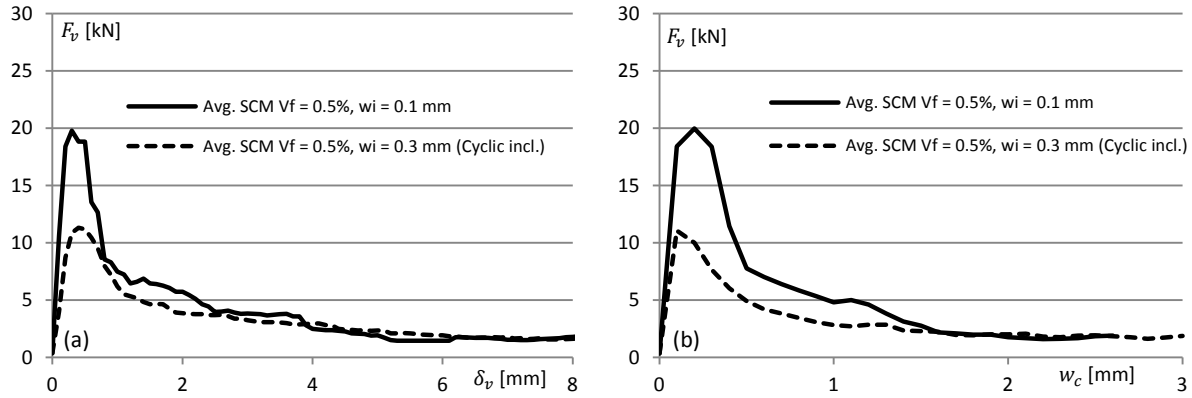

Fig.D.37 – SCM V_f = 0.50%, Shear load, F_v [kN] vs. (a) shear displacement, δ_v [mm] and (b) crack width, w_c [mm]

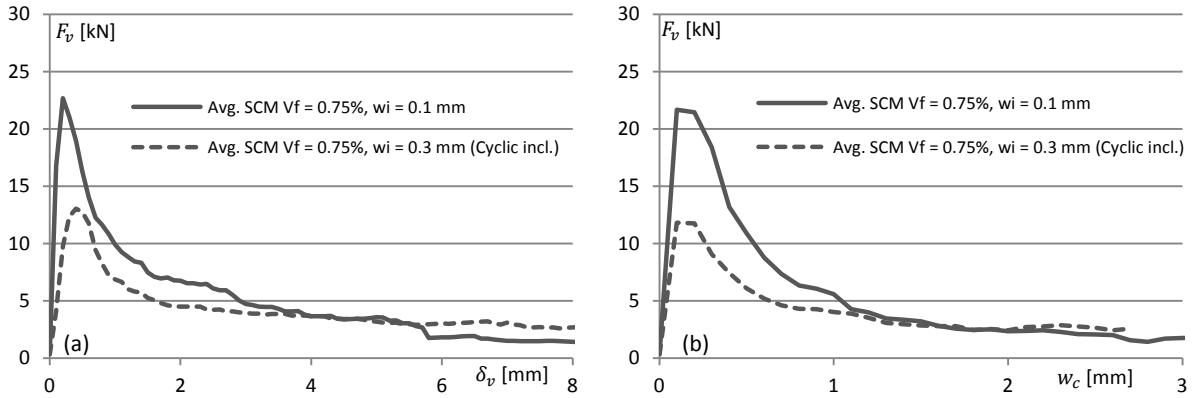

Fig.D.38 – SCM V_f = 0.75%, Shear load, F_v [kN] vs. (a) shear displacement, δ_v [mm] and (b) crack width, w_c [mm]

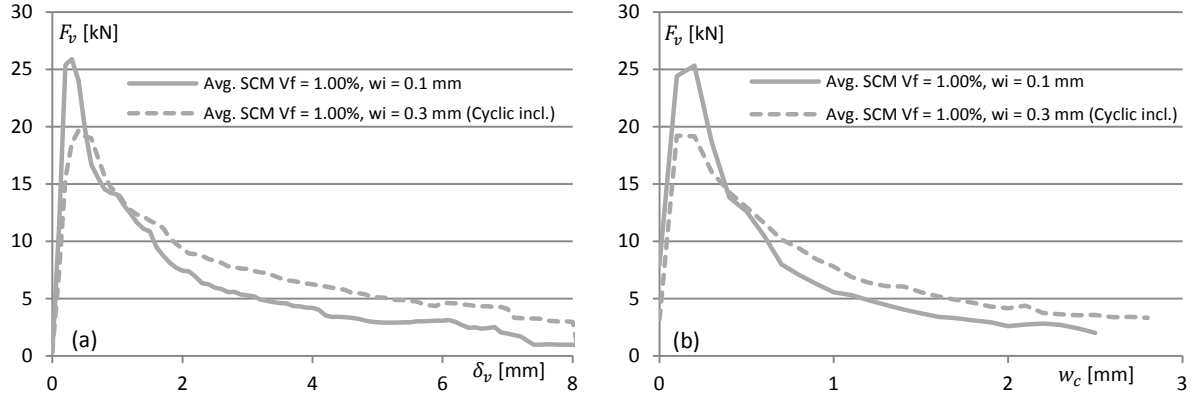

Fig.D.39 – SCM V_f = 1.00%, Shear load, F_v [kN] vs. (a) shear displacement, δ_v [mm] and (b) crack width, w_c [mm]

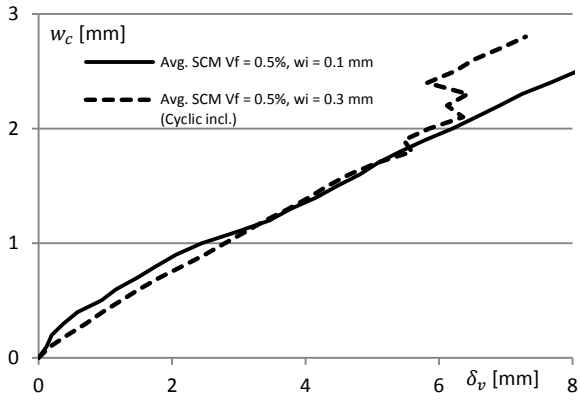

Fig.D.40 – SCM V_f = 0.50%, Shear displacement, δ_v [mm] vs. crack width, w_c [mm]

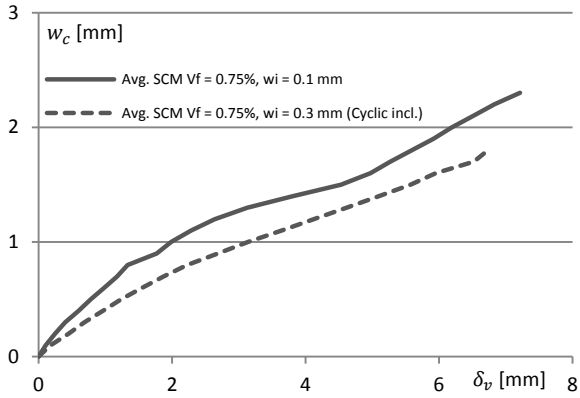

Fig.D.41 – SCM V_f = 0.75%, Shear displacement, δ_v [mm] vs. crack width, w_c [mm]

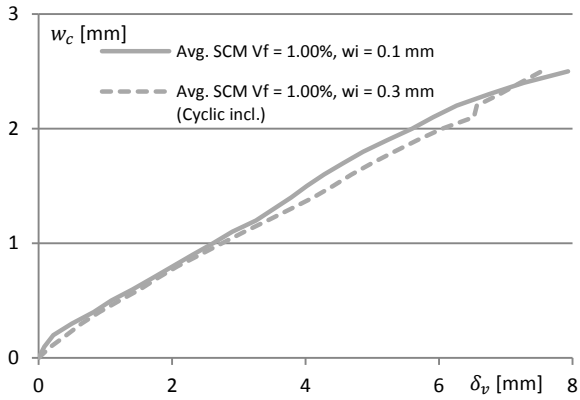

Fig.D.42 – SCM V_f = 1.00%, Shear displacement, δ_v [mm] vs. crack width, w_c [mm]

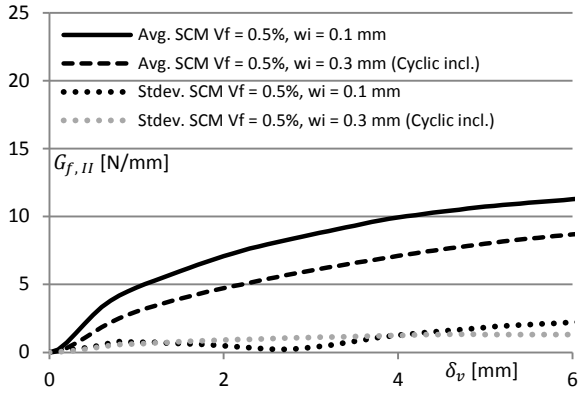

Fig.D.43 – Fracture energy, G_f [N/mm] vs. shear displacement, δ_v [mm] for SCM V_f = 0.50%

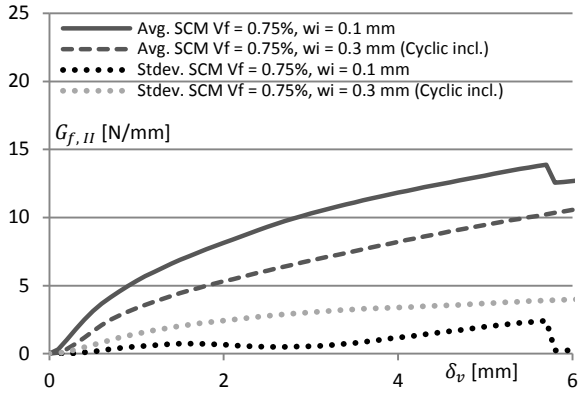

Fig.D.44 – Fracture energy, G_f [N/mm] vs. shear displacement, δ_v [mm] for SCM V_f = 0.75%

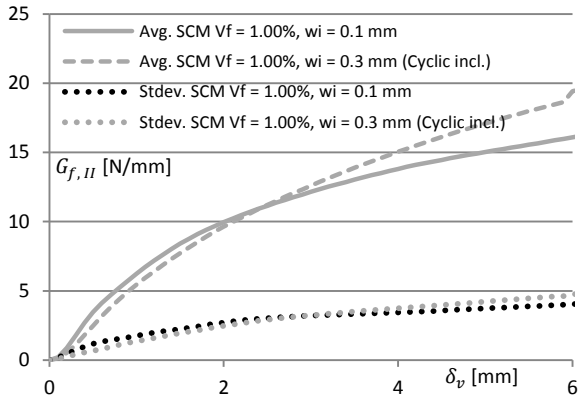

Fig.D.45 – Fracture energy, G_f [N/mm] vs. shear displacement, δ_v [mm] for SCM V_f = 1.00%

D.3.2 Self-consolidating concrete V_a = 450 kg/m^3 (SCC-450)

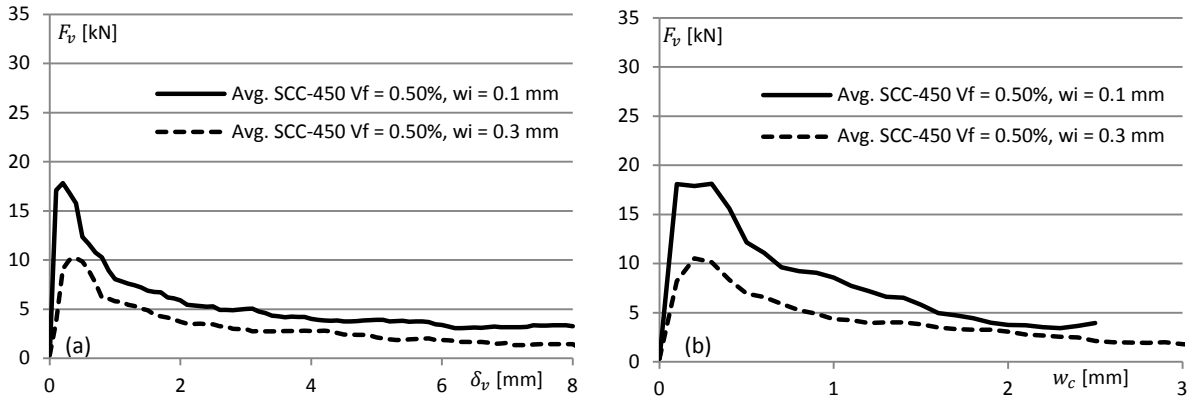

Fig.D.46 – SCC-450 V_f = 0.50%, Shear load, F_v [kN] vs. (a) shear displacement, δ_v [mm] and (b) crack width, w_c [mm]

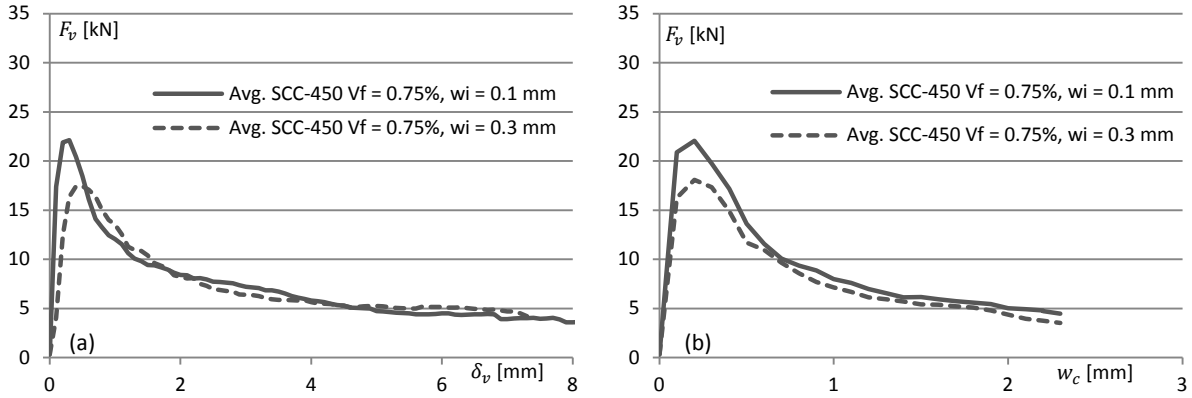

Fig.D.47 – SCC-450 V_f = 0.75%, Shear load, F_v [kN] vs. (a) shear displacement, δ_v [mm] and (b) crack width, w_c [mm]

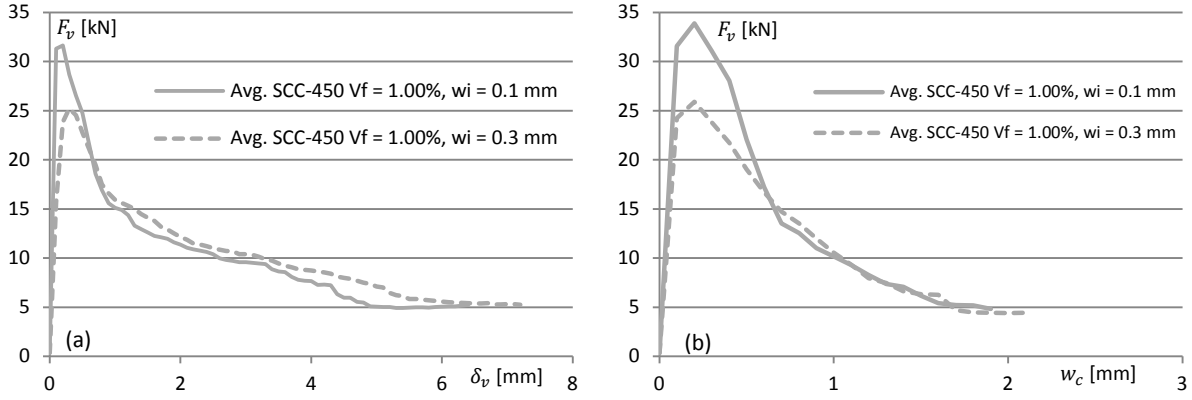

Fig.D.48 – SCC-450 V_f = 1.00%, Shear load, F_v [kN] vs. (a) shear displacement, δ_v [mm] and (b) crack width, w_c [mm]

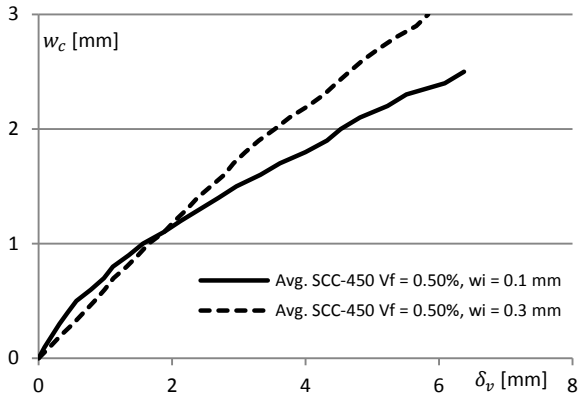

Fig.D.49 – SCC-450 V_f = 0.50%, Shear displacement, δ_v [mm] vs. crack width, w_c [mm]

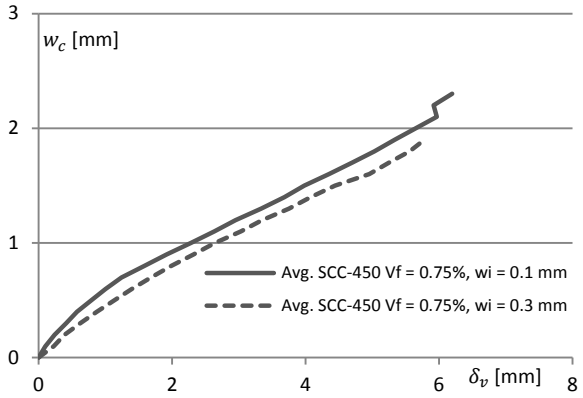

Fig.D.50 – SCC-450 V_f = 0.75%, Shear displacement, δ_v [mm] vs. crack width, w_c [mm]

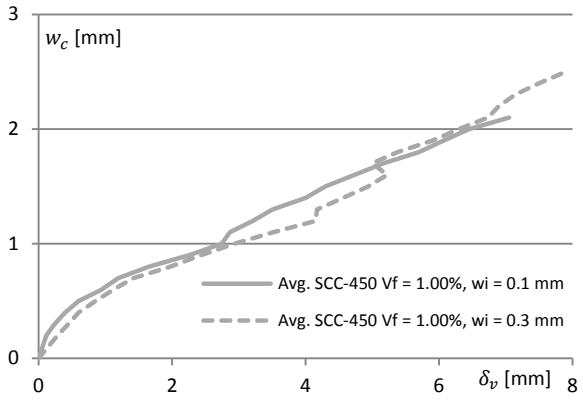

Fig.D.51 – SCC-450 V_f = 1.00%, Shear displacement, δ_v [mm] vs. crack width, w_c [mm]

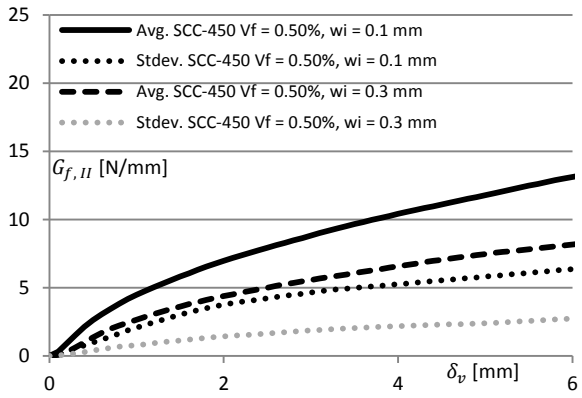

Fig.D.52 – Fracture energy, G_f [N/mm] vs. shear displacement, δ_v [mm] for SCC-450 V_f = 0.50%

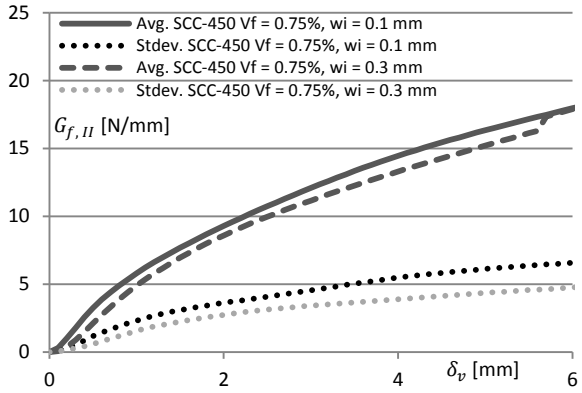

Fig.D.53 – Fracture energy, G_f [N/mm] vs. shear displacement, δ_v [mm] for SCC-450 V_f = 0.75%

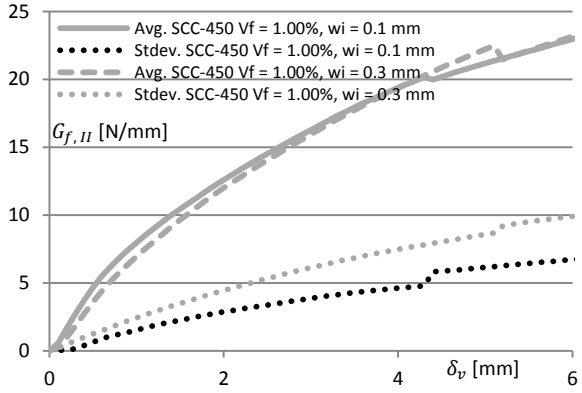

Fig.D.54 – Fracture energy, G_f [N/mm] vs. shear displacement, δ_v [mm] for SCC-450 V_f = 1.00%

D.3.3 Self-consolidating concrete V_a = 600 kg/m^3 (SCC-600)

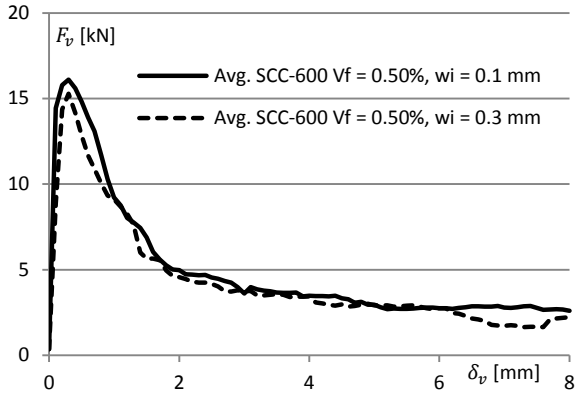

Fig.D.55 – Shear load, F_v [kN] vs. shear displacement, δ_v [mm] for SCC-600 V_f = 0.50%

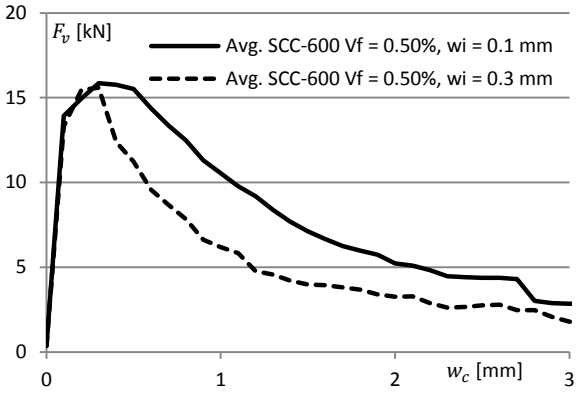

Fig.D.56 – Shear load, F_v [kN] vs. crack width, w_c [mm] for SCC-600 V_f = 0.50%

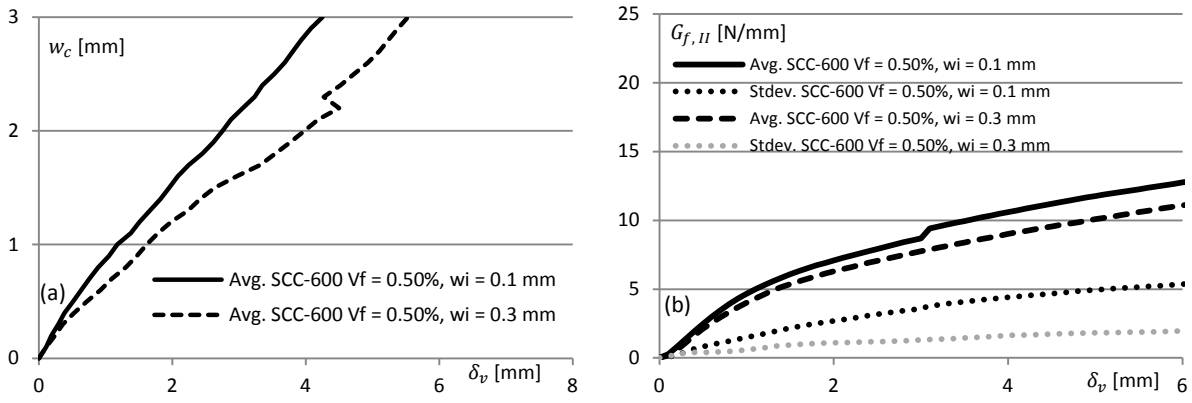

Fig.D.57 – (a) Crack width, w_c [mm] and (b) fracture energy vs. shear displacement, δ_v [mm] for SCC-600 V_f = 0.50

D.4 Effect of composite composition (Aggregate particle size and content)

D.4.1 Shear load F_v vs. shear displacement δ_v

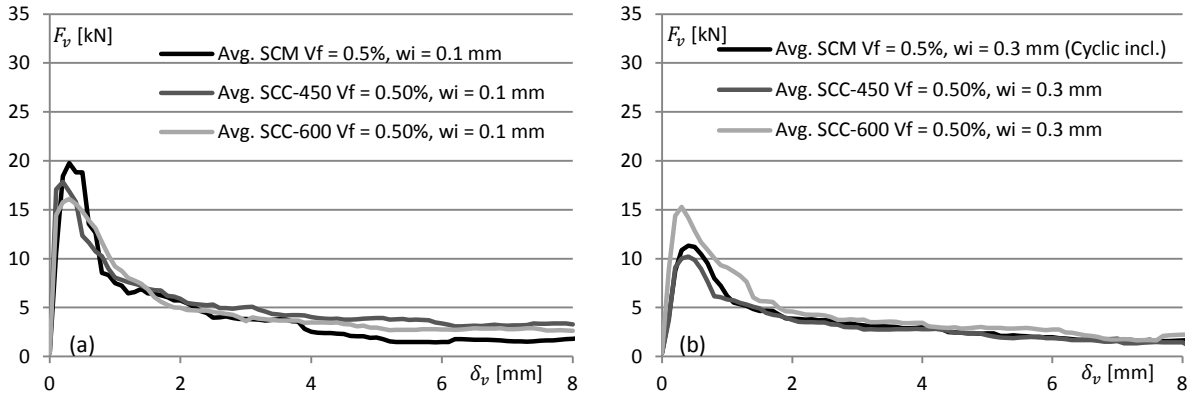

Fig.D.58 – Shear load, F_v [kN] vs. shear displacement, δ_v [mm] for V_f = 0.50% (a) w_i = 0.1 mm (b) w_i = 0.3 mm

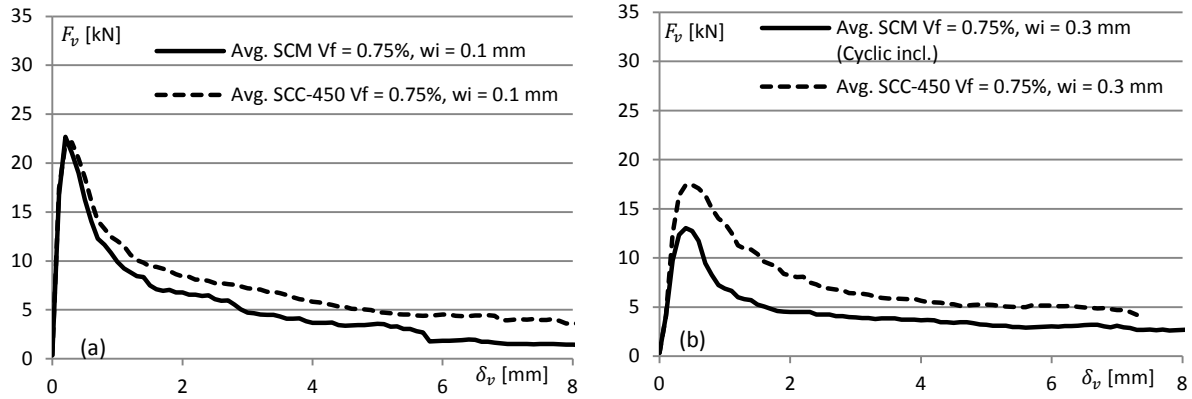

Fig.D.59 – Shear load, F_v [kN] vs. shear displacement, δ_v [mm] for V_f = 0.75% (a) w_i = 0.1 mm (b) w_i = 0.3 mm

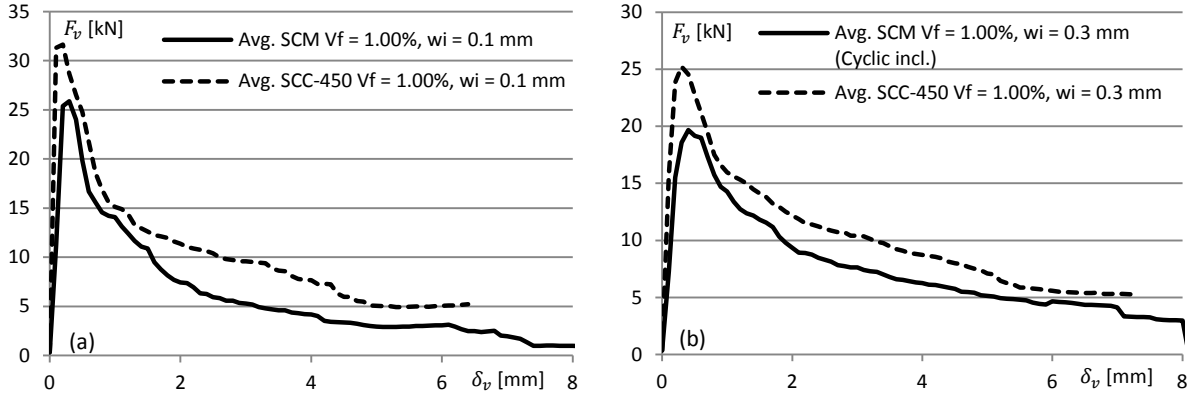

Fig.D.60 – Shear load, F_v [kN] vs. shear displacement, δ_v [mm] for V_f = 1.00% (a) w_i = 0.1 mm (b) w_i = 0.3 mm

D.4.2 Shear load F_v vs. crack width w_c

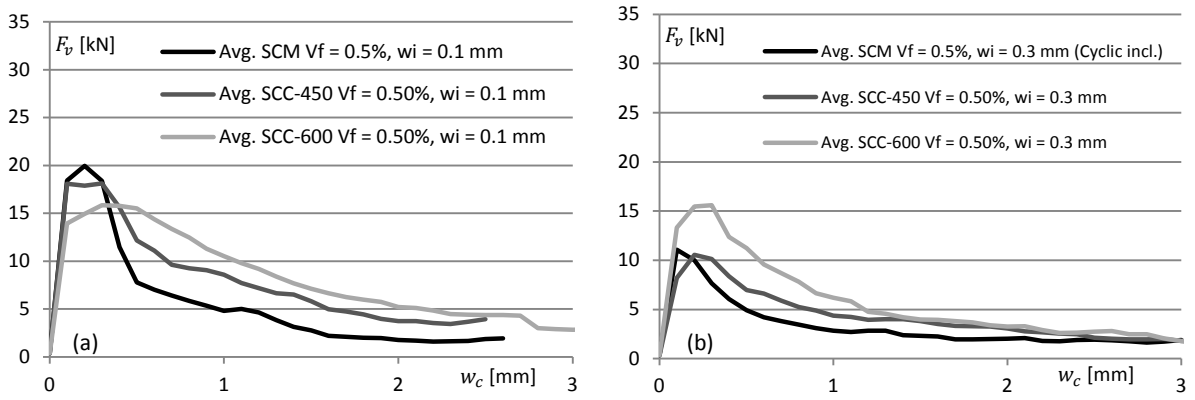

Fig.D.61 – Shear load, F_v [kN] vs. crack width, w_c [mm] for V_f = 0.50% (a) w_i = 0.1 mm (b) w_i = 0.3 mm

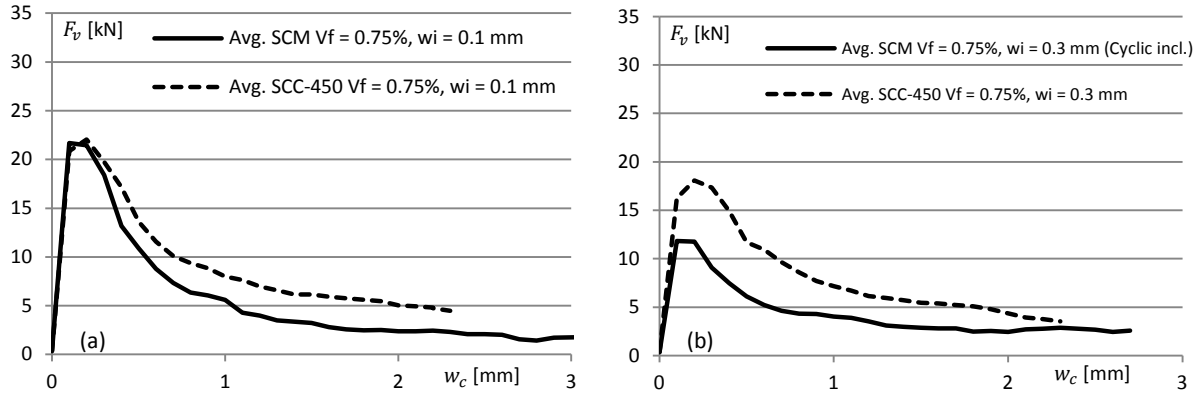

Fig.D.62 – Shear load, F_v [kN] vs. crack width, w_c [mm] for V_f = 0.75% (a) w_i = 0.1 mm (b) w_i = 0.3 mm

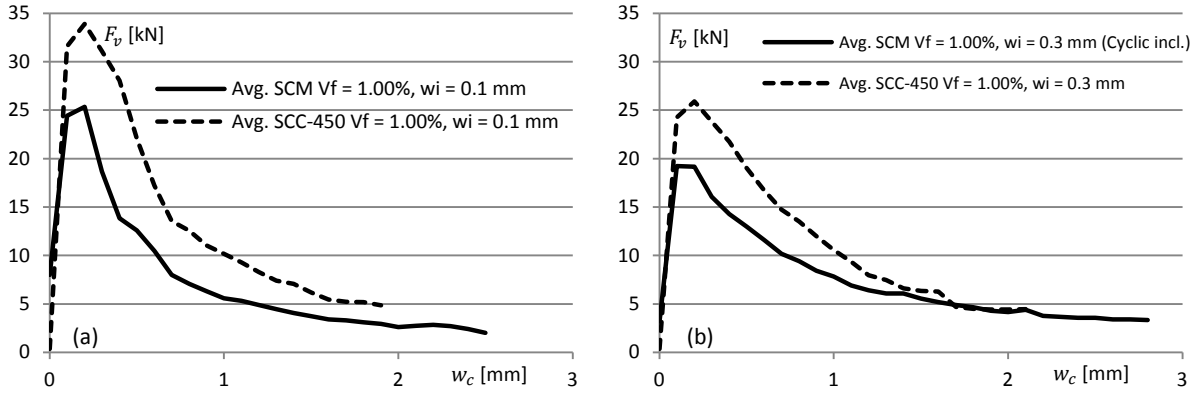

Fig.D.63 – Shear load, F_v [kN] vs. crack width, w_c [mm] for V_f = 1.00% (a) w_i = 0.1 mm (b) w_i = 0.3 mm

D.4.3 Crack width, w_c vs. shear displacement, δ_v

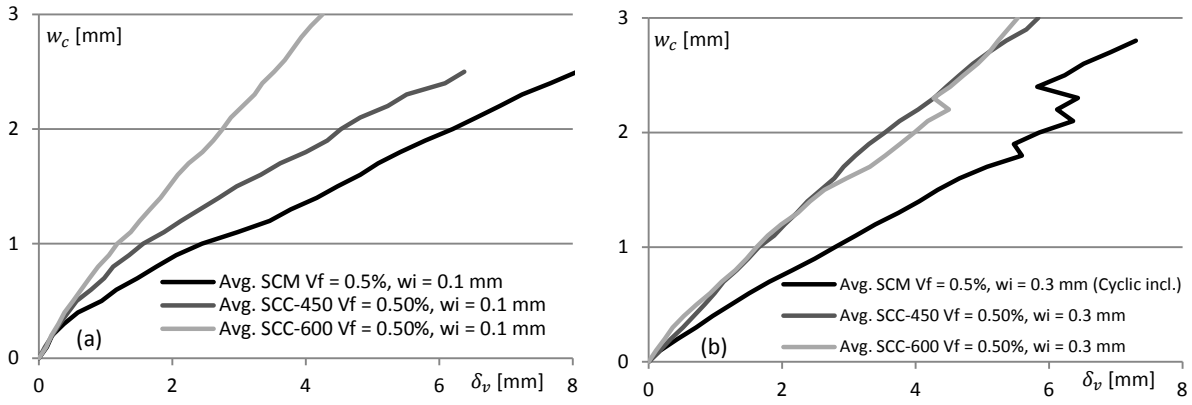

Fig.D.64 – Crack width, w_c [mm] vs. shear displacement, δ_v [mm] for V_f = 0.50% (a) w_i = 0.1 mm (b) w_i = 0.3 mm

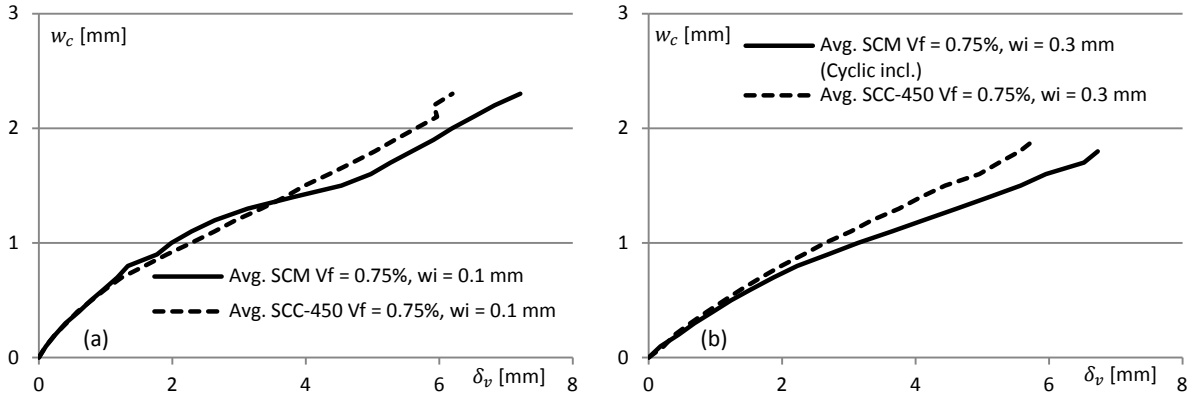

Fig.D.65 – Crack width, w_c [mm] vs. shear displacement, δ_v [mm] for V_f = 0.75% (a) w_i = 0.1 mm (b) w_i = 0.3 mm

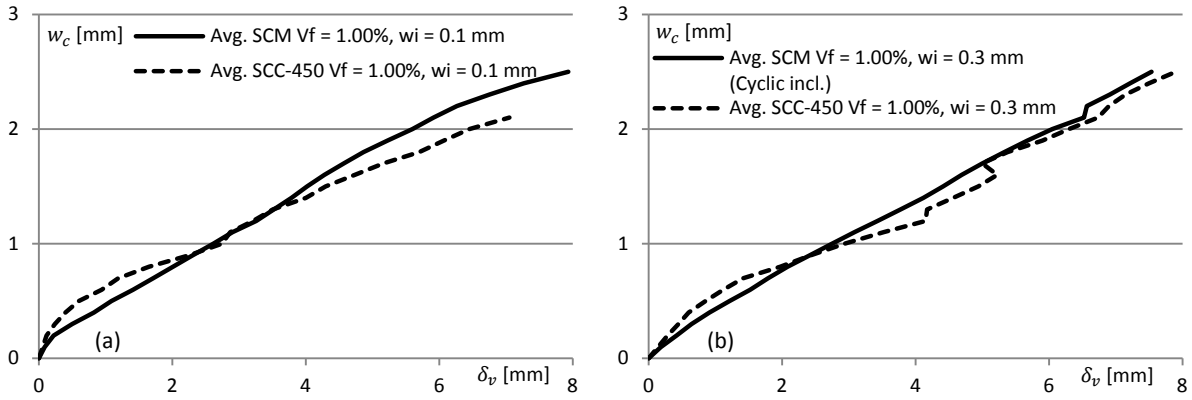

Fig.D.66 – Crack width, w_c [mm] vs. shear displacement, δ_v [mm] for V_f = 1.00% (a) w_i = 0.1 mm (b) w_i = 0.3 mm

D.4.4 Fracture energy, G_f vs. shear displacement, δ_v

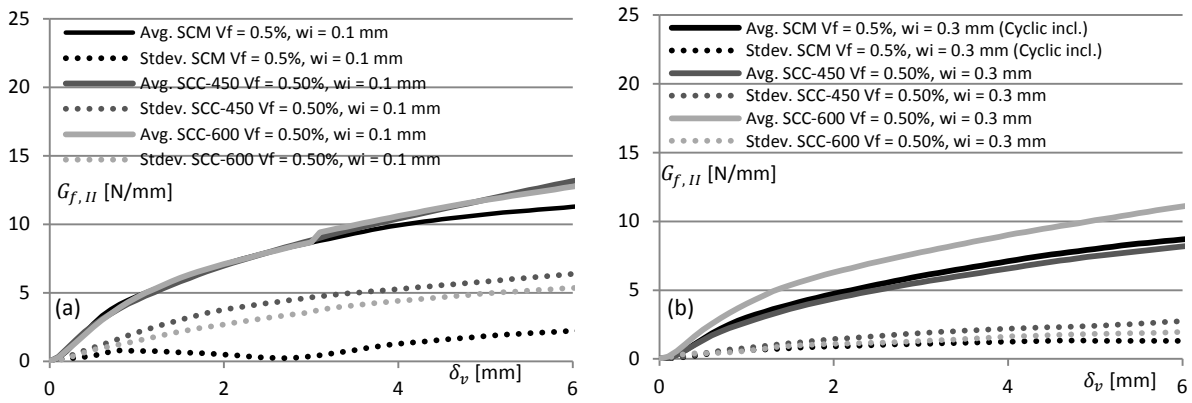

Fig.D.67 – Fracture energy, G_f [N/mm] vs. shear displacement, δ_v [mm] for V_f = 0.50% (a) w_i = 0.1 mm (b) w_i = 0.3 mm

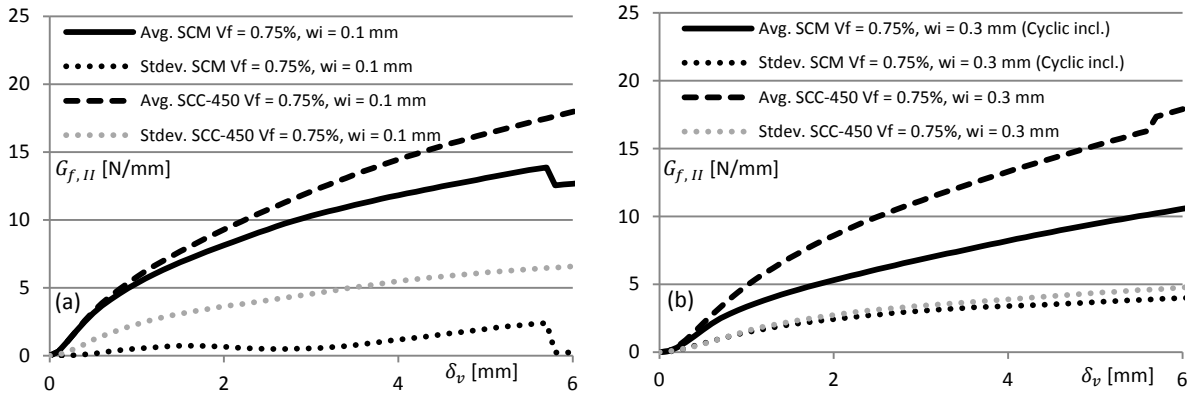

Fig.D.68 – Fracture energy, G_f [N/mm] vs. shear displacement, δ_v [mm] for V_f = 0.75% (a) w_i = 0.1 mm (b) w_i = 0.3 mm

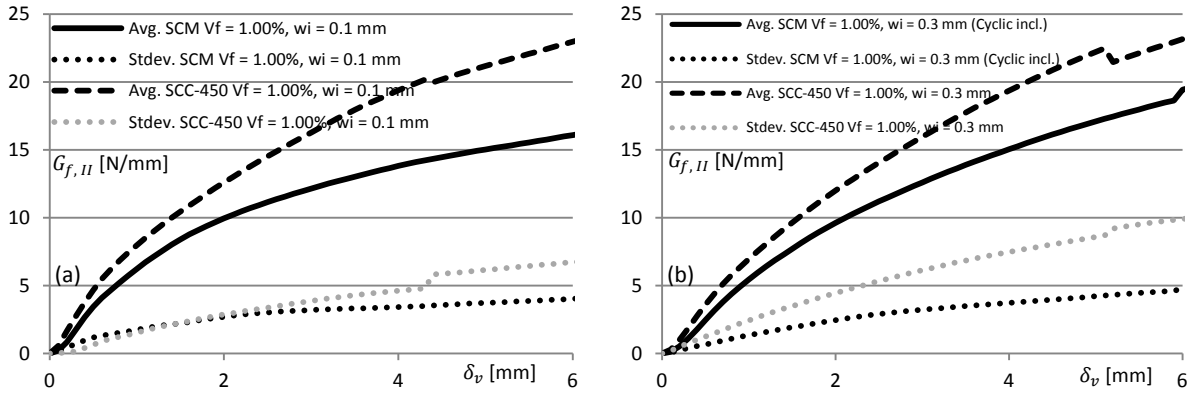

Fig.D.69 – Fracture energy, G_f [N/mm] vs. shear displacement, δ_v [mm] for V_f = 1.00% (a) w_i = 0.1 mm (b) w_i = 0.3 m

D.5 Tables

D.5.1 Phase I – Cyclic tensile loading

Table D.1 – Maximum ($w_{c,max}$) and residual ($w_{c,res}$) crack widths (SCM V_f = 0.50%)

$w_{c,max}$ [mm]	$w_{c,res}^{target}$ = 0.1 mm	$w_{c,res}^{target}$ = 0.3 mm	$w_{c,res}$ [mm]
1	0.175	0.475	0.321
2	0.138	0.413	0.369
3	-	-	-
4	0.176	0.450	0.348
Average	**0.163***	**0.446†**	**0.346**
Standard deviation	0.022	0.031	0.024
Coefficient of variation	**13.5%**	**7.1%**	**6.9%**

* Value used for Phase II (pre-cracking) = 0.150 mm
† Value used for Phase II (pre-cracking) = 0.450 mm

Table D.2 – Maximum ($w_{c,max}$) and residual ($w_{c,res}$) crack widths (SCM V_f = 0.75%)

$w_{c,max}$ [mm]	$w_{c,res}^{target}$ = 0.1 mm	$w_{c,res}^{target}$ = 0.3 mm	$w_{c,res}$ [mm]
1	0.188	0.476	0.316
2	0.188	0.476	0.320
3	0.189	0.463	0.329
4	0.164	0.450	0.333
Average	**0.182**	**0.466**	**0.324**
Standard deviation	0.012	0.012	0.008
Coefficient of variation	**6.8%**	**2.7%**	**2.5%**

Table D.3 – Maximum ($w_{c,max}$) and residual ($w_{c,res}$) crack widths (SCM V_f = 1.00%)

$w_{c,max}$ [mm]	$w_{c,res}^{target}$ = 0.1 mm	$w_{c,res}^{target}$ = 0.3 mm	$w_{c,res}$ [mm]
1	0.164	0.439	0.349
2	0.176	0.476	0.323
3	0.176	0.464	0.330
4	0.188	0.476	0.319
Average	**0.176**	**0.459**	**0.330**
Standard deviation	0.010	0.018	0.013
Coefficient of variation	**5.7%**	**3.8%**	**4.0%**

D.5.2 Phase II – Pre-cracking

Table D.4 – Residual crack widths ($w_{c,res}$) for SCM

$w_{c,res}$ [mm]	V_f = 0.5%		V_f = 0.75%		V_f = 1.00%	
$w_{c,res}^{target}$	0.1 mm	0.3 mm	0.1 mm	0.3 mm	0.1 mm	0.3 mm
1	0.092	0.342	0.107	0.304	0.098	-
2	0.090	0.324	0.104	0.294	-	0.277
3	-	0.311	0.120	0.299	0.104	0.311
4	0.110	0.311	0.119	0.307	0.110	0.298
5	-	-	-	-	-	-
6	-	-	-	-	-	-
Average [mm]	**0.097**	**0.322**	**0.113**	**0.301**	**0.104**	**0.295**
Standard deviation [mm]	0.011	0.015	0.008	0.005	0.006	0.017
Coefficient of variation (C.V.)	**11.0%**	**4.6%**	**7.2%**	**1.8%**	**5.9%**	**5.8%**

Table D.5 – Residual crack widths ($w_{c,res}$) for SCC-450

$w_{c,res}$ [mm]	V_f = 0.5%		V_f = 0.75%		V_f = 1.00%	
$w_{c,res}^{target}$	0.1 mm	0.3 mm	0.1 mm	0.3 mm	0.1 mm	0.3 mm
1	0.087	0.328	0.112	0.328	0.095	0.313
2	0.103	0.291	0.108	0.330	0.104	0.310
3	0.096	0.311	0.117	0.355	0.108	0.312
4	0.105	0.340	0.101	0.345	0.099	0.316
5	0.098	0.318	0.105	0.333	0.100	0.326
6	0.098	0.325	0.130	0.315	0.109	0.323
Average [mm]	**0.098**	**0.319**	**0.112**	**0.335**	**0.103**	**0.317**
Standard deviation [mm]	0.006	0.017	0.010	0.014	0.005	0.006
Coefficient of variation (C.V.)	**6.3%**	**5.2%**	**9.0%**	**4.2%**	**5.3%**	**2.0%**

Table D.6 – Residual crack widths ($w_{c,res}$) for SCC-600

$w_{c,res}$ [mm]	V_f = 0.5%	
$w_{c,res}^{target}$	0.1 mm	0.3 mm
1	0.106	0.305
2	0.092	0.343
3	0.097	0.303
4	0.107	0.302
5	0.099	0.307
6	0.076	0.303
Average [mm]	**0.096**	**0.310**
Standard deviation [mm]	**0.011**	**0.016**
Coefficient of variation (C.V.)	**12.0%**	**5.1%**

D.5.3 Phase III – Iosipescu shear test

Table D.7 – Maximum shear load (F_v^{max}) and shear stress (τ_{avg}^{max}) for SCM

F_v^{max} [N]	V_f = 0.5%			V_f = 0.75%			V_f = 1.00%		
$w_{c,res}^{target}$	0.1 mm	0.3 mm	Cyclic	0.1 mm	0.3 mm	Cyclic	0.1 mm	0.3 mm	Cyclic
1	16911	9491	17905	25167	-	9254	-	-	12749
2	27246	15616	11484	33486	20354	20496	31972	27648	24039
3	-	10537	-	23767	9785	18204	34950	18133	25554
4	20778	13792	8923	23938	6701	16959	17004	21596	21116
5	-	-	-	-	-	-	-	-	-
6	-	-	-	-	-	-	-	-	-
Average [N]	21645	12536		26590	14536		27975	21548	
Std. Dev. [N]	5222	3350		4640	5781		9617	4979	
C.V.	**24.1%**	**26.7%**		**17.4%**	**39.8%**		**34.4%**	**23.1%**	
τ_{avg}^{max} [MPa]†	**7.73**	**4.48**		**9.50**	**5.19**		**9.99**	**7.70**	

† Specimen section area assumed to be approximately 70 x 40 mm.

Table D.8 – Maximum shear load (F_v^{max}) and shear stress (τ_{avg}^{max}) for SCC-450

F_v^{max} [N]	V_f = 0.5%		V_f = 0.75%		V_f = 1.00%	
$w_{c,res}^{target}$	0.1 mm	0.3 mm	0.1 mm	0.3 mm	0.1 mm	0.3 mm
1	20329	6233	31308	12173	34812	26220
2	24303	11253	20203	14984	32557	27248
3	9839	11890	16395	22589	38005	35978
4	25512	10798	29733	19340	33385	35081
5	-	16250	27447	14529	-	18017
6	-	-	11953	26180	-	13870
Average [N]	19996	11285	22840	18299	34690	26069
Std. Dev. [N]	7124	3563	7842	5373	2398	8882
C.V.	**35.6%**	**31.6%**	**34.3%**	**29.4%**	**6.9%**	**34.1%**
τ_{avg}^{max} [MPa]†	**7.14**	**4.03**	**8.16**	**6.54**	**12.39**	**9.31**

† Specimen section area assumed to be approximately 70 x 40 mm.

Table D.9 – Maximum shear load (F_v^{max}) and shear stress (τ_{avg}^{max}) for SCC-600

F_v^{max} [N]	V_f = 0.5%	
$w_{c,res}^{target}$	0.1 mm	0.3 mm
1	11853	19210
2	27715	12736
3	15275	16688
4	13610	16695
5	19364	19556
6	13610	14001
Average [N]	16905	16481
Std. Dev. [N]	5879	2727
C.V.	**34.8%**	**16.5%**
τ_{avg}^{max} [MPa]†	**6.04**	**5.89**

† Specimen section area assumed to be approximately 70 x 40 mm.

Table D.10 – Shear displacement (δ_v^{max}) corresponding to maximum shear load/stress for SCM

$\boldsymbol{\delta_v^{max}}$ **[mm]**	V_f = 0.5%			V_f = 0.75%			V_f = 1.00%		
$w_{c,res}^{target}$	0.1 mm	0.3 mm	Cyclic	0.1 mm	0.3 mm	Cyclic	0.1 mm	0.3 mm	Cyclic
1	0.397	0.190	0.400	0.220	-	0.337	-	-	0.390
2	0.257	0.350	0.460	0.393	0.293	0.540	0.200	0.280	0.540
3	-	0.467	-	0.173	0.410	0.460	0.190	0.400	0.520
4	0.457	0.300	0.370	0.187	0.280	0.357	0.363	0.193	0.480
5	-	-	-	-	-	-	-	-	-
6	-	-	-	-	-	-	-	-	-
Average [mm]	**0.370**	**0.362**		**0.243**	**0.382**		**0.251**	**0.400**	
Std. Dev. [mm]	0.103	0.096		0.102	0.094		0.097	0.128	
C.V.	**27.7%**	**26.6%**		**41.9%**	**24.5%**		**38.8%**	**31.8%**	

Table D.11 – Shear displacement (δ_v^{max}) corresponding to maximum shear load/stress for SCC-450

$\boldsymbol{\delta_v^{max}}$ **[mm]**	V_f = 0.5%		V_f = 0.75%		V_f = 1.00%	
$w_{c,res}^{target}$	0.1 mm	0.3 mm	0.1 mm	0.3 mm	0.1 mm	0.3 mm
1	0.090	0.380	0.247	0.360	0.013	0.170
2	0.217	0.597	0.150	0.287	0.053	0.207
3	0.040	0.180	0.180	0.647	0.213	0.380
4	0.193	0.187	0.280	0.560	0.137	0.120
5	-	0.403	0.187	0.270	-	0.297
6	-	-	0.220	0.433	-	0.320
Average [mm]	**0.135**	**0.349**	**0.211**	**0.426**	**0.104**	**0.249**
Std. Dev. [mm]	0.084	0.173	0.048	0.152	0.089	0.099
C.V.	**62.2%**	**49.6%**	**22.7%**	**35.6%**	**85.5%**	**39.8%**

Table D.12 – Shear displacement (δ_v^{max}) corresponding to maximum shear load/stress for SCC-600

$\boldsymbol{\delta_v^{max}}$ **[mm]**	V_f = 0.5%	
$w_{c,res}^{target}$	0.1 mm	0.3 mm
1	0.060	0.277
2	0.233	0.477
3	0.050	0.190
4	0.047	0.417
5	0.293	0.100
6	0.430	0.417
Average [mm]	**0.186**	**0.313**
Std. Dev. [mm]	0.159	0.148
C.V.	**85.9%**	**47.4%**

Table D.13 – Crack width (w_c^{max}) corresponding to maximum shear load/stress for SCM

w_c^{max} [mm]	V_f = 0.5%			V_f = 0.75%			V_f = 1.00%		
$w_{c,res}^{target}$	0.1 mm	0.3 mm	Cyclic	0.1 mm	0.3 mm	Cyclic	0.1 mm	0.3 mm	Cyclic
1	0.363	0.147	0.075	0.131	-	0.090	-	-	0.160
2	0.178	0.133	0.206	0.457	0.182	0.097	0.128	0.195	0.211
3	-	0.162	-	0.196	0.100	0.203	0.172	0.169	0.134
4	~~1.337~~	0.140	0.111	0.560	0.150	0.157	0.187	0.104	0.142
5	-	-	-	-	-	-	-	-	-
6	-	-	-	-	-	-	-	-	-
Average [mm]	**0.270**	**0.139**		**0.336**	**0.140**		**0.163**	**0.159**	
Std. Dev. [mm]	0.130	0.041		0.205	0.045		0.030	0.037	
C.V.	**48.2%**	**29.4%**		**61.1%**	**32.1%**		**18.8%**	**22.9%**	

Table D.14 – Crack width (w_c^{max}) corresponding to maximum shear load/stress for SCC-450

w_c^{max} [mm]	V_f = 0.5%		V_f = 0.75%		V_f = 1.00%	
$w_{c,res}^{target}$	0.1 mm	0.3 mm	0.1 mm	0.3 mm	0.1 mm	0.3 mm
1	0.106	0.199	0.142	0.199	0.188	0.125
2	0.226	0.282	0.153	0.154	0.150	0.130
3	0.023	0.241	0.197	0.239	0.206	0.294
4	0.248	0.083	0.289	0.212	0.325	0.209
5	-	0.214	0.159	0.172	-	0.149
6	-	-	0.399	0.211	-	0.189
Average [mm]	**0.151**	**0.204**	**0.223**	**0.198**	**0.217**	**0.183**
Std. Dev. [mm]	0.106	0.075	0.102	0.031	0.075	0.064
C.V.	**69.9%**	**36.6%**	**45.6%**	**15.4%**	**34.7%**	**34.8%**

Table D.15 – Crack width (w_c^{max}) corresponding to maximum shear load/stress for SCC-600

w_c^{max} [mm]	V_f = 0.5%	
$w_{c,res}^{target}$	0.1 mm	0.3 mm
1	0.082	0.224
2	0.397	0.381
3	0.052	0.220
4	0.091	0.319
5	0.620	0.178
6	0.327	0.218
Average [mm]	**0.261**	**0.257**
Std. Dev. [mm]	0.226	0.077
C.V.	**86.6%**	**29.9%**

D.5.4 Manual fibre count (Iosipescu specimens, Meso-scale)

Table D.16 – Manual fibre count for SCM, V_f= 0.5, 0.75 & 1.0% (w_i = 0.1 mm & 0.3 mm)

V_f = 0.5%, w_i=0.1 mm

Spec.	N_{f1}	N_{f2}	N_f
0.1 1	-	-	26
0.1 2	-	-	22
Avg.			**24**
Stdev.			**3**
C.V.			**12%**

V_f = 0.5%, w_i=0.3 mm

Spec.	N_{f1}	N_{f2}	N_f	
Cyc 4	-	-	25	SCM, V_f = 0.5%
Cyc 1	-	-	26	
Cyc 2	-	-	20	
0.3 3	-	-	26	
0.3 2	-	-	25	
Avg.			**24**	**Avg. 24**
Stdev.			**3**	**Stdev. 2**
C.V.			**10%**	**C.V. 9.7%**

V_f = 0.75%, w_i=0.1 mm

Spec.	N_{f1}	N_{f2}	N_f
0.1 4	-	-	39
0.1 2	-	-	53
0.1 3	-	-	28
0.1 1	-	-	31
Avg.			**38**
Stdev.			**11**
C.V.			**30%**

V_f = 0.75%, w_i=0.3 mm

Spec.	N_{f1}	N_{f2}	N_f	
Cyc 2	-	-	30	SCM, V_f = 0.75%
Cyc 3	-	-	50	
Cyc 1	-	-	24	
Cyc 4	-	-	31	
0.3.2	-	-	55	
0.3 4	-	-	23	
0.3 3	-	-	26	
Avg.			**34**	**Avg. 35**
Stdev.			**13**	**Stdev. 12**
C.V.			**38%**	**C.V. 33.5%**

V_f = 1.0%, w_i=0.1 mm

Spec.	N_{f1}	N_{f2}	N_f
0.1 4	-	-	36
0.1 3	-	-	61
0.1 2	-	-	50
Avg.			**49**
Stdev.			**13**
C.V.			**26%**

V_f = 1.0%, w_i=0.3 mm

Spec.	N_{f1}	N_{f2}	N_f	
0.3 3	-	-	57	SCM, V_f = 1.0%
0.3 4	-	-	56	
Cyc 1	-	-	54	
Cyc 4	-	-	49	
Cyc 3	-	-	44	
Cyc 2	-	-	60	
Avg.			**53**	**Avg. 52**
Stdev.			**6**	**Stdev. 8**
C.V.			**11%**	**C.V. 15.6%**

Table D.17 – Manual fibre count for SCC-450, V_f = 0.5, 0.75 & 1.0% (w_i = 0.1 mm & 0.3 mm)

V_f = 0.5%, w_i=0.1 mm

Spec.	N_{f1}	N_{f2}	N_f
1 **(CT-11)**	17	13	30
2	11	17	28
3	22	26	48
4 **(CT-14)**	6	7	13
5	16	23	39
6	18	9	27
Avg.			**31**
Stdev.			**12**
C.V.			**38%**

V_f = 0.5%, w_i=0.3 mm

Spec.	N_{f1}	N_{f2}	N_f		
1	9	8	17	SCC-450, V_f = 0.5%	
2	10	9	19		
3	15	15	30		
4	12	13	25		
5	20	16	36		
6	27	19	46		
Avg.			**29**	**Avg.**	**30**
Stdev.			**11**	**Stdev.**	**11**
C.V.			**38%**	**C.V.**	**36.6%**

V_f = 0.75%, w_i=0.1 mm

Spec.	N_{f1}	N_{f2}	N_f
1	26	14	40
2 **(CT-12)**	21	17	38
3	20	12	32
4	21	34	55
5	25	28	53
6 **(CT-13)**	13	14	27
Avg.			**41**
Stdev.			**11**
C.V.			**27%**

V_f = 0.75%, w_i=0.3 mm

Spec.	N_{f1}	N_{f2}	N_f		
1	24	23	47	SCC-450, V_f = 0.75%	
2	28	28	56		
3	30	29	59		
4	23	21	44		
5	35	24	59		
6	50	34	84		
Avg.			**58**	**Avg.**	**50**
Stdev.			**14**	**Stdev.**	**15**
C.V.			**24%**	**C.V.**	**30.6%**

V_f = 1.0%, w_i=0.1 mm

Spec.	N_{f1}	N_{f2}	N_f
1	42	34	76
2	33	48	81
3	33	32	65
4	53	47	100
5 **(CT-9)**	39	37	76
6	36	39	75
Avg.			**79**
Stdev.			**12**
C.V.			**15%**

V_f = 1.0%, w_i=0.3 mm

Spec.	N_{f1}	N_{f2}	N_f		
1	46	43	89	SCC-450, V_f = 1.0%	
2	57	50	107		
3	46	40	86		
4	53	50	103		
5	26	33	59		
6 **(CT-7)**	34	33	67		
Avg.			**85**	**Avg.**	**82**
Stdev.			**19**	**Stdev.**	**15**
C.V.			**22%**	**C.V.**	**18.8%**

Table D.18 – Manual fibre count for SCC-600, V_f = 0.5% (w_i = 0.1 mm & 0.3 mm)

V_f = 0.5%, w_i=0.1 mm

Spec.	N_{f1}	N_{f2}	N_f
1 **(CT-10)**	13	7	20
2	24	21	45
3	13	9	22
4	21	17	38
5	13	9	22
6	11	24	35
Avg.			**30**
Stdev.			**10**
C.V.			**34%**

V_f = 0.5%, w_i=0.3 mm

Spec.	N_{f1}	N_{f2}	N_f		
1	20	20	40	SCC-600, V_f = 0.5%	
2	10	9	19		
3	19	19	38		
4	12	18	30		
5	29	18	47		
6	16	17	33		
Avg.			**35**	**Avg.**	**32**
Stdev.			**10**	**Stdev.**	**10**
C.V.			**28%**	**C.V.**	**30.2%**

D.6 FE refinement of specimen geometry

D.6.1 Effect of notch tip radius, r (Notch depth = 15 mm)

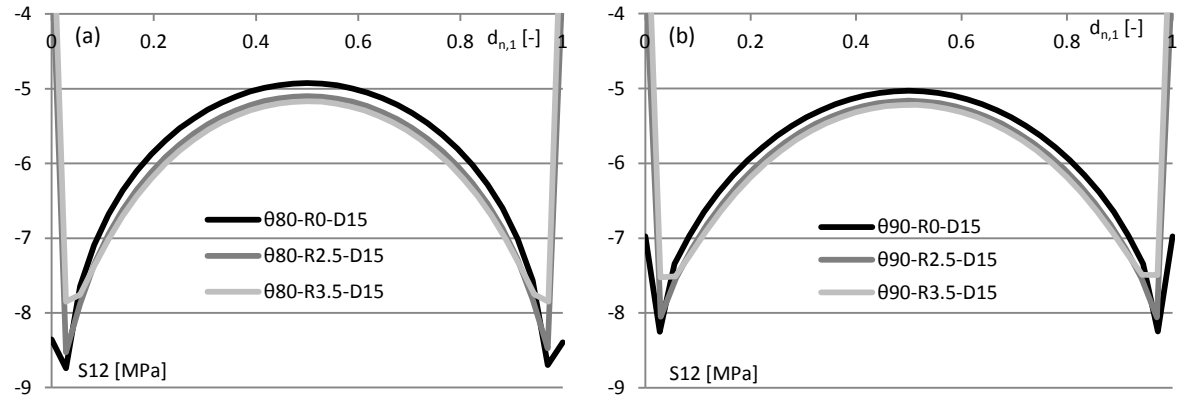

Fig.D.70 – Shear stress (S12) vs normalised distance along line 1 (a) θ = 80° and (b) θ = 90°

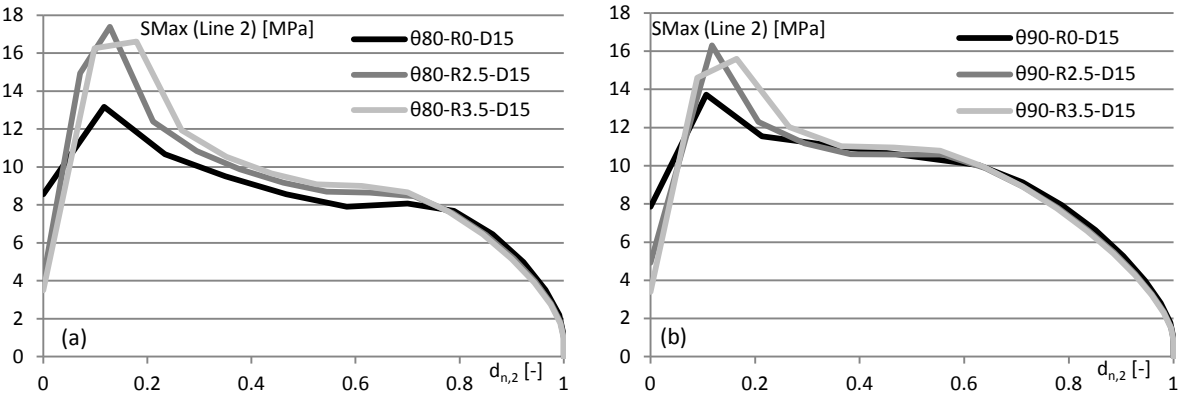

Fig.D.71 – Maximum principal stress (SMax) vs normalised distance along line 2 (a) θ = 80° and (b) θ = 90°

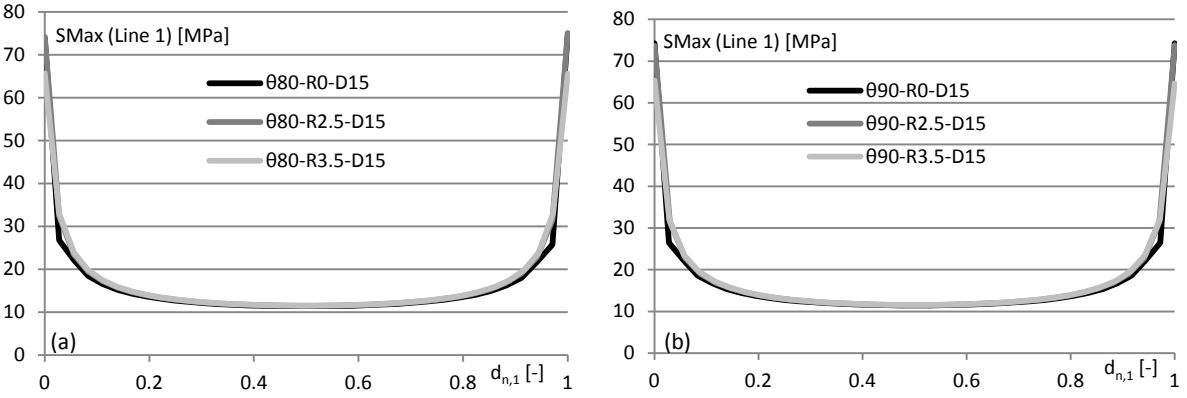

Fig.D.72 – Maximum principal stress (SMax – applied tensile load) vs normalised distance along line 1 (a) θ = 80° and (b) θ = 90°

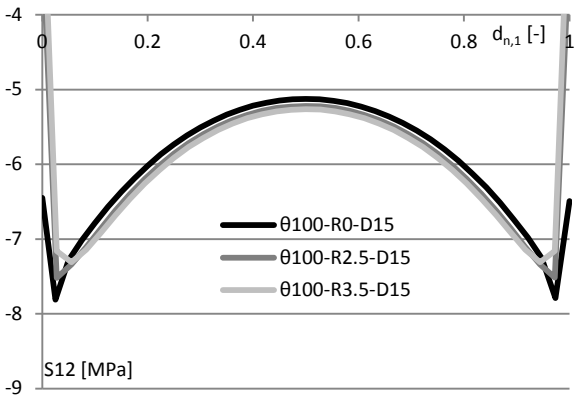

Fig.D.73 – Shear stress (S12) vs normalised distance along line 1 (θ = 100°)

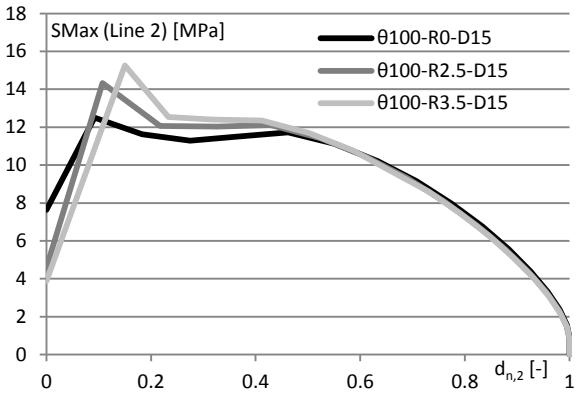

Fig.D.74 – Maximum principal stress (SMax) vs normalised distance along line 2 (θ = 100°)

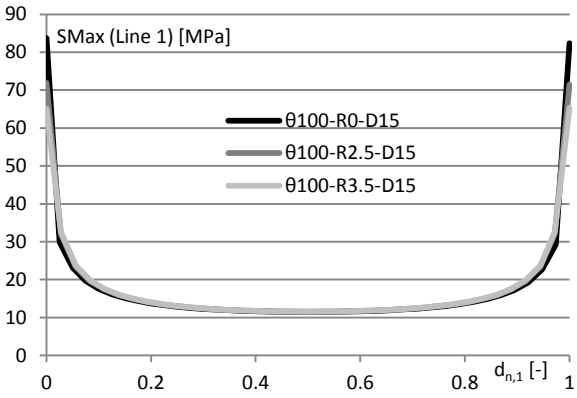

Fig.D.75 – Maximum principal stress (SMax – applied tensile load) vs normalised distance along line 1 (θ = 100°)

D.6.2 Effect of notch angle, θ (Notch depth = 15 mm)

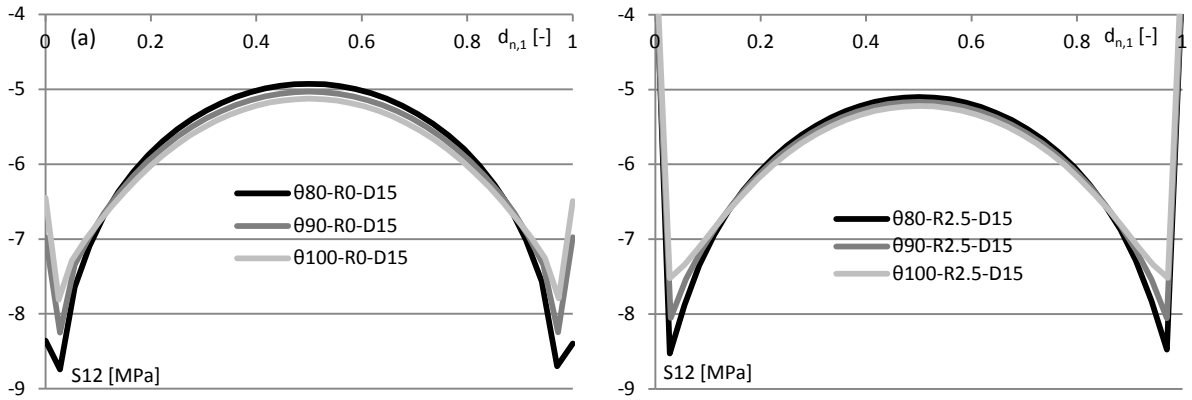

Fig.D.76 – Shear stress (S12) vs normalised distance along line 1 (a) r = 0 mm and (b) r = 2.5 mm

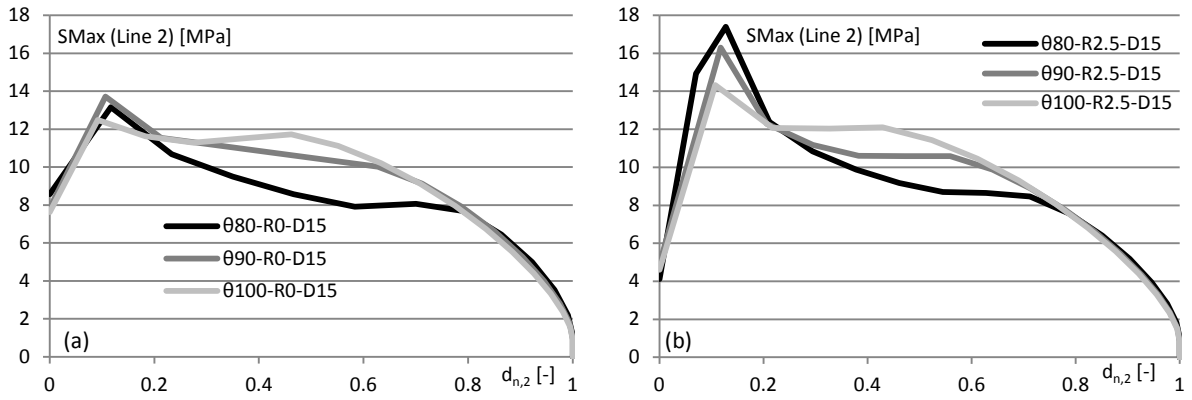

Fig.D.77 – Maximum principal stress (SMax) vs normalised distance along line 2 (a) r = 0 mm and (b) r = 2.5 mm

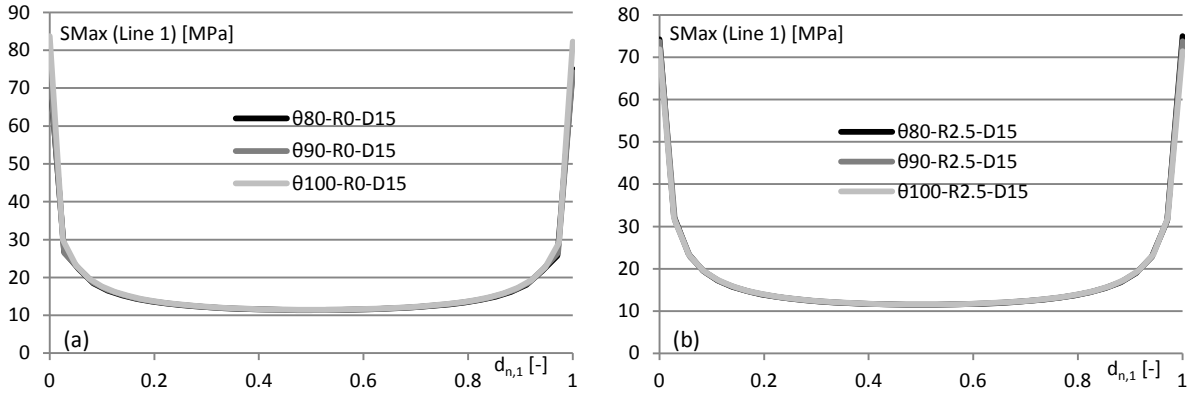

Fig.D.78 – Maximum principal stress (SMax – applied tensile load) vs normalised distance along line 1 (a) r = 0 mm and (b) r = 2.5 mm

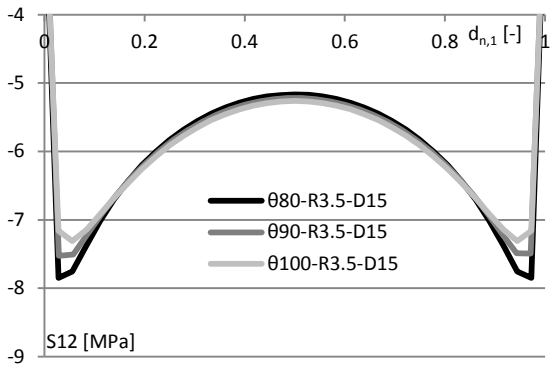

Fig.D.79 – Shear stress (S12) vs normalised distance along line 1 (r = 3.5 mm)

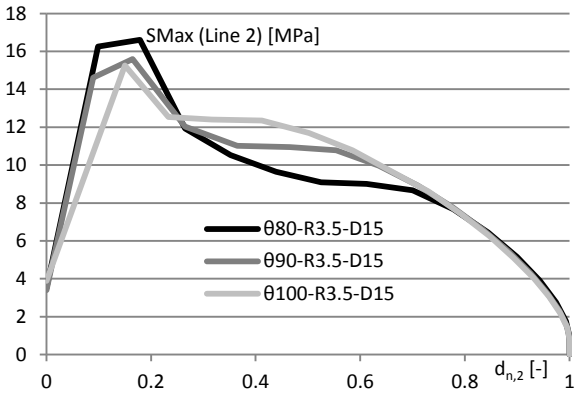

Fig.D.80 – Maximum principal stress (SMax) vs normalised distance along line 2 (r = 3.5 mm)

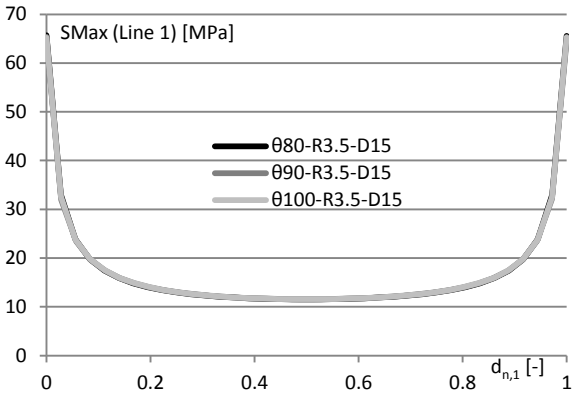

Fig.D.81 – Maximum principal stress (SMax – applied tensile load) vs normalised distance along line 1 (r = 3.5 mm)

D.6.3 Effect of notch depth (Notch angle, θ = 90°; Notch radius, r = 2.5 mm)

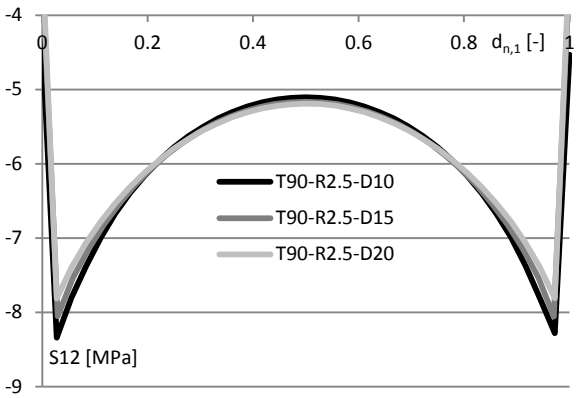

Fig.D.82 – Shear stress (S12) vs normalised distance along line 1 (θ = 90°; r = 2.5 mm)

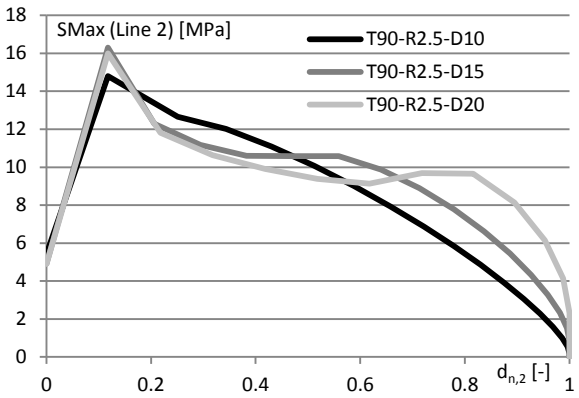

Fig.D.83 – Maximum principal stress (SMax) vs normalised distance along line 2 (θ = 90°; r = 2.5 mm)

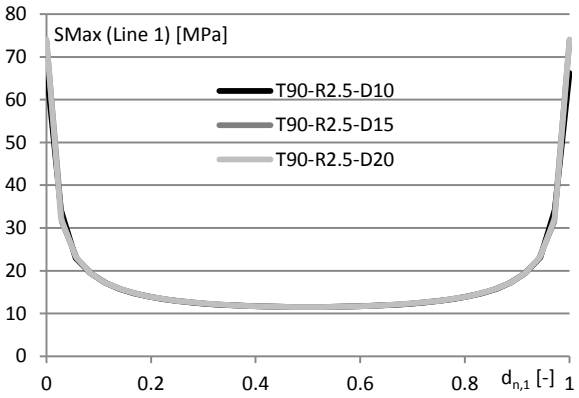

Fig.D.84 – Maximum principal stress (SMax – applied tensile load) vs normalised distance along line 1 (θ = 90°; r = 2.5 mm)

D.7 Experimental investigation at the Micro-scale

D.7.1 Transverse pull-out load vs. transverse pull-out displacement ($L_{fe} = L_f/2$)

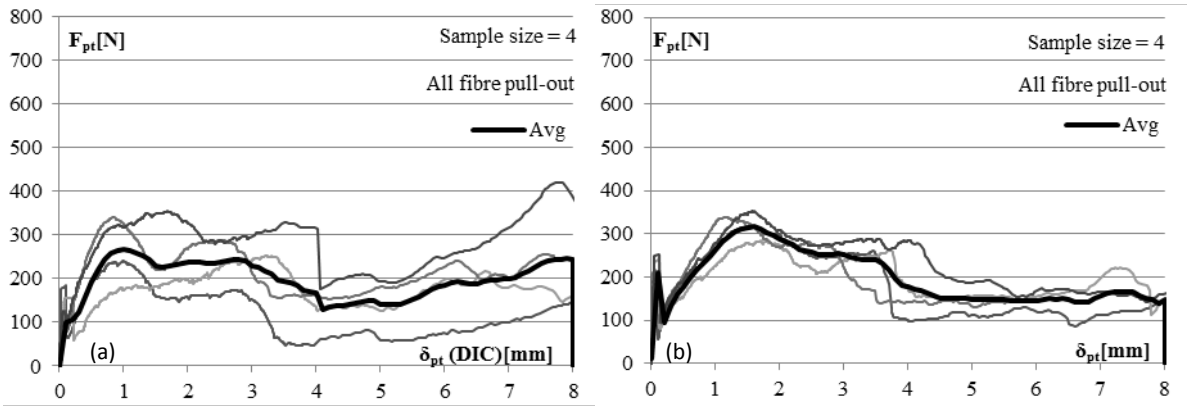

Figure D.85 – Transverse pull-out load (F_{pt}) vs. transverse pull-out displacement (δ_{pt}) for (a) θ = +60°, $L_{fe} = L_f/2$ and (b) θ = +30°, $L_{fe} = L_f/2$

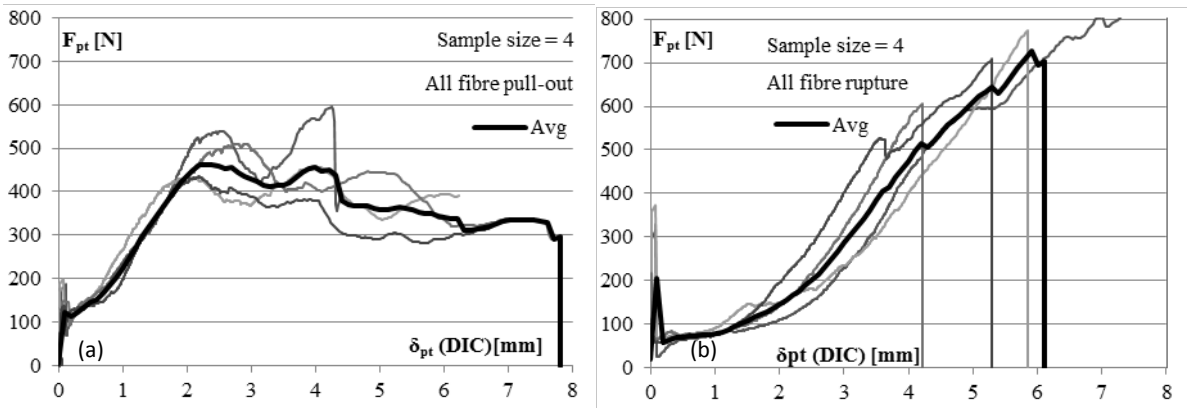

Figure D.86 – Transverse pull-out load (F_{pt}) vs. transverse pull-out displacement (δ_{pt}) for (a) θ = 0°, $L_{fe} = L_f/2$ and (b) θ = -30°, $L_{fe} = L_f/2$

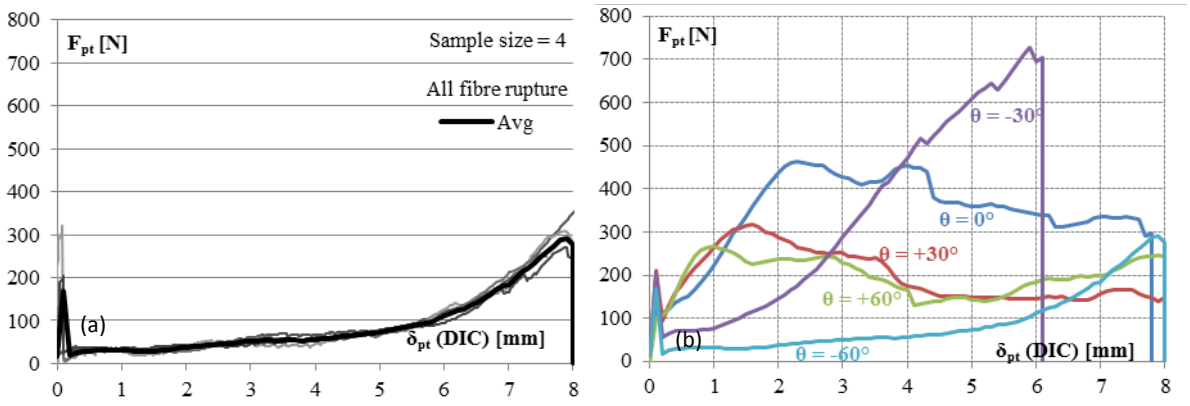

Figure D.87 – Transverse pull-out load (F_{pt}) vs. transverse pull-out displacement (δ_{pt}) for (a) θ = -60°, $L_{fe} = L_f/2$ and (b) average response for θ = -60° to +60°, $L_{fe} = L_f/2$

E FORTRAN code for UMAT

```
      SUBROUTINE UMAT(STRESS,STATEV,DDSDDE,SSE,SPD,SCD,
     1 RPL,DDSDDT,DRPLDE,DRPLDT,
     2 STRAN,DSTRAN,TIME,DTIME,TEMP,DTEMP,PREDEF,DPRED,CMNAME,
     3 NDI,NSHR,NTENS,NSTATV,PROPS,NPROPS,COORDS,DROT,PNEWDT,
     4 CELENT,DFGRD0,DFGRD1,NOEL,NPT,LAYER,KSPT,KSTEP,KINC)

      INCLUDE 'ABA_PARAM.INC'

      CHARACTER*80 CMNAME

      DIMENSION STRESS(NTENS),STATEV(NSTATV),
     1 DDSDDE(NTENS,NTENS),DDSDDT(NTENS),DRPLDE(NTENS),
     2 STRAN(NTENS),DSTRAN(NTENS),TIME(2),PREDEF(1),DPRED(1),
     3 PROPS(NPROPS),COORDS(3),DROT(3,3),DFGRD0(3,3),DFGRD1(3,3),
     4 DTRACE(3),TRACE(3)

      REAL(8) :: TE(3,3),TS12(3,3)
      REAL(8) :: STRANMAT(2,2),QMAT(2,2),QE(2,2),EP(2,2)
      REAL(8) :: DNT(2,2),DCON(3,2),NTDCO(2,3),NTDCON(2,2),DCRCO(3,3)
      REAL(8) :: DC(3,3),N(3,2),NT(2,3),SUMINV(2,2),
      REAL(8) :: S12(3),STRESSLG(3),S12L(3)

      real c, s, angleP, prine1, prinemat
      real(8) detM
      real(8), parameter :: pi = 4*atan(1.0_8)
      real(8), parameter :: gmin = 0.1
      real(8), parameter :: cmin = 1250

      PARAMETER (ONE=1.0D0, TWO=2.0D0)

      E     =PROPS(1)!ELASTIC MODULUS(ISOTROPIC)
      ANU=PROPS(2)!POISSON'S RATIO(ISOTROPIC)
      fct   =PROPS(3)!PEAK MODE I STRESS
      GF    =PROPS(4)!FRACTURE ENERGY (MODE I)
      fcs   =PROPS(5)!PEAK MODE II STRESS
      GFS   =PROPS(6)!FRACTURE ENERGY (MODE II)
      ecru  =PROPS(7)!"maximum normal strain" in crack for Mode II and reduced compression
stiffness calculation
      fi    =PROPS(8)!FACTOR FOR INTIAL SHEAR STIFFNESS (MODE II)

C   (1) COMPUTE THE PRINCIPAL STRAIN VALUES

C         (1.1) Update the global strain

      STRAN = STRAN + DSTRAN

C   (1.2) Compute the principal strain values (emax and emin)
```

```
      exx = STRAN(1)
      eyy = STRAN(2)
      exy = STRAN(3)/TWO

      emax = (exx+eyy)/2 + sqrt(((exx-eyy)/2)**2+(exy)**2)
      emin = (exx+eyy)/2 - sqrt(((exx-eyy)/2)**2+(exy)**2)

C     (2) DEFINE THE CRACKING CRITERIA (CRACKING STRAIN, ECR)

      ECR = fct/E

C     (2.1) Change state variable if crack criteria is met
      IF (emax >= ECR) then

      STATEV(4) = 1

      end if

C     (3) ELASTIC DOMAIN (LINEAR ELASTIC ISOTROPY)

C     (3.1) Define the elastic stiffness matrix (DC)

C           (3.1.1) Initialise the stiffness matrix (DC)
      DO I=1,NTENS
            DO J=1,NTENS
                  DC(I,J)=0.0D0
            ENDDO
      ENDDO

C     (3.1.2) Define the matrix components

      ALAMBDA=E/(ONE-ANU*ANU)

      DC(1,1)=ALAMBDA
      DC(2,2)=ALAMBDA
      DC(3,3)=ALAMBDA*((ONE-ANU)/TWO)
      DC(1,2)=ALAMBDA*ANU
      DC(2,1)=ALAMBDA*ANU

C     (3.2) Return STRESS and DDSDDE if elastic criteria are met

      IF (STATEV(4)==0) THEN

C     (3.2.1) Return DC as DDSDDE
      DDSDDE = DC

C     (3.2.2) Compute and return current STRESS
      DO I=1,NTENS
            DO J=1,NTENS
                  STRESS(I)=STRESS(I)+DDSDDE(I,J)*DSTRAN(J)
```

```
        ENDDO
    ENDDO

    end if

C       (4) CRACKED DOMAIN

C   If principal tensile strain >= cracking strain, update state variables(STATEV), stresses(STRESS) and
stiffness matrix (DDSDDE)

    IF (STATEV(4)==1) THEN

C       (4.1) Compute and store initial crack orientation (Fixed Crack Approach)

C       If material has 'cracked', we do not want to update crack orientation again for fixed crack
model
C       Define a state variable which keeps track of the crack orientation
C       If STATEV(1) == 0, Crack orientation has not yet been fixed
C       If STATEV(1) == 1, Crack orientation has been fixed

C   Determination of crack orientation in the form of cos(angleP) and sin(angleP)
      IF (STATEV(1)==0) THEN

C       We only store the crack orientation once, therefore change the crack status to 1
      STATEV(1) = 1

C       (4.1.1) Assemble the global strain tensor in matrix form
      STRANMAT(1,1) = STRAN(1)
      STRANMAT(1,2) = STRAN(3)/2
      STRANMAT(2,1) = STRAN(3)/2
      STRANMAT(2,2) = STRAN(2)

C   (4.1.2) Compute the principal strain orientation angle
      angleP = ATAN(STRAN(3)/(STRAN(1)-STRAN(2)))/2

C   (4.1.3) Assemble the transformation matrix (QMAT) to transform the global strains into the
principal directions
      QMAT(1,1) = cos(angleP)
      QMAT(1,2) = sin(angleP)
      QMAT(2,1) = -sin(angleP)
      QMAT(2,2) = cos(angleP)

C   (4.1.4) Compute the principal strain tensor
      QE = matmul(QMAT,STRANMAT)
      EP = matmul(QE,transpose(QMAT))

C   (4.1.5) Adjust principal orientation angle if needed
C   Note: The (1,1) entry in the principal strain tensor will correspond to angleP
C   Note: We need to find angleP which corresponds to the positive maximum principal strain
        (emax)
C   Note: If angleP does not correspond to emax, then angleP = angleP + pi/2
```

```
      prine1 = nint(emax*1e8)

      prinemat = nint(EP(1,1)*1e8)

      if(prine1 /= prinemat) THEN

      angleP = angleP + pi/2

      END IF

C   (4.1.6) Store cos(angleP) and sin(angleP)
      STATEV(2) = cos(angleP)
      STATEV(3) = sin(angleP)

      END IF

C   (4.2) Transform the global strain tensor STRAN to the crack basis

C   (4.2.1) Define transformation matrix (TE) to transform global strains to local strains in crack

                  c = STATEV(2)

                  s = STATEV(3)

      TE(1,1)= c*c
      TE(1,2)= s*s
      TE(1,3)= s*c
      TE(2,1)= s*s
      TE(2,2)= c*c
      TE(2,3)= -s*c
      TE(3,1)= -TWO*s*c
      TE(3,2)= TWO*s*c
      TE(3,3)= c*c - s*s

C         (4.2.2) Determine total (TRACE) and incremental (DTRACE) local crack strains from global
strains
      TRACE = MATMUL(TE,STRAN)

      DTRACE = MATMUL(TE,DSTRAN)

C   (4.3) Compute local stress components and corresponding tangent stiffness from material model
C       Note: Compute stress on limit function for loading
C                   Note: Compute stress incrementally for unloading and reloading

C   (4.3.1) Transform STRESS tensor at the beginning of increment to local crack basis

C   (4.3.1.1) Assemble stress transformation matrix TS12

      TS12(1,1) = c*c
      TS12(1,2) = s*s
      TS12(1,3) = TWO*s*c
```

```
      TS12(2,1) = s*s
      TS12(2,2) = c*c
      TS12(2,3) = -TWO*s*c

      TS12(3,1) = -s*c
      TS12(3,2) = s*c
      TS12(3,3) = c*c - s*s

C   (4.3.1.2) Compute local crack stresses at the start of the increment
      S12 = matmul(TS12,STRESS)

C   (4.3.2) Compute crack normal strain  (total strain - cracking strain)
      e1cr = TRACE(1) - ECR

C   (4.3.3) Adjust unload and reload stiffness in Mode I depending on maximum crack width achieved

      IF (e1cr*CELENT <= 0.3 .AND. STATEV(7) == 0) THEN
      STATEV(6) = 0

      END IF

      IF (e1cr*CELENT > 0.3) THEN

      STATEV(6) = 1
      STATEV(7) = 1

      END IF

      IF (STATEV(6)==0) THEN

      EUR = (CELENT*fct*exp(-fct*0.169*GF**-1))/(0.169-0.1045)

      END IF

      IF (STATEV(6)==1) THEN

      EUR = (CELENT*fct*exp(-fct*0.458*GF**-1))/(0.458-0.3148)

      END IF


C   (4.3.4)         Compute traction normal to crack (Mode I) and corresponding tangent stiffness
C         Note: Initially assume unload/reload stiffness
C         Note: Initially assume traction value calculated for unloading/reloading
C         Note: T1A is the traction value for a state of unloading or reloading
C         Note: T1B is the traction value for loading along the limit function
C         Note: Traction value is the lesser of T1A and T1B

            a = -(fct**2)*CELENT*GF**-1
            b = -fct*CELENT*GF**-1
```

```
      DNT(1,1) = EUR

      T1A = S12(1) + EUR*(DTRACE(1))
      T1B = fct*exp(b*e1cr)

      S12(1) = T1A

      IF (ABS(T1B) < ABS(T1A)) THEN

      DNT(1,1) = a*exp(b*e1cr)
      S12(1) = T1B

      END IF

C   (4.3.5)         Compute shear traction parallel to crack (Mode II) and corresponding tangent
stiffness
C         Note: Initially assume unload/reload stiffness
C         Note: Initially assume traction value calculated for unloading/reloading
C         Note: T12A is the traction value for a state of initial loading, unloading or reloading
C         Note: T12B is the traction value for loading along the limit function
C         Note: Traction value is the lesser of T12A and T12B

      as = -(fcs**2)*CELENT*GFS**-1
      bs = -fcs*CELENT*GFS**-1

      DNT(2,2) = max((1-((e1cr*CELENT)/ecru))*DC(3,3)*fi,gmin)

      DNT(2,2) = DNT(2,2)*CELENT

      T12A = S12(3) + DNT(2,2)*(DTRACE(3))
      T12B = (TRACE(3)/ABS(TRACE(3)))*fcs*exp(bs*ABS(TRACE(3)))
      S12(3) = T12A

      IF (ABS(T12B) < ABS(T12A)) THEN

      DNT(2,2) =  as*exp(bs*ABS(TRACE(3)))
      S12(3) = T12B

      END IF

C   (4.3.6) Complete assembly of local tangent stiffness matrix
      DNT(1,2) = 0
      DNT(2,1) = 0

C   (4.3.7) Adjustment to elastic stiffness matrix (Reduced compression stiffness)
C         Note: This adjustment is only valid for a vertical crack where crack basis does not differ from
global basis

      DC(2,2) = max((1-((e1cr*CELENT)/ecru))*DC(2,2)*0.05,cmin)
```

```
C       (4.4) Assemble global cracked material tangent stiffness matrix (DCRCO)

      N(1,1) = c*c
      N(1,2) = -s*c
      N(2,1) = s*s
      N(2,2) = s*c
      N(3,1) = TWO*s*c
      N(3,2) = c*c - s*s

      NT = TRANSPOSE(N)

      DCON = MATMUL(DC,N)
      NTDCO = MATMUL(NT,DC)

      NTDCON = MATMUL(NTDCO,N)
      SUMINV = DNT + NTDCON

      CALL minv(SUMINV,detM)

      DCRCO = DC - MATMUL(DCON,MATMUL(SUMINV,NTDCO))

C   (4.5) Compute local normal stress parallel to crack S12(2) from DCRCO and DSTRAN

      SXX = DCRCO(1,1)*DSTRAN(1) + DCRCO(1,2)*DSTRAN(2)
      SXX = SXX + DCRCO(1,3)*DSTRAN(3)

      SYY = DCRCO(2,1)*DSTRAN(1) + DCRCO(2,2)*DSTRAN(2)
      SYY = SYY + DCRCO(2,3)*DSTRAN(3)

      SXY = DCRCO(3,1)*DSTRAN(1) + DCRCO(3,2)*DSTRAN(2)
      SXY = SXY + DCRCO(3,3)*DSTRAN(3)

       STRESSLG(1) = STRESS(1)+SXX
       STRESSLG(2) = STRESS(2)+SYY
       STRESSLG(3) = STRESS(3)+SXY

      S12L = matmul(TS12,STRESSLG)

      S12(2) = S12L(2)

C       (4.6) Return STRESS and DDSDDE

      STRESS = MATMUL(TRANSPOSE(TE),S12)

      DDSDDE = DCRCO

      END IF

    RETURN

    END
```

```
C   (A) Subroutine to compute inverse of a 2x2 matrix

    subroutine minv(mat,detMF)

    REAL(8) :: mat(2,2), matC(2,2)

    REAL(8) :: detMF

    detMF = (mat(1,1)*mat(2,2)) - (mat(1,2)*mat(2,1))

    if (detMF == 0D0) then

     write (*,*) 'MATRIX HAS NO INVERSE!'

    end if

    if (detMF /= 0D0) then

    !Assemble adjugate matrix
    matC(1,1) = mat(2,2)
    matC(1,2) = -mat(1,2)
    matC(2,1) = -mat(2,1)
    matC(2,2) = mat(1,1)

            !inverse of matrix
    mat = (1/detMF)*matC

    end if

    return

    end subroutine minv
```

F Mode II calibration & verification data (Chapter 6)

F.1 Calibration data

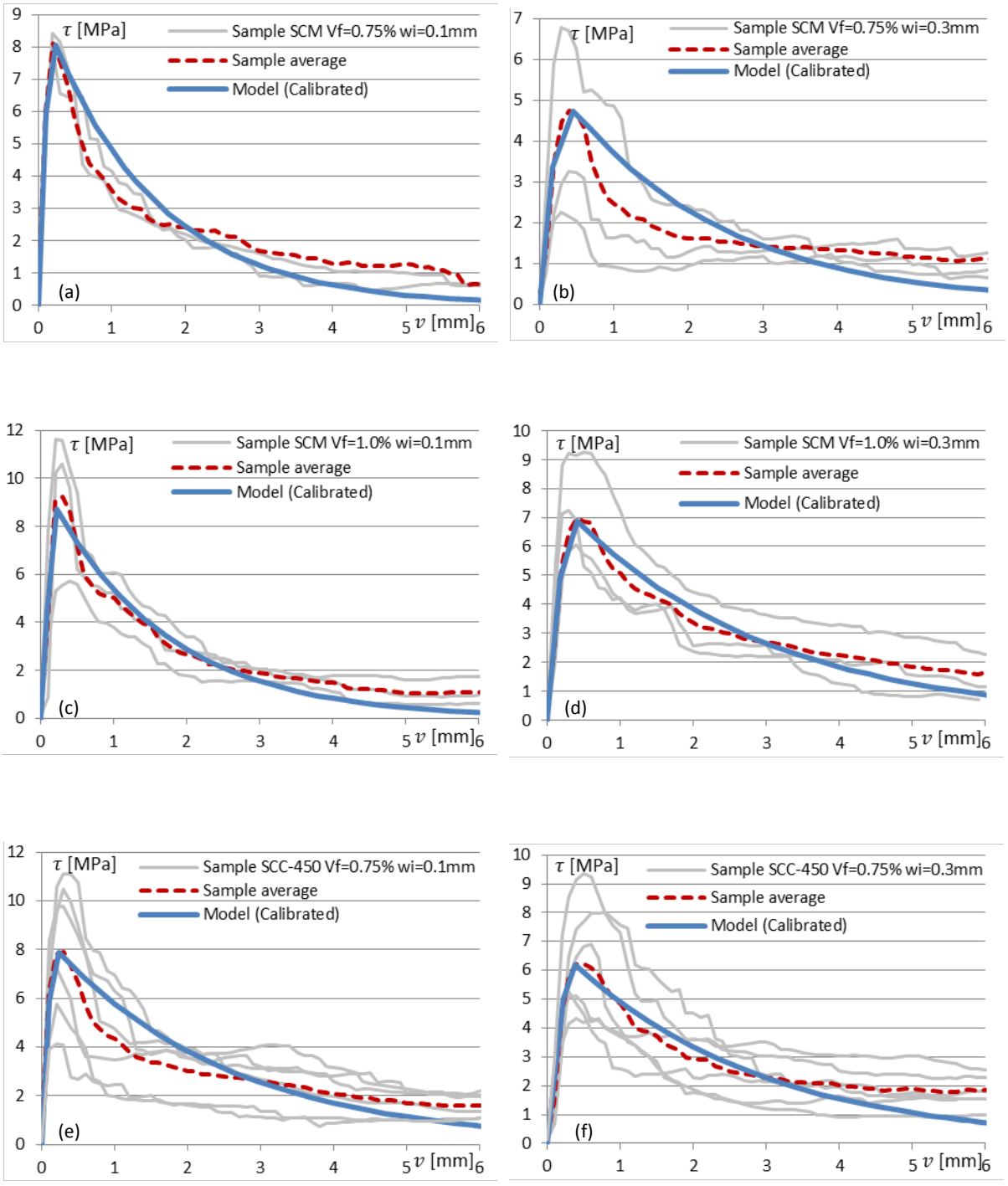

Fig. F.1 – Mode II model calibration: Shear stress τ vs. shear displacement v (a)-(f)

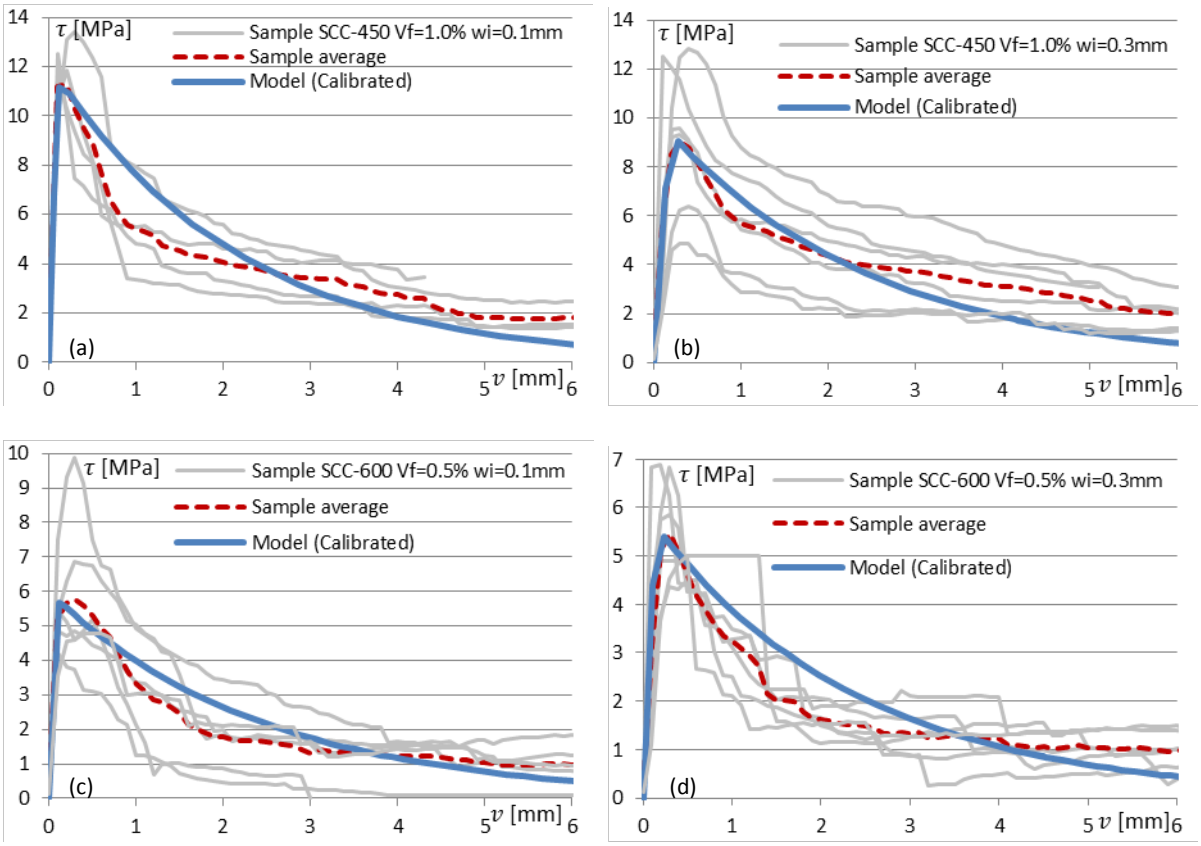

Fig. F.2 – Mode II model calibration: Shear stress τ vs. shear displacement v (a)-(d)

F.2 Verification data

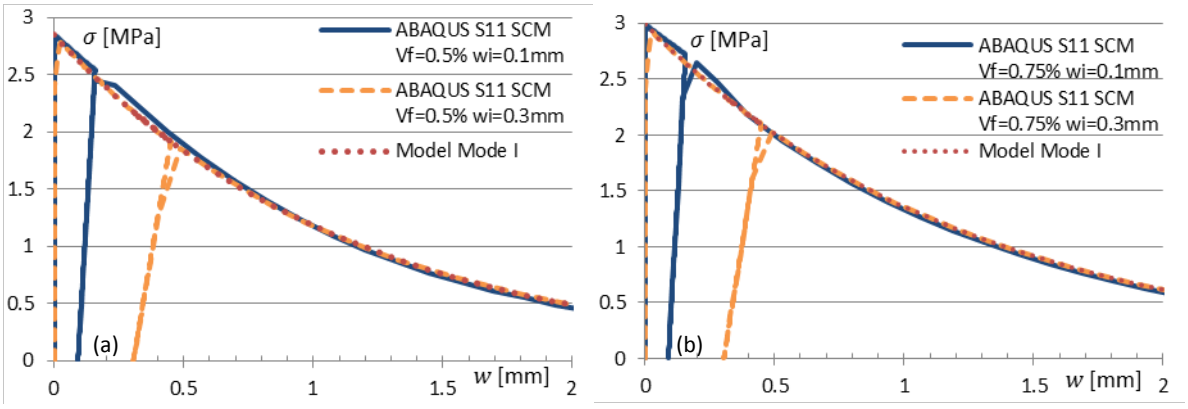

Fig. F.3 – S11 vs crack width, w for w_i=0.1 and 0.3mm (a) SCM Vf=0.5%; (b) SCM Vf=0.75%

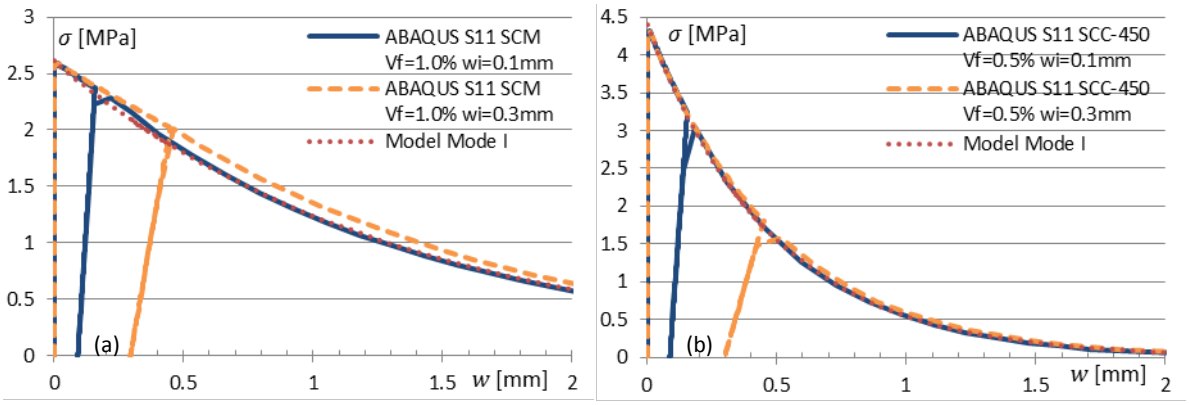

Fig. F.4 – S11 vs crack width, w for w_i=0.1 and 0.3mm (a) SCM Vf=1.0%; (b) SCC-450 Vf=0.5%

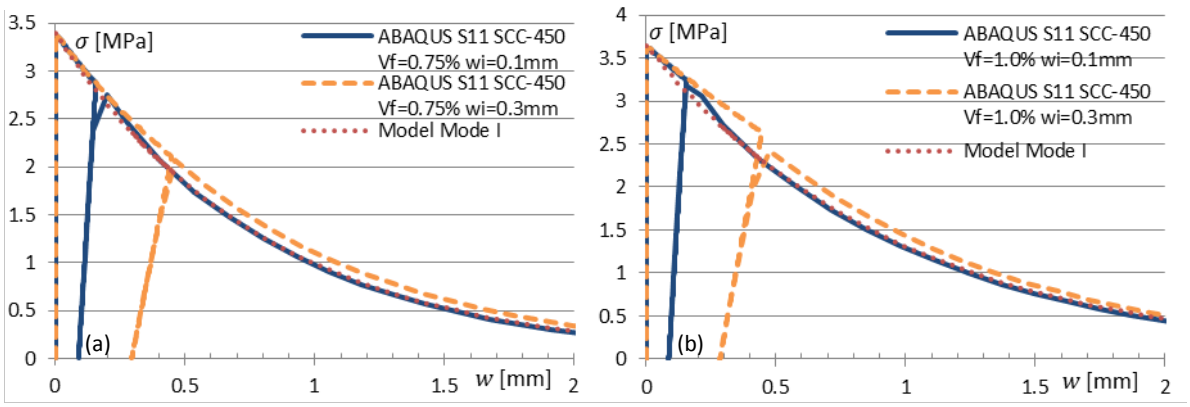

Fig. F.5 – S11 vs crack width, w for w_i=0.1 and 0.3mm (a) SCC-450 Vf=0.75%; (b) SCC-450 Vf=1.0%

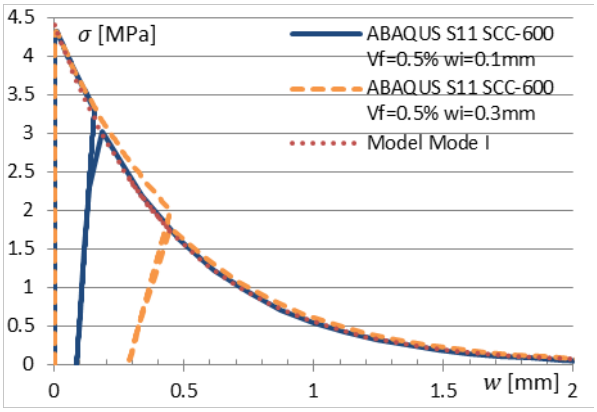

Fig. F.6 – S11 vs crack width, w for w_i=0.1 and 0.3mm (SCC-600 Vf=0.5%)

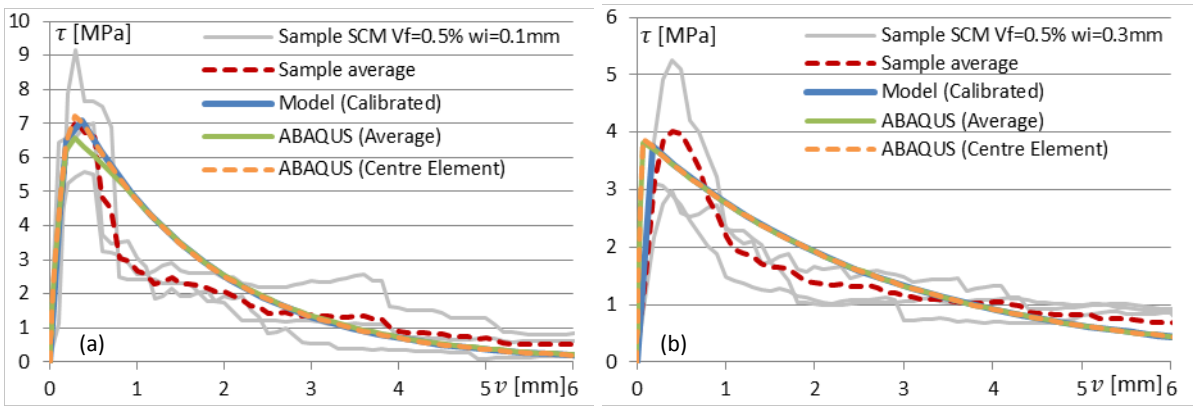

Fig. F.7 – S12 vs v for (a) SCM Vf=0.5% wi=0.1mm and (b) SCM Vf=0.5% wi=0.3mm

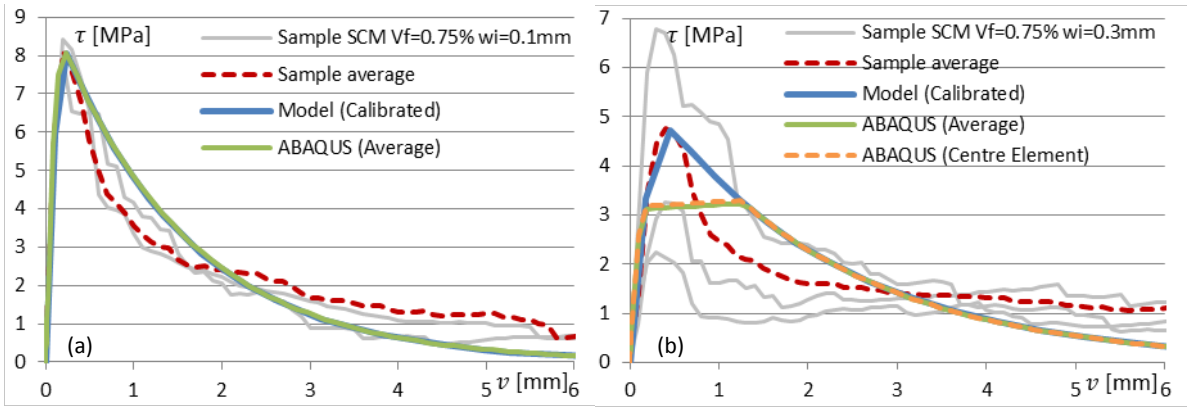

Fig. F.8 – S12 vs v for (a) SCM Vf=0.75% wi=0.1mm and (b) SCM Vf=0.75% wi=0.3mm

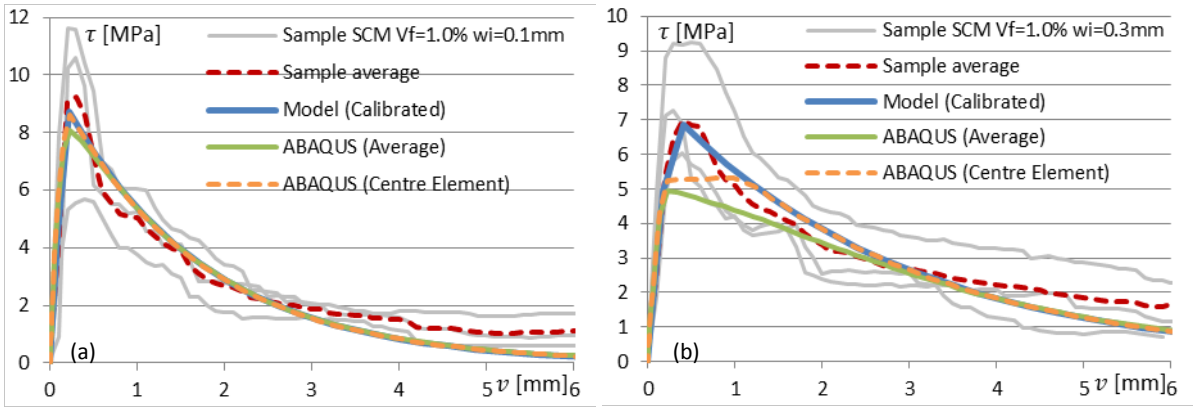

Fig. F.9 – S12 vs v for (a) SCM Vf=1.0% wi=0.1mm and (b) SCM Vf=1.0% wi=0.3mm

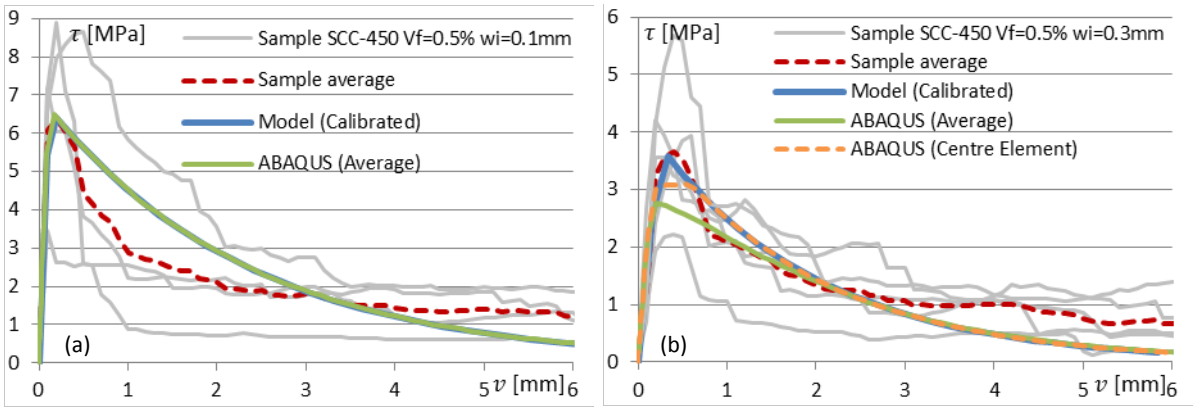

Fig. F.10 – S12 vs v for (a) SCC-450 Vf=0.5% wi=0.1mm and (b) SCC-450 Vf=0.5% wi=0.3mm

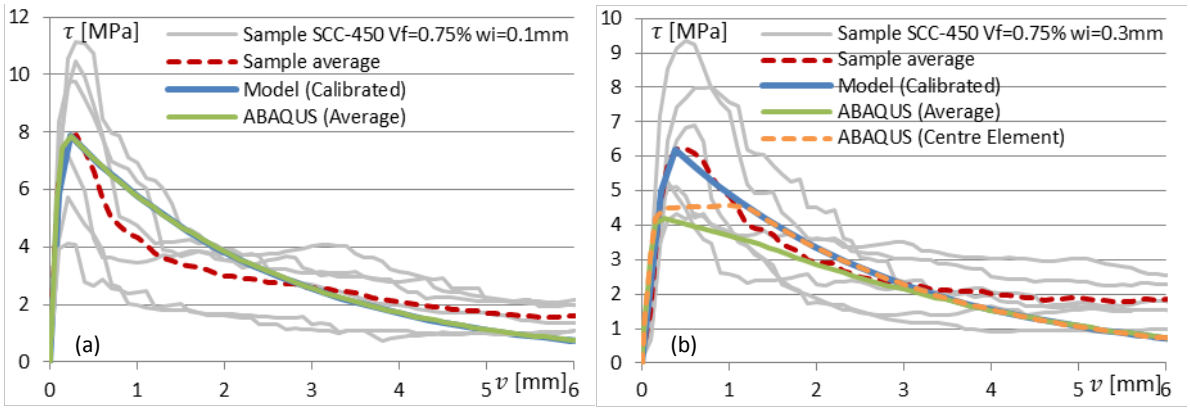

Fig. F.11 – S12 vs v for (a) SCC-450 Vf=0.75% wi=0.1mm and (b) SCC-450 Vf=0.75% wi=0.3mm

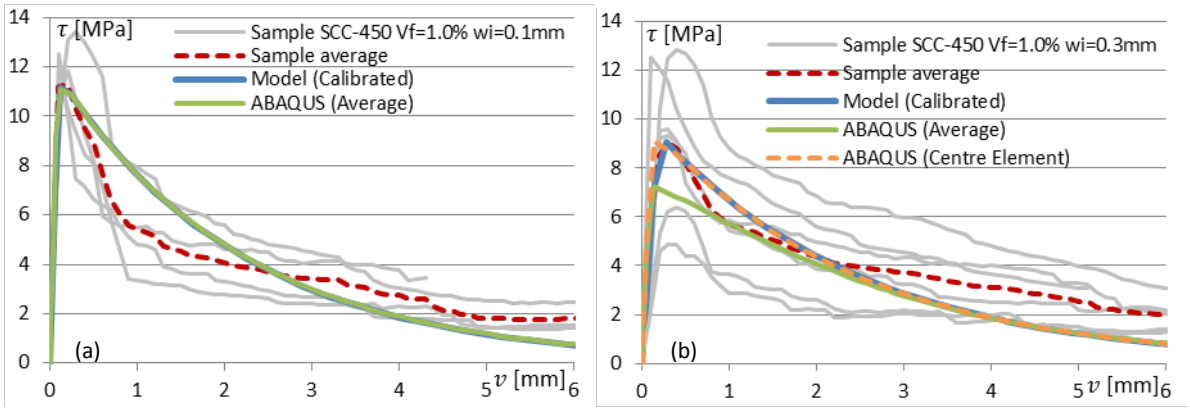

Fig. F.12 – S12 vs v for (a) SCC-450 Vf=1.0% wi=0.1mm and (b) SCC-450 Vf=1.0% wi=0.3mm

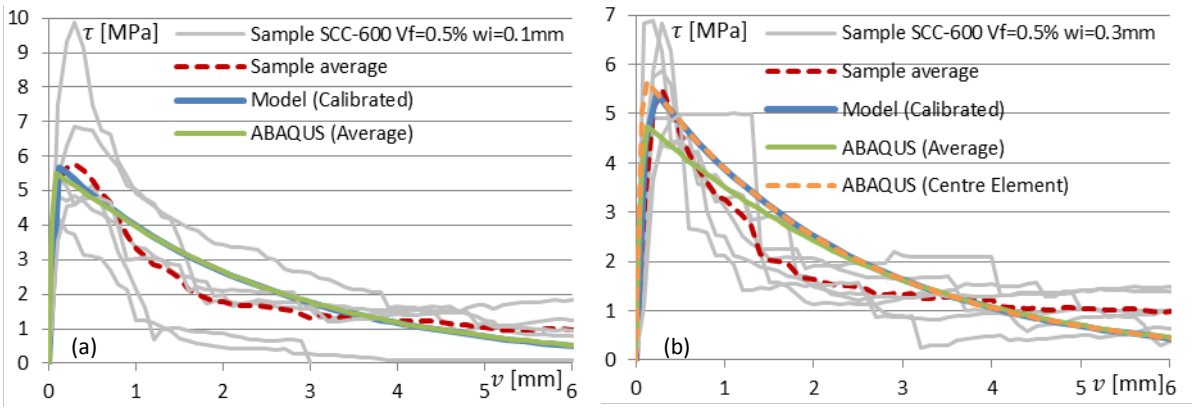

Fig. F.13 – S12 vs v for (a) SCC-600 Vf=0.5% wi=0.1mm and (b) SCC-600 Vf=0.5% wi=0.3mm

G Empirical link between Micro and Meso-scale data

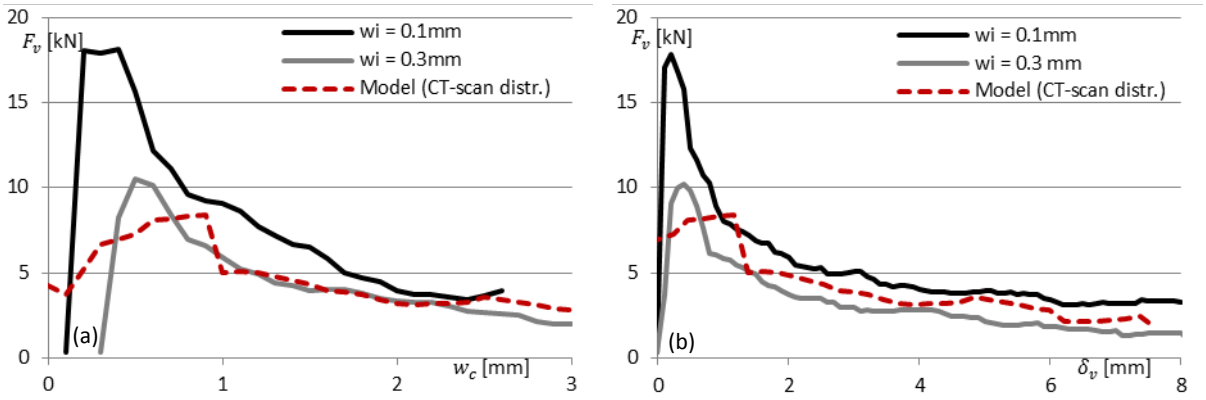

Fig. G.1 – Shear load (F_v [kN]) vs. (a) normal displacement/crack opening (w_c [mm]) and (b) shear displacement (δ_v [mm] for SCC-450 V_f = 0.50%

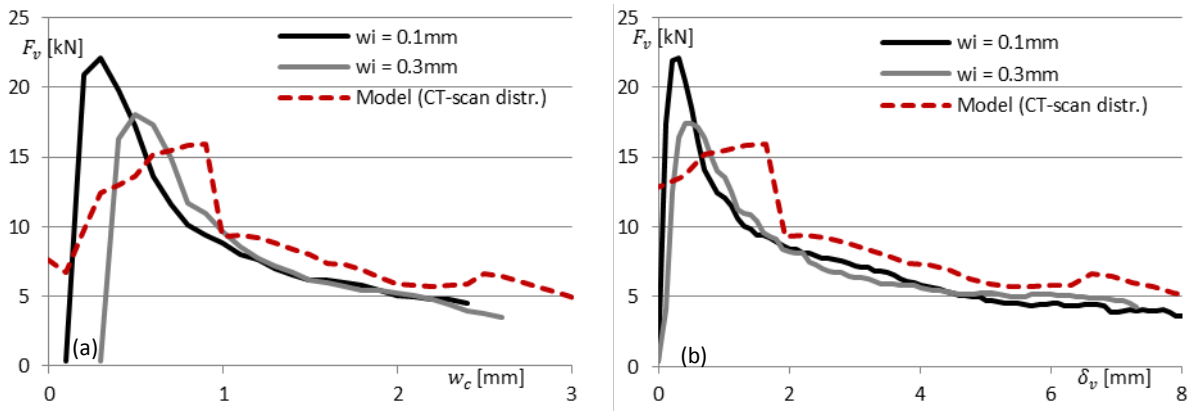

Fig. G.2 – Shear load (F_v [kN]) vs. (a) normal displacement/crack opening (w_c [mm]) and (b) shear displacement (δ_v [mm] for SCC-450 V_f = 0.75%

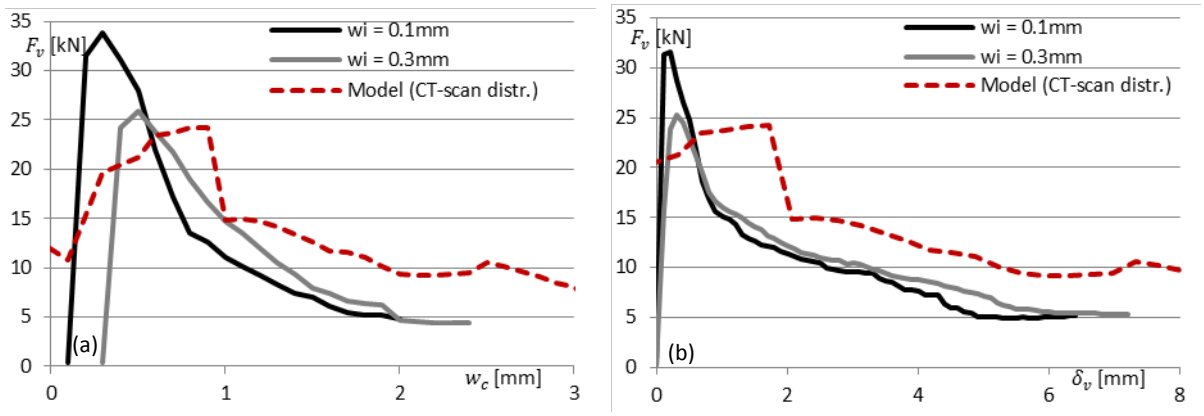

Fig. G.3 – Shear load (F_v [kN]) vs. (a) normal displacement/crack opening (w_c [mm]) and (b) shear displacement (δ_v [mm] for SCC-450 V_f = 1.00%

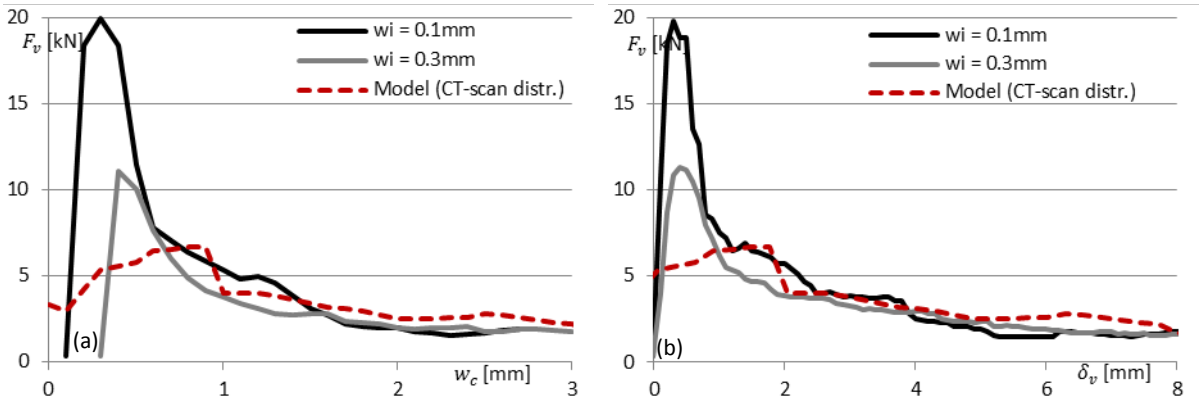

Fig. G.4 – Shear load (F_v [kN]) vs. (a) normal displacement/crack opening (w_c [mm]) and (b) shear displacement (δ_v [mm] for SCM V_f = 0.50 %

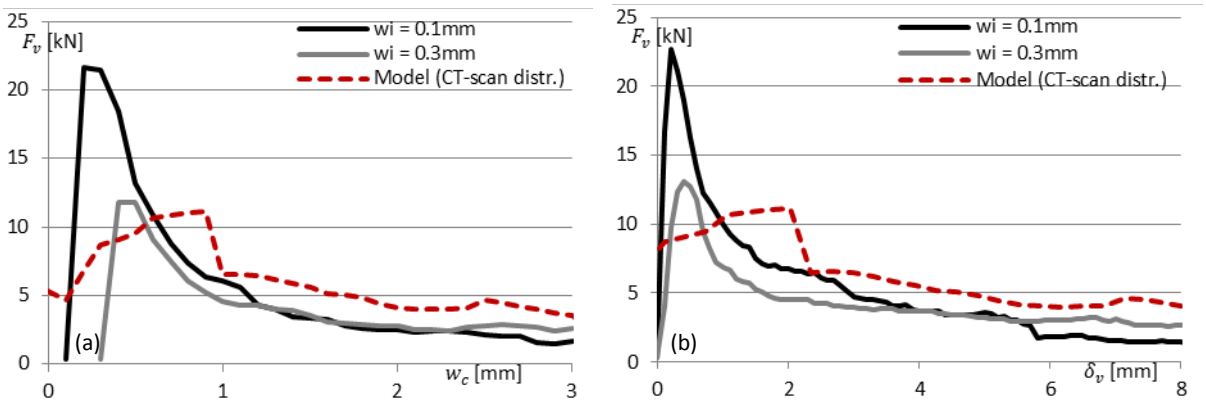

Fig. G.5 – Shear load (F_v [kN]) vs. (a) normal displacement/crack opening (w_c [mm]) and (b) shear displacement (δ_v [mm] for SCM V_f = 0.75 %

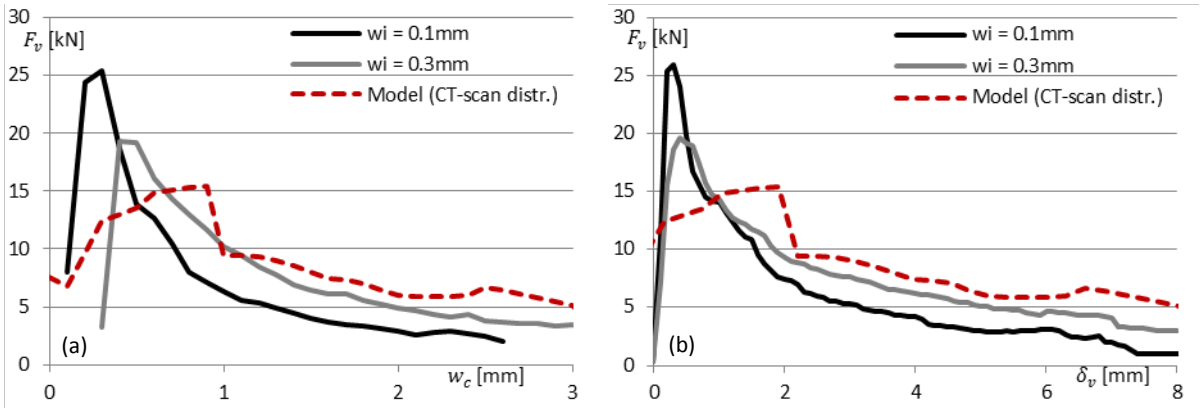

Fig. G.6 – Shear load (F_v [kN]) vs. (a) normal displacement/crack opening (w_c [mm]) and (b) shear displacement (δ_v [mm] for SCM V_f = 1.00 %

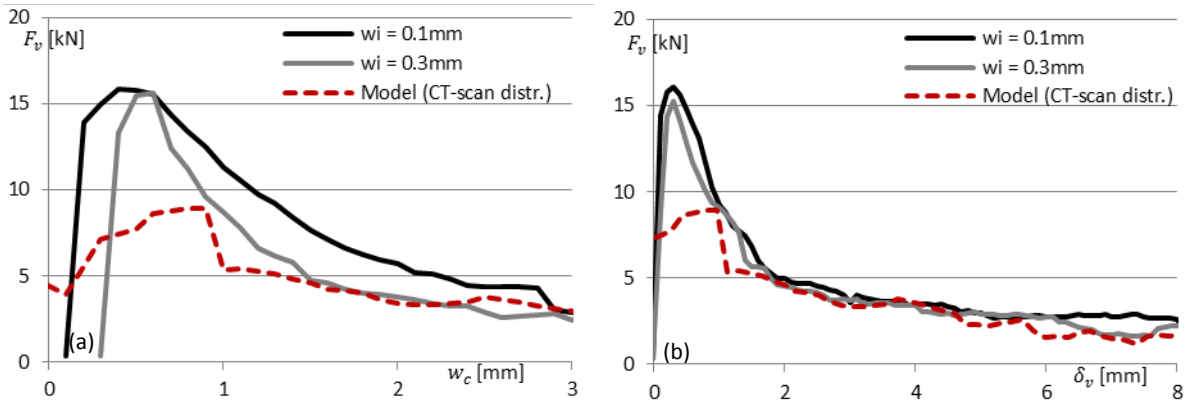

Fig. G.7 – Shear load (F_v [kN]) vs. (a) normal displacement/crack opening (w_c [mm]) and (b) shear displacement (δ_v [mm] for SCC-600 V_f = 0.50 %